Reduction of Se( ), Se( ) and Re( ) by Fe reactive phases present in CEMs and COx

Kaifeng Wang

THÈSE

Pour obtenir le grade de

DOCTEUR DE L'UNIVERSITÉ GRENOBLE ALPES

Spécialité : Sciences de la Terre et de l'Univers et de l'Environnement

Arrêté ministériel : 25 mai 2016

Présentée par

Kaifeng WANG

Thèse dirigée par **Laurent CHARLET**,Professeur, Université Grenoble Alpes
et codirigée par **Alejandro FERNANDEZ-MARTINEZ**,chercheur, Université Grenoble Alpes

préparée au sein du **Laboratoire Institut des Sciences de la Terre**
dans **l'École Doctorale Sciences de la Terre de lEnvironnement et des Planètes**

Réduction Se(IV), Se(VI) et Re(VII) par les phases réactives au Fe présentes dans le CEMs et le COx

Reduction of Se(IV), Se(VI) and Re(VII) by Fe reactive phases present in CEMs and COx

Thèse soutenue publiquement le **30 juin 2022**,
devant le jury composé de :

Monsieur Laurent CHARLET
PROFESSEUR DES UNIVERSITES, Université Grenoble Alpes, Directeur de thèse
Monsieur Anthony CHAPPAZ
PROFESSEUR, Central Michigan University, Rapporteur
Monsieur Horst GECKEIS
PROFESSEUR, Karlsruhe Institute of Technology, Rapporteur
Monsieur Benjamin GILBERT
DOCTEUR EN SCIENCES, Lawrence Berkeley National Laboratory (LBNL) - Energy Geosciences Division (EGD), Examinateur
Monsieur Laurent TRUCHE
PROFESSEUR DES UNIVERSITES, Université Grenoble Alpes, Président
Monsieur Alejandro FERNANDEZ-MARTINEZ
CHARGE DE RECHERCHE, CNRS, Co-directeur de thèse
Monsieur Benoît MADE
DOCTEUR EN SCIENCES, agence nationale pour la gestion des déchets radioactifs (Andra), Examinateur

Abstract

The retention including sorption and redox transformations of radionuclides (RNs) (e.g., ^{79}Se and ^{99}Tc) by multiple barriers is critical for assessing the risks of a nuclear waste repository. Both cementitious materials and the embedded steel corrosion products e.g., magnetite, mackinawite and pyrite, keep the reinforced cementitious structures under hyperalkaline and chemically reducing conditions. A precise determination of the redox potential (Eh) of the system is vital to assess the retention of redox-sensitive RNs. Furthermore, pyrite, magnetite and mackinawite as the naturally present redox-active Fe phases have the potential for the retention of Se and Tc leakage in nuclear waste disposal systems and enriched Se contamination. In my PhD thesis, redox interactions between selenite and mackinawite in cement pore water (CPW) was investigated by a comprehensive characterization on both aqueous and solid speciation. X-ray Absorption Spectroscopy (XAS) reveals that Se(IV) was reduced to a mixture of Se^0 and SeS_2, accompanied by the oxidation of S^{2-}/S_n^{2-} to $S_2O_3^{2-}$ and Fe(II) to Fe(III) in mackinawite identified by X-ray photoelectron spectra (XPS). However, ~99 % of aqueous selenium was present as Se_4S nano-particles confirmed by transmission electron microscopy (TEM) via the dissolution of Se from the solid. In parallel, ~62% of S^{2-}/S_n^{2-} was released into the solution, with mackinawite transforming to magnetite, $Fe(OH)_3$ and $FeS_2O_3^+$ complexed to Cl^- or OH^- species. Furthermore, Se (VI) were used as a molecular probe to explore redox interactions by mackinawite, pyrite and magnetite in CPW and the Eh values of the systems were obtained by using the Nernst equation based on chemical/spectroscopic measurements. Remarkably, the measured Eh value around -0.388 V of Se(VI) reaction with mackinawite in CPW system was mainly controlled by the FeO(OH)/FeS couple. In the system of Se(VI) reaction with magnetite in CPW, the measured Eh was around -0.536 V probably determined by the Fe_3O_4/Fe^{2+} couple. It seems that the Eh value (-0.350 V) of pyrite reaction with Se(VI) in CPW system was imposed by the $Fe(OH)_3/Fe(OH)_3^-$ couple. In addition, the reduction of Se(VI) and Re(VII), as the chemical surrogate for Tc(VII), by

mackinwate, magnetite and pyrite has been investigated by XAS and S/TEM in 0.1 M NaCl solutions under air, N_2 and H_2 atmospheres. The results show that Se(VI) could be reduced to Se(-II, -I and 0) and three different morphologies and structures of Se^0 formed: trigonal γ-Se on magnetite, monoclinic β-Se on mackinawite and amorphous Se on pyrite. Also, the retention mechanisms of Re(VII) follows nonredox complexation and reduction to ReO_3 under air atmosphere, but reductive precipitation, i.e., Re(IV), under N_2 and H_2 atmospheres. The Eh of the suspensions, effected by dissolved aqueous O_2 and H_2, have an impact for the Se and Re retention. Besides, Aqueous analysis shows that Se(VI) uptake was not significant with quite the same value (K_d = 4~5 mL/g) on Callovo-Oxfordian in both N_2 and H_2 conditions. Se(VI) was adsorbed on nature pyrite, and reduced to Se(0) directly under N_2 condition, but stepwise reduction of Se(VI) to Se(IV) and then to Se(0) by natural pyrite was observed under H_2 condition. H_2 could dissociate into H· on pyrite (210) surface and H· probably favor the reduction of Se(VI). The above results obtained could provide valuable data for the safety assessment of nuclear waste disposal and a better understanding for the reductive precipitation of enriched Se contamination in natural confinement.

Acknowledgment

The summer of 2022 has arrived in Grenoble, and the scenery in front of my window is as beautiful as it I saw four years ago. But time flies. My doctoral study is coming to the end. I would like to express my acknowledgment here.

Professor Laurent Charlet and Dr. Alejandro Fernandez-Martinez, my supervisors, greatly helped me in my PhD years. I still remember the first time I met with Laurent Charlet. A monsieur with white hair and smile on his face walked up to me. His kindness told me that he would not “push” me a lot and we would get along well in the following years. As it turns out, I am right. My supervisors have a profound scientific knowledge on chemical reactivity of (nano) particles, international academic frontier vision and a rigorous and pragmatic scientific attitude. They have a deep impact on my academic research during my PhD study, i.e., clarifying the research objectives, dealing with the confusing experimental data, structuring the scientific writing and becoming independent in research. Laurent Charlet is also like a friend. We often share something in our life and his experience encourages me a lot as life is not always “bien”. One of my reasons I applied for to be a PhD student in UGA is to have an opportunity to measure my samples in synchrotron facilities. Fortunately, with the help of my supervisors, I got the beamlines for several times.

Besides my supervisors, I would like to thank all my colleagues in ISTerre: Mr. Nathaniel Findling, Ms. Delphine Tisserand, Dr. Géraldine Sarret, Dr. Roland Hellmann, Ms. Sarah Bureau, Ms. Valérie Magnin, Mr. Campillo Cressot Sylvain, Ms. Denti Simona, Ms. Papaslioti Evgenia-Maria and Ms. Carolina Guida and so on. ISTerre is a big family and full of harmony and warmth.

I express my very grateful to Dr. Bin Ma from PSI and Dr. Jiliang Liu from ESFR for their strong support and collaboration for my PhD research. I also thank my friends Dr. Qi Zhou, Dr. Yang Li, Mr. Hong Li, Dr. Ge Zhu, Mr. Shun Yao and Mr. Xiong Ou and so on.

I deeply appreciate to Dr. Benoît Madé and Dr. Pierre Hénocq for the financial

support from ANDRA (Agence Nationale pour la gestion des Déchets Radioactifs, Châtenay-Malabry) for project funding and laboratory equipment and China Scholarship Council (CSC) for financial support during my PhD study. I also acknowledge to Dr. Andreas C Scheinost from ESRF and Dr. Laura Simonelli from ALBA for the beamline support.

I would like to express my sincere thanks to Prof. Horst Geckeis, Prof. Anthony Chappaz, Prof. Laurent Truche, Dr. Benjamin Gilbert and Dr. Benoît Made for accepting the invitation to be the referees of my thesis.

Finally, I would like to thank my family. They always support me spiritually and encourage me when I am depressed.

Thank myself for maintaining a good mood and good health during the COVID epidemic.

Publications during PhD thesis (2018-2022)

1. **Wang, K. F.**; Fernandez-Martinez, A; Simonelli, L.; Madé, B.; Hénocq, P.; Ma, B.; Charlet, L., Redox Interaction between Selenite and Mackinawite in Cement Pore Water. *Environmental Science & Technology* **2022,** *56* (9), 5602-5610.
2. Ma, B.; Fernandez-Martinez, A.; **Wang, K. F.**; Made, B.; Henocq, P.; Tisserand, D.; Bureau, S.; Charlet, L., Selenite Sorption on Hydrated CEM-V/A Cement in the Presence of Steel Corrosion Products: Redox vs Nonredox Sorption. *Environmental Science & Technology* **2020,** *54* (4), 2344-2352.
3. **Wang, K. F.**, Chen, Y., Findling N., Charlot F., Fernandez-Martinez, A., Charlet, L., Liu J. L., Zhang, Z. T. Formation and evolution of secondary phases and surface altered layers during borosilicate glass corrosion in pore water. *Journal of Colloid and Interface Science.* (in preparation).
4. **Wang, K. F.**; Fernandez-Martinez, A; Nicolas M. ; Simonelli, L.; Madé, B.; Hénocq, P.; Ma, B.; Charlet, L., H_2 or O_2 impact on Se(VI) reduction by mackinawite, magnetite and pyrite. *Water Reaearch* (in preparation).
5. **Wang, K. F.**; Fernandez-Martinez, A; Scheinost A. C.; Madé, B.; Hénocq, P.; Ma, B.; Charlet, L., H_2 impact on the reduction of Se(VI) by claystone pyrite. *Environmental Science & Technology Letter* (in preparation).
6. **Wang, K. F.**; Fernandez-Martinez, A; Findling N., Ma, B.; Simonelli, L.; Madé, B.; Hénocq, P.; Charlet, L., Cement pore water redox reaction: Eh measurement and Eh modeling. *Cement and Concrete Research* (in preparation).

Extended summary

The high level radioactive waste is disposed of by multiple barriers such as surrounding rock - buffer backfill material - metal disposal container and vitrified waste. In 2009, the French government approved ANDRA's proposal for the Bure URL repository site, which is located in the Callovo-Oxfordian (COx) formations. The disposal depth is 420-550 m below the surface. Reinforced cementitious materials are potentially used for the waste matrix, backfill, and tunnel support, which could inhibit the mobility of radionuclides (RNs) in case of eventual leakage. The specially formulated Fe-reinforced cement backfill material would provide a long-lasting alkaline environment that contributes to containment of the waste by preventing many radionuclides from dissolving in the groundwater. After a certain period of time, groundwater passes through the fracture zone of the perimeter rock disturbance layer, penetrates the buffer backfill material, metal disposal container and comes into contact with vitrified waste, which causes the radioactive elements from vitrified waste to be released into the groundwater. For the safety assessment of nuclear waste repositories, a reliable prediction of the key redox-sensitive RNs with long half-life, i.e., ^{79}Se and ^{99}Tc, migration behavior under the relevant geochemical conditions is needed. Oxidized species of selenium, i.e., SeO_3^{2-} and SeO_4^{2-}, and technetium, i.e., TcO_4^-, are highly mobile, which has stimulated the research on selenium interactions with potential anthropogenic or natural barriers such as cements, clays or Fe phases. The various oxidation states of Se (-II, -I, 0, +IV, +VI) and Tc (+VII, +VI, +IV, +III, 0) and their complexation ability with inorganic and organic matter make their chemistry complex. Under oxidizing conditions, Se and Tc often occur as highly soluble and thus mobile oxyanionic forms. In contrast, under reducing conditions Se and Re adopt oxidation states of Se (0, -I and -II) and Tc (IV), respectively, having much lower solubility and mobility. This makes reductive immobilization an important pathway to decrease Se and Tc transport in the environment. Determining the ability of different barrier materials to reduce selenium species is therefore of high importance for the safety

assessment of radioactive waste disposal initiatives.

Redox-active Fe minerals, such as pyrite (FeS_2), magnetite (Fe_3O_4) and mackinawite (FeS), not only are ubiquitous in clay-rich formations, but also occurs as the steel corrosion product in nuclear waste disposal under anaerobic geochemical conditions. Their high reactivity and large specific surface area lead to a high potential to immobilize RNs. In addition, the production of H_2 had also been identified due to the corrosion of the steel in contact with underground pore water, and biotic as well as abiotic pathways in the Earth's crust. Therefore, studies on the adsorption/reduction of Se(VI), Se(IV) and Re(VII), as a chemical surrogate of Tc(VII), by mackinawite, magnetite and pyrite in relative environment is critical to advance our understanding on reactive concrete and natural barriers used in nuclear waste disposal systems.

In cement-rich radioactive waste repositories, mackinawite (FeS) could form at the steel corrosion interface within reinforced concrete and potentially retard the transport of ^{79}Se in cement porous media. The interaction mechanism between SeO_3^{2-} and mackinawite in cement pore water (CPW), the solution from the interconnected pore structure produced by cement hydration, was investigated by a combination of X-ray absorption spectroscopy (XAS), X-ray photoelectron spectroscopy (XPS), transmission electron microscopy (TEM) and wet chemistry methods.

The aqueous analysis of Se in Figure I showed nearly all the aqueous SeO_3^{2-} was removed by mackinawite after 96 h. Specifically, during the first 24 h the aqueous concentration of total Se was equal to that of SeO_3^{2-}, indicating that SeO_3^{2-} was the only species in aqueous phase and that the decreased amount of SeO_3^{2-} was retained in the bulk solid phase. More intriguingly, after reacting for 50 h the aqueous concentration of SeO_3^{2-} continued to decrease while the total concentration of selenium as determined in the filtrate was increasing with reaction time. This suggests that the reduction products of SeO_3^{2-} could be nano-sized zero-valent Se species, resulting in a colloidal dispersion in the suspension. Moreover, the filtrate color continued to change, and turned olive and black from 73 to 192h (Figure II), indicating the possible formation of green rust and magnetite. This was due to the oxidation of FeS and the subsequent

release of iron nanoparticles into the solution, which caused the increased of measured Fe concentrations in Figure I.

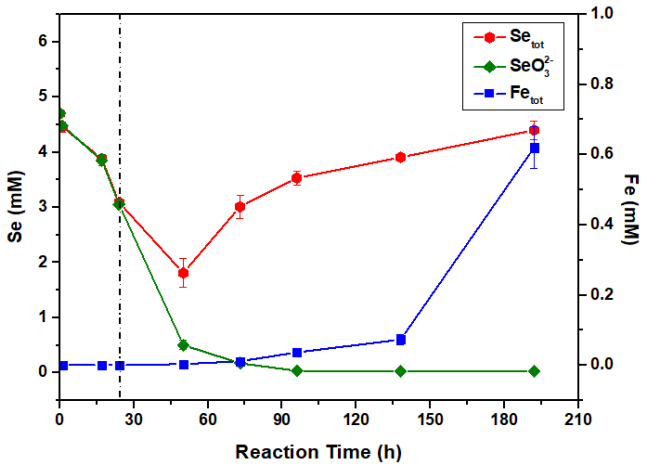

Figure I. Measured concentration of SeO_3^{2-} by IC, total Se and Fe by ICP-OES in CPW as a function of the reaction time.

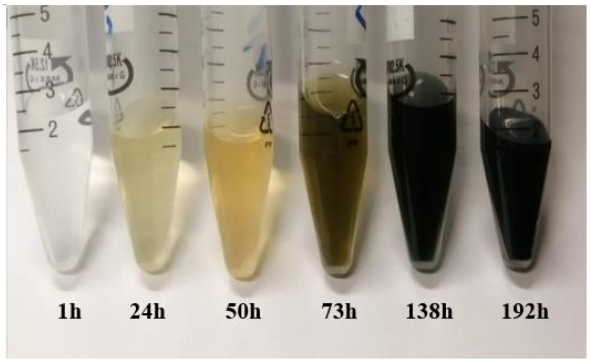

Figure II. The filtrate color of mackinawite reaction with SeO_3^{2-} in CPW at different reaction times.

Se K-edge XANES spectra and LCF results of solid samples at different reaction times (Figure III) showed that SeO_3^{2-} was mainly reduced into $FeSe_2$, FeSe and SeS_2 at 1 h, indicating that SeO_3^{2-} can be quickly adsorbed on the surface and reduced to Se(0, -I, -II). From 24 h to 196 h, all the spectra showed similar features, with ~63% SeS_2 and 30-32% Se^0 identified to be the primary solid Se species. After 192 h, the nanoparticles present in the filtrate were characterized by (S)TEM (Figure IV). The size of nanoparticles was approximately ~20 to 60 nm (Figure 3a). The nanoparticles formed at 192 h consisted of Se, S, Fe and O with a ratio of Se to S roughly at 4:1 according to EDS analysis. The high-resolution transmission electron microscopy (HRTEM) image

in Figure IV b and c illustrated that the interplanar spacing with 4.3 Å and ~2.5 Å corresponded to Se_4S and Fe_3O_4, respectively.

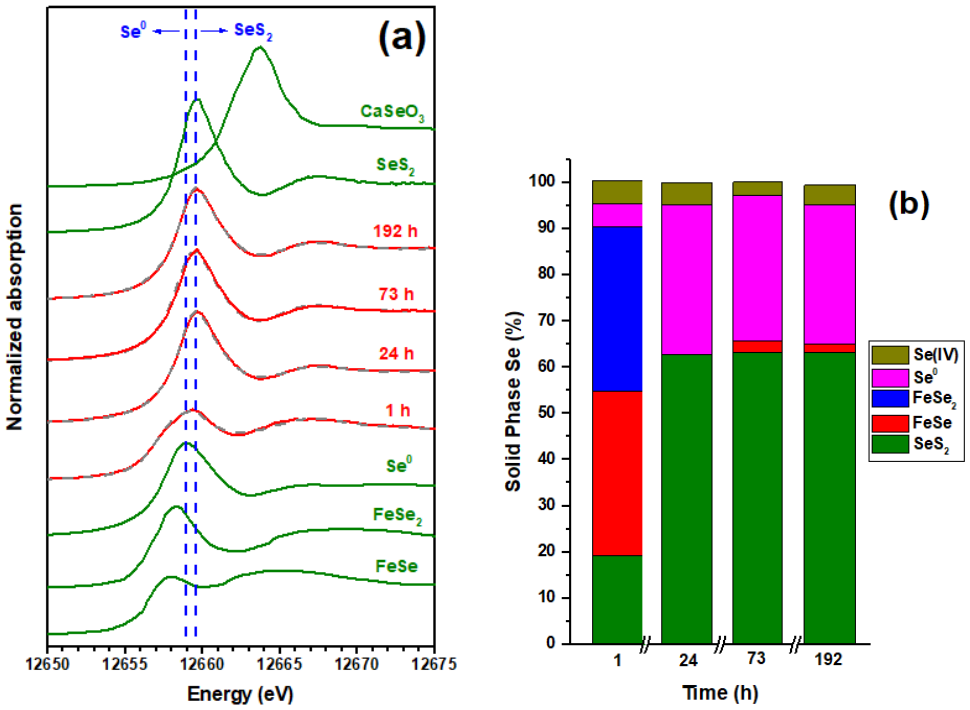

Figure III. (a) Se K-edge normalized XANES spectra of solid samples after reacting for 1, 24, 73 and 192 h, comparing to Se references. (b) The fractions of FeSe, $FeSe_2$, Se^0, SeS_2 and $CaSeO_3$ components in each Se-solid sample determined by LCF method.

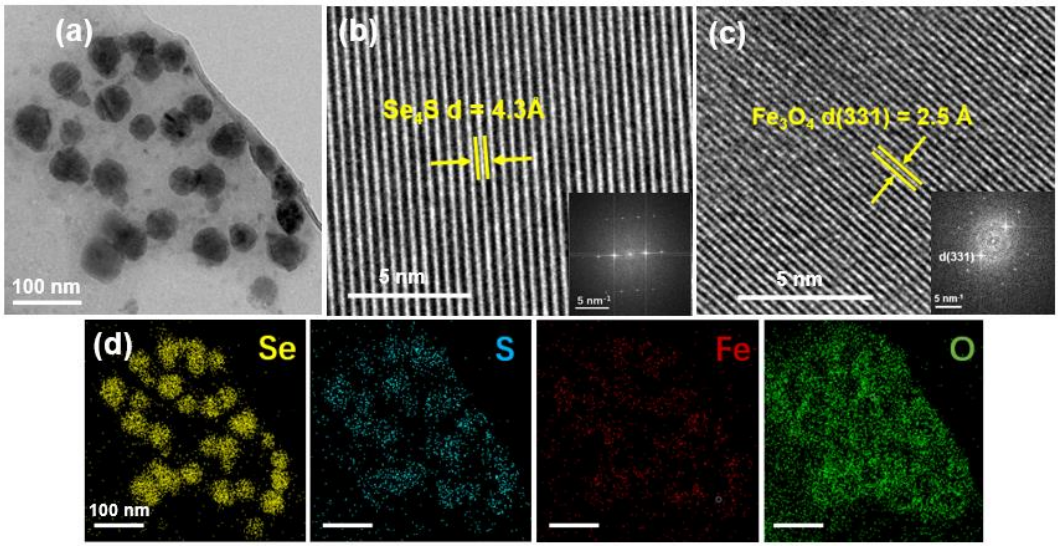

Figure IV. Transmission electron micrographs of nanoparticles found in the filtrate after reaction for 192 h. (a) Transmission electron microscopy image; high resolution transmission electron microscopy (HR-TEM) image on two spots on a single particle (b) SeS_4 and (c) Fe_3O_4 with the corresponding Fast Fourier Transform (FFT); (d)

Elemental mapping by energy-dispersive X-ray spectroscopy analysis with Se in yellow, S in blue, Fe in red and O in green.

The evolution of S was also investigated shown in Figure V. No SeO_3^{2-} was added, the S^{2-}/S_n^{2-} concentration increased very slowly and aqueous SO_4^{2-} (blank) was kept constant with increasing reaction time, suggesting a limited dissolution of mackinawite and no significant amount of aqueous SO_4^{2-} adsorbed onto mackinawite. In contrast, in the presence of SeO_3^{2-}, a critical threshold of reaction time (73 h) was observed based on the concentration change of S^{2-}/S_n^{2-}. Dissolved concentration of S^{2-}/S_n^{2-} originating from the solid increased quickly during the first 73 h, remaining roughly constant at 13-14 mM thereafter; the same tendency for the total concentration of sulfur was observed. This supports the hypothesis that 2 to 3 S^{2-}/S_n^{2-} units were substituted by one SeO_3^{2-} atom according to the concentrations of the two species.

In conclusion, using a comprehensive characterization on both aqueous and solid speciation, The whole interaction process between selenite and mackinawite in hyperalkaline conditions was successfully monitored.

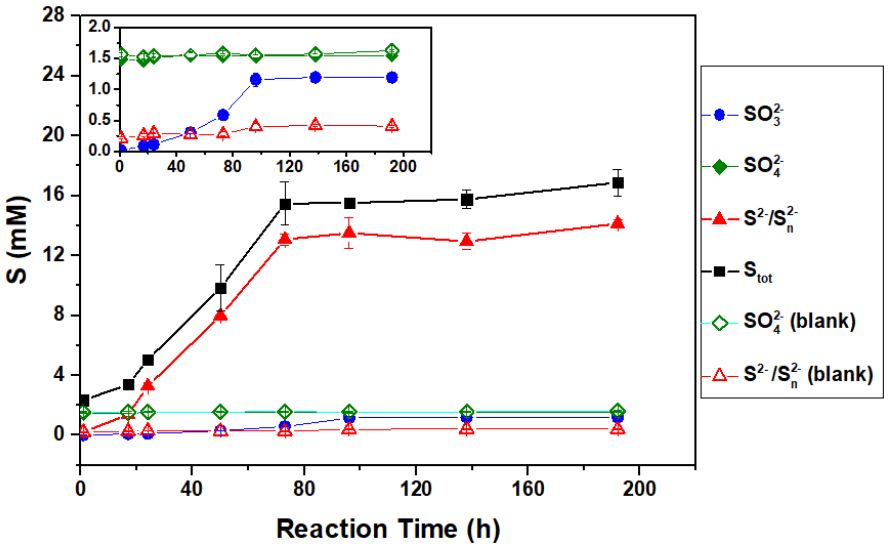

Figure V. Measured concentration profiles of (poly)sulfide (S^{2-}/S_n^{2-}), sulfate (SO_4^{2-}) and sulfite (SO_3^{2-}) of the experiment with SeO_3^{2-} and S^{2-}/S_n^{2-} (blank), SO_4^{2-} (blank) of experiment without SeO_3^{2-} as a function of reaction time. The inset shows an enlarged view of the less abundant species.

The presence of cement, concrete and the embedded steel corrosion products as the

compositions of reinforced cementitious structures keeps the system under hyperalkaline and chemically reducing conditions and the redox potential (Eh) of the system is vital to assess the retention of redox-sensitive radionuclides (RNs) in case of eventual leakage. Se(IV) and Se (VI) were used as molecule probes to explore redox interactions by mackinawite, pyrite and magnetite in CPW and the Eh values of the systems after 8 days reaction were obtained by using the Nernst equation based on chemical/spectroscopic measurements.

Se K-edge XANES spectra of solid samples and the LCF results of the solids and the references are shown in Figure VI. It is found that Se(VI) reduction occurred, to some extent, for mackniwite, pyrite and magnetite in CPW after 8 days reaction. Se(VI) was mainly reduced to 43.9 % FeSe and 27.1 % Se(IV) by mackinawite (labelled as R-I in Figure VI) with the oxidation of mackinawite to goethite, whose presence was confirmed by XPS and XRD analysis in Figure VII and VIII. Besides, 33.9 % Se(VI)-sorbed was also identified in R-I system, probably attributed to the surface complexes to form ≡FeS-Ca-SeO_4^{2-} species. The Eh value around -0.388 V in R-I system (Figure IX) appears to be controlled by the FeO(OH)/FeS couple. In addition, the LCF result of Se(VI) reaction with pyrite (R-II) for 8 days showed that 28.7 % Se(IV) and 77.9 % Se(VI) were identified, indicating that Se(VI) can be adsorbed on pyrite and partly reduced to Se(IV), accompanied by the oxidation of Fe(II) to Fe(III) in Figure VII. The measured Eh was -0.350 V in R-II system was mainly controlled by the $Fe(OH)_3/Fe(OH)_3^-$ couple. The total Fe concentration could have a critical role for the Eh determining. However, only 8.4 % Se-sorbed could be reduced to FeSe by pyrite in CPW (labelled as R-III). Furthermore, in the magnetite reaction with Se(VI) system (R-IV), it can be seen that the mainly Se-sorbed species were 15.2 % Se(0), 61.8 % Se(IV) and 19.8 % Se(VI) and Fe(II) in magnetite was oxidized to Fe(III) in Figure VII, while Se(IV) immobilization mechanism was nonredox complexation (≡Fe-O-Ca-SeO_3^{2-}) in the system of Se(IV) reaction with magnetite in CPW for 8 days (R-V system). The measured Eh around -0.417 V in R-IV system was probably determined by the Fe_3O_4/Fe^{2+} couple. Higher Eh values were imposed by the half-reactions of the

Se(VI)/FeSe, Se(VI)/Se(0) and Se(VI)/Se(IV) couples than the measured data, indicating that the redox reactions between Se(VI), S(-II), and Fe(II) in CPW have not reached equilibrium after 8 days. It was also confirmed by PHREEQC modelling coupling with the THERMOCHIMIE database.

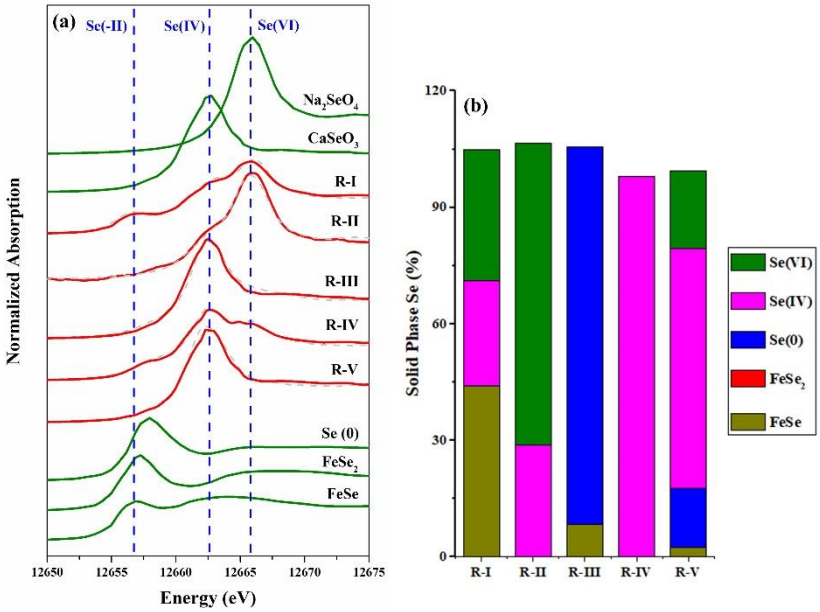

Figure VI. (a) Se K-edge normalized XANES spectra of solid samples comparing to Se references. (b) The fractions of FeSe, $FeSe_2$, Se(0), Se(IV) and Se(VI) components in each Se-solid sample determined by LCF method. R-I: mackinawite with Se(VI), R-II: pyrite with Se(VI), R-III: pyrite with Se(IV), R-IV: magnetite with Se(VI), and R-V: magnetite with Se(IV).

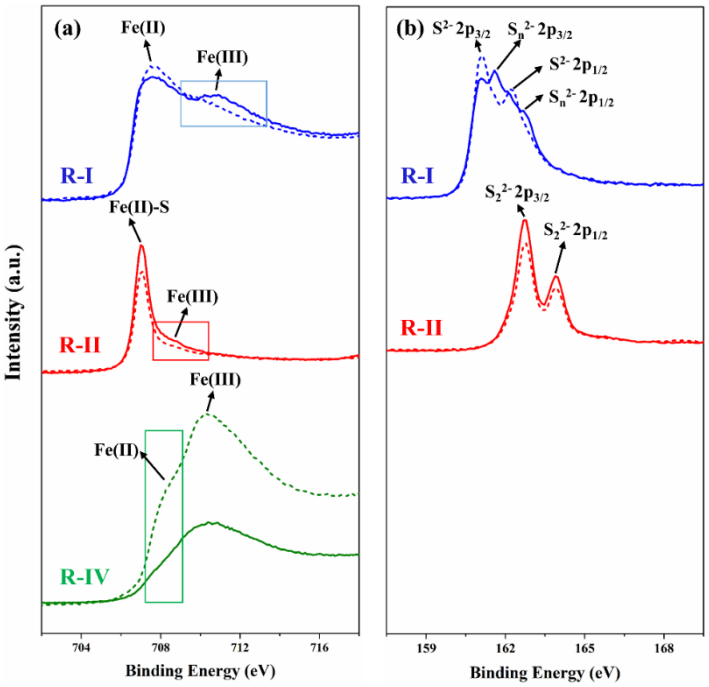

Figure VII. XPS spectra (a) Fe($2p_{3/2}$) and (b) S(2p) XPS scan. The solid lines labeled as R-I, R-II and R-IV represent the solids of macknawite, pyrite and magnetite reaction with Se(VI) in CPW for 8 days, respectively. The dashed lines represent mackinawite, pyrite and magnetite equilibrated with CPW with the same time.

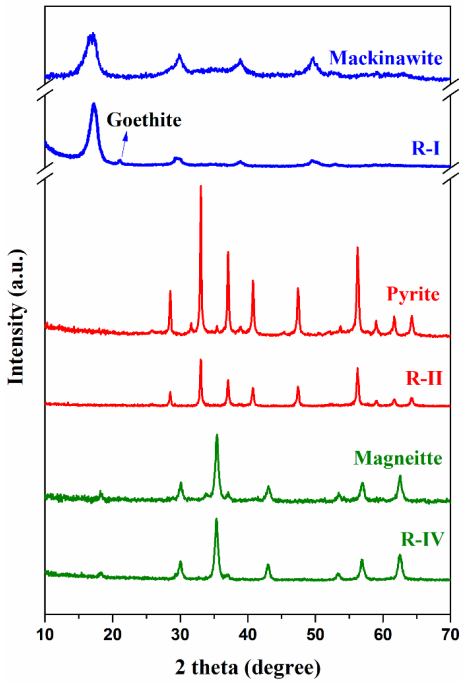

Figure VIII. The solid XRD patterns. R-I, R-II and R-IV represent the solids of macknawite, pyrite and magnetite reaction with Se(VI) in CPW for 8 days, respectively.

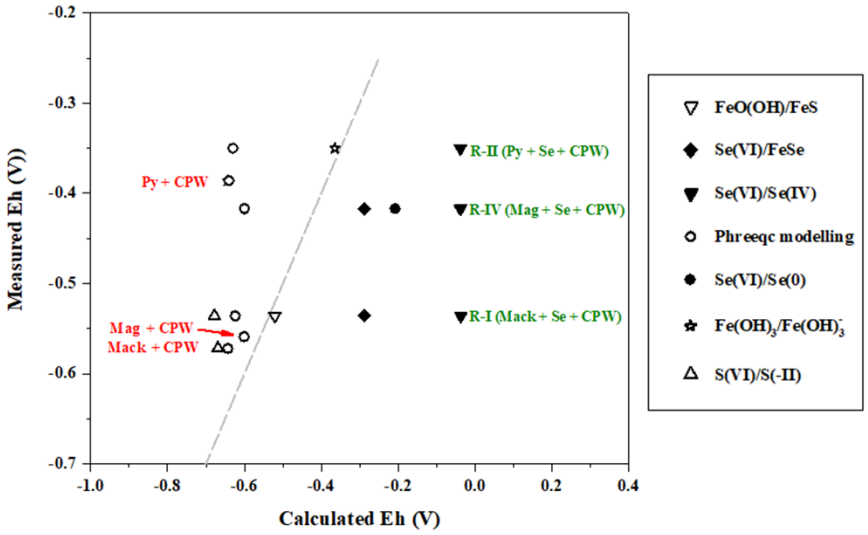

Figure IX. Comparison of Eh measurements of Fe minerals reaction with/without Se(VI) in cement pore water with potentials calculated for individual redox species.

Enriched selenium (Se) compounds by human activities are extremely toxic at high concentrations and the redox transformations of radionuclides (e.g., ^{79}Se and ^{99}Tc) are critical for assessing the risk of a nuclear waste repository. Fe(II)-bearing minerals, ubiquitous in natural system, are critical to the retardation behavior of Se and Tc. In addition, hydrogen (H_2) is not only naturally produced by biotic as well as abiotic pathways in the Earth's crust, but also occurs as the steel corrosion product in nuclear waste disposal under anaerobic geochemical conditions. Here, the reduction of Se(VI) and Re(VII), as the chemical surrogate for Tc(VII), by pyrite, magnetite and mackinawite was investigated under air, N_2 and H_2 atmospheres.

For magnetite system under N_2 atmosphere, The LCF results of Se-solid XANES sample in Figure X showed that the mainly species of Se were 67.5 % Se(0), indicating that Se(VI)-sorbed was mainly reduced to Se(0). 10.3 % FeSe, 16.3% Se(IV) and 11.9 % Se(VI) were also present in the system. Meanwhile, 59.9 % and 96.4 % Se(0) were identified to be the primary Se species under air and H_2 atmospheres, respectively. No Se(IV) and Se(VI) species existed under H_2 atmosphere but 16.3 % Se(IV) was present under N_2 atmosphere, which means aqueous H_2 could promote the reduction of Se(IV) to Se(0). After 105 days reaction, nano needles Se(0), significantly larger than nano-magnetite, was observed in magnetite system by SEM in Figure XI under N_2, air and H_2 atmospheres. The HAADF-STEM image in Figure XII shows nano needle Se(0)

readily identifiable as bright contrast spots. The nano needle was confirmed as solid-phase Se by energy-dispersive X-ray spectroscopy (EDS). Observed nano needle Se(0) was mostly 20-30 nm wide but can be about 620 nm in length. High-magnification imaging and the corresponding Fast Fourier Transform (FFT) with the low-index zone axis [001] in Figure XIIe and XIIh lead to the conclusion that the nano needle is the trigonal γ-Se structure (P_{3121} space group, a=4.366 Å, c=4.955 Å).

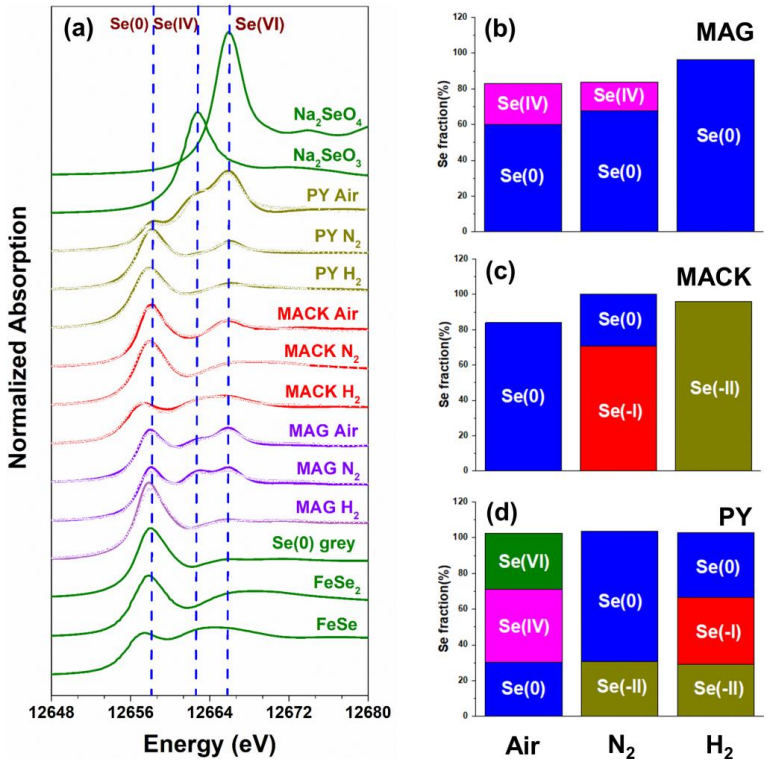

Figure X. Se K-edge normalized XANES spectra of Se-solid samples after reaction with Fe phases for 105 days under air, N_2 and H_2 atmospheres, comparing to Se references (a). The main fractions (>15%) of FeSe, $FeSe_2$, Se^0, Se(IV) and Se(VI) components determined by LCF method. (b) for magnetite (MAG) systems, (c) for mackinawite (MACK) systems and (d) for pyrite (PY) systems.

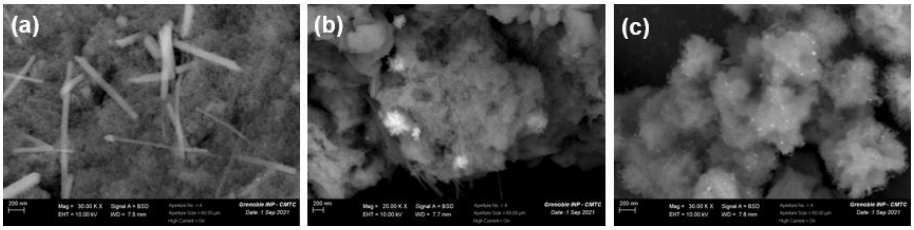

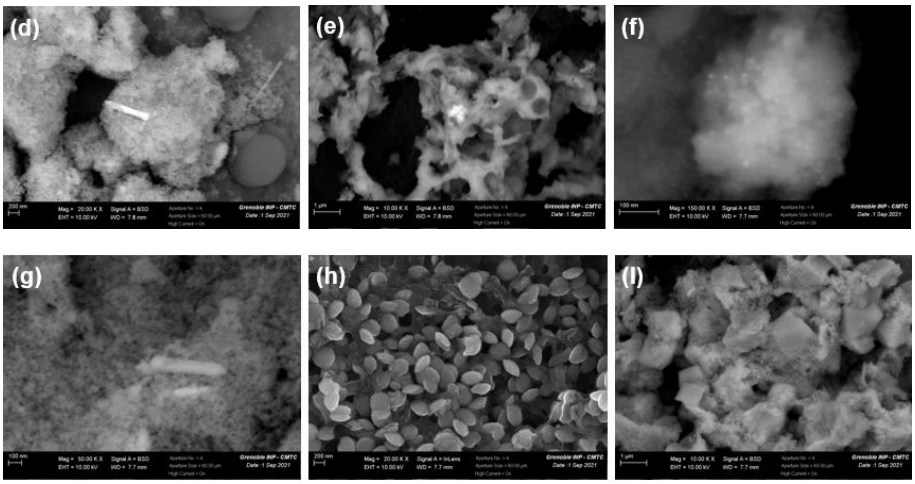

Figure XI. SEM images of different selenium morphologies and other phases. selenium nano needles in magnetite under (a) N_2, (d) H_2 and (g) air atmospheres; selenium nano plates and sulfur nanoparticle in mackinawite systems under (b) N_2, (g) H_2 and (h) air atmospheres; nano-sized selenium or other phases in pyrite systems under (c) N_2, (f) H_2 and (I) air atmospheres.

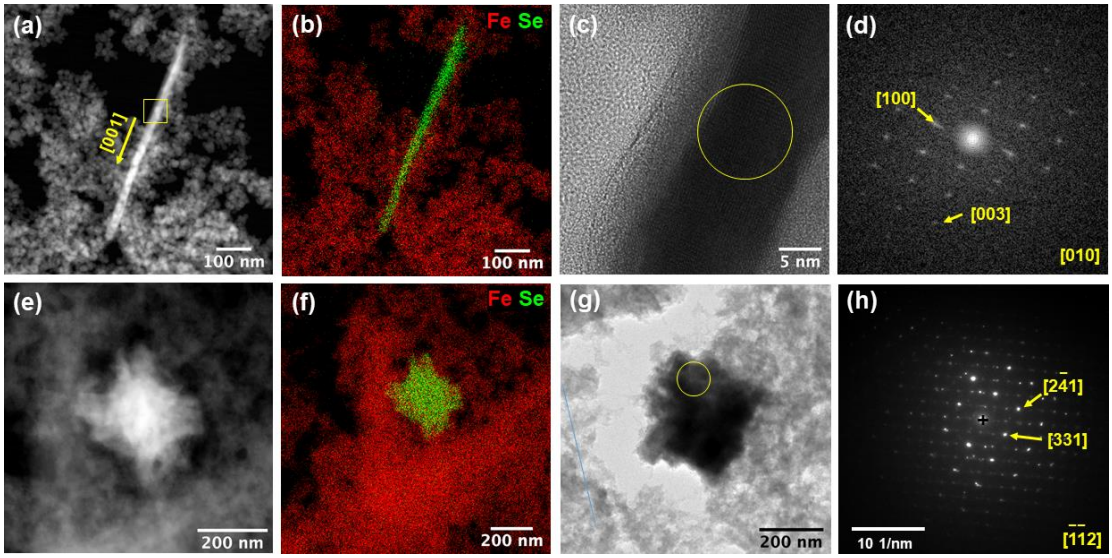

Figure XII. Scanning transmission electron micrographs of Se-magnetite (a, b, c, d) and Se-mackinawite (e, f, g, h) samples under N_2 atmosphere. (a) STEM-HAADF image of a Se nano needle, (b) the corresponding STEM-XEDS elemental mapping, (c) HRTEM image of the select area in figure (a), and (d) the corresponding Fast Fourier Transform (FFT) indexed with the trigonal γ-Se structure (P_{3121} space group, a=4.366 Å, c=4.955 Å) providing the exact orientation of the crystal. The [001] direction indicated in figure (a) is deduced from the indexation. (e) STEM-HAADF image of a Se nano

particle, (f) the corresponding STEM-XEDS elemental mapping, (g) TEM-BF images of Se nano particle, and (h) the SAED related to the area labelled in image (g) and indexed with the monoclinic β-Se structure ($P_{21/n}$ space group, a=9.054 Å, b=9.083 Å, c=11.601 Å and β=90.81 Å).

The Se-XANES and LCF results of Se-mackinawite solid samples in Figure X indicated that 70.6 % $FeSe_2$ and 29.5 % Se(0) were the only two species under N_2 atmosphere, suggesting that Se(VI) was reduced to Se(-I) and Se (0) after 105 days reaction. 83.9 % Se(0) and 95.8 % FeSe were identified to be the primary Se species under air and H_2 atmospheres, respectively, which means that dissolved oxygen and hydrogen had an impact on the reduction species. The STEM-HAADF images of Se obtained after 105 days reaction under N_2 atmosphere (Figure XI) revealed that the presence of irregular nano particle, which is the same shape observed by SEM in Figure Xb and Xe. The observation nano particle was confirmed as solid-phase Se by XEDS analysis in Figure XIIf. The SAED measurement of circle part in TEM-BF image in Figure XIIg suggests the crystal structure as the monoclinic β-Se, which had the different morphology and structure of nano needle Se(0) as the trigonal γ-Se structure in magnetite systems.

LCF results of Se-solid samples after reaction with pyrite for 105 days indicates that the main reduction products of Se(VI) were 72.8% Se(0) and 30.8% FeSe under N_2 atmosphere. Besides, 30.1 % Se(0), 41.0 % Se(IV) and 31.4 % Se(VI) were identified under air atmosphere. The presence of Se(IV) and Se(VI) under air atmosphere probably caused by the presence of dissolved oxygen. Se(VI) was mainly reduced to a mixture of 29.0 % Se(0), 37.4 % $FeSe_2$ and 36.4 % FeSe under H_2 atmosphere. The dissociative adsorption of H_2 probably existed on pyrite (210) face and the hydrogen radical plays a key role for the reduction of Se(VI). From the SEM image under N_2 atmosphere (Figure XIc), the selenium nanoparticles (bright points) with the size ranging from several to several ten nanometers were observed. WAXS results of pyrite and the solid of pyrite reaction with Se(VI) under N_2 atmosphere showed no Se(0) peaks were present. Also, the attempts to detect Se(0) structure by TEM were not successful.

Therefore, it is speculated that the nano Se(0) formed in pyrite systems was amorphous.

The reactions between Re(VII) and magnetite, mackinawite as well as pyrite were also investigated and the Eh values of all the systems from highest to lowest were in order of air > N_2 > H_2. The Re L_1 edge XANES and LCF results of Re-solid samples in Figure XIII showed that 22.6 % ReO_2 and 18.0 % Re(0) formed by the reduction of Re(VII) under H_2 atmosphere but 9.9 % ReO_3 was the only reduced species under air atmosphere. No XANES signal was obtained under N_2 atmosphere as the measurement problem. As for mackinawite system, the main component (> 80 %) of Re-sorbed was ReS_2 under N_2 and H_2 atmospheres by LCF analysis, while Re(VII) was mainly reduced to ReO_3 under air atmosphere. Furthermore, Re-XANES reveals that Re(VII) immobilization mechanisms by pyrite included nonredox complexation and reductive precipitations of ReO_3 under air atmosphere. However, ReS_2 (78.1 %) was the main reduction species of Re with 11.6 % ReO_2 under N_2 atmosphere. Under H_2 atmosphere, a mixture of ReS_2, ReO_2 and ReO_3 was observed by LCF. In conclusion, the retention mechanism of Re(VII) under air atmosphere was followed nonredox complexation and the reduction to ReO_3, while the immobilization mechanism of Re(VII) was reductive precipitation, i.e., Re(IV), under N_2 and H_2 atmospheres.

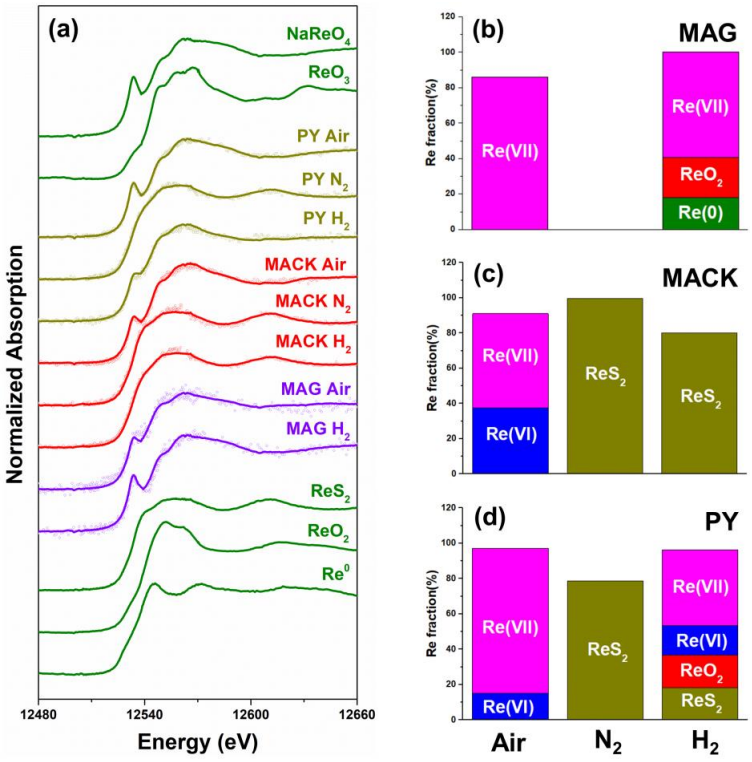

Figure XIII. Re L1 normalized XANES spectra of Re-solid samples under air, N_2 and H_2 atmospheres, comparing to Re references. The result of Re with magnetite (MAG) under N_2 system not shown here as the poor signal quality in (a). The main fractions (>15%) of Re(0), ReS_2, ReO_2, Re(VI), and Re(VII) components determined by LCF method, (b) for magnetite (MAG) systems, (c) for mackinawite (MACK) systems, and (d) for pyrite (PY) systems.

Callovo-Oxfordian (COx) formation at Bure was choose as host rock for the long-term storage of radioactive waste in France and the main minerals present in COx formation are 40-55% carbonates and quartz, 20-55 % clay minerals (mixed layer illite/smectite) with less than 1.1 % of total organic carbon and accessory minerals including 0.5-0.9 % pyrite. The natural pyrite has the potential for Se retention. Here, the interaction mechanism between Se(VI) and natural pyrite in COx pore water under N_2 and H_2 conditions is assessed by combining wet chemistry methods, X-ray absorption spectroscopy (XAS) and Phreeqc modeling using the Andra THERMOCHIMIE database.

The aqueous analysis showed that Se(VI) uptake was not significant with quite the same uptake (K_d = 4~5 mL/g) under both conditions (H_2 and N_2 atmospheres) within the uncertainties, even though the Eh and pH values under H_2 conditions were lower than that under N_2. One reasonable interpretation of the results was probably the competition by S(VI) present in a large amounts in matrix and the other one is allowed by the weak adsorption and outer-sphere complexation on minerals by XAFS measurement and chemical surface complexation model.

The Se XANES spectra of Se-solid are shown in Figure XIV and the relative LCF results, not shown here, suggest that after reacting for 9 days under N_2 condition, 96.8 % $Se(VI)^-$ and 3.2 % Se(0) could be identified, indicating that Se(VI) was mainly adsorbed on the solid and not significant reduced. A Se(0) XANES fingerprint is clear after 55 days, though 88.3 % Se(VI) was still the main species of solid-Se according to LCF result under N_2 condition. Since no aqueous Se(IV) species could be identified by IC and no Se(IV)-solid species determined by Se XANES were present during the reaction,

we speculate that Se(VI) is adsorbed on nature pyrite, and reduced to Se(0) directly under N_2 condition. Furthermore, Phreeqc modelling results using the Andra THERMOCHIMIE database suggest that Se(VI) was mainly reduced to a mixture of Se(0), FeSe and $FeSeO_3$ by the oxidation of FeS_2 to S(VI) and Fe(III) under N_2 condition. The presence of $FeSeO_3$ was that there is no enough pyrite available for the Se(VI) reaction. Combining with the aqueous analysis and the Se-solid species of sample after 55 days reaction under N_2 and the calculated Fe phase, we speculated that the reaction is as follows:

$$5HSeO_4^-{}_{(aq)} + 2FeS_{2(s)} + 2H_2O \rightarrow 5Se(0)_{(s)} + 2Fe(OH)_{3(s)} + 4SO_4^{2-}{}_{(aq)} + 3H^+$$

However, 12.2 % Se(0), 45.7 % Se(IV) and 47.0 % Se(IV) were the primary solid Se species under H_2 condition after 9 days. It means that Se(VI) could be reduced to Se(IV) and Se(0). With reaction time increased to 55 days, Se(0) was the only species existing in solid, implying that all Se adsorbed was reduced. The Se XANES results indicate stepwise reduction of Se(VI) to Se(IV) and then to Se(0) under H_2 condition. The Phreeqc modelling results show that Se(0) and FeS_2 were present as the only Fe-solid and Se-solid species under H_2 condition, suggesting H_2 was the only reducing agent for the transformation of Se(VI) to Se(0). The dissociative adsorption of H_2 existed on pyrite (210) face, a face of importance in the pyrite extracted from COx formation (the illustration in Figure XIV), which probably favored the reduction of Se(VI) by hydrogen radical. Therefore, we concluded that H_2 plays a key role for the reduction of Se(VI) by natural pyrite in COx formation.

$$HSeO_4^- + 6H\cdot + H^+ \rightarrow Se(0) + 4H_2O$$

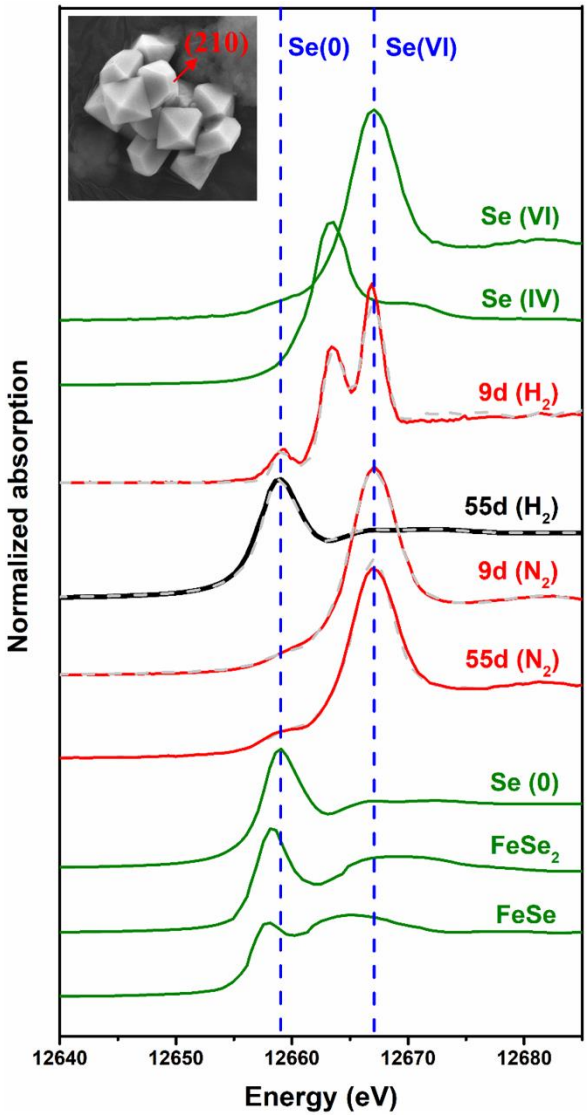

Figure XIV. Se K-edge HERFD XANES of the samples and reference compounds.

Table I. Thermodynamic Simulation by Phreeqc using the Andra THERMOCHIMIE database (concentration are given in mM).

	Distribution of species						**Fe-solid**	**Se-solid**
	Se(-II)	Se(IV)	Fe(II)	Fe(III)	S(VI)	S(-II)		
N_2	1.42	0.88	0.27	0.48	17.3	0	e.g., $Fe(OH)_2$, $Fe(OH)_3$, Fe_2O_3	Se(s), $FeSe_2$, $FeSeO_3$
H_2	2.11	-	-	-	-	14.5	FeS_2	Se(0)

Table of content

Chapter 1. Introduction-Barriers around geologic nuclear waste repositories

1.1. Geological nuclear waste disposal

High-level (HL) radioactive waste is mainly from nuclear fuel reprocessing plants and, to a lesser extent, spent fuel elements that are disposed of directly as waste. HL radioactive waste includes the extracted residue from the uranium-plutonium co-decontamination cycle of the spent fuel reprocessing process, as well as part of the treatment waste from subsequent processes such as the uranium purification cycle and plutonium purification cycle. The high activity, long half-life, high toxicity and serious long-term radiation hazards of HL radioactive waste could pose long-term potential hazards to human beings and the natural environment on which they depend.

The deep geologic repositories, i.e. underground works for the disposal of HL radioactive waste in deep geological deposits, are excavated in a stable geologic environment (usually below 300 meters). The HL radioactive waste is disposed of by multiple barriers such as surrounding rock - buffer backfill material - metal disposal container and vitrified waste, defined in a 1995 Collective Opinion of the Nuclear Energy Agency (NEA) Radioactive Waste Management Committee. A multiple barriers principle shown in Figure 1.1 is applied for the disposal of HL radioactive waste in Sweden.[1]

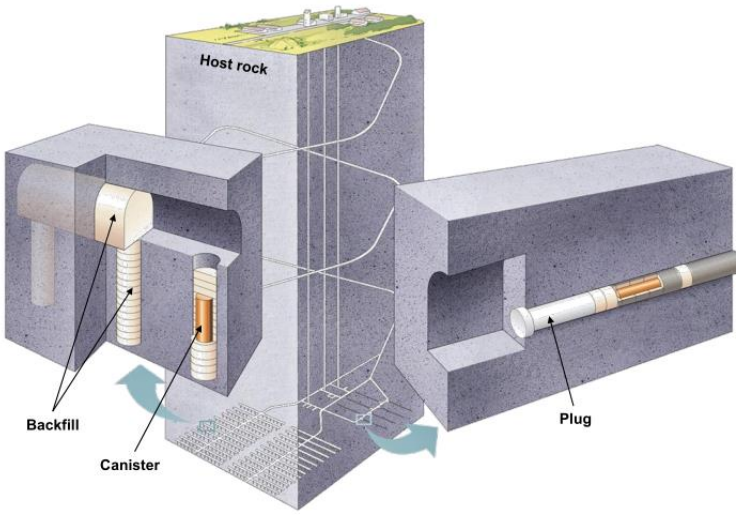

Figure 1.1. The proposed KBS-3 repository concept and multiple barrier system.[1]

1.2. Description of disposal system in France

France will have 5.0 x 10^3 m of HLW glass and 8.3 x 10^4 m of transuranic waste to be disposed by 2040. In 2009, the French government approved ANDRA's proposal for the Bure URL repository site, which is located in the Callovo-Oxfordian (COX) formations. The depth is 420-550 m below the surface. The mudstone is 130 m thick and underlain by Dogger tuff and dolomitic tuff, The COX formations is composed mainly of clay (40%-45%), carbonate minerals (20%-30%), quartz and feldspar (20%) with less than 1.1 % of total organic carbon and accessory minerals including 0.5-0.9 % pyrite.[2]. In terms of hydrogeology, the COX formations and the surrounding rocks above and below the proposed URL are not water-bearing, except for the Barrois Tuff to the west of the Bure URL site, which has been confirmed by drilling to have no impact on the site. The porosity of the granite at this site ranges from 0.15 to 2.2% and is highly correlated with the alteration of the main mineral phases of the granite (amphibole, smectite and feldspar). The percolation rate and diffusion coefficient of the uneroded granite are below 10^{-13} m/s and 10^{-12} m^2 /s respectively. Its thermal conductivity is related to the quartz content and ranges from 2.02 to 3.98 W/m·K. The URL is currently planned for cold tests only and no thermal test work will be carried out. The candidate repository Cigéo is located in and around the Bure URL, with an underground area of 30 km^2. The waste is placed horizontally, disposing of different types of waste in separate disposal lots (Figure 1.3), which shows type B waste as non or slightly heated waste, type C waste as strongly heated waste and type CO as moderately heated waste. The repository design solution is characterized by the disposal of not only HLW glass and spent fuel, but also medium long-lived radioactivity waste. In addition, due to the high adsorption of nuclides by the mudstone and the presence of a 60 m thick natural barrier above and below the repository, no engineered barrier is designed outside the HLW disposal vessel, while the medium long-lived radioactivity waste is placed directly in the trench. The repository has four shafts, 500 m deep, with internal diameters of 11.5 m (e.g. shafts for transporting waste packages),

10 m (e.g. shafts for ventilation) and 6.5 m (e.g. shafts for transporting personnel). Here the shafts have a rectangular main cage in the middle and two balancing facilities on either side of it, in addition to a secondary cage.[3] CO_2 would be produced by claystone oxidation during drilling of galleries and disposal cells and the partial pressure of CO_2 was gave a value of $\log(pCO_2) = -2.0 \pm 0.2$ bar.[4] The production of H_2 had also been identified due to the corrosion of the steel in contact with underground pore water.[5]

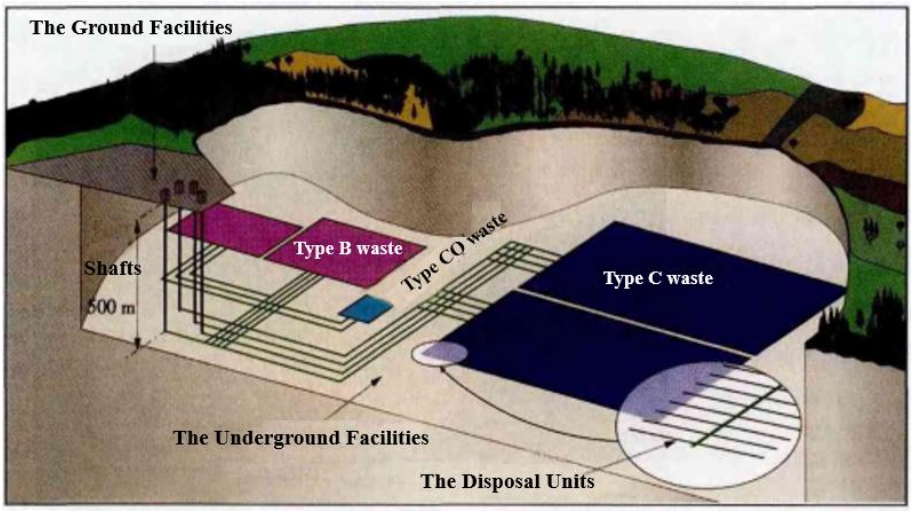

Figure 1.2. Internal structure of the French repository concept design.[3]

The disposal system in France is to adopt the reinforced concrete, backfill (clay or cement), canister and vitrified waste as the engineered barrier system (EBS) and the host rock. The schematic concept is shown in Figure 1.3. Reinforced cementitious materials are potentially used for the waste matrix, backfill, and tunnel support, which could inhibit the mobility of radionuclides (RNs) in case of eventual leakage. The specially formulated Fe-reinforced cement backfill material would provide a long-lasting alkaline environment that contributes to containment of the waste by preventing many radionuclides from dissolving in the groundwater. The selection of a suitable type of cement is critical. The anticipated CEM-V/A cement, highly resistant to sulfate corrosion than CEM-I based barriers and friendly in CO_2 emission, is being evaluated as an engineered barrier for deep underground radioactive waste disposal. CEM-V/A cement, as a ternary blended cement, consist of 50% Portland cement (PC), 25% blast furnace slag (BFS, may contain sulfides) and 25% fly ash (FA).[6] Concrete is a

composite material made of a porous matrix (the hydrated binder) filled with water, into which are embedded filler materials such as quartz and calcite, which act as a granular skeleton. After a certain period of time, groundwater passes through the fracture zone of the perimeter rock disturbance layer, penetrates the buffer backfill material, metal disposal container and comes into contact with vitrified waste, which causes the radioactive elements from body to be released into the groundwater. The total amount of radioactive elements entering the groundwater is known as the source for vitrified waste, and is the core parameter for deep geological disposal. This parameter is determined by the composition of the vitrified waste, the metal disposal vessel and its corrosion products, the composition of the buffer backfill material, the lithology of the surrounding rock, the composition of the groundwater and its disposal parameters (disposal temperature, groundwater flow, redox atmosphere).

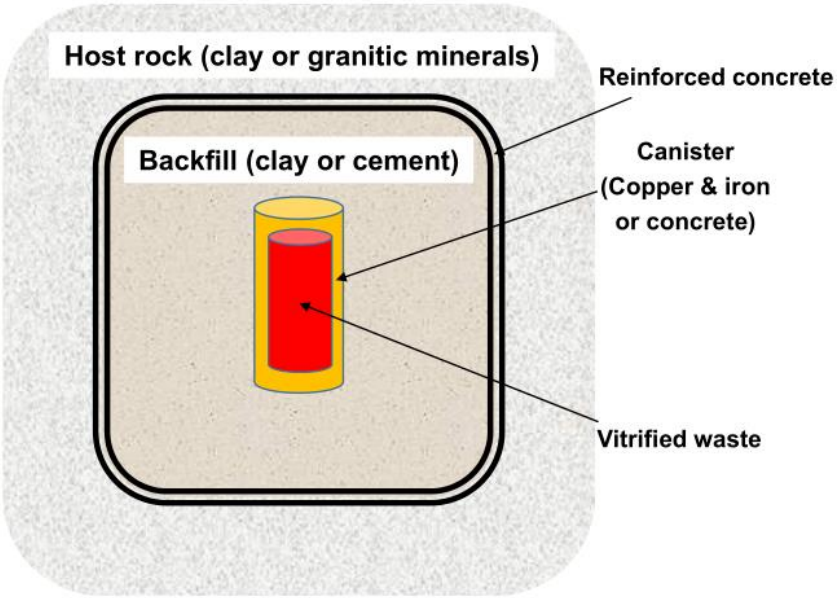

Figure 1.3. Schematic concept of the multiple barriers consisting of natural host rock and engineered materials of the repositories in France

1.3. Geochemistry of redox-sensitive radionuclides

^{79}Se is one of the ^{235}U fission products, with a long half-life of 4.8 $\times 10^5$ years. Moreover, Se is essential to human life at low concentrations, Se compounds at high concentrations are highly toxic, having one of the narrowest ranges between dietary

deficiency (< 40 μg d^{-1}) and toxic excess intake (> 400 μg d^{-1}).[7] Selenium can be present in nature with five oxidation states: selenide (-II), diselenide (-I), elemental selenium (0), selenite (IV), and selenate (VI) (Figure 1.4 a). The various oxidation states of selenium and their complexation ability with inorganic and organic matter make selenium chemistry complex. Under oxidizing conditions, Se often occurs as highly soluble and thus mobile oxyanionic forms, i.e., SeO_3^{2-} and SeO_4^{2-}, which has stimulated the research on selenium interactions with potential anthropogenic or natural barriers such as clays[8-10], cements[11-13] or Fe phases[10, 14-18]. In contrast, under reducing conditions selenium adopts oxidation states of 0, -I and -II, having much lower solubility and mobility. This makes reductive immobilization an important pathway to decrease Se transport in the environment.

^{99}Technetium is a fission product of ^{235}U and ^{239}Pu, which poses a significant environmental hazard due to its long half-life ($t_{1/2}$ = 2.13×10^5 years), abundance in nuclear wastes, and environmental mobility under oxidizing conditions.[19] The redox chemistry of Tc is the key to understanding its mobility. Tc speciation is complex, with oxidation states ranging from VII to 0, but Tc(VII) and Tc(IV) are prevailing oxidation states in the absence of any complexing ligand other than water under non reducing and reducing conditions, respectively.[20-21] Under Eh-pH conditions for the oxidative corrosion of spent nuclear fuel (Figure 1.4 b), TcO_4^- is the predominant Tc species. It is found that Tc(VII) has a very high solubility and weak sorption affinity over the entire pH range. In contrast, the low solubility of TcO_2 can limit the $[Tc(IV)]_{aq}$ below 10^{-8} M under reducing environments and Tc(IV) could be strongly precipitated on the surface of mineral.[19, 22-23] Therefore, reductive immobilization of ^{99}Tc(VII) on barriers acting as reducing agents has attracted extensive attention recently, which is of great importance for the assessment of the performance of nuclear waste repositories.

Other redox-sensitive RNs such as U, with long half-life isotopes, accounts for 96 % of the mass of the spent nuclear fuel. U is redox-sensitive and can occur in several oxidation states, mainly existing as U(VI) and U(IV) in the environment, and its solubility is largely dependent on the oxidation state. Due to its amount and chemical

and radioactive toxicity, U sorption and redox behavior have been always of large interest in nuclear waste disposal studies.[24]

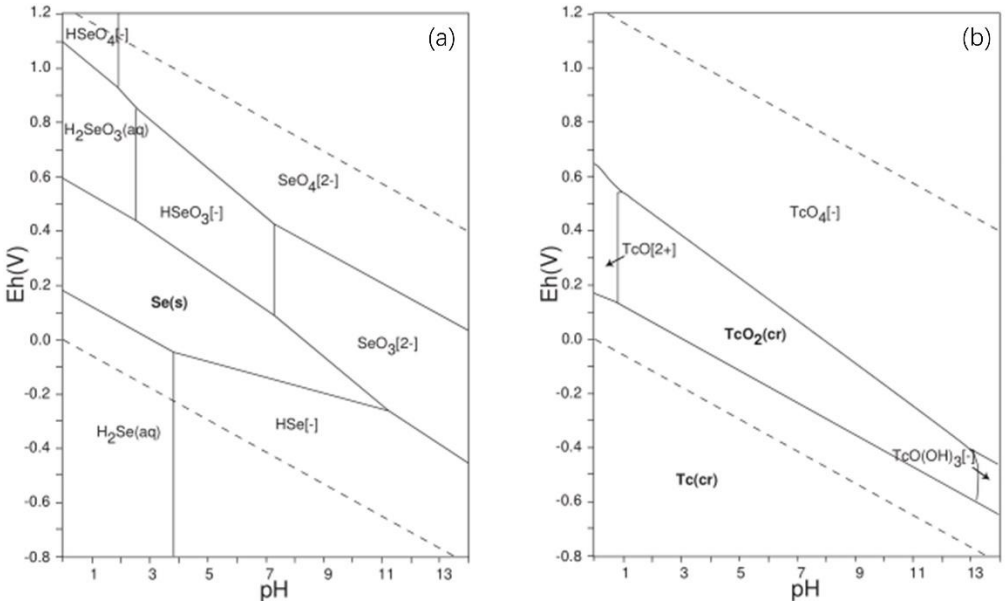

Figure 1.4. Eh-pH diagrams of the system Se-O-H (a) and Tc-O-H. [Se] = [Tc] = 10^{10} M, 298.15K, 10^5 Pa.[25]

1.4. Sorption behavior of radionuclides in potential barriers

An important issue for the radionuclide mass transport is the scientific credibility and accuracy of predictions made with these so-called 'performance assessment' (PA) models depend on the quality of the scientific understanding of these processes, and on how this understanding is represented conceptually and mathematically in the PA model.[26] PA calculations for the French concept show that three radionuclides, ^{36}Cl, ^{129}I and ^{79}Se, in some cases including ^{14}C and ^{99}Tc,[27] are able to diffuse through the Callovo-Oxfordian and enter the biosphere. Less mobile RNs on barriers will result in a larger distribution coefficient (K_d). Figure 1.5 shows the effect even a small K_d would have on ^{129}I fluxes at the top of the Callovo-Oxfordian GBS.[26] A detailed understanding of the chemical form of solid-phase associated iodine, and of the possible reaction mechanisms which could lead to equilibrium with dissolved iodine species, constitute a priority research area for the safety case.

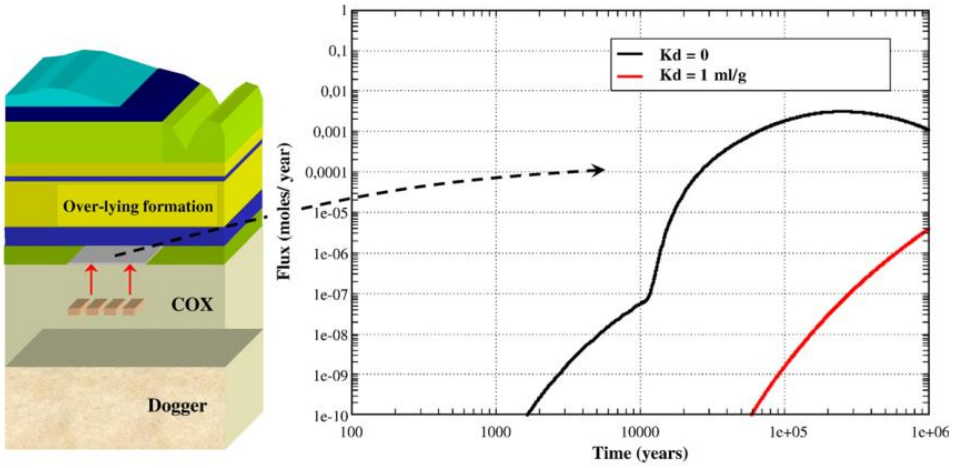

Figure 1.5. Example of the effect of a non-null K_d on ^{129}I fluxes (mol/year) exiting the upper surface of the Callovo-Oxfordien GBS.[3]

1.5. Corrosion of steel

Steel contains alloying elements such as copper, chromium and silicon to improve the corrosion resistance. Figure 1.6 shows chronogram of phenomena occurring in repository infrastructures. After a relatively short initial oxic process (<100 years) by occluded oxygen in the closed cells, corrosion of the steel embedded in concrete could result in Fe(III) oxides and hydroxides. Hematite (α-Fe_2O_3) is the thermodynamically stable phase of Fe(III) oxides in the stability field of water followed by goethite (α-FeOOH) and ferrihydrite or hydrous ferric oxides. However, after the consumption of oxygen, the redox potential is expected to become reducing in a reinforced concrete structure by thermodynamic calculations, due to the reaction between steel reinforcements (Fe^0) and groundwater. The redox potential is even lower than the stability domain of water, in which H_2 (g) exists and the released redox-sensitive RNs from cracked container tend to be immobilized totally by reductive precipitation. Redox potential will be mainly influenced by the corrosion of steel, which produces a thin magnetite film on the metal surface, a film over a few microns that will dramatically inhibit the corrosion. Furthermore, the presence of soluble species (carbonates and sulphides) may cause the formation of other compounds: siderite ($FeCO_3$) and pyrite (FeS_2).

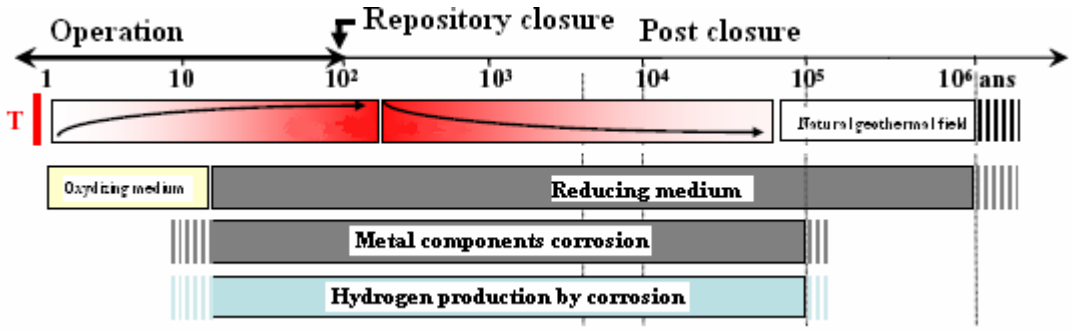

Figure 1.6. Chronogram of phenomena occurring in repository infrastructures

1.6. Reduction of RNs by Fe phases

Redox-active minerals, such as pyrite, magnetite and mackinawite, are naturally present in water-logged soils, ore deposits, anoxic aquifers and sedimentary.[2, 28-30] In addition, the minerals occurs as the steel corrosion products in nuclear waste disposal under anaerobic geochemical conditions.[31] Due to their high reactivity and large specific surface area, The Fe phases has tremendous potential to immobilize the environmental contaminants such as Se(IV) and Se(VI)[16, 29, 32-35], U(VI)[36-38], Tc(VII)[19, 39-40] as well as other heavy metals.[41-47] As reported previously, Se(IV) could be reduced to a tetragonal FeSe-like phase after being in contact with mackinawite under acidic and anoxic conditions. However, red Se(0) nanoparticles could be formed though the reduction of Se(IV) by mackinawite at higher pH.[16] Along with the Se(IV) reduction, mackinawite was oxidized to green rust firstly and then to magnetite or goethite. Besides, both aqueous Fe(II) and S(-II) were able to reduce Se(IV) to Se(0) under highly alkaline conditions (e.g., at pH ~13.29)[19]. Mackinawite can also reduce Tc(VII) to Tc(IV) to from co-precipitates. Yalçıntaş et al. reported that the formation of TcS_x -like phase and the precipitation of $TcO_2 \cdot xH_2O$ were observed during the reduction of Tc(VII) in 0.1 M NaCl solutions and strictly anoxic conditions.[19] XAS was used by Wharton et al. to define the local chemical environments of Tc and its chemical analogue, Re, on coprecipitation with mackinawite. Their results suggested that Tc(VII) was reduced to Tc(IV) in presence of TcS_2-like phase on coprecipitation with FeS, which is similar for Re(VII). However, no reduction of Tc(IV) and Re(IV) existed and it remained as the phase similar to TcO_2 and ReO_2, respectively.[39]

In addition, magnetite could catalyze the reduction of Se oxyanions to produce non-soluble Se(0) and Fe selenides. Thermodynamic calculation suggested that the reduction product of Se oxyanions by Fe(II) minerals was mainly governed by HSe^- concentration and Se(0) formed only at lower HSe^- concentrations with slower Se(IV) reduction kinetices.[48] This retention mechanism of Tc(VII) by magnetite has also been studied extensively. For example, Marshall et al. reported that Tc(VII) was reduced to Tc(IV) during magnetite crystallization in cement leachates (pH 10.5-13.1) and Tc(IV) predominantly incorporated into the octahedral site of magnetite.[49] Saslow et al. study suggested the reduction of Tc(VII) to Tc(IV) was accompanied by the oxidation of $Fe(OH)_2$ to magnetite.[50] In 0.1 M NaCl solutions under anoxic conditions, EXAFS results suggested Tc(VII) was reduced by magnetite and formed the Tc-Tc dimers sorbed to magnetite at high concentrations; whereas at low Tc(VII) concentrations and less alkaline pH conditions Tc incorporation prevailed.[19]

Furthermore, Se(IV)/Se(VI) could be reduced to Se(0) on adsorption onto natural pyrite.[34-35, 51] Thermodynamic calculations predicted that Se(0, -II) oxidation states existed under conditions existing in Callovo-Oxfordian formation and, Se(-II) might be formed giving the low concentration levels and presence of dissolved H_2.[26] Recent research about the mobility of selenite and selenite in Callovo-Oxfordian claystone showed that some correlations existed between reduced Se(0, -I or/and –II) and Fe content by μXRF mapping, suggesting Se reduction by Fe containing solids (pyrite, ankerite, and/or siderite).[52] Several studies also found that Se(IV) was reduced to Se(0) or/and Se(-II) by natural Fe(II)-bearing minerals in Boom clay (Belgium), Tamusu clay (China) and Opalinus Clay under anoxic conditions.[28, 53-54] Also, Charlet et al., reported that $FeSe_2$ was the predominant thermodynamic species in pyrite-containing systems under reducing and neutral conditions.[32] Tc(VII) reduction by pyrite through abiotic processes has also been studied. Sorption experiments of Tc(VII) by pyrite at initial pH 7 conducted by Bock et al.[55] showed that the drastic pH decrease producing positively charged mineral surfaces favored the adsorption of TcO_4^- under aerobic conditions and Fe^{2+} was present in localized reducing environments where the reduction of Tc(VII) to

TcO_2 is promoted. However, Under anaerobic conditions, an increase of aqueous Fe^{2+} concentration occurred in the presence of pyrite, resulting in a decrease in the redox potential, and making sorption/precipitation of Tc onto pyrite more favorable.[56] The synthesized pyrite nanoparticles could rapidly and completely remove Tc(VII) by reduction to insoluble Tc(IV).[43] Under sulfidic conditions, the aqueous sulfide had the potential to reduce Tc(VII) to TcO_2-like species and TcS_x species (such as TcS_2 and Tc_2S_7).[57-58] Bruggeman et al.[59] studied the sorption behavior of Tc(IV), not Tc(VII) on pyrite and they found that sorption dynamics could be modeled as a Langmuir isotherm and proposed that the adsorbing species is $TcO(OH)_2$, which is different with the precipitation of TcS_2 or co-precipitation of $TcO_2 \cdot xH_2O$ in other studies. The retention of Re(VII) by pyrite was been evaluated by Wang er al.[60] by through batch kinetic experiments under anoxic and oxic conditions. In this study, they observed Re(VII) was quickly removed in acidic solution due to the abundant presence of Fe^{2+} and S_2^{2-} and the major reduction products was ReO_2/ReS_2, which were highly stable under anoxic conditions but were sensitive to oxygen oxidation.

1.7. Retention behavior of RNs on cements and concrete

Once RNs have diffused through the canister, they will encounter backfill/buffer and cementitious materials (tunnels and alveoli). Unlike redox-reactive iron oxides, the cementitious structure can add potentially a retardation factor for RNs diffusion via surface adsorption, ion exchange, or co-precipitation reactions.[13, 61-62] During the last decade, several studies have been conducted to unravel the sorption behavior of Se onto cementitious materials, including AFm phases (aluminate ferrite monosulphate). Selenate was sorbed more efficiently by monosulfate-rich cement, while the cement composition is of minor importance for selenite sorption.[61] Uptake of Tc(IV) on cement CEM I and CSH phases was studied by ANDRA[25] and the Rd values of Tc(IV) on CEM I and CSH phases were quite similar, therefore it can be supposed that the main uptake sinks for Tc(IV) in cements were CSH phases. Rojo et al.[63] reported that HSe^- was retained much more strongly by AFm-MC (monocarbonate) ($R_d = 100 \pm 50$ L kg^{-1}) than that on AFm-HC (hemicarbonate) ($R_d = 4 \pm 2$ L kg^{-1}) under strongly reducing conditions

at pH ~12. XAFS results revealed that Se(-II) prevalently sorbed on the outer surfaces of AFm-MC but in the interlayers of AFm-HC, which could better protected the oxidation of Se(II). The uptake of Tc(VII) by CEM I, CEM II, CEM V and CEBAMA mix studied by Grambow et al.[64] suggested the high mobility and low retention of Tc(VII) in cementitious environments in the absence of reductants. Also, the limited uptake of Tc(VII) was observed on calcium silicate hydrates (C-S-H) and AFm phases with no significant adsorption onto ettringite or calcium aluminates.[65] Furthermore. the redox potential (Eh) of the system is vital to the retention of redox-sensitive radionuclides (RNs) in case of eventual leakage. Ma et al.[66] used Fe(II)/Fe(III)-rich products of steel corrosion (e.g., magnetite, hematite or goethite and ferrihydrite) mixed with cement and RNs, to study the control exerted by reactive Fe on RN speciation. Based on concentration distributions of a given RN redox couple in cement pore water and steel corrosion products, the theoretical Eh values has been determined. As shown in Figure 1.7, the experimental "in-situ" Eh values for each RN with Fe^0 are centered between -368 and -434 mV, suggesting Eh values charging RN reactions are mainly dominated by $Fe(OH)_3/Fe(OH)_2$ couples, instead of $Fe^0/Fe(OH)_2$. For the Fe-oxide couples, the experimental "in-situ" Eh values are centered between -346 and -427 mV, which are not around the Eh values imposed by the Fe-couples but also closed to that of $Fe(OH)_3/Fe(OH)_2$.

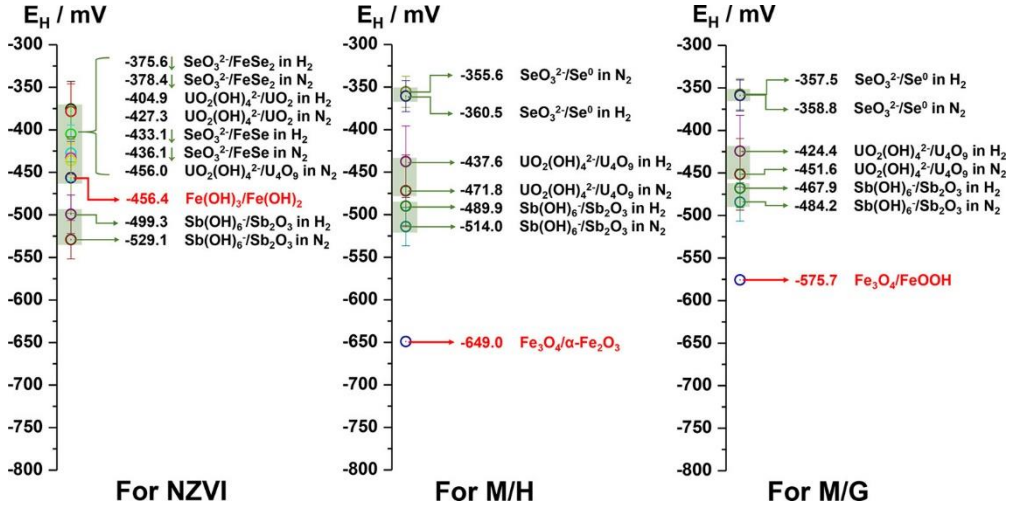

Figure 1.7. "In-situ" experimental Eh values for all the RNs systems and Eh values imposed by Fe-oxyhydroxides couples in stability domain of water. Down arrows put

on SeO_3^{2-}/FeSe and SeO_3^{2-}/$FeSe_2$ indicates even lower Eh values due to possibly more diluted $Fe(OH)_4^-$.[66]

1.8. Objectives of the thesis

In my PhD thesis, I aim to study the sorption including redox and nonredox sorption of Se(IV), Se(VI) and Re(VII) on the redox-active Fe minerals, such as pyrite (FeS_2), magnetite (Fe_3O_4) and mackinawite (FeS). Stable isotopes were always used as analogues of RNs. Furthermore, the impact of H_2, , as the real atmosphere existing in evolution of long-term storage of radioactive waste and producing by various reaction processes occurring in the the Earth's crust,[67] for the reduction of Se(VI) and Re(VII) on Fe phases is to be evaluated. Through employing a combination of wet chemistry methods, synchrotron-based X-ray spectroscopic analysis, transmission & scanning electron microscope and thermodynamic modelling. I attempt to provide valuable data about the retardation mechanisms of redox-sensitive radionuclides by redox-active Fe minerals, which is critical to advance our understanding on natural Callovo-Oxfordian formation and reactive concrete barriers in nuclear waste disposal systems. Specifically, the objectives are below:

1) Considering that the geochemistry of Se has close relationship with the chemical cycles of iron and sulfur in cement-rich repositories, a deeper knowledge about the interplay between selenite and mackinawite under the chemical environment of underground concrete structures (i.e., hyperalkaline and reducing conditions) is strongly required. I aim to investigate the interaction mechanism between Se(IV) and mackinawite in cement pore water (CPW) using a combination of X-ray absorption spectroscopy (XAS), X-ray photoelectron spectroscopy (XPS), transmission electron microscopy (TEM) and wet chemistry methods. (Chapter 2)
2) The redox potential (Eh) of cement porous media is vital to assess the retention of redox-sensitive radionuclides (RNs) (e.g., ^{79}Se) in case of eventual leakage. The Eh is largely controlled by both S and Fe but hard to be determined experimentally. In this Chapter, Se(IV) and Se (VI) were used as molecular probes to explore redox interactions by mackinawite, pyrite and magnetite in CPW and the Eh values of the

systems were obtained by using the Nernst equation based on chemical/spectroscopic measurements. (Chapter 3)

3) A deeper knowledge about the fate of Se(VI) and Re(VII) induced by magnetite, mackinawite and the impact of dissolved O_2 and H_2 for the retention mechanism of Se(VI) and Re(VII) is strongly required. In this chapter, I investigated the interaction mechanism and the reduction products between Se(VI)/Re(VII) and pyrite, magnetite and mackinawite in 0.1 NaCl solutions under air, N_2 and H_2 conditions by a combination of XAS, SEM, TEM, XRD and wet chemistry methods. (Chapter 4)
4) In order to investigate the reaction mechanism between Se(VI) and natural pyrite in COx system as well as the impact of H_2, which deeply affects the Eh of solution, for the reduction of Se(VI) by natural pyrite. I conducted the experiments between Se(VI) and natural pyrite present in COx formation in COx pore water under N_2 and H_2/CO_2 atmospheres. (Chapter 5)

Chapter 2. Redox interaction between selenite and mackinawite in cement pore water

Abstract

In cement-rich radioactive waste repositories, mackinawite (FeS) could form at the steel corrosion interface within reinforced concrete and potentially retard the transport of redox-sensitive radionuclides (e.g., ^{79}Se) in cement porous media. Redox interactions between selenite and mackinawite in hyperalkaline conditions remain unclear and require further investigations. Here, using a comprehensive characterization on both aqueous and solid speciation, we successfully monitored the whole interaction process between selenite and mackinawite in hyperalkaline conditions. Results show similar chemical environments for SeO_3^{2-} and S^{2-}/S_n^{2-} at the mackinawite-water interface, verifying an immediate reduction. After 192 h reaction, SeO_3^{2-} was reduced to solid Se^0 and SeS_2 species, accompanied by the oxidation of S^{2-}/S_n^{2-} to $S_2O_3^{2-}$ and Fe(II) to Fe(III) in mackinawite. Aqueous results showed that ~99 % of aqueous selenium was present as Se_4S nano-particles due to the dissolution of Se from the solid. In parallel, ~62% of S^{2-}/S_n^{2-} was released into the solution, with mackinawite transforming to magnetite, $Fe(OH)_3$ and $FeS_2O_3^+$ complexed to Cl^- or OH^- species, and magnetite subsequently dispersed in the solution. This study provides valuable data about the retardation mechanisms of redox-sensitive radionuclides by soluble iron sulfides, which is critical to advance our understanding on reactive concrete barriers used in nuclear waste disposal systems.

Key words: mackinawite, selenium, cement pore water, redox, retention mechanism

2.1. Introduction

The trace element selenium (Se) is essential for human health, but highly toxic when exceeding the appropriate intake range.[68] ^{79}Se is one of the ^{235}U fission products, with a long half-life of 4.8×10^5 years. Its safe disposal is a requisite to the sustainable development of nuclear industry. Oxidized species of selenium are highly mobile, which has stimulated the research on selenium interactions with potential anthropogenic or natural barriers such as clays[8-10], cements[11-13] or Fe phases.[10, 14-18] The various oxidation states of selenium (-II, -I, 0, +IV, +VI) and their complexation ability with inorganic and organic matter make selenium chemistry complex. Under oxidizing conditions, Se often occurs as highly soluble and thus mobile oxyanionic forms, i.e., SeO_3^{2-} and SeO_4^{2-}. In contrast, under reducing conditions selenium adopts oxidation states of 0, -I and -II, having much lower solubility and mobility. This makes reductive immobilization an important pathway to decrease Se transport in the environment. Determining the ability of different barrier materials to reduce selenium species is therefore of high importance for the safety assessment of radioactive waste disposal initiatives.

The CEM-V/A cement, highly resistant to sulfate corrosion, is being evaluated as an engineered barrier for deep underground radioactive waste disposal in France. Mackinawite (FeS), a precursor of thermodynamically more stable iron sulfides minerals (e.g., greigite and pyrite), can be present naturally in host rocks of claystone and granite, and also in engineered concrete structures, such as at steel corrosion interfaces.[24] Its high reactivity and large specific surface area lead to a high potential to immobilize soluble ions, e.g., heavy metals and radionuclides.[19, 39, 45-47] Previous studies have shown that Se(IV) can be reduced to a tetragonal FeSe-like phase after being in contact with mackinawite under acidic and anoxic conditions. However, red Se(0) nanoparticles could be formed though the reduction of Se(IV) by mackinawite at higher pH.[16] Along with the Se(IV) reduction, mackinawite was oxidized to green rust firstly and then to magnetite or goethite. Besides, both aqueous Fe(II) and S(-II) were able to

reduce Se(IV) to Se(0) under highly alkaline conditions (e.g., at pH ~13.29).[69] Meanwhile, other studies observed that Se(IV) could be reduced to Se^0 or Se-S precipitates (e.g. Se_nS_{8-n}) by aqueous sulfide species.[70] However, to the best of our knowledge, little data on selenite sorption on mackinawite in the presence of cement pore water (at high pH) has been reported in literature. More specifically, precise information about the detailed interaction mechanism and the fate of each reactant in abiotic reduction processes by mackinawite under hyperalkaline conditions have not been fully unravelled. Considering that the geochemistry of selenite has close relationship with the chemical cycles of iron and sulfur in cement-rich repositories, a deeper knowledge about the interplay between selenite and mackinawite under the chemical environment of underground concrete structures (i.e., hyperalkaline and reducing conditions) is strongly required.

In this study, we have investigated the interaction mechanism between SeO_3^{2-} and mackinawite in cement pore water (CPW), the solution from the interconnected pore structure produced by cement hydration, using a combination of X-ray absorption spectroscopy (XAS), X-ray photoelectron spectroscopy (XPS), transmission electron microscopy (TEM) and wet chemistry methods. This work contributes to advance the understanding on the interaction mechanisms between redox-sensitive radionuclide oxyanions and iron sulfides and to promote our knowledge on redox chemical processes within reactive concrete barriers.

2.2. Materials and methods

2.2.1. Materials and chemicals.

All chemicals used for synthesis of mackinawite (FeS) and stock solution (CPW) were analytical reagents. Boiled and N_2-degassed Milli-Q water (18.2 MΩ·cm) was used for all solutions and suspensions. Sodium selenite ($Na_2SeO_3 \cdot 5H_2O$) and chemicals used for FeS synthesis and stock solution were purchased from Sigma–Aldrich. Synthetic fresh CPW at pH ~13.5 according to the recipe from CEA[71] was used as matrix solution in all reactors, with its chemical composition shown in Table S2.1. All experiments were performed in a 99.99% N_2-filled glovebox (O_2 < 2 ppm, using NaOH

as the CO_2 trap) to prevent oxidation and possible CO_2 contamination. The mackinawite suspension was prepared following the method reported previsouly.[16] More details are shown in Text S2.1 of the Supporting Information. The synthesized mackinawite solid was prepared on a silicon plate, sealed in the air-tight powder holder, and then checked by powder X-ray diffraction (XRD) (Bruker axs, D8 advance) with Vortex-EX detector (Hitachi) under Cu Kα radiation, showing no distinct impurity diffraction peak (Figure S2.1). The specific surface area of mackinawite was determined to be 102.3 m^2/g by the Brunauer−Emmett−Teller (BET) N_2 absorption method. The surface site density was assumed to be 4 site nm^{-2} and thus the corresponding surface-site concentration was 1.36 mM. The size and shape of the mackinawite particles were further characterized by TEM as illustrated in Figure S2.

2.2.2. Wet chemistry experiments.

Sorption experiments of SeO_3^{2-} on mackinawite were performed at 25 °C under constant shaking and anoxic conditions (< 2 ppm O_2). The system was tightly closed, except during sampling, to avoid CO_2 contamination. The solid-to-liquid (S/L) ratio in all the reaction suspensions was set to 2 g/L. The initially added concentration of SeO_3^{2-} was 4.70 mM. Prior to introducing SeO_3^{2-}, mackinawite was equilibrated with CPW for 24 h. The pH of suspension was measured by a combined glass Micro-pH electrode (Metrohm 6.0234.100) during the reaction after its calibration by pH 4.00, 7.01, 10.00 and 12.00 standard solutions. A combined Pt-ring ORP electrode (Metrohm 6.0451.100) was used for the Eh measurement, after being calibrated with Zobell's solution (200 mV at 25 °C).[72] Samples of 10 mL of the suspension were filtered by 0.22 μm nitrocellulose membrane by vacuum filtration at reaction times of 1, 17, 24, 50, 73, 96, 138 and 192 hours. Extreme care was taken to minimize the potential for sample oxidation during subsequent solid characterizations (see the details in Text S2.2). Total aqueous concentrations of S, Fe and Se in the filtrates were analyzed by inductively coupled plasma optical emission spectrometry (ICP-OES) with a Varian 720-ES apparatus. The concentrations of SeO_3^{2-} and sulfur species, including S^{2-}/S_n^{2-}, SO_3^{2-} and SO_4^{2-}, were analyzed by ion chromatography (Dionex ICS-6000) with an Dionex™

IonPac™ AS9-HC IC Columns with 0.8 mL/min Na_2CO_3 (12.5 mM) as eluent. The retention time and calibration curves for SeO_3^{2-} and sulfur species were shown in Figure S2.3 and the standards of IC were cross-checked by ICP-OES.

2.2.3. X-ray absorption spectroscopy (XAS).

Iron and selenium K-edge X-ray absorption near-edge structure (XANES) and extended X-ray absorption fine structure (EXAFS) spectra were collected at the Core Level Absorption & Emission Spectroscopy (CLÆSS, BL22) beamline at the Spanish synchrotron ALBA-CELLS, Barcelona, Spain. Elemental Se foil and Fe foil were used for energy calibrations in parallel with the measurements at the Se K-edge (12.658 keV) and Fe K-edge (7.112 keV), respectively. Si(111) and Si(311) double crystal monochromators were used with approximately 0.3 eV resolution at 2.5 keV. A silicon drift detector (KETEK GmbH AXAS-M with an area of 80 mm^2) was employed to collect the fluorescence signal. All the samples for XAS were double-face sealed using polyimide tape, mounted on a sample holder, and measured in fluorescence mode, except for Se and Fe references, which were prepared as pellets with a cellulose matrix and measured in transmission mode. Before being transferred into the vacuum experimental chamber, samples were stored under N_2 atmosphere. For EXAFS signal collection, a liquid N_2 cryostat was used to lower the temperature to 77 K, in order to minimize the effects of thermal disorder due to atomic vibrations. The data integration and reduction of XANES and EXAFS spectra were performed by the Demeter software package.[73] Linear combination fits (LCF) were applied to identify and quantify the components in samples. Regarding the quantitative EXAFS fit of Se samples, radial distribution functions were obtained by Fourier Transform (FT) of k^3-weighted EXAFS oscillations (k-range: 3.0–12.0 $Å^{-1}$) using a Kaiser-Bessel window. FEFF8.4 was used to calculate the theoretical backscattering paths to perform the fits of radial distribution functions.[74] Only the first atomic shell ($R+\Delta R$: 1.0–2.7 Å) was fitted considering the quality of the EXAFS data.

2.2.4. Transmission electron microscopy (TEM).

The pristine mackinawite, as well as the solids and nano-sized colloids after reaction,

were analyzed by TEM (JEM-2100F) with energy dispersive X-ray spectroscopy (EDS). The solid samples were dispersed in ethanol and sonicated for 5 min, while no treatment was performed for the supernatant. A drop of treated samples was deposited on ultra-thin carbon grids for the measurement. TEM images were collected at 200 keV. Gatan Digital Micrograph software was used to analyze the images.

2.2.5. X-ray photoelectron spectra (XPS).

XPS was recorded with a Kratos Axis Ultra electron spectrometer equipped with a delay line detector. The reacted solid was collected and dried in the glove box and then brought to the XPS facility using an anaerobic jar. To avoid any oxidation, the samples were quickly transferred to the XPS chamber. A monochromatic Al Kα source operated at 150 W, a hybrid lens system with a magnetic lens providing an analysis area of 0.3 mm × 0.7 mm, and a charge neutralizer were employed for the measurement. The energy step was set to 0.1 eV for collecting Fe and S data. The binding energy was always calibrated using C 1s peak (284.8 eV). The XPS spectra of Fe 2p and S 2p were fitted using the CasaXPS software with Gaussian Lorentzian function through background-subtraction corrections using a Shirley-type optimization.

2.3. Results and discussion

2.3.1. Selenium reduction kinetics

The pH of the suspension stayed constant for the entire duration of the experiment, whereas the Eh decreased during the first 50 h and then remained stable until 192h (Figure S2.4). The Eh decrease could result from the continuous consumption of oxidants (i.e., Se(IV)), in good accordance with the Se(IV) concentration decrease. As shown in Figure 2.1, nearly all the aqueous SeO_3^{2-} was removed by mackinawite after 96 h. Specifically, during the first 24 h the aqueous concentration of total Se was equal to that of SeO_3^{2-}, indicating that SeO_3^{2-} was the only species in aqueous phase and that the decreased amount of SeO_3^{2-} was retained in the bulk solid phase. More intriguingly, after reacting for 50 h the aqueous concentration of SeO_3^{2-} continued to decrease while the total concentration of selenium as determined in the filtrate was increasing with reaction time. This suggests that the reduction products of SeO_3^{2-} could be nano-sized

zero-valent Se species, resulting in a colloidal dispersion in the suspension, which could not be separated out by the 0.22 μm membrane. Although previous studies also showed that mackinawite had an extremely strong affinity towards Se(IV), the formation and structure of nano-sized zero-valent Se colloids were rarely reported.[8, 75-76] The distinct reaction kinetics and products observed here could be probably related to the hyperalkaline nature of CPW. The disassociation of nano-sized zero-valent Se species from the solid adsorbent was likely to be accompanied with a dissolution of makinawite, which will be discussed afterwards in details. Meanwhile, the filtrate colors turned yellow after 24 h reaction from transparent (1 h) to orange (50 h), olive (73 h) and black (138 h and 192 h), as shown in Figure S2.5. The orange color at 50 h might suggest that SeO_3^{2-} was reduced to zero-valent Se species and then released to the solution. Han et al and Breynaert et al. also observed that the makinawite suspension turned red after interacting with Se(IV) regardless of the ratios of Se(IV)/FeS, they speculated that Se(0) particles formed through Fe-mediated Se(IV) reduction.[8, 75] Therefore, the total Se concentration of the filtrate took into account both aqueous SeO_3^{2-} and dispersed nano-sized zero-valent Se species. The composition and structure of the zero-valent Se species were further determined by TEM-EDS. At 192 h, the concentrations of Se_{tot} and Se(IV) measured in the filtrate were 4.40 mM and 0.031 mM, respectively, indicating that ~ 0.3 mM (6 %) of Se was adsorbed on the solid and ~99 % of aqueous Se was reduced species. The mass balance of Se in the filtrate (measured) and filtered solid (calculated) at different reaction times is listed in Table S2.2. Moreover, the filtrate color continued to change, and turned olive and black from 73 to 192h, indicating the possible formation of green rust and magnetite. This was due to the oxidation of FeS and the subsequent release of iron nanoparticles into the solution, which caused the increased of measured Fe concentrations (Figure 2.1). The chemical interactions between mackinawite and SeO_3^{2-} in CPW (pH ~13.5) were simulated by Phreeqc modelling using the Andra THERMOCHIMIE database.[20] The experimental aqueous Fe concentration (0.62 mM at 192 h) is comparable with but lower than the calculated values of 1.5 mM $Fe(OH)_3^-$ and 1.7 mM $Fe(OH)_4^-$, respectively. This is probably due to

the lack of thermodynamic equilibrium. Note that the measured Fe concentrations in the filtrates also include the contributions from nano-sized magnetite as indicated by the dark colour of filtrates in Figure S2.5. The precise forms of Se-solid species were further explored using XAS.

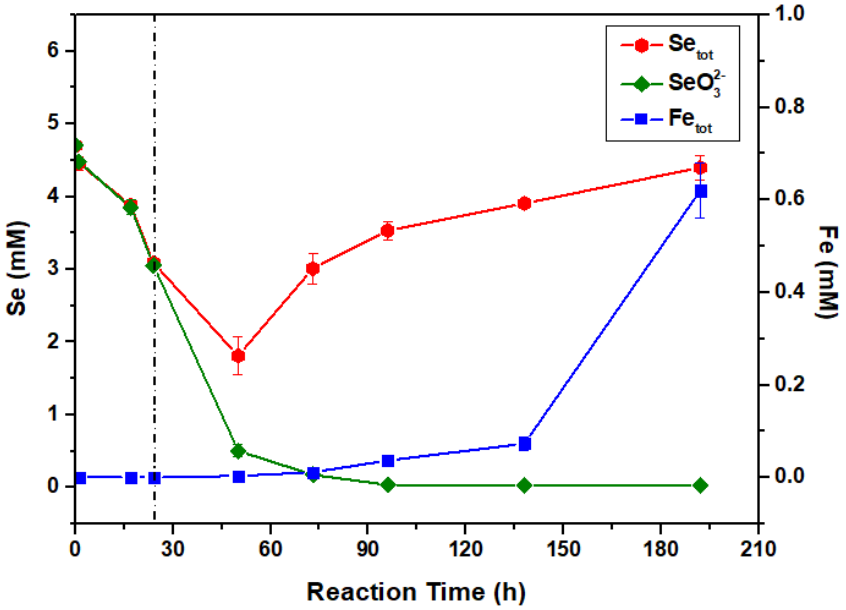

Figure 2.1. Measured concentration of SeO_3^{2-} by IC, total Se and Fe by ICP-OES in CPW as a function of the reaction time.

In XAS, the XANES region of the probed element can be used as a fingerprint of the chemical species. Se K-edge XANES spectra were collected for solid samples at different reaction times. LCF results of the solids and the references are shown in Figure 2.2. After reacting for 1 h, SeO_3^{2-} was mainly reduced into 35.8(3.0)% $FeSe_2$, 35.5(9.2)% FeSe and 19.2(1.0)% SeS_2, while only 4.9(2.9)% Se^0 and 4.9(1.2)% SeO_3^{2-} could be identified, indicating that SeO_3^{2-} can be quickly adsorbed on the surface and reduced to Se(0, -I, -II). From 24 h to 196 h, all the spectra showed similar features, with ~63% SeS_2 and 30-32% Se^0 identified to be the primary solid Se species. In contrast, previous studies at lower pH demonstrated that nano Se^0 was the main reduced Se product.[16, 69, 75] Kang et al. found that Se(-II) was transformed to elemental Se in the presence of remaining non-reduced selenium oxyanions.[77] Therefore, the reduced species of FeSe and $FeSe_2$ at 1 h could be oxidized by the residual SeO_3^{2-} forming Se(0) at 24h and the corresponding reaction would be:

$$SeO_3^{2-}{}_{(aq)} + 2FeSe_{(s)} + 3H_2O \rightarrow 3Se^0{}_{(s)} + 2Fe(OH)_{2(cr)} + 2OH^-$$

EXAFS data were fitted to determine the coordination environments of adsorbed selenium, as shown in Figure S6. Fitting the main peak in *R* space allowed obtaining interatomic distances and coordination numbers (CN) for the first two coordination shells. As shown in Table S2.3, the spectrum of the 1 h sample yielded a CN ~1.7 Se-Fe pair at 2.31 Å and CN ~1.1 Se-Se pair at 2.61 Å. The Se-Se backscattering path used was the average from the Se-Se paths of FeSe, $FeSe_2$, SeS_2 and Se^0. Regarding samples from 24, 73 and 192 h, apart from the Se-Se pair that was fitted at ~2.3 Å with a CN ~ 1.5, a backscattering signal from Se-S pair was also observed, resulting in a CN of ~0.6-0.9 with d_{Se-S} = ~2.1 Å. The EXAFS fits also confirmed the existence of SeS_x species in the solid product. Diener et al. reported that selenium, belonging to the family of chalcophile, can incorporate into the structure of mackinawite and pyrite by replacing S sites and consequently forming zero-valent Se. Also, the decreased coordination number of the neighbour Se atoms around the incorporated Se^0 site indicated a small cluster size,[78] which was in good agreement with our study. Previous study has showed that Se_nS_{8-n} are susceptible to form and precipitate as a result of Se(IV) reduction by sulfide, though the resulting sulfur-to-selenium ratio varied from 1.7 to 2.3.[79] However, TEM imaging and EDS mapping analysis did not succeed in identifying Se^0 nanoparticles and Se-S precipitates on the surface of solid sample for 192 h (the expected shape of Se-S particles is irregular and the elemental Se can adopt nanospheres and nanorod-like morphologies).[80-81] Furthermore, no obvious selenium peaks of 50 and 192 h filtered solids were detected by XRD probably due to the poor crystallinity or detection limit (Figure S2.7). The Se was therefore likely to be present forming very small precipitates or amorphous atomic level cooperation with S (Figure S2.8). By combining with Se XANES results, we proposed that SeO_3^{2-} was adsorbed onto surface sites corresponding to the S^{2-}/S_n^{2-} environment of mackinawite, and it was reduced by neighboring S^{2-}/S_n^{2-} or Fe^{2+}, forming a very fine Se^0 phase or amorphous cluster followed by the formation of Se-S through the immediate bonding to Se^0 and S. The S^{2-}/S_n^{2-} that was substituted by SeO_3^{2-} dissolved into the solution (see Section 2.3.2). The Eh-pH diagrams of Se and Fe species calculated using Andra THERMOCHIMIE

database are shown in Figure S2.9. It is worth noting that after 192 h zero-valent Se predominated among Se species, even though ferroselite ($FeSe_2$) was predicted to be more stable under the experimental conditions of pH ~13.5 and Eh ~ -0.4 V as indicated in Figure S2.9(a). The zero-valent Se is therefore a metastable phase, with slow transformation kinetics from Se^0 to Se(-I). These results allow making a hypothesis to explain the fact mentioned above: the total concentration of selenium was higher than that of SeO_3^{2-} after 24 h. It can be speculated here that ≡Fe-S-Se^0 could break down to its constituent parts in CPW, i.e. into ≡Fe-S and nano-Se^0, or ≡Fe-OH and nano-sized SeS species. After 192 h, the nanoparticles present in the filtrate were characterized by (S)TEM (Figure 2.3). As it can be seen, the size of nanoparticles was approximately ~20 to 60 nm (Figure 2.3a). The nanoparticles formed at 192 h consisted of Se, S, Fe and O with a ratio of Se to S roughly at 4:1 according to EDS analysis (Figure S2.10). Generally, elemental Se occurs in three forms: trigonal Se (t-Se), monoclinic Se (m-Se) and amorphous Se (a-Se). The interplanar spacings of trigonal Se that is considered as the most stable allotropic form are 4.96 Å and 3.78 Å along and perpendicular to the helicoid growth direction respectively,[82] which was different from that (4.3 Å) observed in nanoparticles in the filtrate as shown in Figure 2.3b. Taking into account the EDS results, the interplanar spacing may belong to Se_4S crystalline phase, whereas no data is available to identify the lattice plane of Se_4S. Se species in the filtered solids and filtrates at different reaction times are shown in Table S2.4. The high-resolution transmission electron microscopy (HRTEM) image (Figure 2.3c) illustrated that the interplanar spacing was ~2.5 Å, corresponding to the (331) lattice plane of magnetite (Fe_3O_4).[83] This indicates that mackinawite transformed to nanosized magnetite during the reaction, resulting in the increased Fe concentration with time shown in Figure 2.1.

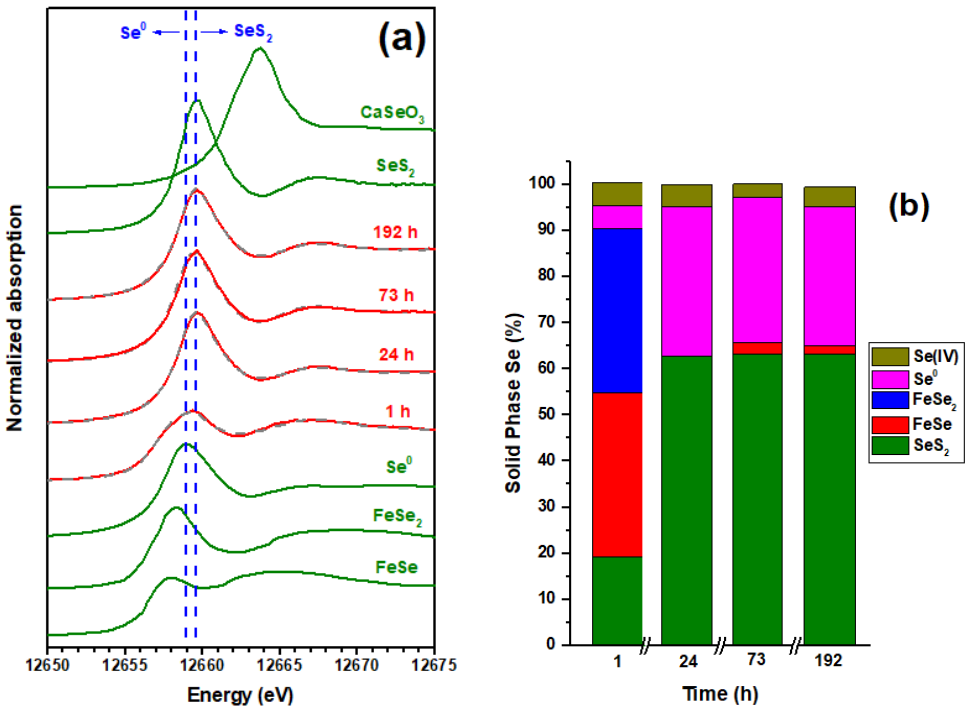

Figure 2.2. (a) Se K-edge normalized XANES spectra of solid samples after reacting for 1, 24, 73 and 192 h, comparing to Se references. (b) The fractions of FeSe, $FeSe_2$, Se^0, SeS_2 and $CaSeO_3$ components in each Se-solid sample determined by LCF method.

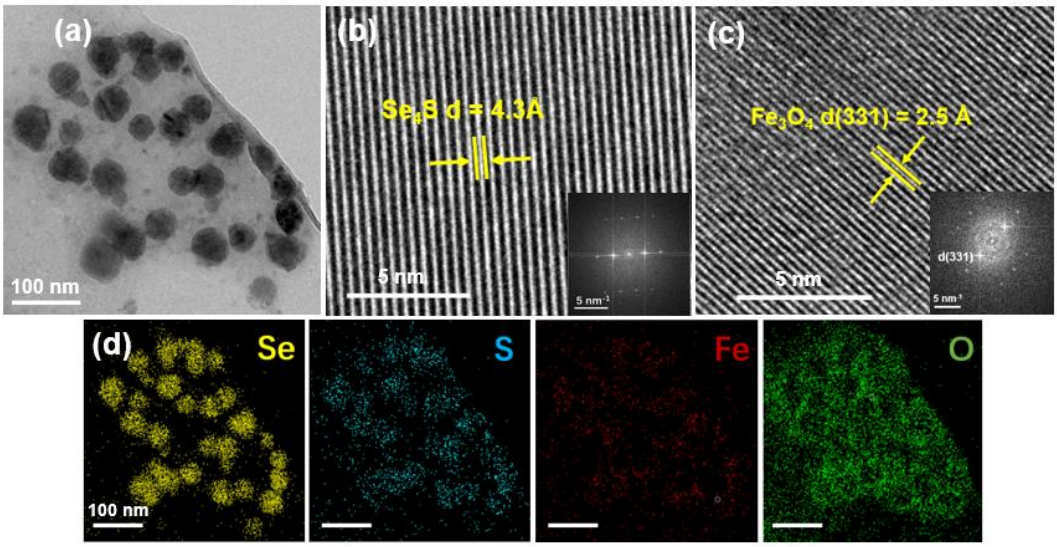

Figure 2.3. Transmission electron micrographs of nanoparticles found in the filtrate after reaction for 192 h. (a) Transmission electron microscopy image; high resolution transmission electron microscopy (HR-TEM) image on two spots on a single particle (b) SeS_4 and (c) Fe_3O_4 with the corresponding Fast Fourier Transform (FFT); (d) Elemental mapping by energy-dispersive X-ray spectroscopy analysis with Se in yellow, S in blue, Fe in red and O in green.

2.3.2. Dissolution kinetics of mackinawite with/without SeO_3^{2-}

The ion concentrations of CPW equilibrated with mackinawite for 24 hours are shown in Table S2.5. 1.28 mM Ca^{2+} was removed from the original CPW by mackinawite after 24 h equilibration, nearly equal to the value of the mackinawite surface-site concentration of (1.36 mM). Considering the zero charge of mackinawite (7.5),[84] it is reasonable to think thus that the negatively charged surface of mackinawite favored the adsorption of Ca^{2+} from CPW leading to the formation of $\equiv FeSCa^{2+}$ surface species. 0.24 mM S^{2-} and almost no Fe were detected after 24 h, suggesting that mackinawite was not congruently dissolved. However, Phreeqc calculations predicted that 0.06 mM of both HS^- and Fe^{2+} should be released once the dissolution reached equilibrium. A plot of S concentration versus reaction time is shown in Figure 2.4. It can be seen that when no SeO_3^{2-} was added, the S^{2-}/S_n^{2-} concentration increased very slowly and aqueous SO_4^{2-} (blank) was kept constant with increasing reaction time. This suggests a limited dissolution of mackinawite and no significant amount of aqueous SO_4^{2-} adsorbed onto mackinawite. The color of filtrate after 192 h was clear and the measured Eh of the suspension was about – 0.402 V, which is closed to the Eh value (-0.398 ± 0.005 V) of the suspension with SeO_3^{2-} (Figure S2.4). In contrast, in the presence of SeO_3^{2-}, a critical threshold of reaction time (73 h) was observed based on the concentration change of S^{2-}/S_n^{2-}. Dissolved concentration of S^{2-}/S_n^{2-} originating from the solid increased quickly during the first 73 h, remaining roughly constant at 13-14 mM thereafter; the same tendency for the total concentration of sulfur was observed. This supports the hypothesis that 2 to 3 S^{2-}/S_n^{2-} units were substituted by one SeO_3^{2-} atom according to the concentrations of the two species. The measured concentrations of SO_4^{2-}, S^{2-}/S_n^{2-}, SO_3^{2-} and total S with the addition of SeO_3^{2-} are shown in Table S6. After reaction for 1 h, the summation (1.74 mM) of SO_4^{2-}, S^{2-}/S_n^{2-} and SO_3^{2-} concentrations by IC was lower than the total concentration of S (2.34 mM) by ICP, suggesting other soluble S species, probably S^0, existing. In contrast, the total S concentration from ICP is nearly equal to the sum from IC from 24 h to 192 h, indicating that no other S species were present in the filtrates. 14.12 mM S^{2-}/S_n^{2-} was detected in the filtrate and the dissolution efficiency was ~ 62% after 192h. The mass balance of S

in the filtrate (measured) and filtered solid (calculated) at different reaction times is listed in Table S2.2. Han et al. proposed a mechanism where Se(IV) was reduced to FeSe or $FeSe_2$ by mackinawite at pH 8 following substituting the lattice sulfide, with no detection of aqueous sulfide release.[75] The SO_4^{2-} concentration remained 1.55 mM during the reaction, which means that no SO_4^{2-} adsorbed on the surface of the solid during reaction. A considerable amount of aqueous SO_3^{2-} was observed following the same kinetic tendency of sulfide, resulting in 1.20 mM SO_3^{2-} after 192 h. SO_3^{2-} can be present as intermediate but stable species at high pH, as the presence of S^{2-} seems to inhibit further oxidation of SO_3^{2-}.[85]

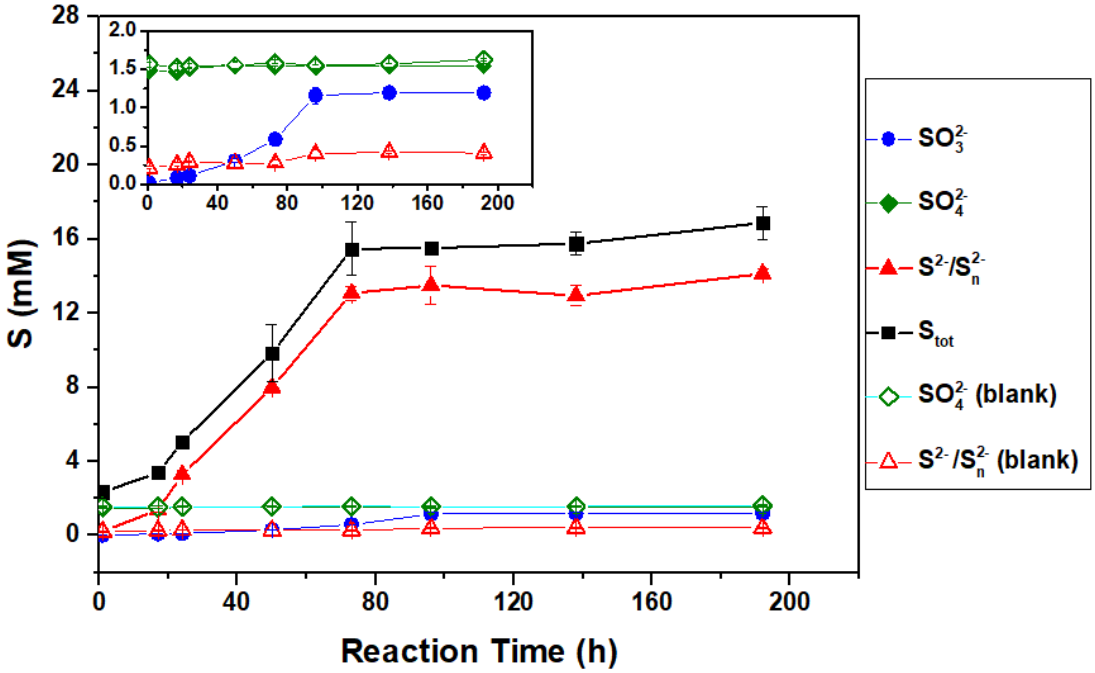

Figure 2.4. Measured concentration profiles of (poly)sulfide (S^{2-}/S_n^{2-}), sulfate (SO_4^{2-}) and sulfite (SO_3^{2-}) of the experiment with SeO_3^{2-} and S^{2-}/S_n^{2-} (blank), SO_4^{2-} (blank) of experiment without SeO_3^{2-} as a function of reaction time. The inset shows an enlarged view of the less abundant species.

2.3.3. Possible Reaction Involving Fe, S and Se

S(2p) and Fe($2p_{3/2}$) XPS spectra of Se-reacted mackinawite nanoparticles at different reaction times are shown in **Figures 2.5**. In Figure 5a, to adequately fit the S(2p) spectrum of pure mackinawite (0h), three $2p_{3/2}$ components at 160.9 eV (S^{2-}), 162.7 eV (S_n^{2-}) and 164.4 eV (S^0) were required (Table S7).[80] The S:Fe ratio of 1.2 derived from

TEM-EDS analysis experiments was consistent with the data of previous studies,[86] and suggests the formation of greigite ($Fe_2^{III}Fe^{II}S_4$) on the surface of mackinawite, although this solid was not identified by XRD.[87] Recent studies revealed the existence of Fe_3S_4 species in FeS_{nano}, as a solid-phase precursor of mackinawite, and of edge-sharing FeS_4 species to stabilize FeS structure to form mackinawite.[88-89] In our case, we speculate that Fe_3S_4, as the representative species of solid S_n^{2-}, reacted with SeO_3^{2-} especially at 1 h. A set of redox and oxidation reactions susceptible to occur between Se couples and the considered solid product couples are listed in Table S2.8. After reacting with SeO_3^{2-}, the S(2p) spectra exhibited different features, which were characterized by the energy increases (0.6-0.7 eV) of S^{2-} and S_n^{2-} species and probably attributed to surface defects, Ca or Se impact. After 1 h reaction, there is evidence for thiosulfate ($S_2O_3^{2-}$) species at 168.0 eV by XPS and an obvious decrease of S_n^{2-} signal of solid coupled to an increase in S^0 and $S_2O_3^{2-}$ contributions, indicating that S_n^{2-} ($Fe_2^{III}Fe^{II}S_4$) on the surface of mackinawite was oxidized to S^0 and $S_2O_3^{2-}$ accompanied with SeO_3^{2-} reduction to FeSe, $FeSe_2$ and zero-valent Se (Figure 2.2). Here it should be noted that zero-valent Se represents both solid species of Se^0 and SeS_2 and aqueous species of Se_4S. The corresponding half reactions (1)-(5) are listed in Table S2.8. Oxidation reaction (4) and (5) suggest that S_n^{2-} ($Fe_2^{III}Fe^{II}S_4$) was the active reductant of aqueous SeO_3^{2-} within a short reaction time and was responsible for the formation of FeSe and $FeSe_2$ at high pH via the formation of $Fe(OH)_2$ and $Fe(OH)_3$ species, which was also confirmed in acid solution.[90] Previous studies showed that SO_3^{2-} reacted with S^0 to form thiosulfate ($S_2O_3^{2-}$), which is thermodynamically stable and is a strong complexing agent with Fe^{3+} (as indicated by the stability constant of $FeS_2O_3^+$ at $10^{3.9}$).[20] $Fe(OH)_4^-$ predominates the aqueous species of Fe(III) at pH ~13.5 as shown by the thermodynamic calculation. Thus, $FeS_2O_3^+$ complex rarely forms in the solution and makes nearly no contribution to the dissolved S species (as indicated in Table S2.2). Therefore, the $S_2O_3^{2-}$ species detected in our system were probably formed though the disproportionation reaction. Also, $S_2O_3^{2-}/S_4O_6^{2-}$ was observed in the reaction between Se(IV) and pyrite by Han et al.,[33] while Scheinost et al. reported that the sulfide in mackinawite was oxidized to

elemental sulfur at pH 5.7, coupled to the reduction of Se(IV).[48] The content of S^{2-} decreased from 67.6% at 1 h to 36.1% after 24 h contact, while an increase of S_n^{2-} and $S_2O_3^{2-}$ content occurred simultaneously. As the oxidation state S within S^{2-} and S_n^{2-} is same, it suggests that S^{2-} was primarily oxidized to $S_2O_3^{2-}$ through the reduction of aqueous SeO_3^{2-} to zero-valent Se (solid SeS_2 and Se^0 species). The increase of solid S_n^{2-} suggests the formation of an intermediate amorphous solid phase $Fe_2^{III}Fe^{II}S_4$ (later transformed to pyrite), which could account for Fe(III) species in Fe($2p_{3/2}$) XPS part.[91-93] Finck et al. reported that sulfide, instead of Fe(II), contributed to the reduction of SeO_3^{2-}, as indicated by the detection of FeS_2 by XRD.[69] Here, it should be noted as the content of Se-sorbed was quite lower than the mass of solid matrix and the primary Se XPS region is 3d, the interference of Se $3p_{3/2}$ (161.7 eV) could be neglected. After 73h, the percentage of $S_2O_3^{2-}$ peak area increased to 40.5% and 10.8% of S^0 species were also detected. In contrast, the percentages of S^{2-} and S_n^{2-} contributions decreased to 27.1% and 21.5%, respectively, suggesting that S^{2-} and S_n^{2-} were oxidized to $S_2O_3^{2-}$ and S^0 (equation 5 and 6). From 73h to 192h, more S_n^{2-} was oxidized to $S_2O_3^{2-}$, which should be responsible for the reduction of SeO_3^{2-}. Usually, the oxidation of S^{2-} followed S^{2-}- S_n^{2-} - S^0 pathway during Se(VI) reduction and more than 90% of S^{2-}/S_n^{2-} was oxidized to S^0 with little amount of $S_2O_3^{2-}$ and SO_4^{2-} at acid or weakly alkaline conditions.[90, 94] In the present study, $S_2O_3^{2-}$ was the only oxidation product after 192 h reaction with Se(IV). The summed concentration of S^{2-}/S_n^{2-}, SO_3^{2-} and SO_4^{2-} is almost the same value with the total S and the concentration of SO_4^{2-} kept constant during the reaction (Figure 2.4), indicating that Se(VI)-sorbed onto mackinawite was reduced by solid S^{2-}, not by aqueous S^{2-} species. The reduction mechanism is not totally consistent with the one reported for U(VI) reduction by FeS by Hua et al, who found U(VI)-sorbed to be reduced by either S^{2-}-solid or dissolved HS^-.[95] A direct reduction of Se(IV) by aqueous S^{2-} was shown to be the dominant reaction at low initial pH.[69] Probably aqueous solid S^{2-} was more reactive for the reduction of Se(IV) than aqueous S^{2-} in CPW. Aqueous S^{2-} was stabled at pH 12.2 under reducing conditions for a long time.[96]

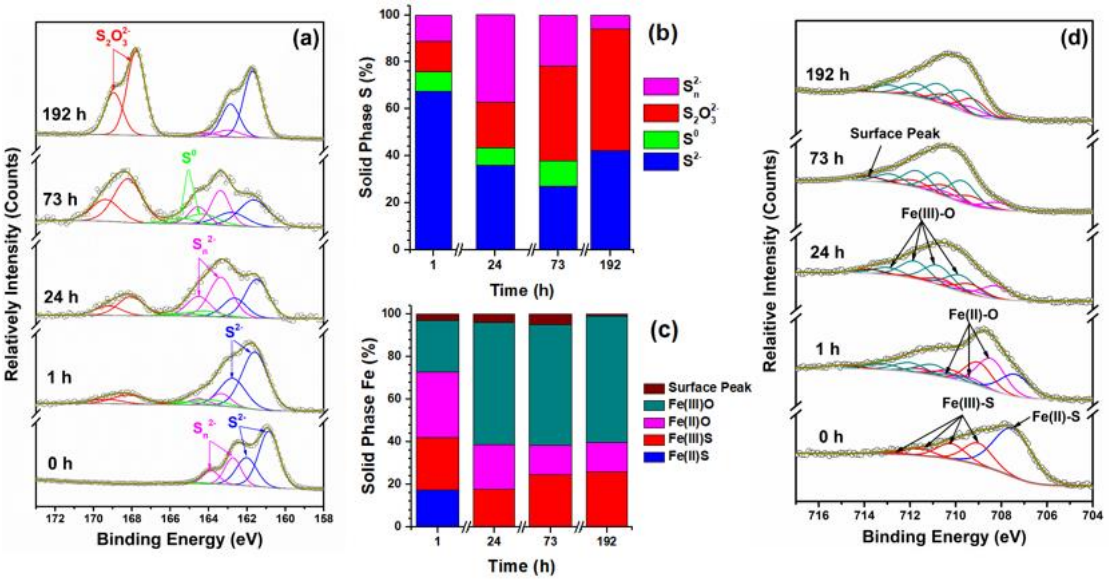

Figure 2.5. XPS spectra (a) narrow S(2p) and (d) Fe($2p_{3/2}$) (d) XPS scan, and the fractions of corresponding components of (b) S and (c) Fe species. Circles were experimental data; bottom solid line was the Shirley background; dashed lines were the fit to each spectrum and top solid line was the sum of background and fitted peaks.

The broad Fe($2p_{3/2}$) spectrum of mackinawite (Figure 5d, 0 h reaction time) could be fitted by one Fe(II)-S peak at ~707.5 eV and one main peak of Fe(III)-S at 709.1 eV with three multiple peaks.[86-87] The Fe($2p_{3/2}$) peaks fitted in the current study are listed in Table S2.9. Compared with the XPS result of pristine mackinawite, three multiple peaks of Fe(II)-O and four multiple peaks of Fe(III)-O were observed in the Fe 2p spectrum of SeO_3^{2-}-reacted mackinawite at 1 h. This suggests the oxidation of Fe(II) to Fe(III) (equation 7), coupled to SeO_3^{2-} reduction (equation 1). Also, the Fe(II) hydroxyl-complexes are important in alkaline solution and $Fe(OH)_2$ is probably formed. An increased (33.2%) Fe(III)-O peak intensity and an absence of Fe(II)-S peak are observed after 24 h reaction compared with the 1 h sample, which was probably related to the oxidation of Fe(II) and the further release S^{2-} by the solid. The XPS peak of S^{2-} in Figure 2.5a at 24 h may be attributed to Fe(III)-S species. Similar results of Fe(II) oxidation to Fe(III) were observed in mackinawite reacted with Se (IV) at different pH values.[48, 75] As reaction time increased to 73 h, the content of Fe(III)-O remained constant, indicating that no more SeO_3^{2-} was reduced by Fe(II). Mixtures of Fe(II)-O and Fe(III)-O observed on the solid surface may imply a formation of multi-valent iron

(oxyhydr)oxides such as green rust, magnetite, or other phases containing both ferrous and ferric sites.[97] Furthermore, the metastable green rust (GR) is known to have the potential to reduce SeO_3^{2-} to Se^0 via being oxidized to magnetite.[29] The presence of Fe(III)-S species was probably due to the transformation of FeS to amorphous $Fe_2^{III}Fe^{II}S_4$ resulting in the enrichment of S combined with Fe(III) or/and the formation of $Fe^{III}S_2O_3^+$ species via Se reduction. Lan et al. suggested that Fe_3S_4 was present beneath Fe(III) (hydr)oxide precipitation during FeS transformation at pH 8.[98]

The XRD patterns of 50 and 192 h solid samples show a poor crystallinity and differed from the original mackinawite in Figure S2.7. The XRD pattern from the 50 h sample probably indicated that the formation of poor crystallized Fe_3S_4 and $Fe(OH)_3$, in agreement with the XPS results. The very broad XRD reflections in 192 h sample is attributed to magnetite and $Fe(OH)_3$ with very poor crystallinity. Normalized Fe K-edge XANES spectra of the 192 h solid sample in Figure S2.11 shows that the Fe species in solid was similar to magnetite, in good accordance with black color of the filtrate at 192 h. Furthermore, the ratio of Fe(II)-O/Fe(III)-O identified by XPS at 192 h was 0.23, less than the ideal value of 0.5, and the presence of Fe(III)-S species suggested the final solid contained amorphous $Fe(OH)_3$ and $FeS_2O_3^+$ complexed to Cl^- or OH^- species except very poor crystallization magnetite. The Eh-pH diagram of Fe species as shown in Figure S2.9b indicated that mackinawite tends to dissolve and to form magnetite.

2.4. Environmental relevance

It is critical to waste depository safety to improve our understanding of reductive precipitation of mobile radionuclides in hyperalkaline conditions, and specifically to measure the surface complexes, aqueous speciation and solubility in order to decipher immobilization pathways and the underlying interaction mechanisms when contaminations are in contact with cement media. Mackinawite, as one of the steel corrosion products and one of the common naturally-occurring iron sulfides, showed an extremely high sorption and reduction ability towards SeO_3^{2-} within a relatively short interaction time (~96 hours). SeO_3^{2-} can be reduced to a mixture of SeS_2 and Se^0 solid species, as confirmed by Se K-edge XAS. However, the solid zero-valent selenium

species shows a relatively high solubility and thus mobility in CPW, with ~99% of reduction products released to the solution in the form of Se_4S nanoparticles confirmed by TEM-EDS after 192 hours. The surface chemistry of the mackinawite evolved during the reaction in the following wasy: 2 to 3 S^{2-}/S_n^{2-} units were substituted by one SeO_3^{2-} atom. 62% of initial solid S^{2-}/S_n^{2-} was released into solution when in presence of SeO_3^{2-} and mackinawite was transformed to magnetite, $Fe(OH)_3$ and $FeS_2O_3^+$ complexed to Cl^- or OH^- species after 192 h. The current study provides valuable information about the reduction mechanisms of redox-sensitive radionuclides in presence of iron sulfides that have strongly reduction capacity.

Supporting Information

Associated content

The composition of CPW. XRD patterns, and TEM micrograph of synthesized mackinawite. The calibration curves of SO_4^{2-}, SO_3^{2-},S^{2-}/S_n^{2-}, SeO_3^{2-} and the relative retention time of the ions. Experimental pH and Eh values. Picture of the filtrate color. The mass balance of S and Se. Se K-edge EXAFS of solid samples. STEM image and EDS mapping results of solid sample. Se and Fe species Eh-pH diagrams. Aqueous concentration of SO_4^{2-}, SO_3^{2-},S^{2-}/S_n^{2-} in the filtrate. Half-Cell Reduction and Oxidation Reactions. Binding energies (BE), Peak full width at half maximum (FWHM) and peak areas for S(2p) and Fe($2p_{3/2}$). Fe K-edge normalized XANES spectra and LCF result of solid samples.

Table S2.1. Experimental concentrations (measured by ICP-OES) of main ion species in CPW (pH ~13.5). The preparation procedure consists in two steps: (i) a solution containing NaOH (72 mM), KOH (211 mM), Na_2SO_4 (1.5 mM), and NaCl (1 mM) is saturated with CaO powder, and (ii) then filtered through a Millipore® 0.22-µm membrane filter.

Ion Species	Content / Mol L^{-1}
K^+	2.11×10^{-1}
Na^+	7.60×10^{-2}
Ca^{2+}	1.30×10^{-3}
Cl^-	1.00×10^{-3}
SO_4^{2-}	1.55×10^{-3}

Text S2.1. Mackinawite systhesis: The FeS suspension (0.3 M Fe) was prepared in the glovebox by mixing 100 mL of a 0.6 M Fe(II) solution $Fe(NH_4)_2(SO_4)_2{\cdot}4H2O$ with 100 mL of a 0.6 M S(-II) solution ($Na_2S{\cdot}9H2O$) under stirring. Black precipitate occurred instantly and aged for 1 day. After, the suspension was filtered through a 0.22 µm pore size membrane and was washed by replacing the supernatant with degassed water six times in the glovebox

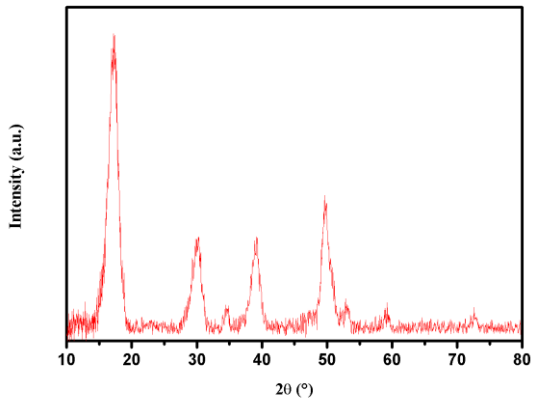

Figure S2.1. X-ray diffraction patterns of synthesized mackinawite.

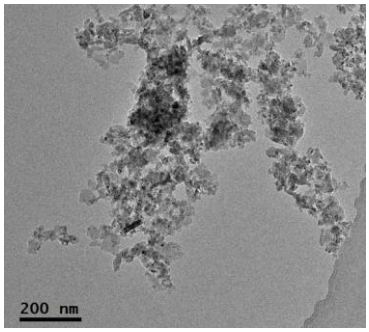

Figure S2.2. TEM images of synthesized mackinawite.

Text S2. Detailed procedures taken to minimize the potential sample oxidation during subsequent solid characterizations. Firstly, the solid samples were put into tightly sealed plastic tube, which was further wrapped in a disposable plastic sealed bag and put into a glass bottle with a sealing rubber ring. All these steps were finished in N_2-filled glove box. After, the sealed bottle was moved quickly from the glove box and put into an aluminum foil package, which was flushed with N_2 for 15 minutes and then sealed. The package was taken into the place for measurement on the same day and stored in the glove box on-site. Finally, the solid samples were quickly transferred to XAS and XPS sample chambers that were in high vacuum.

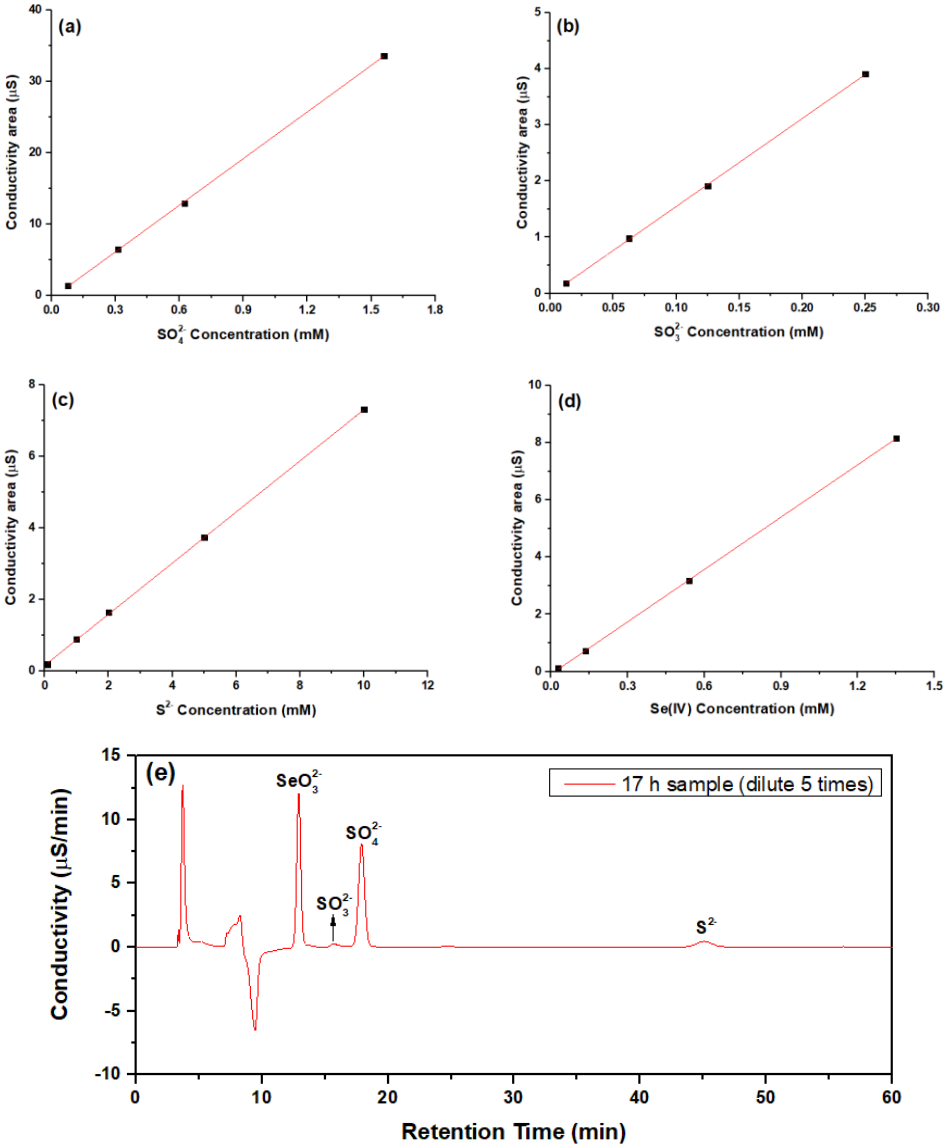

Figure S2.3. The calibration curves of (a) SO_4^{2-}, (b) SO_3^{2-}, (c) S^{2-}/ S_n^{2-} , (d)SeO_3^{2-} and (e) the relative retention time of ions by ion chromatography.

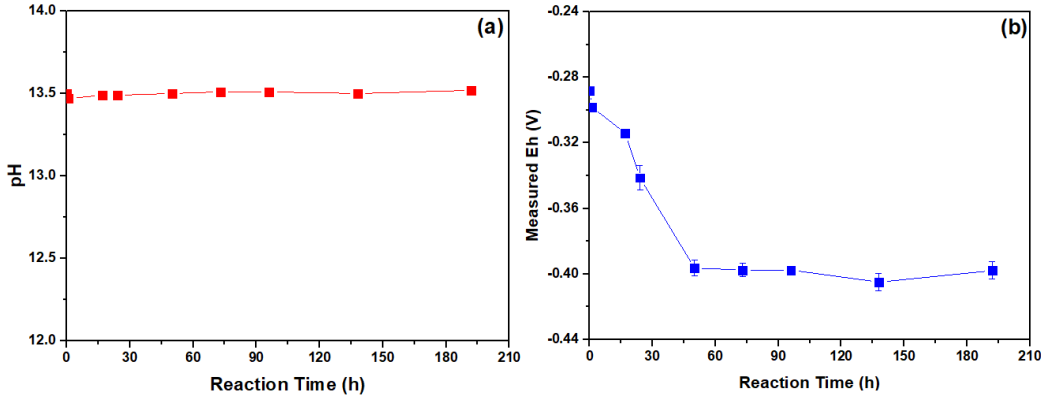

Figure S4. Experimental (a) pH and (b) Eh values with reaction time. As the pH of CPW was extremely high (~13.5), the pH of the suspension stayed constant within the

error (0.1) for the entire duration of the experiment, whereas the Eh decreased during the first 50 h and then remained stable until 192h.

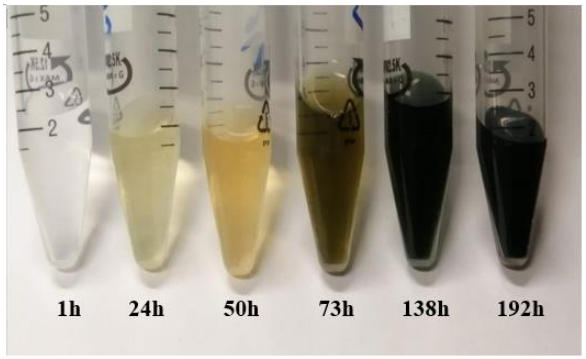

Figure S5. Picture of the filtrate at different reaction time.

Table S2.2. The mass balance of S and Se in the filtrate (measured) and filtered solid (calculated) at different reaction times. Initial concentrations of Se and S (FeS) were 4.7 and 22.8 mM respectively.

Reaction Time (h)	Aqueous S (mM)	Solid S (mM)	Aqueous Se (mM)	Solid Se (mM)
1	2.34	20.46	4.48	0.22
24	5.04	17.76	3.06	1.64
73	15.47	7.33	3.01	1.69
192	16.87	5.93	4.40	0.30

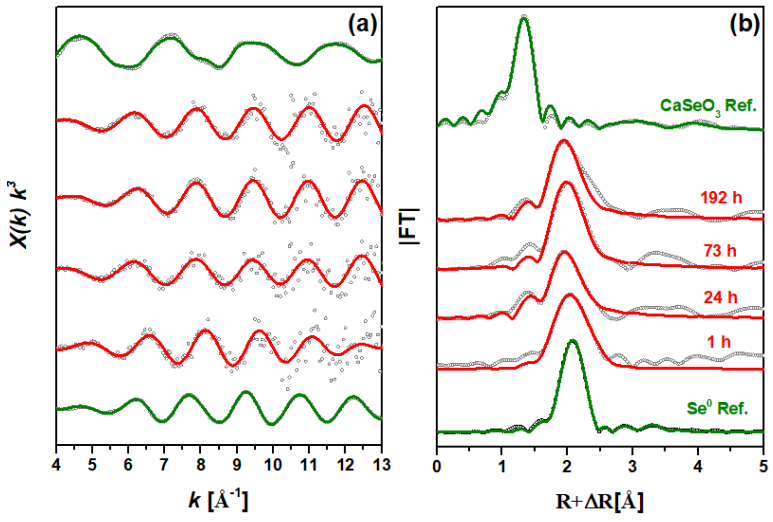

Figure S2.6. Experimental Se K-edge EXAFS spectra of solid samples after reaction 1, 24, 73 and 192 h and reference compounds. (a) k^3-Weighted EXAFS oscillations. (b) Fourier transformed (not corrected for phase shift) EXAFS signals. The reference

spectra and fits of $CaSeO_3$ and Se(0) were extracted from Ma et al., 2020.[12]

Table S3. Local structure obtained from EXAFS refinement at Se K-edge[a].

Sample	Atomic pair	CN	R (Å)	σ^2 (Å$^2\cdot10^3$)	ΔE^0 (eV)	S_0^2	R factor %
$CaSeO_3$_Ref.	Se-O	2.9(1)	1.70(1)	1.8(3)	9.7(1.1)	0.90	4.1
	Se-Ca	1.0(5)	3.24(4)	7.8(4.6)			
	Se-Ca	1.0(5)	3.57(4)	6.7(4.8)			
1h	Se-Fe	1.7(3)	2.31(3)	2.4(1.5)	- 1.2(6.7)	0.70	2.2
	Se-Se	1.1(6)	2.61(3)	1.5(2.3)			
24h	Se-S	0.9(2)	2.05(5)	0.2(1.4)	- 7.6(3.7)	0.70	1.4
	Se-Se	1.4(2)	2.30(1)	0.2(5)			
73h	Se-S	0.6(3)	2.11(8)	0.2(2.2)	3.2(8.7)	0.70	3.1
	Se-Se	1.6(3)	2.32(3)	0.2(7)			
192h	Se-S	0.9(3)	2.07(6)	1.4(2.4)	- 5.6(6.9)	0.70	3.8
	Se-Se	1.5(2)	2.30(2)	0.1(6)			
Se^0_Ref.	Se-Se	2.0(1)	2.37(1)	4.0(1)	6.1(8)	0.90	0.66
	Se-Se	4.3(9)	3.39(3)	14.4(2.3)			
	Se-Se	2.1(5)	3.70(3)	13.9(2.1)			

[a] CN: coordination numbers; R: atomic distances; σ^2: Debye-Waller factors; ΔE^0: shift of the threshold energy; R factor: goodness of fit. S_0^2: amplitude reduction factor, 0.70, was obtained from the experimental EXAFS fit of Na_2SeO_4 reference (measured in the same campaign with the 1h - 192h samples) by fixing the known CN ~4 of first-shell Se-O and was applied for all the samples. The reference data and EXAFS fits of CaSeO3 and Se(0) were taken from Ma et al., 2020.[12] Uncertainties are given by the number in brackets on the last digit(s), i.e., 7.8(4.6) represents 7.8 ± 4.6, and 2.9(1) means 2.9 ± 0.1.

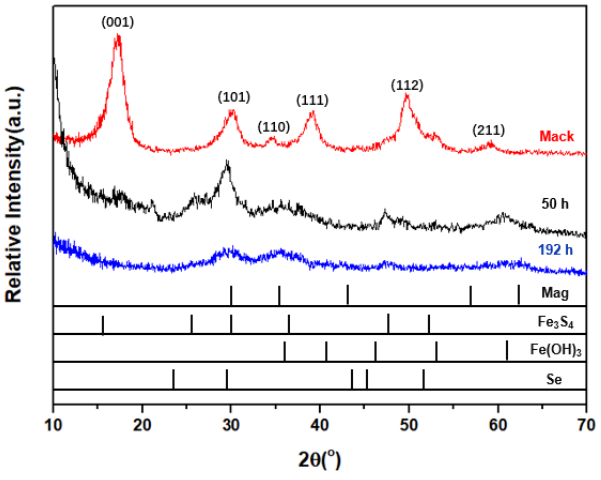

Figure S2.7. The XRD results of mackinawite (Mack), filtered solid at 50 h (50 h) and 192 h (192h), and the XRD patterns of magnetite (Mag) (PDF #19-0629), Fe_3S_4 (PDF #23-1122) $Fe(OH)_3$ (PDF #29-0712) and synthetic Selenium (Se) (PDF #06-0362). For 50 h solid sample, the absence of main lattice planes of (001), (111) and (112) in FeS and the appearance reflections at 2θ around 25, 35 and 61 indicted the dissolved and chemical reactions of mackinawite and the probably formation of poor crystallized Fe_3S_4 and $Fe(OH)_3$. The selenium content at 50h was highest in all filtered solid samples, reaching ~8 wt%. However, no obvious selenium peak was visible. It is most probably because the crystallinity of nano-sized selenium particles is quite poor. The very broad reflections at 2θ around 30 and 35 of 192 h solid sample seems magnetite and $Fe(OH)_3$ with very poor crystallinity.

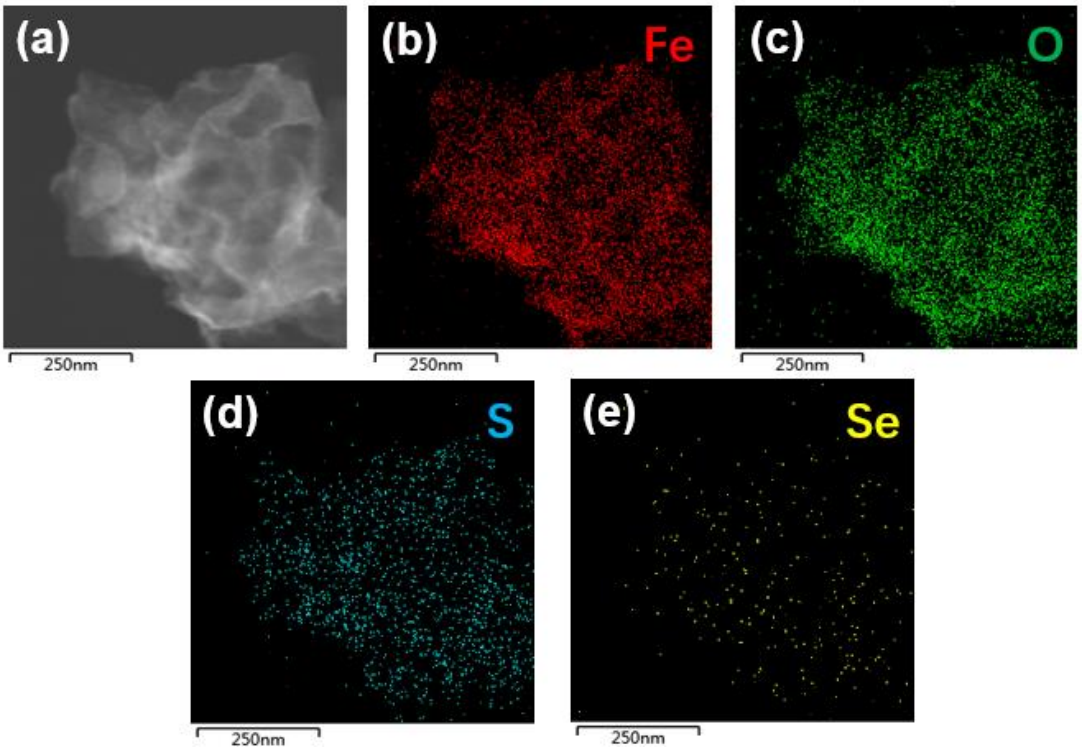

Figure S2.8. Scanning transmission electron micrographs of filtered solid sample after reaction for 192 hours. (a) High-angle annular dark-field scanning transmission electron microscopy image; Energy-dispersive X-ray spectroscopy showing Fe in red (b), O in green (c), S in blue (d) and Se in yellow (e).

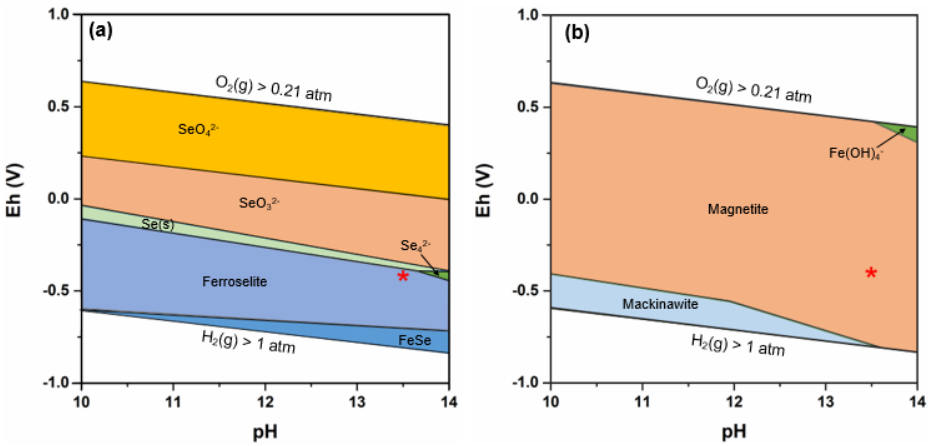

Figure S2.9. The Eh-pH diagrams of (a) Se (4.7 mM) and (b) Fe species (22.8 mM). Experimental content of CPW was input as the background matrix. The measured Eh and pH conditions after reaction for 192 h were marked as the red star.

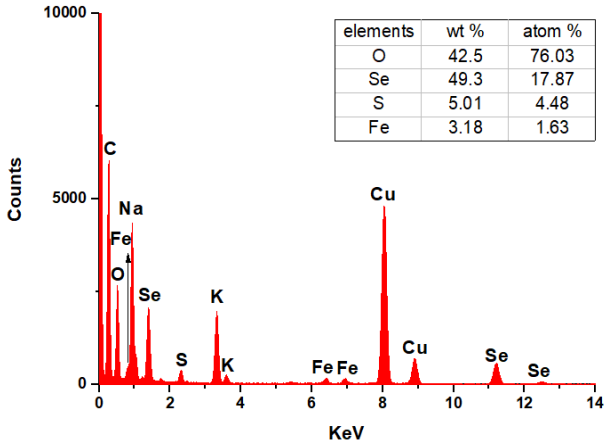

elements	wt %	atom %
O	42.5	76.03
Se	49.3	17.87
S	5.01	4.48
Fe	3.18	1.63

Figure S2.10. EDX spectra of the nanoparticles in the filter after 192 h reaction

Table S4. Major Se species in the filtrate and filtered solid at different reaction times

Reaction Time (h)	Se in the filtrate	Se filtered solid
1	SeO_3^{2-}	FeSe, FeSe2, Se0
24	SeO_3^{2-}	SeS_2 and Se^0
73	SeO_3^{2-} and Nano-Se_4S (possible)	SeS_2 and Se^0
192	Nano-Se_4S	SeS_2 and Se^0

Table S2.5. The measured concentration of SO_4^{2-}, S^{2-}/S_n^{2-}, SO_3^{2-}, Ca^{2+} and Fe

SO_4^{2-} (mM)	S^{2-} (mM)	SO_3^{2-} (mM)	Ca^{2+}(mM)	Fe^{2+}(mM)
1.55 (0.01)	0.24 (0.01)	0.02(0.00)	0.016 (0.005)	< DL

Table S2.6. The measured concentration of SO_4^{2-}, S^{2-}/S_n^{2-}, SO_3^{2-} by IC and the total sulfur concentration by ICP in present of SeO_3^{2-}.

	1h	**17h**	**24h**	**50h**	**73h**	**96h**	**138h**	**196h**
[S_{total}]	2.34(0.35)	3.39(0.35)	5.04(0.02)	9.84(1.55)	15.47(1.44)	15.51(0.07)	15.76(0.61)	16.87(0.88)
[S^2/S_n^{2-}]	0.23(0.02)	1.37(0.09)	3.28(0.20)	7.98(0.31)	13.08(0.37)	13.51(0.99)	12.94(0.57)	14.12(0.23)
[SO_3^{2-}]	0.02(0.00)	0.09(0.01)	0.11(0.01)	0.31(0.02)	0.59(0.01)	1.18(0.12)	1.20(0.06)	1.20(0.09)
[SO_4^{2-}]	1.49(0.04)	1.47(0.02)	1.52(0.01)	1.56(0.04)	1.54(0.04)	1.54(0.03)	1.55(0.02)	1.55(0.03)

Table S2.7. Binding energies (BE), peak full width at half maximum (FWHM), and peak areas for S 2p photoelectron spectra at different reaction time. The S(2p) spectra were fitted with doublet peaks ($S(2p_{3/2})$ and $S(2p_{1/2})$) of the S(2p) spin-orbit splitting, separated by 1.16 eV with an intensity ratio of 2:1 and with an identical full width at half of maximum (FWHM).[86]

Reaction Ti	**Chemical State**	**BE (eV)**	**FHWM(eV)**	**Area(%)**
0 h	S^{2-}	160.9	1.2	71.3
	S_n^{2-}	162.7	1.0	27.3
	S^0	164.4	1.2	1.4
1 h	S^{2-}	161.6	1.6	67.6
	S_n^{2-}	163.3	1.2	11.1
	S^0	164.0	2.0	8.3
	$S_2O_3^{2-}$	168.2	2.0	13.0
24 h	S^{2-}	161.5	1.4	36.1
	S_n^{2-}	163.4	1.4	37.3
	S^0	164.2	2.0	7.2
	$S_2O_3^{2-}$	168.0	1.5	19.5
73h	S^{2-}	161.6	1.8	27.1
	S_n^{2-}	163.4	1.1	21.5
	S^0	164.3	1.9	10.8

	$S_2O_3^{2-}$	168.2	1.7	40.5
192h	S^{2-}	161.7	1.1	42.4
	S_n^{2-}	163.1	1.5	5.8
	$S_2O_3^{2-}$	167.8	1.1	51.8

Table S2.8. Half-Cell Reduction and Oxidation Reactions

System	Half reaction equation	Number
Se(IV)/Se(0)	$SeO_3^{2-}{}_{(aq)} + 4e^- + 3H_2O \Leftrightarrow Se(0) + 6OH^-$	1
Se(IV)/Se(-I)	$2SeO_3^{2-}{}_{(aq)} + Fe(OH)_{2(cr)} + 10e^- + 6H_2O \Leftrightarrow FeSe_{2(s)} + 14OH^-$	2
Se(IV)/Se(-II)	$SeO_3^{2-}{}_{(aq)} + Fe(OH)_{2(cr)} + 6e^- + 3H_2O \Leftrightarrow FeSe_{(s)} + 8OH^-$	3
Fe_3S_4/S(0)	$Fe_3S_{4(s)} - 8e^- + 8OH^- \Leftrightarrow 4S^0 + Fe(OH)_{2(cr)} + 2Fe(OH)_3$	4
Fe_3S_4/FeS_2O_3	$Fe_3S_{4(s)} - 16e^- + Fe(OH)_{2(cr)} + 16OH^- \Leftrightarrow 2FeS_2O_{3(s)} + 2Fe(OH)_3 + 6H_2O$	5
FeS/FeS_2O_3	$2FeS_{(s)} - 8e^- + 8OH^- \Leftrightarrow FeS_2O_{3(s)} + Fe(OH)_{2(cr)} + 3H_2O$	6
$Fe(OH)_2$/$Fe(OH)_3$	$Fe(OH)_{2(cr)} - e^- + OH^- \Leftrightarrow Fe(OH)_{3(s)}$	7
GR-Cl/Fe_3O_4	$3Fe_3^{II}Fe^{III}(OH)_8Cl_{(s)} - 5e^- + 8OH^- \Leftrightarrow 4Fe_3O_{4(s)} + 16H_2O + 3Cl^-$	8

Table S2.9. Binding energies (BE), peak full width at half maximum (FWHM), and peak areas for $Fe2p_{3/2}$ photoelectron spectra at different reaction time. The broad $Fe(2p_{3/2})$ spectrum of mackinawite indicates a major contribution at ~707.5 eV, which corresponds to the binding energy of Fe(II)-S. However, the FWHM of $Fe(2p_{3/2})$ spectrum is too wide to be fitted by only a Fe(II)-S component. Following the approach of Herbert et al.,[87] the signal at relatively high binding energy was fitted with a Fe(III)-S component, taking into account multiple contributions predicted from crystal field theory.

Reaction Time	Chemical State	BE (eV)	FHWM(eV)	Area(%)
0 hour	Fe(II)S	707.5	1.9	60.2
	Fe(III)S	709.1, 710.3, 711.7, 713.1	1.5	39.8
1 hour	Fe(II)S	707.5	1.6	17.3
	Fe(III)S	709.0, 710.2, 711.6	1.5	24.7

	Fe(II)O	708.3, 709.3, 710.4	1.5	30.6
	Fe(III)O	710.0, 711.0, 712.0,713.2	1.6	24.3
	Surface Peak	714.8	1.9	3.1
24 hour	Fe(III)S	709.2, 710.4, 711.8	1.4	17.5
	Fe(II)O	708.3, 709.3, 710.4	1.5	21.2
	Fe(III)O	709.8, 710.8, 711.8, 713.0	1.5	57.5
	Surface Peak	713.7	1.5	3.9
73h	Fe(III)S	709.2, 710.4, 711.8	1.4	24.6
	Fe(II)O	708.2, 709.2, 710.3	1.5	13.6
	Fe(III)O	709.7, 710.7, 711.7, 712.9	1.4	56.8
	Surface Peak	713.8	1.8	5.1
192h	Fe(III)S	709.2, 710.4, 711.8	1.4	25.8
	Fe(II)O	708.3, 709.3, 710.4	1.5	13.9
	Fe(III)O	709.7, 710.7, 711.7, 712.9	1.6	59.3
	Surface Peak	714.0	1.7	1.0

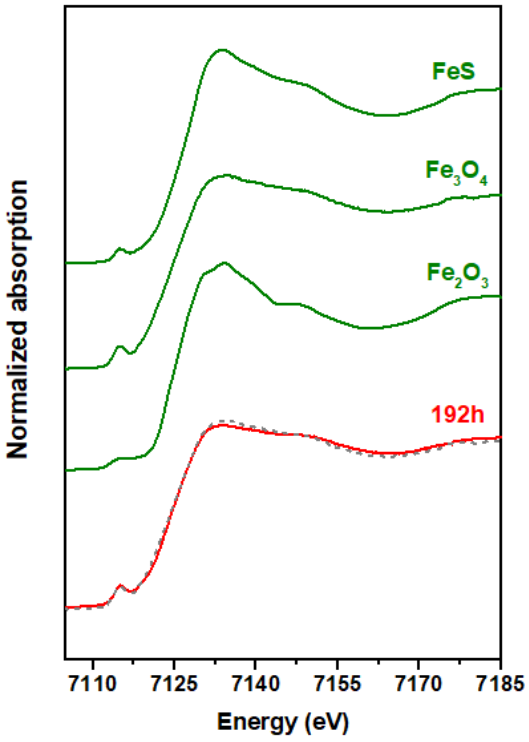

Figure S2.11. Fe K-edge normalized XANES spectra and the LCF result of solid sample at 192 h, compared with Fe references.

Chapter 3. Cement pore water redox reaction: Eh measurement and Eh modeling

Abstract

Determining the redox potential (Eh) in cement porous media is vital to assess the retention of redox-sensitive radionuclides (RNs) (e.g., ^{79}Se) in case of eventual leakage. The Eh is largely controlled by both S and Fe but hard to be determined experimentally. Here, Se(IV) and Se (VI) were used as molecular probes to explore redox interactions by mackinawite, pyrite and magnetite in CPW and the Eh values of the systems were obtained by using the Nernst equation based on chemical/spectroscopic measurements. Se(VI) was mainly reduced into FeSe and Se(IV) coupled with the oxidation of mackinawite to goethite. This measured Eh value around -0.388 V appears to be controlled by FeO(OH)/FeS couple. Furthermore, magnetite could catalyze the reduction of Se(VI) to form $Se(IV)_{(s)}$ and Se(0), accompanied by the oxidation of Fe(II) to Fe(III), and the measured Eh (-0.536 V) was probably determined by the Fe_3O_4/Fe^{2+} couple. However, no redox transformation of Se(IV) by magnetite occurred. Besides, Se(VI) immobilization mechanisms included non-redox and reductive complexation on pyrite whereas Se(IV) on pyrite was reduced to FeSe in CPW. The measured Eh (-0.350 V) in Se(VI) reaction with pyrite system was mainly controlled by the $Fe(OH)_3/Fe(OH)_3^-$ couple. The total Fe concentration could have a critical role for correcting Eh calibration. The overall redox potential imposed by Fe phases was determined, hinting to a redox shift in underground cementitious structures.

Key words: redox potential, Fe phases, Selenium reduction, redox couple

3.1. Introduction

Reinforced cementitious structures have been selected as the potential engineered barriers of the near-field nuclear waste repository in the Callovo-Oxfordian clay system in France.[99] The presence of cement, concrete and the embedded steel corrosion products as the compositions of reinforced cementitious structures keeps the system under hyperalkaline and chemically reducing conditions. A precise determination of the redox potential (Eh) of the system is vital to be able to predict the retention of redox-sensitive radionuclides (RNs) in case of eventual leakage.[31] Eh measurements are related to the activities of the redox active species in the system. Therefore, understanding the redox conditions of a reinforced cementitious system requires the investigation of the oxidation-reduction processes of the existing materials or chemicals expected to prevail in the system.

In cement-rich radioactive waste repositories, corrosion of the steel embedded in concrete could result in magnetite (Fe_3O_4), white rust ($Fe(OH)_2$) mackinawite (FeS) and pyrite (FeS_2) in the presence of carbonate, sulphide or chloride under anaerobic conditions[12, 31, 100] The formation of Fe phases could control the Eh of the system and potentially retard the transport of redox-sensitive radionuclides (e.g., ^{79}Se) in cement porous media.[24, 31] After the oxidative alteration of spent nuclear fuel, aqueous selenite (SeO_3^{2-}) and selenate (SeO_4^{2-}), as the dominant Se oxidized species, present a relatively high solubility and low adsorption under alkaline conditions, while the reductive precipitation into insoluble Se(0), $FeSe_2$ and FeSe, may significantly reduce the mobility of selenium. Previous studies reported that mackinawite showed a good affinity to Se via the reduction of Se(IV) to a tetragonal FeSe-like phase and Se(0) in acidic and alkaline solutions, respectively.[16] Scheinost et al,. observed that the reactions between mackinaiwte and Se(IV) resulted in a mixture of Se(0) and FeSe as well as the reducing conditions (Eh: -0.22V at pH 9.7 and 0.11V at pH 7.6).[48] Se(IV)/Se(VI) could also be immobilized by natural pyrite through reductive precipitation to Se(0) or via surface adsoprtion.[34-35, 51] Also, Charlet et al., reported that $FeSe_2$ was the predominant thermodynamic species in synthetic pyrite-greigite under neutral conditions and the

measured Eh was in agreement the the oxidation of Fe_3S_4 to S^0.[32] Aqueous ferrous iron released from magnetite can generated a very reducing condition (Eh lower than -0.7 V) and promoted the preservation of Se by the precipitation of $FeSe_x$.[101] Magnetite could catalyze the reduction of Se oxyanions to produce non-soluble Se(0) and FeSe.[102] Thermodynamic calculation suggested that the reduction product of Se oxyanions by Fe(II) minerals was mainly governed by HSe^- concentration and Se(0) formed only at lower HSe^- concentrations with slower Se(IV) reduction kinetices.[48]

Redox reactions are kinetically slow and so the redox systems are not in thermodynamic equilibrium. This implies that large discrepancies exist between the experimentally Eh values commonly measured by a Pt-electrode and the computed Nernstian Eh values, which was proved by most natural water systems.[103-105] Furthermore, the Eh values measured by Pt-electrode may pose large uncertainties under hyperalkaline conditions. However, far fewer studies have addressed the determination of redox potential in cementitious environment via abiotic redox transformations, even if this is a crucial parameter to assess the retention and diffusion behavior of RNs. In this study, we have aimed to model the Eh of the matrix based on the investigation of Se(IV) and Se(VI) reduction and sorption behavior by mackinawite, pyrite and magnetite in CPW by means of a combination of wet chemistry methods, X-ray absorption spectroscopy (XAS), X-ray photoelectron spectroscopy (XPS) and thermodynamic modeling.

3.2. Materials and methods

All chemicals used were analytical grade (Sigma-Aldrich) and Milli-Q water (18.2 MΩ·cm) was boiled and N_2-degassed for all solutions and suspensions.

3.2.1. The synthesis of Fe phases

The synthesis experiments of magnetite, pyrite and mackinawite were performed in a 99.99 % N_2-filled glovebox (O_2 < 2 ppm, using NaOH as the CO_2 trap). The magnetite and mackinawite suspensions were prepared following the method reported previously.[16] The pyrite was synthesized according to the protocol published by D. Wei et al., Liu X et al. and Ma et al.[106-108] More details were shown in the Supporting

Information. The synthesized Fe solids were prepared on a silicon plate, sealed in the air-tight powder holder, and then checked by powder X-ray diffraction (XRD) (Bruker axs, D8 advance) with Vortex-EX detector (Hitachi) under Cu Kα radiation, showing no distinct impurity diffraction peak in magnetite and mackinawite but containing 4% marcasite (Figure S3.1). The specific surface area of Fe phases (SSA) was determined to be 102.3 m^2/g (mackinawite), 63.6 m^2/g (magnetite) and 2.5 m^2/g (pyrite) with a multipoint N_2-BET (Brunauer−Emmett−Teller) method using a Belsorp-Max (Bel Japan) volumetric gas sorption instrument. The size and shape of the iron phases were further characterized by TEM/SEM as illustrated in Figure S3.2.

3.2.2. Adsorption experiments.

All the sorption experiments were done in cement pore water (CPW) at room temperature under anaerobic condition (O_2 < 2 ppm) and synthetic fresh CPW at pH ~13.5 according to the recipe from CEA was used as background solution in all reactors; the chemical composition of CPW is shown in Table S1.1. Concentration of Fe phases was set to 2g/L in the polypropylene tubes and the initial concentration of Se(IV) and Se(VI) was ~5.4 mM for all sorption experiment. The iron phases were equilibrated with CPW for 24 h and then Se(VI) and Se(IV) were introduced to the suspensions. The reactors names as R-I (mackinawite reaction with Se(VI)), R-II (pyrite reaction with Se(VI)), R-III (pyrite reaction with Se(IV)), R-IV (magnetite reaction with Se(VI)) and R-V (magnetite reaction with Se(IV)). The reactors were placed in a shaker during reaction. At each defined time interval, the pH of suspensions were measured by a combined glass Micro-pH electrode (Metrohm 6.0234.100) during the reaction after its calibration by pH 4.00, 7.01, 10.00 and 12.00 standard solutions. The Eh of the suspensions was monitored using a combined Pt-ring ORP electrode (Metrohm 6.0451.100), after being calibrated with Zobell's solution (200 mV at 25 °C).[72] Then a 4 mL aliquot of the suspension was sampled by filtration through a 0.22 μm pore size membrane filter (Millpore). Extreme care was taken to minimize the potential for sample oxidation during subsequent solid characterizations. Total aqueous concentrations of S, Fe and Se in the filtrates were analyzed by inductively coupled

plasma optical emission spectrometry (ICP-OES) with a Varian 720-ES apparatus. The concentrations of Se(VI) was analyzed by ion chromatography (Dionex ICS-6000) with an Dionex™ IonPac™ AS9-HC IC Columns with 1.5 mL/min Na_2CO_3 (12.5 mM) as eluent. The retention time and calibration curves for Se(VI) are shown in Figure S3.3 and the standards of IC were checked by ICP-OES. Control experiments were conducted under the same conditions in the absence of Se.

3.2.3. X-ray absorption spectroscopy (XAS).

Se-containing solid samples, prepared as pellets, sealed with Kapton windows and mounted in Al samples holders under N_2 conditions. All the samples for selenium K-edge X-ray absorption near-edge structure (XANES) spectra were measured in fluorescence mode using a multichannel silicon drift detector, except for Se references, which were prepared as pellets and collected in transmission mode with ionization chambers filled with appropriate mixtures of N_2 and Kr gases. Before being transferred into the vacuum experimental chamber, samples were stored under N_2 atmosphere. Se XANES spectra was collected at the Core Level Absorption & Emission Spectroscopy (CLÆSS, BL22) beamline at the Spanish synchrotron ALBA-CELLS, Barcelona, Spain. Elemental Se foil was used for energy calibrations in parallel with the measurements at the Se K-edge (12.658 keV). Si(111) and Si(311) double crystal monochromators were used with approximately 0.3 eV resolution at 2.5 keV. A silicon drift detector (KETEK GmbH AXAS-M with an area of 80 mm^2) was employed to collect the fluorescence signal. The data integration and reduction of XANES spectra was performed by the Demeter software package.[73] Linear combination fits (LCF) were applied to identify and quantify the components in samples.

3.2.4. X-ray photoelectron spectra (XPS).

The reacted solid samples were collected in the glove box and then brought to the XPS facility using an anaerobic jar. To avoid any oxidation, the samples were quickly transferred to the XPS chamber. XPS data recorded with a Thermo Scientific Kα spectrometer equipped with a monochromatic Al X-ray source operated at 150 W (spot size = 400 μm). All spectra were acquired using an electron flood gun to compensate

possible positive charge accumulation during measurements. The energy step was set to 0.1 eV for collecting Fe and S data. The binding energy was always calibrated using C 1s peak (284.8 eV). The XPS spectra of Fe 2p and S 2p were analyzed using the Thermo Scientific™ Advantage Software.

3.2.5. Thermodynamic modeling and Eh computation

The Phreeqc code, coupling with the THERMOCHIMIE database, was used to calculate the saturation index (SI) value of each potentially formed solid phase. The activity of each aqueous ion was calculated based on the Extended Debye-Huckel approach for activity coefficients, whose parameters were provided in the thermodynamic database. The Eh values of corresponding half-reactions were calculated via the Nernst equation using the analytical data for redox-active species and other constituents as outputs to the equilibrium speciation calculated by PHREEQC modelling. The Nernst equation is as follows:

$$\mathrm{Eh} = -\frac{\Delta_r G^0}{nF} - \frac{RT}{nF} ln \frac{a_{red}}{a_{ox}} \qquad (1)$$

where R is the universal gas constant, T is the temperature in Kelvin, F is the Faraday constant, n is the stoichiometric number of electrons transferred, a_{red} and a_{ox} are the chemical activities for the oxidants and reactants, respectively, and $\Delta_r G^0$ is the standard Gibbs free energy of reaction. The $\Delta_r G^0$ values in the reaction taken into account are given in Table S1.

3.3. Results and discussion

3.3.1. Aqueous Analysis

The ion concentrations of CPW equilibrated with mackinawite, magnetite and pyrite for 24 h are shown in Table S3.2. 1.19 mM Ca^{2+} was removed from the original CPW by mackinawite after 24 h equilibration, in an amount nearly equal to the value of the mackinawite surface-site concentration (1.36 mM). Considering the point of zero charge of mackinawite (7.5),[84] it is reasonable to think that the negatively charged surface of mackinawite in CPW favored the adsorption of Ca^{2+} from CPW leading to

the formation of ≡FeSCa^{2+} surface species. The total concentration of Se decreased rapidly from ~5.4 mM to 5.32 mM within the first hour and then continued to decrease slowly or remain constant for the rest of the reaction time (R-I). Compared with our previous study in Chapter 2 about the adsorption of Se(IV) on mackinawite in CPW, the distinct reaction kinetics between Se(VI) and Se(IV) could be probably related to the different reduction mechanisms. The filtrate color of Se(VI) systems were transparent during reaction (not shown) but it turned with reaction time for Se(IV) systems as the release of Se_4S nano-particles or nano magnetite from the solid into the solution. The Ca and S concentration profiles of the kinetic experiments in Figure 3.1b and 3.1c indicates that the sorbed-Ca^{2+} and S could release into solution during reaction. After for 8 days reaction times, the total concentrations of Ca and S remained constant around 0.32 mM and 5.98 mM, respectively. The IC results showed that the concentration of SO_4^{2-} kept the same value as the original CPW SO_4^{2-} concentration (2.0 mM) and the rest S was present as S^{2-}/S_n^{2-} species, suggesting the dissolved S^{2-}/S_n^{2-} would be oxidized to SO_4^{2-} by the reaction of Se(VI). In addition, the aqueous concentrations of aqueous Fe decreased with reaction time.

For pyrite systems (R-II and R-III), 0.63 mM Ca^{2+} was adsorbed on the surface of pyrite after 24 h equilibrated with CPW in Table S3.2, which are much higher than the value of the pyrite surface-site concentration (0.03 mM). As the pH of CPW is much higher than the pzc (1.4) of pyrite,[109] the adsorption of cations such as Ca^{2+} is strongly favored. The total concentration of Se decreased rapidly from ~5.4 mM to 5.17 mM (R-II) and 5.01 mM (R-III) within the 24 h and then remained constant afterwards, which suggested that the Se(IV) had a better affinity with pyrite than Se(VI) in CPW. The Ca and S total concentration reminded almost constant during the reaction and the S concentration equal to 2.0 mM, suggesting that no pyrite dissolution during reaction. The aqueous Fe concentration was close to detection limit, which also confirmed lack of pyrite dissolution.

For magnetite systems (R-IV and R-V), a 1.09 mM Ca^{2+} had been removed by magnetite though adsorption after 24 h equilibrated with CPW, which is comparable

with but lower than the concentration of the magnetite surface-site with 1.84 mM. It was reported that the point of zero charge of magnetite is 7.4,[44] which is in favor of Ca^{2+} adsorption to form $\equiv Fe_3O_4Ca^{2+}$ surface species. In Se(IV) system (R-V), the total concentration of Se decreased rapidly to 4.79 mM within the 1 h and then stayed constant for the rest reaction time, which is extremely different from the gradual decrease of Se(VI) in R-IV system. In addition, the concentrations of aqueous Fe remained low and constant in these systems which suggested that the magnetite does not dissolve during reaction in presence of Se(IV) and Se(VI) in CPW.

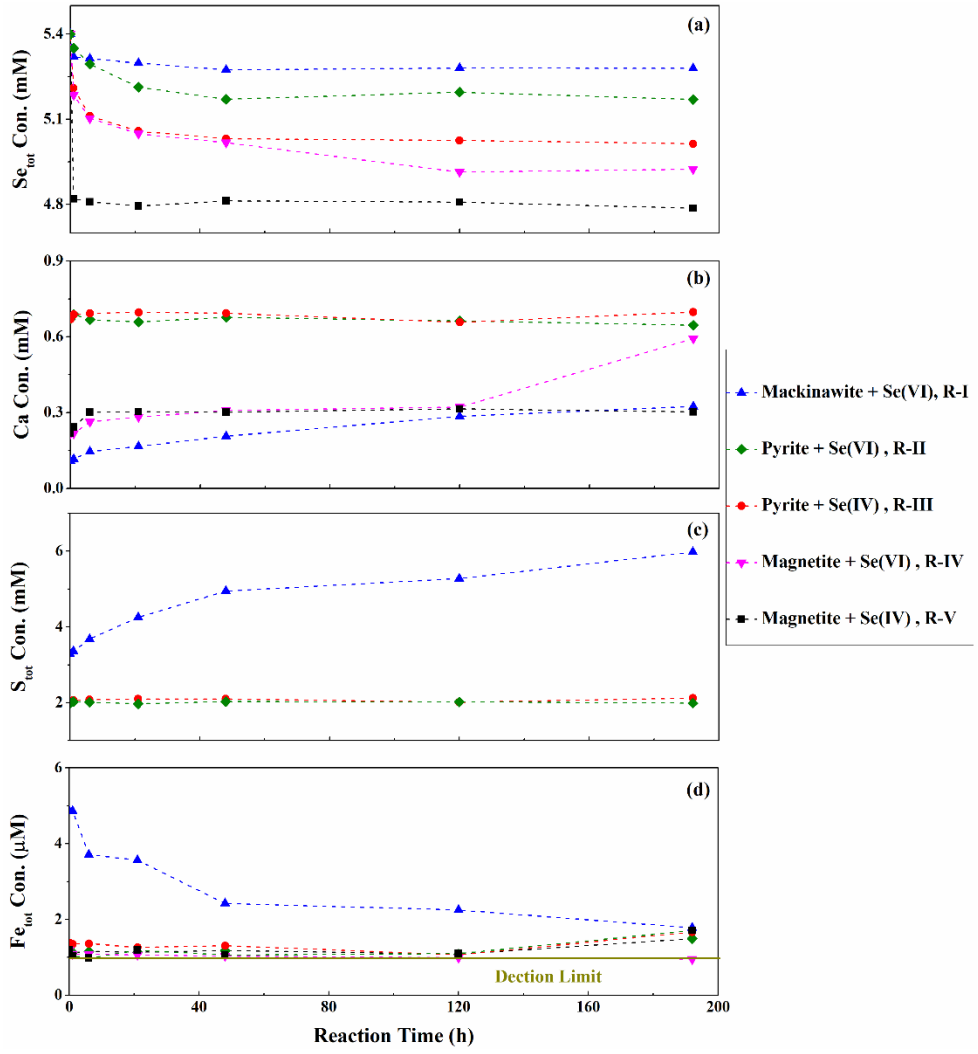

Figure 3.1. Time evolution of total aqueous Se (a), Ca (b), total S (c) and total Fe (d).

3.3.2. Se-solid Species

Se K-edge XANES spectra were collected for solid samples and the LCF results of solid samples and references are given in Figure 3.2. It is found that Se(VI) reduction

occurred, to some extent, for mackniwite, pyrite and magnetite in CPW. Se(VI) was mainly reduced into 43.9(1.1) % FeSe and 27.1(0.8) % Se(IV) by mackinawite (R-I). Besides, a 33.9(0.6) % Se(VI)-sorbed was quantified by LCF, probably attributed to the formation of surface complex with Ca^{2+} and Se(VI) or with Ca^{2+} and Se(IV), as about 1 mM Ca^{2+} was adsorbed on the surface of mackinawite after 8 days reaction (Figure 3.1b). The thermodynamics equilibrium dominant Se species computed to be Se(-II) after Se(VI) reaction with mackinawite in CPW (pH ~13.5) by Phreeqc modelling using the Andra THERMOCHIMIE database. It suggested that R-I system had not reached thermodynamic equilibrium after 8 days reaction. Here it should be noted that the exact Se(VI) and Se(IV) solid species (e.g., Na_2SeO_3, $CaSeO_3$ and $FeSeO_3$) were not measured as the Se oxidation state of Se(IV) and Se(VI) could be identified from XANES spectra, which is the key requirement for Eh computation based Nernstian equation. The Se XANES spectra and LCF result of R-II system indicated that 28.7(0.6) % Se(IV) and 77.9(0.6)% Se(VI) were present, thus that Se(VI) could be adsorbed on pyrite and partly reduced to Se(IV), while only 8.4(1.1%) Se-sorbed could be reduced to FeSe by pyrite (R-III). The calculated results by Phreeqc modelling suggested that Se(-II) was the only solid species in R-II and R-III systems. The difference between experimental data and calculated results is probably due to the lack of thermodynamic equilibrium. The reduction of Se(IV) and Se(VI) by natural pyrite was observed to produce Se(0) at 80 °C under slightly base solutions after 8 months reaction.[35] Also, Charlet et al., reported $FeSe_2$ to be the predominant thermodynamic species in pyrite-containing systems under reducing and neutral conditions.[32] Furthermore, for the R-IV system, it can be seen that the main Se-sorbed species on magnetite were 15.2(1.9) % Se(0), 61.8(0.9) % Se(IV), 19.8(0.5) % Se(VI), and only a tiny amount (2.5 %) of FeSe could be identified but the low value falls within the uncertainty value. However, the Phreeqc modeling results showed that only 0.02 mM Se(VI) was reduced to Se(IV) by the oxidation of Fe(II) to Fe(III). Se(VI)-sorbed reduction to a mixture of Se(0) and Se(IV) was also shown to occur by Goberna-Ferrón et al,. though the pH of the solution was different than in our study.[102] In addition, Se(IV)

was only absorbed on the surface magnetite (R-V) and no reduction of Se(IV) occurs by Phreeqc modelling, suggesting Se(IV) could not be reduced by magnetite in CPW. Previous study illustrated that Se(IV) can be rapidly reduced by magnetite under slightly acid conditions,[16, 102] while no reduction occurred within a shorter time in the 4.8-8.0 pH range.[94]

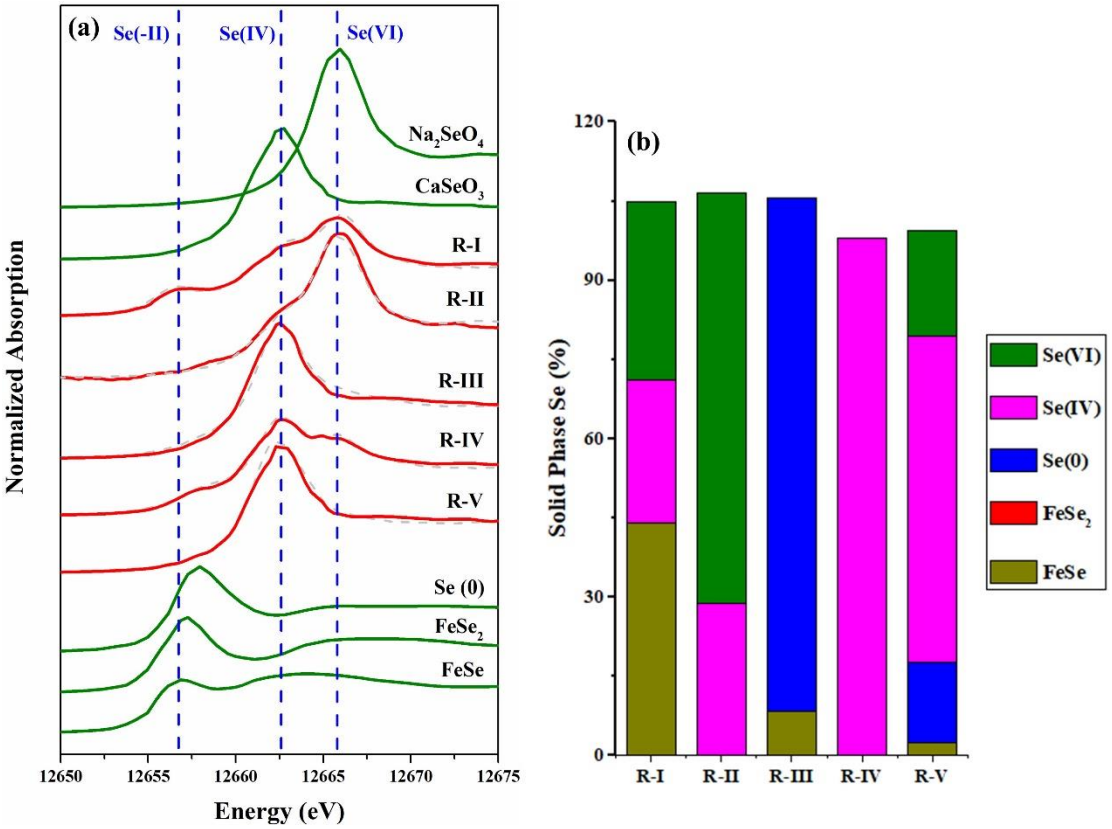

Figure 3.2. Se K-edge normalized XANES spectra of solid samples comparing to Se references. R-I (mackinawite reaction with Se(VI)), R-II (pyrite reaction with Se(VI)), R-III (pyrite reaction with Se(IV)), R-IV (magnetite reaction with Se(VI)) and R-V (magnetite reaction with Se(IV)).

Table 3.1. Quantificaiton of Se species (molar fraction) by LCF of XANES

Sample	FeSe (%)	$FeSe_2$ (%)	Se^0 (%)	$CaSeO_3$ (%)	Na_2SeO_4 (%)	∑(%)
R-I	43.9(1.1)			27.1(0.8)	33.9(0.6)	105.0
R-II				28.7(0.6)	77.9(0.6)	106.6
R-III	8.4(1.1)			97.1(0.1)		105.5
R-IV	2.5(2.7)		15.2(1.9)	61.8(0.9)	19.8(0.5)	99.3
R-V				98.0(0.9)		98.0

3.3.3. Possible reactions involving Fe, S and Se

To elucidate the mechanisms for Se(VI) reductive mobilization by mackinawite, pyrite and magnetite in CPW, we conducted XPS and XRD analyses on the solid samples reacted or not with Se(VI). The XPS characterization provides a direct investigation on the oxidation states of Fe and S at or near surface of solid mixtures. Compared to macknawite equilibrated with CPW without Se(VI) for the same time, on sample of mackinawite reacted with Se(VI) for 8 days (R-I), XPS spectra changes in the Fe2p and S2p binding energies (Figure 3.5a). The Fe_{2p} peak in high resolution scan displayed a noticeable shift in the binding energy from 707.6 to 710.8 eV after Se(VI) reduction. The $S2p_{3/2}$ and $S2p_{1/2}$ spectra with a fixed 2:1 intensity ratio and 1.18 eV energy separation in Figure 3.5b showed a decrease of S^{2-} content and an increase of S_n^{2-} in presence of Se(VI) of R-I system in compassion with the data on mackinawite without reacted with Se(VI) (dash line). The XRD results of R-I showed little amount of goethite (FeO(OH)) to be identified in Figure S3.4. These findings suggest that both reductants present within mackinawite, S^{2-} and Fe(II) could be oxidized to S_n^{2-} and Fe(III) species, accompanied by the reduction of Se(VI) to both $FeSe_{(s)}$ and $Se(IV)_{(s)}$. The $Fe(2p_{3/2})$ and S(2p) spectra of pyrite samples reacted or not with aqueous Se(VI) were quite similar. The $Fe(2p_{3/2})$ spectrum included a major peak at 707.1 eV attributed to Fe(II)-S species and the high energy tail at about 708.7 eV was attributed to Fe(III) as well as to a the major $S(2p_{3/2})$ component located at 162.7 eV assigned to S_2^{2-} within pyrite.[110-111] About 0.2 mM Se(VI) was adsorbed on the surface of pyrite in CPW after 8 days and 28.7% $Se(IV)_{(s)}$ was checked by LCF in Table 3.1. Thus, 0.1 mM electron was transferred during reaction. As the concentration of pyrite in CPW was 16.7 mM (2g/L), only 1.2 % Fe(II) could be oxidized to Fe(III) coupled to Se(VI) reduction to Se(IV), which is at the limit of XPS detection. It seems that a slight increase of Fe(III) peak at about 708.7 eV is observed but no obvious change for S2p peak of pyrite compared with the XPS result of mackinawite equilibrated with CPW for the same time (Figure 3.3). No other phases except for pyrite was observed for the XRD pattern of R-II sample in Figure 3.4. Han et al,. reported that no important changes of S2p and

$Fe2p_{3/2}$ spectra of pyrite in contact with Se(VI) for 30d at pH 8 were observed, but sulfide and tetrathionate were formed on the surface by via S_2^{2-} disproportionation in the case of Se(VI)-contacted pyrite system.[33] S_2^{2-} and Fe^{2+} in pyrite could be oxidized to S(0)/S(IV)/S(VI) or/and Fe^{3+} by the reduction of other redox-sensitive elements such as U(VI) and Tc(VII).[41, 112-113] The different reactivity of S_2^{2-} and Fe^{2+} with respect to different inorganic contaminants could be related to involution of different reaction mechanisms. As for magnetite systems in Figure 3.3, it can been seen that the content of Fe(II) peak in the Se(VI)-free magnetite sample (green box) was less than that of R-IV system, indicating an oxidation of Fe(II) to Fe(III) on magnetite surface coupled to the reduction of Se(IV) to either Se(IV) and Se^0. The XRD patterns of R-IV shown in Figure 3.4 indicated that the solid of magnetite reaction with Se(VI) for 8 d in CPW had the same pattern with magnetite equilibrated with CPW at the same time, suggesting no other phases including Se^0 phase (below detection) was checked by XRD. It's important to note that the XRD pattern of magnetite and maghemite (Fe_2O_3) are quite similar and the only difference is that the unit cell of maghemite (a = 8.34 Å) is smaller than that of magnetite (a = 8.40 Å).[102, 114] Therefore electron transfer was still occurring confirmed by XPS even no obvious XRD result supported the transformation of magnetite to maghemite.

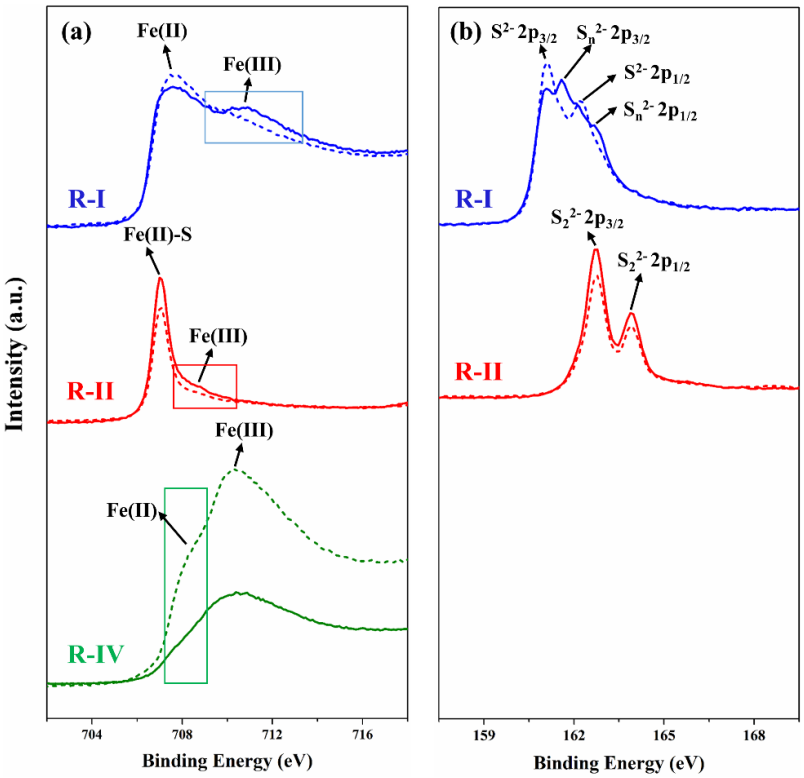

Figure 3.3. XPS spectra (a) Fe($2p_{3/2}$) and (b) S(2p) XPS scan. The solid lines labeled as R-I, R-II and R-IV represent the solids of macknawite, pyrite and magnetite reaction with Se(VI) in CPW for 8 days, respectively. The dashed lines represents mackinawite, pyrite and magnetite equilibrated with CPW at the same time.

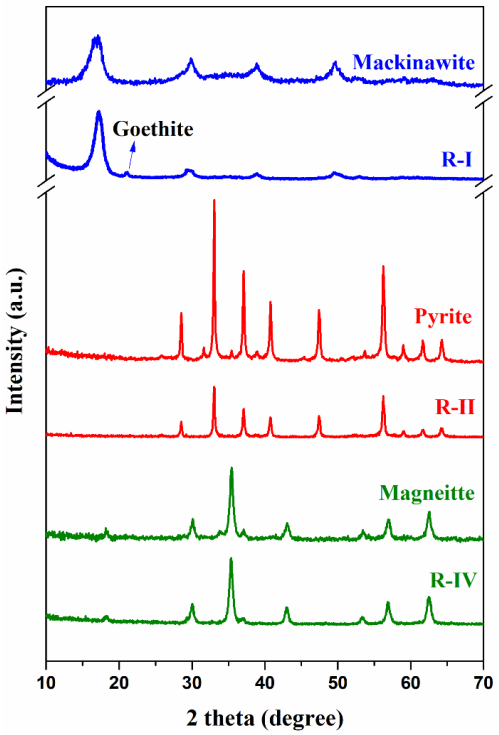

Figure 3.4. The solid XRD patterns. R-I, R-II and R-IV represent the solids of macknawite, pyrite and magnetite reaction with Se(VI) in CPW for 8 days, respectively.

3.3.4. "In-Situ" experimental Eh Values.

The Eh measurements and Eh modeling values, according to individual redox couples involved in mineral reaction with/without Se(VI) in CPW are shown in Figure 3.5. In the system of CPW with mackinawite, SO_4^{2-} with 2.0 mM predominates for aqueous S together with HS^- (0.08 mM) existed in CPW, according to thermodynamic modelling by Phreeqc. Also, the calculated values of Fe species concentrations was found to be 0.04 mM $Fe(OH)_3^-$ and 0.03 mM $Fe(OH)_4^-$, respectively. The calculated Eh value, controlled by SO_4^{2-}/HS^- and $Fe(OH)_4^-/Fe(OH)_3^-$ couples, was -0.643 V in the system. Aqueous SeO_4^{2-} species predominated for Se(VI) in CPW and 5.4 mM Se(-II), mainly as HSe^- species, was predicted at equilibrium in mackinawite reaction with Se(VI) in CPW system. However, as Se(-II) concentration are controlled by the precipitation of very insoluble FeSe, aqueous concentrations of HSe^- can be assumed to be extremely low below the detection limit and the aqueous Se(VI)/Se(-II) couple can not be an available system to compute Eh. A set of redox reactions susceptible to occur with Se(VI) leading to various reactions product are identified and listed in Table 3.2. All the $\Delta_f G^0$ of reaction species were taken from Andra ThermoChimie database,[20] and are listed in Table S3.1. The activities of solid phases and water were set equal to 1.0 as first approximation, although this may not be fully true due, for example, to the nanosize of reductively precipitated solid phases. Besides, surface adsorption of anions can be negligible at pH ~ 13.5 and we assumed the activity of adsorbed Se species to be equal to 1.0. "In-situ" experimental Eh values were then calculated according to eq 1. The obtained Eh of the system of mackinawite reacted with Se(VI) in CPW for 8 days (R-I) was -0.536 V, which was higher the thermodynamic equilibrium Eh (-0.643 V) calculated by Phreeqc. Based on the measured concentrations of S(-II) with 4.0 mM and S(VI) with 2.0 mM and the XRD result, the FeO(OH)/FeS and SO_4^{2-}/S^{2-} couples should impose the Eh values of -0.521 V and -0.678 V, respectively. The calculated Eh

of the FeO(OH)/FeS couple is closed to the measured data, suggesting the suspension Eh was mainly controlled by FeO(OH)/FeS couple. For Se species, experimental Eh values were -0.288 V (Se(VI)/FeSe couple) and -0.037 V (Se(VI)/Se(IV) couple), which were higher than the measured data. This indicates that the reduction of Se(VI) have not reached equilibrium after 8 days and more Se(VI) should be reduced to FeSe with a longer reaction time.

In the system of pyrite equilibrated with CPW for 9 days, the measured Eh of the suspension was -0.386 V. The calculated Eh by Phreeqc was -0.630 V and the potentials calculated for S(VI)/S(-II) and $Fe(OH)_4^-/Fe(OH)_3^-$ couples based on the thermodynamic equilibrium concentrations were the same value. For the system of Se(VI) reaction with pyrite in CPW (R-II), the measured Eh was -0.350 V after 8 days reaction at pH 13.5. The XPS result showed less obvious evidence of Fe(II) oxidation to Fe(III) but no change has occurred for S species during the reduction of Se(VI) to Se(IV). We can speculate that am-$Fe(OH)_3$ phase could be formed on the surface of FeS_2. In addition, am-$Fe(OH)_3$ is predicted to form by Phreeqc modelling, leading with am-$Fe(OH)_3$/am-$Fe(OH)_2$ half-reaction to an Eh value of -0.456 mV and the calculated Eh of $Fe(OH)_3/Fe(OH)_3^-$ couple to -0.365 V based on the Fe concentration, The later was affected by the concentration of Fe. In conclusion, whether the systems of pyrite in CPW contains Se(VI) or not, the Eh were mainly controlled by $Fe(OH)_3/Fe(OH)_3^-$ couple during the reaction and the Fe concentration is a critical key for correcting Eh computation.

The measured Eh value obtained in the magnetite equilibrated with CPW system after 9 days reaction was -0.559 V, lower than the Eh of R-IV system (-0.417 V) due to in presence of Se(VI). The calculated Eh by Phreeqc modelling was -0.601 V and the potential calculated for $Fe(OH)_4^-/Fe(OH)_3^-$ couple based on the thermodynamic equilibrium concentrations was -0.601 V. The reduction of Se(VI) to Se(VI) and Se(0) was accompanied by the oxidation of Fe(II) to Fe(III) in magnetite. The calculated potential of Fe_2O_3/Fe_3O_4 couple was -0.333 V and it was not affected by aqueous iron concentration, suggesting the couple was not the main factor for Eh determination.

However, the calculated Eh of $Fe_3O_{4(s)}/Fe^{2+}_{(aq)}$ couple was -0.388 V, which was closed to the measured value. Therefore, we can speculated that in this system, the measured Eh is probably determined by $Fe_3O_{4(s)}/Fe^{2+}_{(aq)}$ couple and the thermodynamic equilibrium Eh was caused by the $Fe(OH)_4^-/Fe(OH)_3^-$ couple.

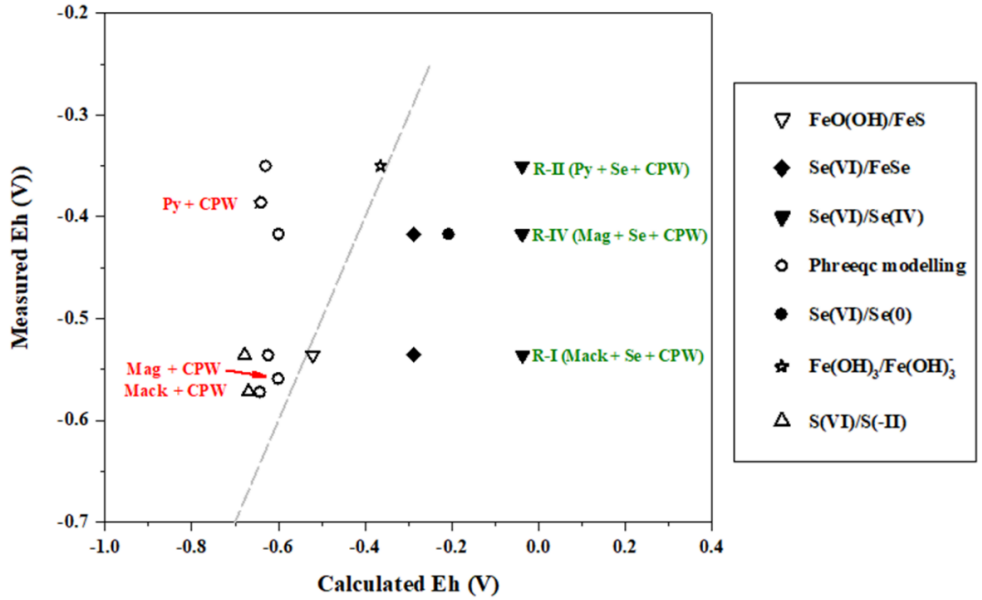

Figure 3.5. Comparison of Eh measurements of mackinawite, pyrite and magnetite reaction with/without Se(VI) in CPW with potentials calculated for individual redox species.

Table 3.2. Half-Cell Reduction and Oxidation Reactions

System	Half reaction equation	Eh^0 (V)
Se(VI)/Se(0)	$SeO_4^{2-}{}_{(aq)} + 6e^- + 4H_2O \rightarrow Se_{(s)} + 8OH^-$	-0.225
Se(IV)/Se(-II)	$SeO_4^{2-}{}_{(aq)} + 8e^- + 4H_2O + Fe(OH)_2 \rightarrow FeSe_{(s)} + 10OH^-$	-0.308
Se(IV)/Se(IV)	$SeO_4^-{}_{(aq)} + 2e^- + H_2O \rightarrow SeO_3^-{}_{(s)} + 2OH^-$	-0.001
FeO(OH)/ FeS	$FeO(OH)_{(s)} + S^{2-}{}_{(aq)} + e^- + H_2O \rightarrow FeS_{(s)} + 3OH^-$	-0.468
SO_4^{2-}/S^{2-}	$SO_4^{2-}{}_{(aq)} + 8e^- + 4H_2O \rightarrow S^{2-}{}_{(aq)} + 8OH^-$	-0.706
Fe_2O_3/Fe_3O_4	$3Fe_2O_{3(s)} + 2e^- + H_2O \rightarrow 2Fe_3O_{4(s)} + 2OH^-$	-0.333
$Fe(OH)_3/Fe(OH)_3^-$	$Fe(OH)_3 + e^- \rightarrow Fe(OH)_3^-{}_{(aq)}$	-0.710
$Fe(OH)_4^-/Fe(OH)_3^-$	$Fe(OH)_4^- + e^- \rightarrow Fe(OH)_3^-{}_{(aq)} + OH^-$	-0.668
Fe_3O_4/Fe^{2+}	$Fe_3O_{4(s)} + 2e^- + 4H_2O \rightarrow 3Fe^{2+} + 8OH^-$	-0.388

3.4. Environmental Implications.

In cement-rich radioactive waste repositories, the corrosion products, i.e., magnetite, mackinawite and pyrite, formed on the surface of the reinforcing steel significantly influence the Eh of cement porous media, which is vital to the retention of redox-sensitive radionuclides (RNs) (e.g., ^{79}Se) in case of eventual leakage. In our cases, the measured Eh using Pt electrode are compared with all the experimental Eh obtained from Se(VI) half-reactions and redox coupled species using the Nernst equation based on chemical/spectroscopic measurements. The measured Eh represents a mixed potential resulting from many different simultaneous ongoing electro-chemical reactions. Among the different redox couples studied in our systems, FeO(OH)/FeS couple can be considered as a master redox couple in the Se(VI) reaction with mackinawite in CPW system. The Eh value of Se(VI) reaction with magnetite in CPW system is probably imposed by the Fe_3O_4/Fe^{2+} couple. As for the system of Se(VI) reaction with pyrite in CPW, the Eh was mainly controlled by $Fe(OH)_3/Fe(OH)_3^-$ couple and the Fe concentration could have a critical role for correcting Eh calibration. In addition, Se couples including Se(VI)/Se(IV), Se(VI)/Se(0) and Se/(FeSe) in our study are not useful as “indicator” couples due to the redox reactions of Se(VI) by Fe phases in CPW lack of equilibrium among themselves within 8 days. This study will facilitate the estimation of the “experimental” redox potential in reinforced cement matrix, allowing a better evaluation of RNs redox behavior and mobility.

Supporting Information

Table S3.1. Standard Gibbs free energies of formation (Δ_fG^0, kJ mol^{-1}) used for performing thermodynamic calculations. All the data is from ANDRA Thermo-Chimie database.

Reactants/Products	Δ_fG^0 (kJ/mol)	Uncertainty
H_2O	-237.14	0.041
OH^-	-157.22	0.040
S^{2-}	109.850	2.721
$SO_4^{2-}{}_{(aq)}$	-744.004	0.418
$Se_{(s)}$	0.00	0.00
SeO_3^{2-}	-362.39	2.395
SeO_4^{2-}	-439.485	1.431
β-FeSe	-70.1	4.0
$Fe(OH)_3$	-688.352	-
Goethite	-488.334	4.698
Fe_3O_4	-1012.204	0.343
Fe_2O_3	-723.888	7.141
Fe^{2+}	-90.530	1.000
$Fe(OH)_3^-$	-619.865	8.621
$Fe(OH)_4^-$	-841.547	-
am-$Fe(OH)_3$	-713.202	1.245

Table S3.2. The ion concentrations of CPW equilibrated with mackinawite, pyrite and magnetite for 24 h

	S (mM)	Ca^{2+}(mM)	Fe^{2+}(μM)
Mackinawite	3.3	0.11	4.9
Pyrite	2.0	0.67	1.2
Magnetite	2.0	0.22	1.4

Chapter 4. H_2 or O_2 impact on Se(VI) and Re(VII) reduction by magnetite, mackinawite and pyrite

Abstract

Fe(II)-bearing minerals have the potential to uptake selenium (Se) enriched compounds in natural confinement and radionuclides (e.g., ^{79}Se and ^{99}Tc) in case of eventual leakage in nuclear waste repositories. Here, we investigated the reduction of Se(VI) and Re(VII), as the chemical surrogate for Tc(VII), by pyrite, magnetite and mackinawite under air, N_2 and H_2 atmospheres. Results indicate that Se(VI) was mainly reduced to trigonal γ-Se structure as nanoneedles by magnetite. Aqueous H_2 favored the reduction of Se(IV) and Se(VI) to Se(0). Furthermore, Se(VI) was reduced to monoclinic β-Se and FeSe by mackinawite under N_2 atmosphere, accompanied by the oxidation of mackinawite to goethite, magnetite and sulfur. Only β-Se was formed under air atmosphere and aqueous H_2 favored the production of FeSe. The formation of amorphous Se(0) and FeSe via Se(VI) reduction by pyrite under N_2 atmosphere, of Se(IV) species under air atmosphere and of $FeSe_2$ under H_2 atmosphere. Aqueous H_2, not FeS_2, probably play a key role for the reduction of Se(VI) by pyrite. The retention mechanism of Re(VII) by magnetite, mackinawite and pyrite followed non-redox complexation and reduction to ReO_3 under air atmosphere, but reductive precipitation, i.e., Re(IV), under N_2 and H_2 atmospheres. This work has implications for a better understanding of redox sensitive radionuclides reductive precipitation and of selenium contamination in natural confinement induced by interaction with Fe(II)-bearing minerals under different atmospheres.

Key words: Selenate reduction, Rhenate reduction, Fe(II)-bearing minerals, Selenium structure, Dissolved oxygen, Dissolved hydrogen.

4.1. Introduction

Se pollution with high concentration has attracted significant attention and is associated with human activities such as manufacturing processes, coal combustion and mining processes.[115-117] Furthermore, redox-sensitive ^{79}Se and ^{99}Tc, as the fission products of ^{235}U, have long half-life (4.8×10^5 y for ^{79}Se and 2.13×10^5 y and ^{99}Tc) and potentially high environmental mobility. Redox transformations from aqueous soluble Se(IV)/Se(VI) and Tc(VII) to insoluble Se(0, -I, -II) and Re(IV) under reducing conditions are closely related to the fate of Se and Re in the environment, especially for nuclear waste disposal. This has stimulated the research on Se and Re interactions with potential anthropogenic or natural barriers such as clays[8-10, 22, 50], cements[11-13, 65, 118] or Fe phases[10, 14-16, 39].

Redox-active Fe(II) minerals, e.g., pyrite, magnetite and mackinawite, not only are naturally present in water-logged soils, ore deposits, anocix aquifers and sedimentary,[2, 28-30] but also occur as the steel corrosion product in nuclear waste disposal under anaerobic geochemical conditions.[119-120] Due to their high reactivity and large specific surface area, they have tremendous potential to immobilize the environmental contaminants such as Se(IV) and Se(VI)[16, 29, 32-35], U(VI)[36-38], Tc(VII)[19, 39-40] as well as other heavy metals.[41-47] Most laboratory studies reported insoluble reduction species Se(0) or/and $FeSe_x$ could be formed on the surface of mackinawite, pyrite and magnetite.[16, 29, 33-35, 51, 75, 102] As reported previously, Se(IV) was reduced to a tetragonal FeSe-like phase after being in contact with mackinawite under acidic and anoxic conditions. However, red Se(0) nanoparticles could be formed though the reduction of Se(IV) by mackinawite at higher pH.[16] Mackinawite can also reduce Tc(VII) to Tc(IV) to from co-precipitates. Yalçıntaş et al., reported that the formation of TcS_x -like phase and the precipitation of $TcO_2 \cdot xH_2O$ was observed during the reduction of Tc(VII) in 0.1 M NaCl solutions and strictly anoxic conditions.[19] Se(IV)/Se(VI) could be reduced to Se(0) onto natural pyrite[34-35, 51] Also, Charlet et al., reported that $FeSe_2$ was the predominant thermodynamic species in pyrite-containing systems under reducing and neutral conditions.[32] The synthesized pyrite nanoparticles could rapidly and completely

remove Tc(VII) by reduction to insoluble Tc(IV).[43] Under sulfidic conditions, the aqueous sulfide had the potential to reduce Tc(VII) to TcO_2-like and TcS_x species (such as TcS_2 and Tc_2S_7).[57-58] Magnetite could catalyze the reduction of Se oxyanions to produce non-soluble Se(0) and FeSe. Marshall et al. reported that Tc(VII) was reduced to Tc(IV) during magnetite crystallization in cement leachates (pH 10.5-13.1) and Tc(IV) predominantly incorporated into the octahedral site of magnetite.[49]

Hydrogen (H_2) is naturally produced by biotic as well as abiotic pathways in the Earth's crust, e.g. (1) the activity of certain fermentative anaerobic bacteria and cyanobacteria, (2) the radiolysis of water due to U, Th, and K radioactive decay, and (3) the oxidation of Fe(II)-bearing minerals (e.g. olivine, pyroxene) into magnetite leading to the concomitant reduction of water into H_2. However, to the best of our knowledge, rare data reported the effect of H_2, even it is not likely to be reactive without specific catalysis, on the reduction of Se(VI) and Re(VII), as the chemical surrogate for Tc(VII), on magnetite, mackinawite and pyrite in literatures. In this study, we investigated the interaction of Se(VI) and Re(VII) with pyrite, magnetite and mackinawite under air, N_2 and H_2 atmospheres. The impact of aqueous O_2 and H_2 on the reduction species and the reaction mechanisms was deciphered by a combination of X-ray absorption spectroscopy (XAS), scanning electron microscopy (SEM), transmission electron microscopy (TEM), X-ray diffraction (XRD) and wet chemistry methods.

4.2. Material and methods

4.2.1. Materials.

Se(VI) and Re(VII) stock solutions were prepared by dissolving Na_2SeO_4 and $NaReO_4$ (Sigma-Aldrich). Boiled and N_2-degassed deionized water (DIW) (18.2 MΩ·cm) was used for all solutions and suspensions. All chemicals were analytical grade for the synthesis of iron phases (magnetite, pyrite and mackinawite) in this study. The synthesis experiments of iron phases were performed in a 99.99 % N_2-filled glovebox (O_2 < 2 ppm, using NaOH as the CO_2 trap) and more details were shown in the Supporting Information. The synthetic Fe solids were prepared on a silicon plate, sealed in the air-tight powder holder, and then checked by powder X-ray diffraction (XRD) (Bruker axs,

D8 advance) with Vortex-EX detector (Hitachi) under Cu Kα radiation, showing no distinct impurity diffraction peak in magnetite and mackinawite but containing 4% marcasite in pyrite (Figure S4.1). The specific surface area of Fe phases was determined to be 102.3 m^2/g (mackinawite), 63.6 m^2/g (magnetite) and 2.5 m^2/g (pyrite) by the Brunauer−Emmett−Teller (BET) N_2 absorption method. The size and shape of the iron phases were further characterized by TEM/SEM as illustrated in Figure S4.2.

4.2.2. Wet chemistry experiments.

All the sorption experiments were done in 0.1 M NaCl solutions at room temperature. An identical solid-to-liquid ratio was set 10g/L and the initial concentrations of Se(VI) and Re(VII) was ~12 mM for all experiments. After equilibration of the iron phases and 0.1 M NaCl solution for 7 days at pH 7.5 using 0.01/0.1 M HCl and NaOH to adjust, Se(VI) and Re(VII) were introduced to the suspensions respectively and then the pH was adjusted to 7.5 immediately. Each sample with about 30 mL was divided to three groups. One group of sorption experiment was conducted under a mix gas of 2 % H_2 and 98 % N_2 (P_{tot} = 10 bars) atomphere. The other two groups of sorption experiments run under air and N_2 (O_2 < 2 ppm) atompheres. After reaction for 105 days in free pH drift mode, the pH of suspensions was measured by a combined glass Micro-pH electrode (Metrohm 6.0234.100) after its calibration by pH 4.00, 7.01 and 10.00 standard solutions and the Eh of the suspensions was monitored by a combined Pt-ring ORP electrode (Metrohm 6.0451.100), after being calibrated with Zobell's solution (200 mV at 25 °C).[72] Then the suspensions were filtred through a 0.22 μm pore size membrane filter (Millpore). Extreme care was taken to minimize the potential for sample oxidation during subsequent solid characterizations. Total aqueous concentrations of S, Fe, Se and Re in the filtrates were analyzed by inductively coupled plasma optical emission spectrometry (ICP-OES) with a Varian 720-ES apparatus. The concentrations of Se(VI) was analyzed by ion chromatography (Dionex ICS-6000) with an Dionex™ IonPac™ AS9-HC IC Columns with 1.5 mL/min Na_2CO_3 (12.5 mM) as eluent. The retention time and calibration curves for Se(VI) were shown in Figure S2 and the standards of IC were checked by ICP-OES.

4.2.3. X-ray absorption spectroscopy (XAS).

Selenium K-edge and Rhenium L_1 X-ray absorption near-edge structure (XANES) spectra were used to determine the oxidation state of Se and Re in solid samples, which collected at the Core Level Absorption & Emission Spectroscopy (CLÆSS, BL22) beamline at the Spanish synchrotron ALBA-CELLS, Barcelona, Spain. Elemental Se and Re foils were used for energy calibrations in parallel with the measurements at the Se K-edge (12.658 keV) and Re L_1 (12.527 keV). Si(111) and Si(311) double crystal monochromators were used with approximately 0.3 eV resolution at 2.5 keV. A silicon drift detector (KETEK GmbH AXAS-M with an area of 80 mm^2) was employed to collect the fluorescence signal. All the samples for XAS were double-face sealed using polyimide tape, mounted on a sample holder, and measured in fluorescence mode, except for Se references, which were prepared as pellets with a cellulose matrix and measured in transmission mode. Before being transferred into the vacuum experimental chamber, samples were stored under N_2 atmosphere. The data integration and reduction of XANES spectra was performed by the Demeter software package.[73] Linear combination fits (LCF) were applied to identify and quantify the components in samples.

4.2.4. Scanning and transmission electron microscopy (SEM and TEM).

The samples of synthetic pyrite, Se nanoparticle in the filter of pyrite reaction with Se(VI) system and Se-sorbed particles on three Fe-phases were directly dispersed on the carbon tape and covered with ~ 1 nm gold layer, and then analyzed by SEM (ZEISS Ultra 55) equipped with energy selected X-Ray microanalysis system (EDS) and SDD Detector (BRUKER AXS-30mm^2). Synthetic magnetite, mackinawite and Se-sorbed particles on three Fe-phases were analyzed by TEM (JEOL-2100F) operating at 200 kV with energy dispersive X-ray spectroscopy (EDS). The TEM samples were dispersed in ethanol and sonicated for 5 min and a drop of treated samples was deposited on ultra-thin carbon grids for the TEM measurement. Gatan Digital Micrograph software was used to analyze the images.

4.3. Results and discussion

4.3.1. Se(VI) and Re(VII) reduction by magnetite

The aqueous analysis of magnetite system is given in Table S4.1. After 105 days reaction, the aqueous concentration of Se(VI) was equal to that of total Se under the three atmospheres, indicating that Se(VI) was the only species in aqueous phase. The decreased Se amount in solution, i.e., Se retention in the bulk solid phase, was a little larger under N_2 atmosphere than that under air and H_2 atmospheres. This leads to a higher K_d value (27.4 mL/g) under N_2 atmosphere. Under air atmospheres, 4.0 μM aqueous Fe was detected after reaction for 105 days under air atmosphere, suggesting that magnetite was weakly dissolved by reaction with aqueous O_2. In contrast, only 0.8 and 1.0 μM aqueous Fe were present in solutions under N_2 and H_2 atmospheres respectively, a concentration closed to the detection limit of Fe (0.7 μM) by ICP-OES. The chemical interactions between magnetite and Se(VI) in 0.1 M NaCl solutions were simulated by Phreeqc modelling using the Andra THERMOCHIMIE database.[20] Based on the final pH and Eh under N_2 atmosphere, 0.9 μM aqueous Fe (mainly as aqueous $Fe(OH)^{2+}$ species) was predicted to exist in solution, which is closed to the measured value. The final pH value of the suspensions decreased to 5.45 under N_2 atmosphere and 5.21 under air atmosphere after 105 days reaction, while it increased to 8.76 under H_2 atmosphere. The difference in pH probably suggest that the reaction mechanism to be different. In addition, the Eh values of the suspensions under three atmospheres were also extremely different and this could affect the reduction species of Se further explored using XAS.

The XANES region of the probed element can be used as a fingerprint of its oxidation state. Se K-edge XANES spectra was collected for Se-solid samples under air, N_2 and H_2 atmospheres. LCF results of the solids and the references are shown in Figure 4.1 and Table S4.2. For magnetite system under N_2 atmosphere, the mainly species of Se were 67.5(2.8) % Se(0), while only 10.3(4.3) % FeSe, 16.3(1.3) % Se(IV) and 11.9(0.6) % Se(VI) could be identified, indicating that Se(VI)-sorbed was mainly reduced to Se(0). Meanwhile, 59.9(2.3) % and 96.4(2.8) % Se(0) were identified as the primary Se species under air and H_2 atmospheres, respectively. Also, no Se(IV) and

Se(VI) species existed under H_2 atmosphere but they were present under air and N_2 atmospheres, which means aqueous H_2 could promote the reduction of Se(IV) and Se(VI) to Se(0). The corresponding half reactions of Se couples are listed in Table S4.3. Goberna-Ferrón et al., recently reported that Se(VI) adsorbed onto magnetite under Ar atmosphere was reduced to Se(0) and Se(IV) with Se(IV) being predominantly species after 1000 hours.[102] The main Se species difference, compared to our result under N_2 atmosphere, probably originate from the longer reaction time in our case. The reduction of Se(VI) could follow two irreversible reduction steps, i.e., Se(VI) reduced to Se(IV), and then to Se(0), and the first reduction step would be rate controlling in the overall kinetics.[102, 121] The point of zero charge of magnetite is about 7.5 and at pH 5.45 in our case, i.e., the positively charged magnetite could strongly adsorb Se(IV) through electrostatic interaction.[44] For this reason, the reduced Se(IV) could not release into solution and no aqueous Se(IV) could be identified by IC. The Eh-pH diagrams of Se species that were calculated using Phreeqc code coupling with Andra THERMOCHIMIE database are shown in Figure 4.2. Se(0) is predicted to be more stable under H_2 atmosphere, i.e., under experimental conditions of pH 8.76 and Eh -0.12 V, in good agreement with the experiment data where 96.4 % Se(0) was observed by LCF analysis. Under N_2 atmosphere, the measured pH and Eh values were 5.45 and 0.311 V, respectively, and the data fell on the borderline between Se(IV) and Se(0) stability fields. The LCF result showed that the main Se species in solid were 67.5 % Se(0) but with 16.3 % Se(IV), this in good agreement with pH and Eh inferred values. Se(IV) was supposed to be the predominant thermodynamic species in magnetite-containing system under air, i.e., oxidizing (Eh 0.573 V) and acid (5.21) conditions, while experimental results showed Se(0) and Se(IV) to be the main reduction species. It's likely that Se(0) is therefore a metastable phase, with slow oxidation transformation kinetics from Se^0 to Se(IV) by aqueous O_2.

Three primarily allotropic Se forms including trigonal Se (t-Se), monoclinic Se (m-Se) and amorphous Se (α-Se) were reported in literatures and α-Se is the thermodynamically unstable phase and could transform into t-Se at a low glass-

transition temperature (~31 °C).[122-123] Here, SEM and (S)TEM were used to monitor the morphology and the structure of reduced Se(0) nanoparticles. After reaction for 105 days, nano needles Se(0), significantly larger than nano-magnetite, was observed in magnetite systems under N_2, air and H_2 atmospheres by SEM in Figure 4.3. The formation of Se(0) via Se(IV) and Se(VI) reduction by magnetite was also demonstrated by previous studies.[29] The HAADF-STEM image of magnetite system under N_2 atmosphere in Figure 4.4 showed that aggregates of nano-magnetite particles with nano needle Se(0) readily identifiable as bright contrast spots on the surface. The nano needle was confirmed as solid-phase Se by energy-dispersive X-ray spectroscopy (EDS). Observed nano needle Se(0) was mostly 20-30 nm wide but can be about 620 nm in length. High-magnification imaging and the corresponding Fast Fourier Transform (FFT) with the low-index zone axis [001] in Figure 4.4e and 4.4h lead to the conclusion that the nano needle is the trigonal γ-Se structure (P_{3121} space group, a=4.366 Å, c=4.955 Å). The XRD patterns of magnetite system under N_2 atmosphere in Figure S4.1 indicated that the solid of magnetite reaction with Se(VI) for 105 days had the same pattern with pure magnetite. No other phases including Se phase (below detection) was checked by XRD. It's important to note that the XRD pattern of magnetite and maghemite (Fe_2O_3) are quite similar and the only difference is that the unit cell of maghemite (a = 8.34 Å) is smaller than that of magnetite (a = 8.40 Å).[102, 114] Therefore, electron transfer was still occurring even no obvious XRD result supported that magnetite was slightly oxidized to maghemite (equation 5 in Table S4.3). Furthermore, maghemite was oversaturated in magnetite system in presence of Se(VI) by Phreeqc modelling.

The summary of Se(VI) reduction by magnetite under three different atmospheres is as follows: (1) Magnetite was almost insolubleand aqueous Se(VI) was the only species present in solution; (2) Se(VI) was mainly reduced to Se(0) by magnetite under air, N_2 and H_2 atmospheres by the oxidation of magnetite to maghemite but aqueous H_2 could promote the reduction of Se(IV) and Se(VI) to Se(0); (3) The reduction Se(0) particles with nano needle morphology was with trigonal γ-Se structure.

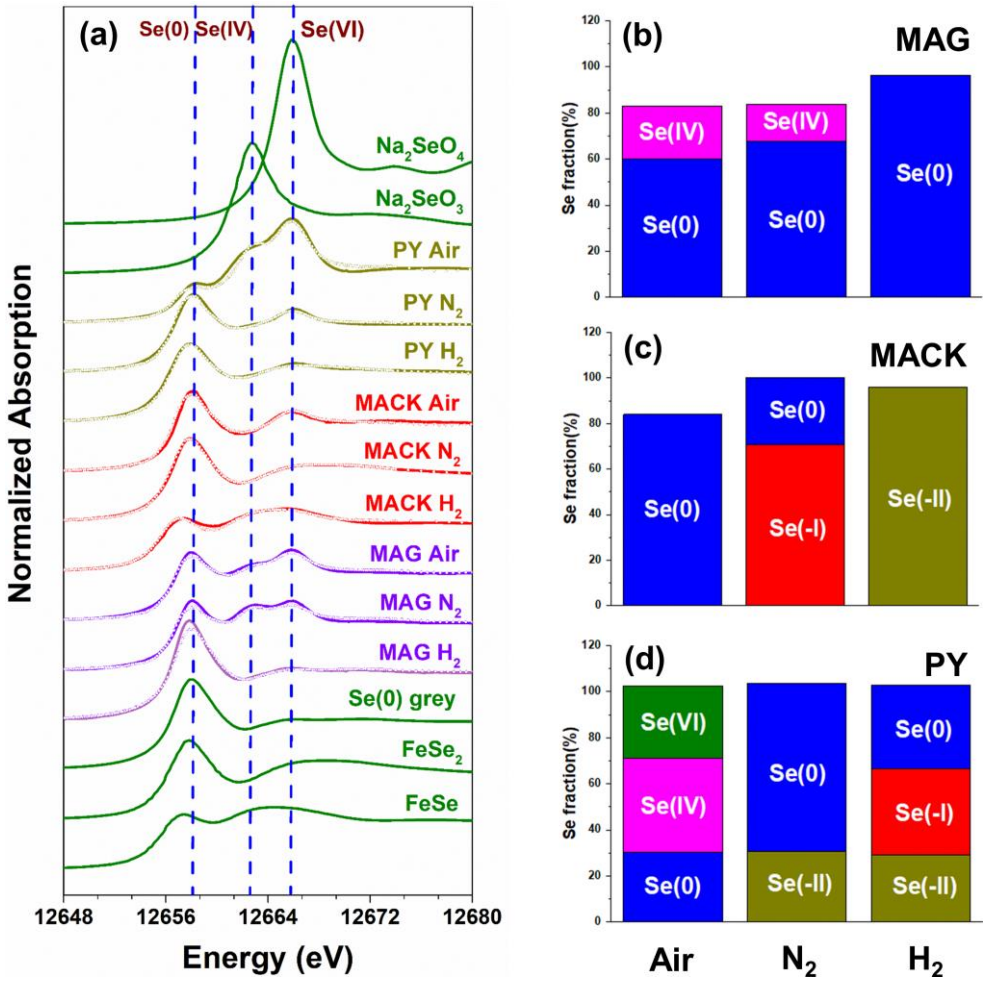

Figure 4.1. Se K-edge normalized XANES spectra of Se-solid samples after reaction with Fe phases for 105 days under air, N_2 and H_2 atmospheres, comparing to Se references (a). The main fractions (>15%) of FeSe, $FeSe_2$, Se^0, Se(IV) and Se(VI) components determined by LCF method (b) for magnetite (MAG) system, (c) for mackinawite (MACK) system and (d) for pyrite (PY) system.

The aqueous results of Re(VII) reaction and magnetite systems was listed in Table S4.4. After reaction for 105d, the total concentration of Re (0.1 Mm) under H_2 atmosphere was much lower than that under air (7.21 mM) and N_2 (7.53 mM) atmospheres, which leads to a very high K_d value (9900 mL/g) under H_2 atmosphere. Furthermore, the measured Fe concentrations under three different atmosphere were μM but they are higher than that of the systems with Se(VI). The Re-solid samples were investigated by XANES and the results are shown in Figure 4.5. From the normalized Re L_1 edge XANES, we can see that Re(VII) with a tetrahedral coordination of Re,

lacking an inversion center, exhibits a strong pre-edge peak, whereas, the pre-edge peak has nearly totally disappeared in case of ReO_2 with an octahedral coordination of Re. This is in good accordance with a previous report.[124] For magnetite sample under N_2 atmosphere, no XANES signal was obtained as the measurement problem. The LCF results shows that the formation of 22.6(2.3) % ReO_2 and 18.0(2.9) % Re(0) by Re(VII) reduction by magnetite under H_2 atmosphere and 9.9(2.1) % ReO_3 was the only reduced species under air atmosphere (Table S4.5). Usually, Re(IV), ReO_2, is the main species under reducing conditions, with the solubility in the range $4*10^{-7}$-10^{-6} mM.[125] Previous studies suggested that Tc(IV) incorporation to magnetite structure followed by the reduction of Tc(VII) to Tc (VI) by magnetite was the main retention mechanism for Tc(VII).[49, 126]

4.3.2. Se(VI) and Re(VII) reduction by mackinawite

As shown from the aqueous analysis of mackinawite reaction with Se(VI) systems in Table S1.1, the measured Se total concentrations were almost equal to Se(VI) concentrations under air, N_2 and H_2 atmospheres, suggesting that Se(VI) was the only aqueous species in the filtrates. Unlike the magnetite systems, the Se concentrations under N_2 and air atmospheres were lower than that under H_2 atmosphere and the obtained K_d values indicates a decreasing affinity of mackinawite for Se in the order of N_2 > air > H_2 atmosphere. In addition, aqueous iron concentrations remained μM level under three atmospheres, while the measured total concentration of S (5.07 mM) under air atmosphere was quite much higher than that under the other two atmospheres (0.20 mM for N_2 and 0.13 mM for H_2). It means that the dissolved oxygen was in favor of the dissolution of S from mackinawite. The simulated results of chemical interaction between mackinawite and Se(VI) in 0.1 M NaCl under N_2 atmosphere by Phreeqc modelling predicted that 5.7 mM Fe(II) (mainly as $Fe(OH)_3^-$ and $Fe(OH)_2$ species) and 3.6 mM Fe(III) (mainly as $Fe(OH)_4^-$ species) could release into solution. Also, 9.4 mM aqueous S(VI) but no aqueous S(-II) were present in the system by Phreeqc modeling, indicating the oxidation of S(-II) to S(VI) coupled with Se(VI) reduction. The experimental Fe and S concentrations under N_2 atmosphere is quite lower than the

calculated data, probably due to the unreached thermodynamic equilibrium. Clearly, the concentrations of Fe and S in the filtrates under N_2 and H_2 conditions were quite low compared with that of Se-reacted. It means that the reduction of Se(VI) mainly occurred on the surface of mackinawite, not in solution, if the adsorption of Se(VI) was mainly reduced. In addition, the final pH of three suspensions was close (H_2 atmosphere) or higher (air and N_2 atmospheres) than that the point of zero charge of mackinawite (7.5) and its solubility was mainly determined by the intrinsic solubility of aqueous FeS in more neutral and alkaline solution.[84] It may explained the μM level of aqueous iron concentrations during reaction.

The Se-XANES and LCF results of Se-solid samples indicates that 70.6(0.9) % $FeSe_2$ and 29.5(0.8) % Se(0) were the only two species under N_2 atmosphere, suggesting that Se(VI)-sorbed was completely reduced to Se(-I) and Se (0) after reaction with mackinawite for 105 days. Previous studies reported that Se(VI) was reduced to Se(IV), Se(0) or Se(-II) identified by XPS after being in contact with mackinawite for 100 h at pH 10 under anoxic conditions, but the reduction species was not assured as no report for Se references.[75] However, it seems that no reduction of Se(VI) existed under acidic and neutral pH.[75, 97] Kristen et al., found that 25% of aqueous Se(VI) was adsorbed on mackinawite at pH 7 after 24 h reaction and the remaining Se-solid was in form of presumably Se(0) or Se(-II) confirmed by XANES, which was similar to our result.[76] 83.9(0.5) % Se(0) and 95.8(0.4) % FeSe were identified to be the primary Se species under air and H_2 atmospheres respectively, which means that dissolved O_2 and H_2 had an impact on the reduction species. The Eh-pH diagrams of Se species in mackinawite systems showed in Figure 4.2(b). Base on the pH (9.70) and Eh (0.028 V), Se(0) was predicted to be more stable under N_2 atmosphere, whereas, except for Se(0), $FeSe_2$, as the main species, was also be identified by LCF analysis. According to the calculated $\Delta_r G^0$, the oxidation of $FeSe_2$ by remaining non-reduced Se(VI) is thermodynamically feasible (equation 1), but the phase transformation from $FeSe_2$ to Se(0) is extremely slow due to the low solubility of $FeSe_2$ (log K = -17.12).[20, 77] Under H_2 atmosphere (pH 7.70 and Eh -0.164 V), the calculated data fell on the borderline of $FeSe_2$ and Se(0)

species but FeSe was the predominant species by LCF analysis. Se(IV) was the predominant thermodynamic species under oxidizing (Eh 0.270V) and weakly base (pH 7.97) conditions, which is different with experimental measured Se(0) was the main species. It was probably the same situation with Se(VI)-magnetite systems under air atmosphere that the oxidation kinetics from Se(0) to Se(IV) was quite slow under air.

$$SeO_4^{2-} + 3FeSe_2 + 8H^+ = 7Se(0) + 3Fe^{2+} + 4H_2O \quad \Delta_rG° = -476.765 \text{ kJ/mol} \qquad (1)$$

The SEM images of Se nanoparticles in the solid samples under N_2 and H_2 atmospheres are shown in Figure 4.3b and 4.3c. Here it should be note that no Se(0) species was identified by LCF result in solid sample under H_2 atmosphere. The discrepancy exists between SEM observation and LCF results probably caused by the low content of Se(0) and the resolution of XANES to accurately distinguish Se(-II), Se(-II) and Se(0) species. The size of observed nanoparticle ranged from tens to several hundred nanometers and the morphology of bright Se particles was like nano plates. The STEM-HAADF image obtained from 105 days under N_2 atmosphere (Figure 4.4e) reveals the presence of irregular nanoparticles, which is the same shape observed by SEM. The observed nanoparticle is confirmed as solid-phase Se by EDS in Figure 4.4f. The circle part of TEM-BF image in Figure 4.4g from SAED measurement confirms the crystal structure as the monoclinic β-Se, which has the different morphology and structure of nano needle Se(0) as the trigonal γ-Se structure in magnetite systems. Furthermore, plenty of pill morphology sulfur particles and nano needles Fe oxides were formed under air atmosphere (Figure 4.3h and Figure S4.3). It is proposed Fe(II) was oxidized prior to S(-II) at neutral pH and Fe(II) can be quickly oxidized by O_2 to Fe(III), which was in turn reduced to Fe(II) by S(-II) and S(-II) was oxidized to elemental sulfur. XRD patterns of the solid under N_2 atmosphere suggest that goethite (14.0 %), magnetite (11.6 %), sulfur (5.7 %) and lepidocrocite (3.4 %) were produced except for mackinawite during Se(VI) reduction and the relative half-cell oxidation reactions (6)-(8) are listed in Table S4.3. No literature reported that the final oxidation products of mackinawite reaction with Se(VI) by XRD. Tanya et al,. found goethite, sulfur and trace amount of magnetite from upon the oxidation of mackinawite by U(VI).[30] Furthermore,

previous XPS studies evidenced the oxidation of sulfide to polysulfide/elemental sulfur and Fe(II) to Fe(III) in mackinawite coupled with selenite reduction.[48, 97]

In summary, Se(VI) could be reduced to $FeSe_2$ and monoclinic β-Se via the oxidation of mackinawite mainly to goethite and magnetite under N_2 atmosphere, and the dissolved oxygen and hydrogen by changing the Eh of the suspensions promoted the formation of Se(0) and FeSe, respectively.

The efficiency of mackinawite to immobilize aqueous Re(VII) under air, N_2 and H_2 atmospheres is listed in Table S4.4. We can see that the K_d value under air atmosphere (46 mL/g) was a little higher than that under the other two atmospheres (33 mL/g for N_2 and 38 mL/g for H_2). Under H_2 atmosphere, more S dissolved from mackinawite comparing with that under N_2 atmosphere and an increase of the pH existed in the two atmospheres. About 6.6 % of mackinawite dissolved under air atmosphere based on calculation from aqueous S concentration after reaction with Re for 105 days. In addition, the Eh values from highest to lowest was in order of air > N_2 > H_2. Figure 4.5 shows the Re L_1 XANES spectra of mackinawite systems. The main component (> 80 %) of Re-sorbed was ReS_2 under N_2 and H_2 atmospheres by LCF analysis, while Re(VII) was mainly reduced to ReO_3 under air atmosphere. The Re center in ReS_2 structure is surrounded by 3 pairs of S atoms at distances between 2.3 Å and 2.5 Å.[127] Yalçıntaş et al. reported that the formation of TcS_x-like phase and the precipitation of $TcO_2 \cdot xH_2O$ (~ 20 %) were observed during the reduction of Tc(VII) by mackinawite in 0.1 M NaCl solutions and under strictly anoxic conditions.[19] XAS was used by Wharton et al. to define the local chemical environments of Tc and its chemical analogue, Re, on coprecipitation with mackinawite. Their results suggested that Tc(VII) was reduced to Tc(IV) in presence of TcS_2-like phase on coprecipitation with FeS, which was similar for Re(VII) reduction.[39]

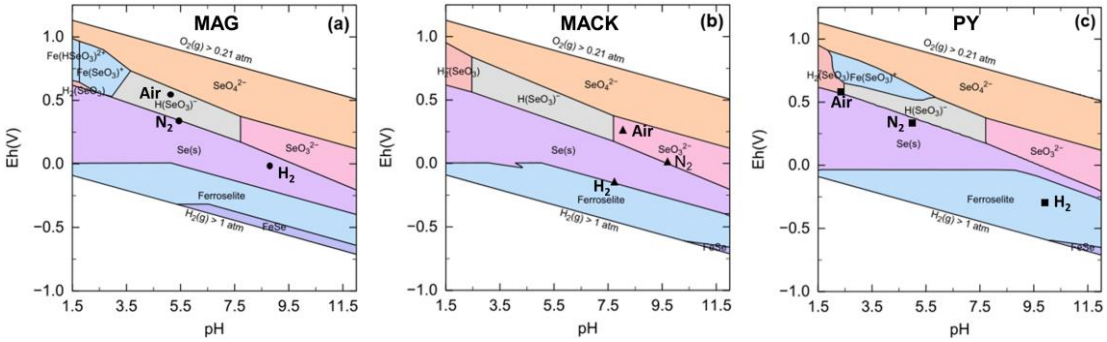

Figure 4.2. The Eh-pH diagrams of Se (12 mM) species in (a) magnetite (MAG), (b) mackinawite (MACK) and (c) pyrite (PY) systems. Experimental content of 0.1 M NaCl was input as the background matrix. The measured Eh and pH under air, N_2 and H_2 conditions after reaction for 192 h were marked as black points.

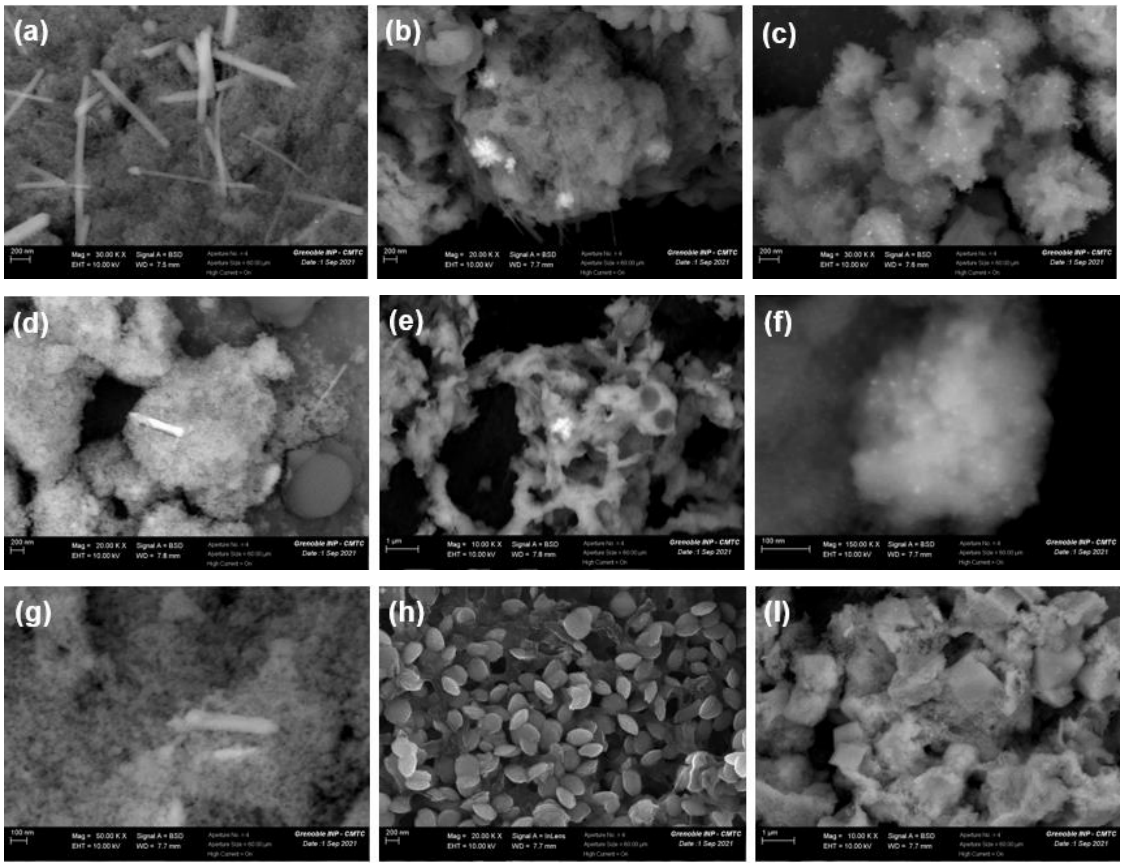

Figure 4.3. SEM images of different selenium morphologies and other phases. selenium nano needles in magnetite under (a) N_2, (d) H_2 and (g) air atmospheres; selenium nanoplates and sulfur nanoparticle in mackinawite systems under (b) N_2, (g) H_2 and (h) air conditions, nano selenium or other phases in pyrite system under (c) N_2, (f) H_2 and (I) air conditions

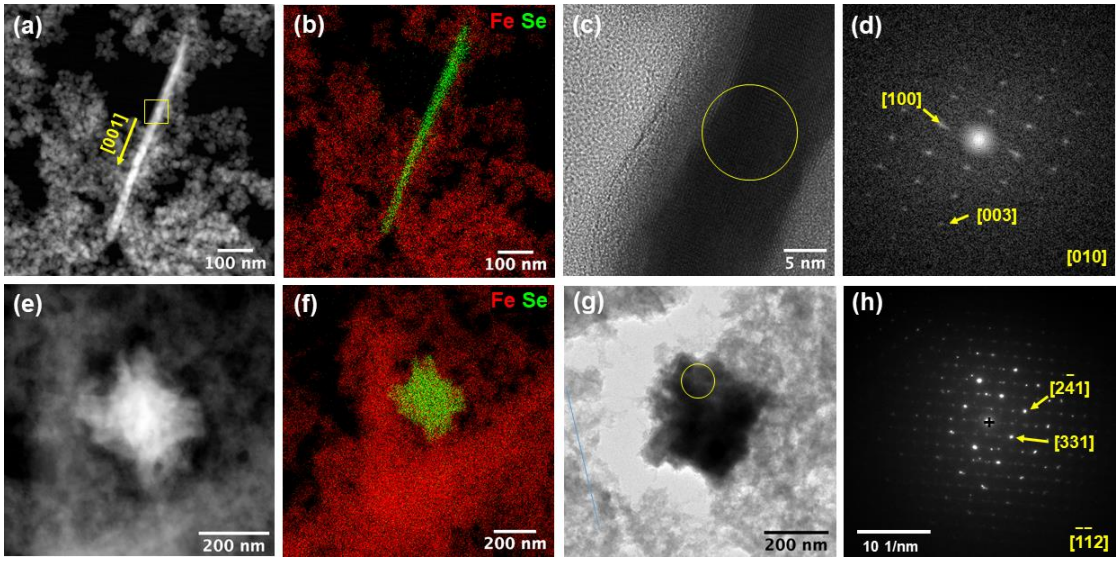

Figure 4.4. Scanning transmission electron micrographs of Se-magnetite (a, b, c, d) and Se-mackinawite (e, f, g, h) samples under N_2 conditions. (a) STEM-HAADF image of a Se nano needle, (b) the corresponding STEM-XEDS elemental mapping, (c) HRTEM image of the select area in figure (a), and (d) the corresponding Fast Fourier Transform (FFT) indexed with the trigonal γ-Se structure (P_{3121} space group, a=4.366 Å, c=4.955 Å) providing the exact orientation of the crystal. The [001] direction indicated in figure (a) is deduced from the indexation. (e) STEM-HAADF image of a Se nano particle, (f) the corresponding STEM-XEDS elemental mapping, (g) TEM-BF images of Se nano particle, and (h) the SAED related to the area labelled in image (g) and indexed with the monoclinic β-Se structure ($P_{21/n}$ spacegroup, a=9.054 Å, b=9.083 Å, c=11.601 Å and β=90.81 Å).

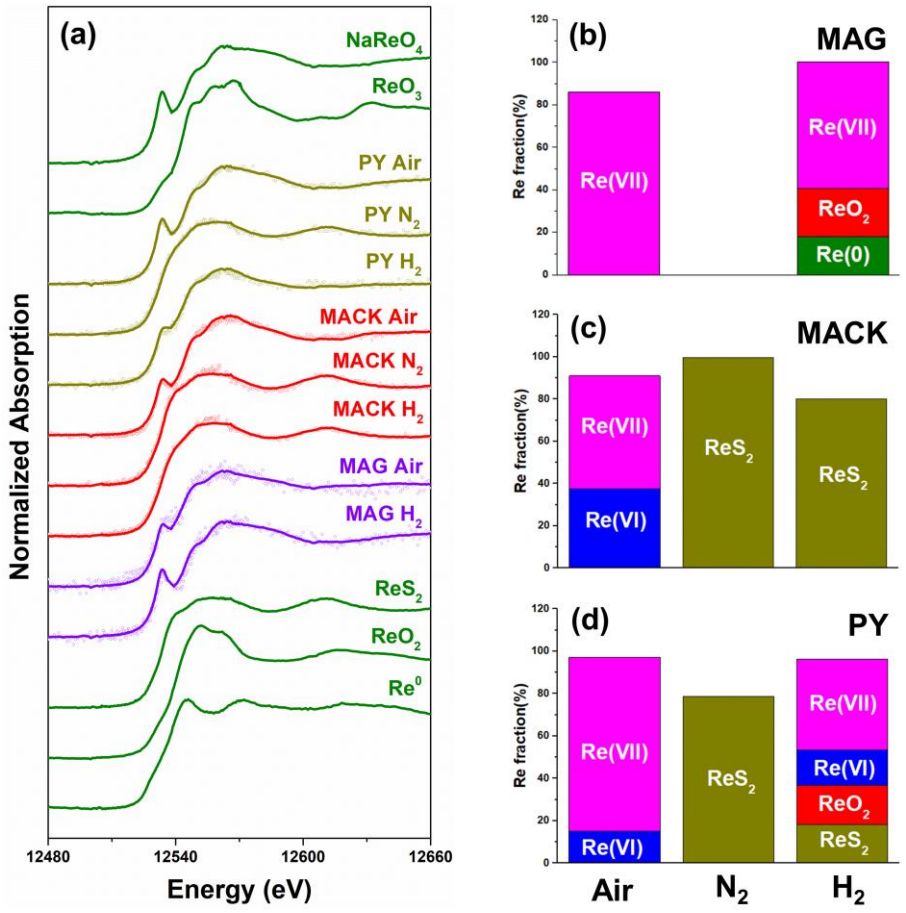

Figure 4.5. Re L1 normalized XANES spectra of Re-solid samples under air, N_2 and H_2 atmospheres, comparing to Re references. The result of magnetite (MAG) system under N_2 atmosphere not shown here as the poor signal quality. (a). The main fractions (>15%) of Re(0), ReS_2, ReO_2, Re(VI), and Re(VII) components determined by LCF method, (b) for magnetite system, (c) for mackinawite system and (d) for pyrite system.

4.3.3 Se(VI) and Re(VII) reduction by Pyrite

In the systems of pyrite reaction with Se(VI) for 105 days, it can be seen that the aqueous concentration of total Se (7.88 mM) was equal to that of Se(VI) (7.79 mM) under air atmosphere in Table S4.1, indicating that no other aqueous Se species except for Se(VI) was present in the filter and that the decreased amount of Se(VI) was retained in the bulk solid phase. More intriguingly, the total Se concentration was higher than that of Se(VI) under N_2 and H_2 atmospheres, which suggests that the reduction products of Se(VI) could be nano-sized, such as nano-Se^0, resulting in a colloidal dispersion in the suspension. The released Se(0) colloids was strongly supported by the observation

of SEM in Figure S4.3c. Mitchell et, al. reported that 13% of aqueous Se(VI) was adsorbed by pyrite after 24 hours reaction, which was higher than 3.8 % in our case calculated by the total concentration. The difference was probably caused by the release of nano-Se^0 colloids. The removal efficiency was about 16 % calculated from Se(VI) concentration. Under air conditions, pyrite had a higher K_d value (52.3 mL/g) for Se(VI) than the other two atmospheres, which maybe relate to the oxidation of pyrite by aqueous O_2 to form aqueous active Fe^{2+}, and Fe^{2+} has the potential to reduce Se(VI) to Se(0) proved by the previous studies.[69, 121] Meanwhile, measured mM concentrations of aqueous S were present in the systems under N_2 and H_2 atmospheres (Table S4.1). The Phreeqc simulated results of the reaction with Se(VI) and pyrite in 0.1 M NaCl solutions predicted that 11.1 mM S(VI) and 0.8 mM Fe(III) (mainly as $Fe(OH)_4^-$ species) could be produced coupled with all Se(VI) reduction to Se(-II) under N_2 atmosphere. However, only 0.2 mM S(-II) (mainly as HS^- species) and 0.2 μM Fe(III) but no S(VI) were predicted by Phreeqc modeling under H_2 atmosphere, even all aqueous Se(VI) was reduced to Se(-II). This suggests that aqueous H_2, not FeS_2, probably plays a key role for the reduction of Se(VI) by pyrite. Previous study reported that the dissociative adsorption of H_2 existed on pyrite (210) face,[128] a face of importance in the synthetic pyrite (Figure S4.1), which probably favor the reduction of Se(VI) by hydrogen radical. Here it should be noted that the comparable deviation of S concentrations between the measurement and calculation is probably caused by the unreached thermodynamic equilibrium.

Figure 4.2 presented the Se-solid XANES spectra of the Se-solid samples after reaction with pyrite for 105 days under air, N_2 and H_2 atmospheres. LCF results indicates that the main reduction products of Se(VI) were Se(0) (72.8 %) and FeSe (30.8 %) under N_2 atmosphere. Mitchell et, al. reported that Se(VI) was reduced to Se(IV) and Se(0)/Se(-II) by pyrite after 24 hours, while at a longer reaction time (14 days), a considerable amount of $FeSe_2$ and elemental Se formed though Se(VI) reduction on pyrite/greigite.[32, 76] Thus, the reaction time was one of the main influencing factors for Se reduction products in pyrite system. Besides, 30.1(0.8) %

Se(0), 41.0(0.8) % Se(IV) and 31.4(0.6) % Se(VI) were identified under air atmosphere. The presence of Se(IV) and Se(VI) probably caused by the presence of dissolved O_2. Se(VI) was mainly reduced to a mixture of 29.0(0.9) % Se(0), 37.4(1.6) % $FeSe_2$ and 36.4(1.2) % FeSe under H_2 atmosphere and H· was likely to be reducing agent for Se(VI) reduction. Based on the Eh-pH diagram of Se-containing pyrite system under N_2 atmosphere, Se(0) is predicted to be the thermodynamically stable phase, in consistent with the experimental data. $FeSe_2$ is expected to be more stable under H_2 atmosphere, i.e., the experimental pH 9.96 and Eh -0.259 V. $FeSe_2$, as one of the main experimental Se reduction species confirmed by the LCF result. Under air atmosphere, the measured Eh and pH values were 2.36 and 0.649 V, respectively, and the data fell on the borderline between Se(0) and Se(IV). The reduction species of Se(VI) by pyrite were Se(0) and Se(IV). Both of them matched very well.

The SEM images of Se-solid samples under three atmospheres were shown in Figure 4.3. It can be seen that the size of selenium nanoparticles (bright points) ranged from several to several ten nanometers presented in the sample under N_2 atmosphere (Figure 4.3c). The XRD pattern of the sample in Figure S4.1 suggests that no other phases were present except for pyrite and less amount of marcasite. As the content of Se(0)-sorbed on pyrite accounted for 0.4 % of the total mass, which is less than the detection limit of XRD (1 %) under N_2 atmosphere, it's not impossible to observed the diffraction peaks of Se(0) by XRD. We seek to identify the Se(0) structure by wide-angle X-ray scattering (WAXS) in Figure S4.4 and TEM (not shown here) but it was not successful. Thus, we speculate that the Se(0) nanoparticles observed in Figure 4.3c was amorphous. No literature reported that the final oxidation products of pyrite-Se(VI) by XRD. Han et al. reported that Se(IV) reduction was related to somewhat oxidation of Fe(II) to Fe(III) in pyrite, but no obvious changes in S_{2p} and Se_{3d} spectra were observed in Se(VI)-contacted pyrite system.[33]

In conclusion, Se(VI) was reduced to FeSe and nano-sized amorphous Se on synthetic pyrite and nano-Se^0 could result in a colloidal dispersion in the suspension. In addition, Dissolved O_2 promoted the formation Se(IV) species but aqueous H_2, not FeS_2,

probably play a key role for the reduction of Se(VI) by pyrite.

In the systems of Re(VII) reaction with pyrite, aqueous Fe released from pyrite remained low value under N_2 (93 μM) and H_2 (26 μM) atmospheres, but much higher under air atmosphere (27.14 mM) as the oxidation of pyrite by O_2. However, the S concentration under H_2 atmosphere (8.53 mM) was one order of magnitude higher than that under N_2 atmosphere (0.53 mM), which probably caused by the dissolution of pyrite was pH-dependent. Previous study reported that pyrite in alkaline conditions (pH 10) appeared to promote the oxidation of pyrite.[129] Wang et al. reported that the reaction between Re(VII) and pyrite was pH-dependent and the lower pH resulted in the greater Re(VII) removal rate.[60] Rodriguez's study suggested that all Tc could be removed from pH 3.5 to 10.5 after 35 days reaction.[113] The LCF result of Re-solid sample under air atmosphere shows that the main species were Re(VII) and ReO_3. The adsorbed Re is more likely to be oxidized rather than reduced in the presence of oxygen, though aqueous Fe^{2+} and H^+ were present in solution. However, ReS_2 (78.1 %) was the main reduction species with 11.6 % ReO_2 under N_2 atmosphere, which is consistent with those of the retention of Re(VII) via reducing it to Re(IV) by pyrite observed by Wang et al,.[60] Under H_2 atmosphere, a mixture of ReS_2, ReO_2 and ReO_3 was observed by LCF. Previous study reported that two different Tc species were formed depending on the pH in pyrite system: the formation of an inner-sphere sorption complex between hematite and Tc(IV) dimers at pH 6.00, and Tc(IV) incorporated into magnetite, replacing an Fe in an octahedral position at pH 10.00.[113]

4.4. Conclusions

Fe(II)-bearing minerals as the naturally present redox-active phases have the potential for the retention of selenium (Se) enriched compounds with high concentrations. In this study, a combination of XAS, SEM, TEM and wet chemistry methods was used to investigate the interaction between Se(VI) and Fe(II)-bearing minerals (magnetite, mackinawite and pyrite) under different atmospheres. Results indicate the reduced Se nanoparticles had three different morphologies and structures

as well as aqueous O_2 and H_2, deeply affecting the Eh of solutions, had an impact for the reduction species of Se after 105 d reaction. Se(VI) was mainly reduced to trigonal γ-Se structure as nano needles by magnetite. Aqueous H_2 was in favor of the reduction of Se(IV) and Se(VI) to Se(0). In addition, Se(VI) was reduced to a mixture of monoclinic β-Se and $FeSe_2$ under N_2 atmosphere, accompanied by the oxidation of mackinawite to goethite, magnetite and sulfur. Aqueous H_2 promoted to produce FeSe. Besides, Se(VI) was proved to be reduced Se^0 and FeSe by pyrite under N_2 and the forming amorphous Se^0 was several nanometers. Dissolved O_2 promoted the formation Se(IV) species but aqueous H_2, not FeS_2, probably play a key role for the reduction of Se(VI) by pyrite. As for Re(VII) reduction, the XANES results showed that Re(VII) can be mainly reduced into Re(IV) by the three Fe(II)-phases under N_2 and H_2 atmospheres, while ReO_3 was the main reduced species under air atmosphere. Also, magnetite and pyrite displayed a very good retention performance to Re under H_2 atmosphere. As a result, Se(VI) and Re(VII) reduction by Fe(II)-bearing minerals is a potential approach for sustainable Se(VI)-contaminated wastewater treatment and provides valuable information about the impact for redox-sensitive radionuclides under the aqueous H_2 and O_2 atmospheres.

Supporting Information

Associated content

XRD patterns, SEM and TEM micrograph of synthesized mackinawite, magnetite and pyrite. Synthesis of iron phases, The parameters of the suspensions, Quantificaiton of Se and Re species by LCF of XANES, SEM images and EDS analysis and wide-angle X-ray scattering (WAXS) results

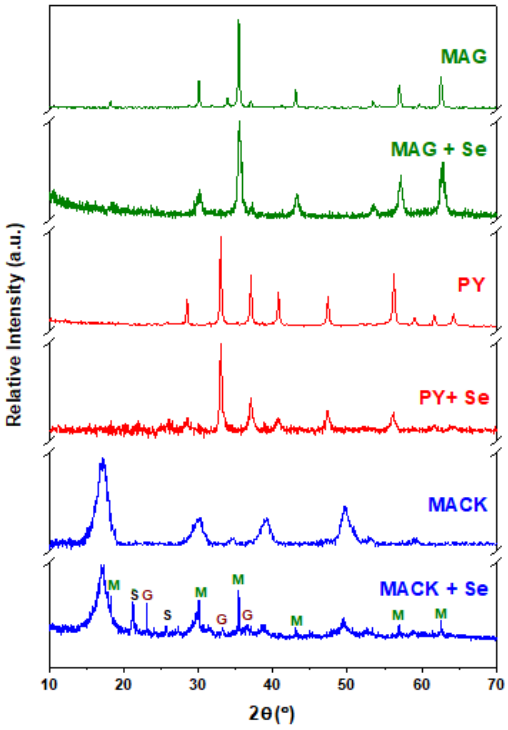

Figure S4.1. XRD pattern of synthetic magnetite (MAG), pyrite (PY) and mackinawite (MACK) and the relative solids after reaction with Se(VI) for 105 days under N_2 atmosphere. G, M and S represent goethite, magnetite and sulfur.

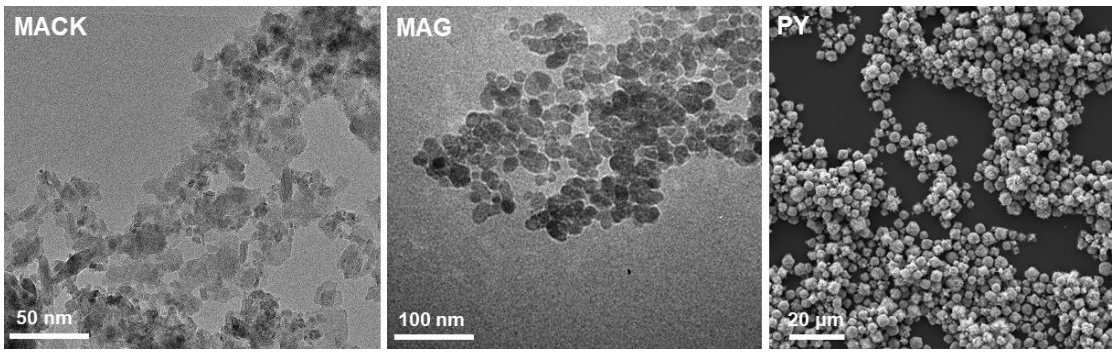

Figure S4.2. Characterization synthetic magnetite (MAG), mackinawite (MACK) and

pyrite (PY) by TEM for mackinawite and magnetite as well as SEM for pyrite.

Text S4.1. Synthesis of Iron Phases

Magnetite: Magnetite was synthesized by slowly adding 50 ml of a mixed ferrous/ferric chloride solution (Fe^{II}/Fe^{III} = 0.5 and $[Fe]_{total}$ = 1.2 M, $[FeCl_2]$ = 0.4 M and $[FeCl_3]$ = 0.8 M)) into 400 ml of 0.9 M NH_3 solution. Both the ammonia solution and aqueous Fe^{II}+Fe^{III} solutions were prepared with N_2 degassed water prior to the mineral synthesis. The suspension was washed by replacing the supernatant with degassed DIW for six times and then dried in the anaerobic chamber.

Mackinawite: The mackinawite suspension (0.3 M Fe) was prepared in the glovebox by mixing 100 mL of a 0.6 M Fe(II) solution $Fe(NH_4)_2(SO_4)_2{\cdot}4H2O$ with 100 mL of a 0.6 M S(-II) solution ($Na_2S{\cdot}9H2O$) under stirring. Black precipitate occurred instantly and aged for 1 day. After, the suspension was filtered through a 0.22 μm pore size membrane and was washed by replacing the supernatant with degassed DIW for six times in the glovebox and then dried in the anaerobic chamber [4].

Pyrite: Pyrite was synthesized by reacting 0.05 M $FeCl_3$ with 0.15 M NaHS. The $FeCl_3$/NaHS ratio was 1:3, because the interaction of NaHS with $FeCl_3$ produces a large amount of acid that can volatilize the HS^- reactant, resulting in the formation of greigite impurities in the final product[5]. Also, during the reaction process, a determined amount of NaOH was continuously added to neutralize the formed acid, maintaining the solution's pH at ~4.5. After aging for 7 days, the FeS_2 precipitation was washed by 0.2 M HCl to removal FeS as intermediates followed by acetone and carbon disulfide to remove sulfur, then by degassed DIW for 6 times. Finally, the synthesized pyrite solids were dried in the anaerobic chamber.

Table S4.1. The parameters of the suspensions of Se(VI) reaction with magnetite (MAG) /mackinawite (MACK) /pyrite (PY) for 105 days.

		pH	**Eh (mV)**	**$[Fe]_{tot}$ (μM)**	**$[S]_{tot}$ (mM)**	**$[Se]_{tot}$ (mM)**	**[Se(VI)](mM)**	**K_d(mL/g)**
MAG	N_2	5.45	331	0.8	-	9.42.	9.40	27.4

	H_2	8.76	-12	1.0	-	9.74	9.46	23.2
	Air	5.21	573	4.0	-	9.85	9.27	21.8
MACK	N_2	9.70	28	3.0	0.20	4.79	4.81	150.5
	H_2	7.70	-164	4.4	0.13	10.90	10.66	10.1
	Air	7.97	270	1.2	5.00	6.97	6.66	72.1
PY	N_2	4.97	476	6.2	0.90	11.55	10.09	3.4
	H_2	9.96	-259	0.8	1.41	10.53	8.83	14
	Air	2.36	649	44.6 *10^3	65.56	7.88	7.79	52.3

Table S4.2. Quantification of Se species (molar fraction) by LCF of XANES

		FeSe (%)	**$FeSe_2$ (%)**	**Se^0 (%)**	**Na_2SeO_3 (%)**	**Na_2SeO_4 (%)**	**∑(%)**	**χ^2 (10^{-3})**
MAG	N_2	10.3(4.3)		67.5(2.8)	16.3(1.3)	11.9(0.6)	106.0	2.4
	H_2		5.3(2.8)	96.4(2.8)			101.7	2.3
	Air	9.9(3.5)		59.9(2.3)	23.1(1.1)	6.7(0.5)	99.6	2.2
MACK	N_2		70.6(0.9)	29.5(0.8)			100.1	0.1
	H_2	95.8(0.4)				2.0(0.3)	97.8	0.7
	Air			83.9(0.5)	2.3(0.5)	8.9(0.5)	95.1	1.7
PY	N_2	30.8(1.7)		72.8(1.4)		5.8(0.4)	109.4	1.5
	H_2	29.0(0.9)	37.4(1.6)	36.4(1.2)			102.8	0.4
	Air			30.1(0.8)	41.0(0.8)	31.4(0.6)	102.6	0.4

Table S4.3. Table S8. Half-Cell Reduction and Oxidation Reactions

System	**Half reaction equation**	**Number**
Se(VI)/Se(IV)	$HSeO_4^-{}_{(aq)} + 2e^- + H_2O \Leftrightarrow HSeO_3^-{}_{(s)} + 2OH^-$	1

Se(VI)/Se(0)	$HSeO_4^-{}_{(aq)} + 6e^- + 3H_2O \Leftrightarrow Se(0) + 7OH^-$	2
Se(VI)/Se(-I)	$2HSeO_4^-{}_{(aq)} + Fe^{2+}{}_{(aq)} + 14e^- + 6H_2O \Leftrightarrow FeSe_{2(s)} + 14OH^-$	3
Se(VI)/Se(-II)	$HSeO_4^-{}_{(aq)} + Fe^{2+}{}_{(aq)} + 8e^- + 3H_2O \Leftrightarrow FeSe_{(s)} + 7OH^-$	4
Fe_3O_4/Fe_2O_3	$2Fe_3O_{4(s)} - 2e^- \Leftrightarrow 3Fe_2O_3$	5
FeS/Fe_3O_4	$3FeS_{(s)} - 2e^- + 5OH^- \Leftrightarrow Fe_3O_4 + 3HS^-{}_{(aq)} + H_2O$	6
FeS/FeO(OH)	$FeS_{(s)} - e^- + 2OH^- \Leftrightarrow FeO(OH)_{(s)} + HS^-{}_{(aq)}$	7
$S(0)/HS^-$	$HS^-{}_{(aq)} - 2e^- + OH^- \Leftrightarrow S(0)_{(s)} + H_2O$	8
H_2O/H_2	$H_{2(aq)} - 2e^- + 2OH^- \Leftrightarrow 2H_2O$	9

Table S4.4. The parameters of the suspensions of Re(VII) reaction with magnetite (MAG), mackinawite (MACK) and pyrite (PY) for 105 days.

		pH	Eh (mV)	$[Fe]_{tot}$ (mM)	$[S]_{tot}$ (mM)	$[Re]_{tot}$ (mM)	K_d (mL/g)
MAG	N_2	5.99	220	0.19	-	7.53	33
	H_2	8.80	-214	0.027	-	0.10	9900
	Air	3.99	400	0.041	-	7.21	39
MACK	N_2	9.22	-153	0.032	0.11	7.53	33
	H_2	11.16	-452	0.025	0.66	7.25	38
	Air	3.16	403	5.07	7.56	6.85	46
PY	N_2	5.16	218	0.093	0.53	2.26	342
	H_2	11.17	-492	0.026	8.53	0.13	7592
	Air	1.01	434	27.14	28.00	7.20	39

Table S4.5. Quantification of Re species (molar fraction) by LCF of XANES

		Re (%)	ReS_2 (%)	ReO_2 (%)	ReO_3 (%)	$NaReO_4$ (%)	∑(%)	χ^2 (10^{-3})
MAG	H_2	18.0(2.9)		22.6(2.3)		59.4(4.2)	100.0	2.8

	Air			9.9(2.1)	86.1(2.2)	96.0	2.1
MACK	N_2	99.6(1.9)	2.5(1.7)			102.0	0.8
	H_2	80.2(1.9)	11.6(1.5)		10.0(1.2)	101.9	0.6
	Air	6.3(1.3)		37.7(1.3)	53.4(1.7)	97.3	0.8
PY	N_2	78.1(1.8)	11.6(1.3)		10.8(1.1)	100.5	0.4
	H_2	18.4(2.9)	18.2(3.4)	16.7(2.7)	43.1(2.3)	96.4	0.8
	Air		1.2(1.1)	15.1(1.3)	82.1(0.9)	98.5	0.4

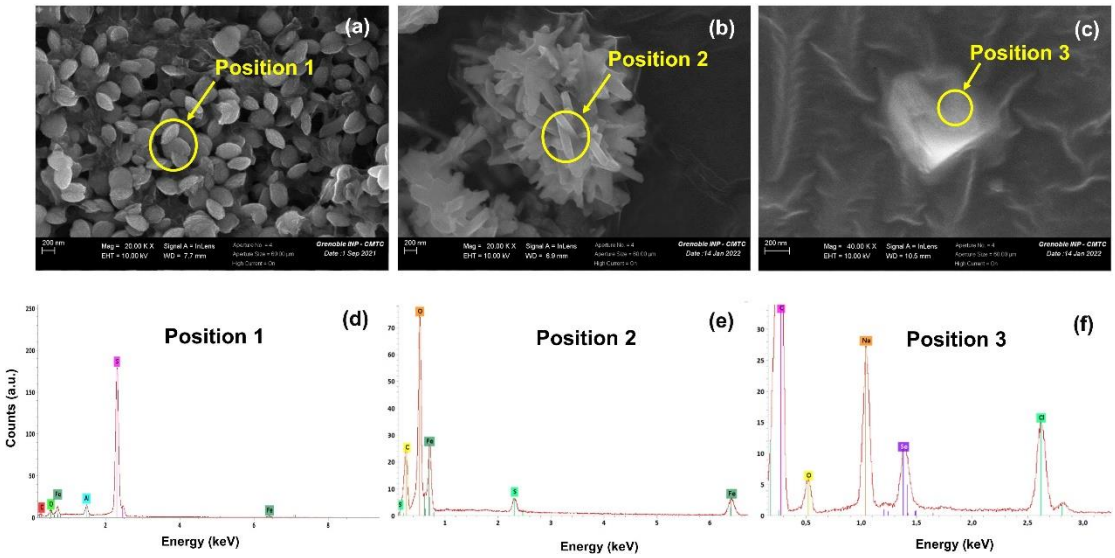

Figure S4.3. SEM images and EDS analysis of samples. The formation of plenty of pill morphology particles (a) and nano needles (b) in the solid samples of Se(VI) reaction with mackinawite for 105 days under air atmosphere, and the EDS results suggesting these particles were sulfur (d) and Fe oxides, (c) and (f) The amorphous Se(0) nanoparticles precipitated on the surface of NaCl cubic solid during drying of the filter sample of Se(VI) reaction with pyrite for 105 days under N_2 atmosphere.

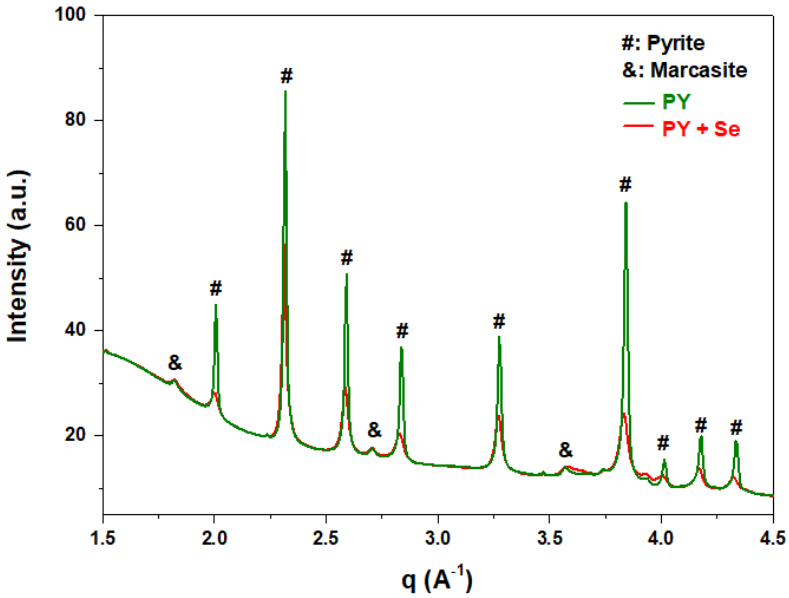

Figure S4.4. Wide-angle X-ray scattering (WAXS) results of synthetic pyrite and the solid of pyrite reaction with Se(VI) for 105 days under N_2 atmosphere showing no Se(0) peaks present

Chapter 5. H_2 impact on the reduction of Se(VI) by claystone pyrite

Abstract

Soluble Se oxyanions reductive transformations to insoluble Se (0, -I and -II) species largely limit Se mobility biogeochemical behavior. Numerous reports focused on Se(VI) retention by pyrite under N_2 condition, but only very scarce studies report on the impact of H_2 on Se(VI) retention by pyrite, although H_2 is naturally present in the Earth's crust and produces by steel corrosion in confined environment. Here, Se(VI) reduction by natural pyrite extracted from Callovo-Oxfordian formation claystone was investigated under N_2 and H_2 conditions. Results showed that Se(VI) uptake was not significant with quite the same uptake (K_d = 4~5 mL/g) under both conditions. Among Se(VI)-sorbed under N_2 condition, 8.0 % was reduced to Se(0) after reaction for 55 days identified by Se K-edge X-ray absorption spectroscopy (XAS). However, under H_2 condition, 12.2% Se(0) and 45.7% Se(IV) were checked after 9 days reaction and all adsorption Se(VI) was reduced to Se(0) by natural pyrite after 55 days, which indicated stepwise reduction of Se(VI) to Se(IV) and then to Se(0). The dissolved H_2 has therefore a key impact for the reduction of Se(VI) by natural pyrite. This work provides valuable data about the retardation mechanisms of redox-sensitive elements by pyrite under different conditions, especially in the real geological waste disposal sites.

Key words: Selenium, Natural pyrite, Retention mechanism, Hydrogen

5.1. Introduction

Se pollution has attracted significant attention and is associated with human activities such as manufacturing processes, coal combustion and mining processes, which has increasingly.[115-117] Furthermore, the ^{79}Se isotope has attracted great concern due to its potential mobility in deep geological repositories. The fate of selenium, i.e., solubility and mobility, is significantly determined by its oxidation state. Se(IV) and Se(VI), with highly soluble and mobile, was main species under oxidizing conditions, In contrast, under reducing conditions, the expected selenium oxidation states, namely Se(0, -I and –II), is restricted by the low solubility and mobility.[27] Redox transformations from soluble Se oxyanions to insoluble species by redox-active minerals including Fe(II) or sulfide-bearing phases largely constrain biogeochemical behavior in water-logged soils, ore deposits, anoxic aquifers and sedimentary.

Pyrite not only is ubiquitous in clay-rich formations.[2, 28, 130] but also occurs as the steel corrosion product in nuclear waste disposal under anaerobic geochemical conditions. It has tremendous potential to immobilize the environmental contaminants such as Se(IV) and Se(VI)[32-35], uranium(VI)[36-37] , as well as other heavy metals.[41-43] Se(IV)/Se(VI) could be reduced to Se(0) on adsorption onto natural pyrite[34-35, 51] Also, Charlet et al., reported that $FeSe_2$ was the predominant thermodynamic species in pyrite-containing systems under reducing and neutral conditions.[32]

Callovo-Oxfordian (COx) formation at Bure was choose as host rock for the long-term storage of radioactive waste in France and the main minerals present in COx formation are 40-55% carbonates and quartz, 20-55 % clay minerals (mixed layer illite/smectite) with less than 1.1 % of total organic carbon and accessory minerals including 0.5-0.9 % pyrite.[2] CO_2 would be produced by claystone oxidation during drilling of galleries and disposal cells and the partial pressure of CO_2 was gave a value of $\log(pCO_2) = -2.0 \pm 0.2$ bar.[4] The production of H_2 had also been identified due to the corrosion of the steel in contact with underground pore water,[5] and biotic as well as abiotic pathways in the Earth's crust.[67] Thermodynamic calculations predicted that Se(0, -II) oxidation states existed under conditions existing in Callovo-Oxfordian formation

and, Se(-II) might be formed giving the low concentration levels and presence of dissolved H_2.[26] Recent research about the mobility of selenite and selenite in Callovo-Oxfordian claystone showed that some correlations existed between reduced Se(0, -I or/and –II) and Fe content by μXRF mapping, suggesting Se reduction by Fe containing solids (pyrite, ankerite, and/or siderite).[52] Several studies also found that Se(IV) was reduced to Se(0) or/and Se(-II) by natural Fe(II)-bearing minerals in Boom clay (Belgium), Tamusu clay (China) and Opalinus Clay under anoxic conditions.[28, 53-54]

To our knowledge, the reduction of Se(VI), if any, by nature pyrite in COx are rather scarce, only one recent report studied the diffusion of Se(VI) in COx rock disk and found that no significant sorption or reduction of Se(VI) exisited.[52] More importantly, the impact of H_2, which deeply affects the Eh of solution, for the reduction of Se(VI) is evaluated for the first time and the Se(VI) reduction mechanism is not well-understood. Considering this, we investigated the interaction mechanism between Se(VI) and natural pyrite in COx pore water under N_2 and H_2 conditions by a combination of wet chemistry methods, X-ray absorption spectroscopy (XAS) and Phreeqc modeling using the Andra THERMOCHIMIE database. This work contributes to advance the understanding on the interaction mechanisms and between redox-sensitive radionuclide oxyanions and pyrite and on the effect of H_2 for the reduction pathway and species of redox-sensitive radionuclide oxyanions by pyrite.

5.2. Material and methods

5.2.1. Materials and chemicals.

Degassed Milli-Q water (18.2 MΩ·cm) was used for all solutions. Sodium selenate (Na_2SeO_4) and chemicals used for COx pore water synthesis were purchased from Sigma-Aldrich. The chemical composition of synthetic fresh COx pore water used as matrix solution was shown in Table S5.1. The Callovo-Oxfordian formation (COx) core extracted at 420-550 m depth below ground level was collected from the borehole OHZ1202 of the Meuse/Haute Marne Underground Laboratory. The rock core was inserted right after extraction into an airtight aluminum foil package and transported into a N_2 glove box.

5.2.2. Claystone pyrite isolation.

The dissolution of claystone carbonates, including calcite ($CaCO_3$) and trace little amount of ferriferous carbonates such as ankerite $Ca(Fe,Mg,Mn)(CO_3)_2$ and siderite ($FeCO_3$), in COx by 0.5 M HCl was performed at 25 °C under anoxic conditions (< 2 ppm O_2). After carbonates have been totally dissolves (no bubbles production), the suspension is filtered through 0.22 μm pore size membrane and washed six times with degassed DIW in the glovebox. The solid is vacuum dried after the washing. The XRD result of the solid sample with ~0.9 % pyrite was shown in Figure S5.1 and it mainly existed two different sizes (~5 μm and ~1 μm) of pyrite with diamond morphology in Figure S5.2.

5.2.3. Wet chemical experiments.

The SeO_4^{2-} sorption experiment of on natural pyrite is conducted at 25 °C under either anoxic or 1% CO_2 / 99% H_2 conditions (P_{tot} = 5 bars) in stainless steel auto-clave. Here we used H_2 as the presentative of 1% CO_2 / 99% H_2. The S/L ratios in two reaction suspensions is set to be 10 g/L and the initial concentration of SeO_4^{2-} is 2.3 mM. Prior to introducing SeO_4^{2-}, the solid is equilibrated with synthetic COx pore water for 9 days under anoxic conditions. After reaction for 9 and 55 days, The Eh and pH of suspensions were measured by a combined glass Micro-pH electrode (Metrohm 6.0234.100) and a combined Pt-ring ORP electrode (Metrohm 6.0451.100) respectively.

5.2.4. Solid and liquid analysis.

The solid phases were analyzed by Se-XANES spectroscopy to determine the Se species. Details about RIXS experiments and analysis are provided as supporting information in Text S1. Total aqueous concentrations of S, Fe and Se were analyzed by inductively coupled plasma optical emission spectrometry (ICP-OES) with a Varian 720-ES apparatus. S(VI) and Se(VI) concentrations were analyzed by ion chromatography (Dionex ICS-6000) with an Dionex™ IonPac™ AS9-HC IC Columns with 1.5 mL/min Na_2CO_3 (12.5 mM) as eluent. The retention time and calibration curves for Se(VI) and S(IV) were shown in Figure S5.3.

5.3. Results and discussion

5.3.1. Aqueous analysis

The parameters of the suspensions after reaction for 9 and 55 days under N_2 and H_2 conditions are shown in Table S5.2. Se(VI) uptake was not significant with quite the same uptake under both conditions (H_2 and N_2 atmospheres) within the uncertainties, even though the Eh and pH values under H_2 conditions were lower than that under N_2. This observation is in agreement with Se(VI) retention on Boom clay and argillaceous rocks under N_2.[52, 131-132] One reasonable interpretation of the results was probably the competition by S(VI) present in a large amounts in matrix and the other one is allowed by the weak adsorption and outer-sphere complexation on minerals by XAFS measurement and chemical surface complexation model.[52, 133-134] Interestingly, compared to the trace amounts of Fe (0.8 μM) almost reaching the limit of ICP (0.7 μM) in solution after 9 days reaction under N_2 condition, 15 μM Fe was present under H_2 condition and the dissolved Fe was probably in favor of surface catalyzer Se(VI) reduction.[121, 135] Furthermore, even though the total measured concentrations of S analyzed by ICP under H_2 condition was 0.3~0.4 mM higher than that under N_2 conditions at the same reaction time, it can not be proved directly that the S was related with the reduction of Se(VI) considering a significantly lower increase of S concentration compared to the initial background concentration (~16 mM) and the uncertainties. However, we found that the no aqueous S(-II) nor S(IV) species were present but instead of aqueous S(VI) was present in solution as identified by IC, suggesting that pyrite would not dissolve and S_2^{2-} in $FeS_{(s)}$ was probably oxidized to S(VI) or S(0) and this oxidation coupled to the reduction of Se(VI). The chemical interactions between pyrite and Se(VI) in COx pore water in both conditions were simulated by Phreeqc modelling using the Andra THERMOCHIMIE database.[20] The calculated results are shown in Table S4 and suggest that Se(VI) was mainly reduced to a mixture of Se(0), FeSe and $FeSeO_3$ by the oxidation of FeS_2 to S(VI) and Fe(III) under N_2 condition. However, Se(0) and FeS_2 were present as the only Fe-solid and Se-solid species under H_2 condition, suggesting H_2 was the only reducing agent for the

transformation of Se(VI) to Se(0). The experimental reduced species of Se will be discussed in detail below.

5.3.2. Se-solid species

The Se K-edge XANES spectra of Se-solid are shown in Figure 5.1 and the relative LCF results (Table S5.3) showed that after reacting for 9 days under N_2 condition, 96.8(0.6)% $Se(VI)^-$ and 3.2(0.4)% Se(0) could be identified, indicating that SeO_4^{2-} was mainly adsorbed on the solid and not significant reduced. A Se(0) XANES fingerprint is clear after 55 days, though 88.3(0.5) % Se(VI) was still the main species of solid-Se according to LCF result under N_2 condition. Since no aqueous Se(IV) species could be identified by IC in Figure S5.3 and Se(IV)-solid species determined by Se XANES were present during the reaction, we speculated that Se(VI) is adsorbed on nature pyrite, and reduced to Se(0) directly under N_2 condition. Previous studies showed no significant absorption or reduction of Se(VI) in COx and Boom formations.[52, 132] while (μ)XAF results supported that Se(IV) was reduced to Se(-II) and/or Se(0) by natural pyrite in COx and Boom clay.[28, 52] Curti et al, reported that Se(VI) could be reduced to Se(0) by natural pyrite at 80 ℃ after 8 months reaction.[35] There is no obvious Se(VI) reduction by synthetic pyrite within 30 days as checked by high resolution Se 3d XPS and SEM, while solid SO_4^{2-} species is present in the solid.[33] We proposed that the amount of reduction species, e.g., Se(0) or/and Se(-II), was low enough not to be exactly identified by XPS, and that the size of reduced Se species, of nanometer scale, forbid its identification by SEM. Combining with the aqueous analysis and the Se-solid species of sample after 55 days reaction under N_2, we speculated that the reaction is as follows:

$$5HSeO_4^-{}_{(aq)} + 2FeS_{2(s)} + 2H_2O \rightarrow 5Se(0)_{(s)} + 2Fe(OH)_{3(s)} + 4SO_4^{2-}{}_{(aq)} + 3H^+$$

However, 12.2(0.8)% Se(0), 45.7(0.8)% Se(IV) and 47.0(0.8)% Se(IV) were the primary solid Se species under H_2 condition after 9 days. It means that Se(VI) could be reduced to Se(IV) and Se(0). With reaction time increased to 55 days, Se(0) was the only species existing in solid, implying that all Se adsorbed was reduced, which was in agreement with the thermodynamic calculated result by Phreeqc modelling. The Se

XANES results indicate stepwise reduction of Se(VI) to Se(IV) and then to Se(0) under H_2 condition. Previous study report that the dissociative adsorption of H_2 existed on pyrite (210) face,[128] a face of importance in the pyrite extracted from COx formation (Figure S1 and the illustration in Figure 1), which probably favored the reduction of Se(VI) by hydrogen radical. Therefore, we concluded that H_2 plays a key role for the reduction of Se(VI) by natural pyrite in COx formation.

$$HSeO_4^- + 6H\cdot + H^+ \rightarrow Se(0) + 4H_2O$$

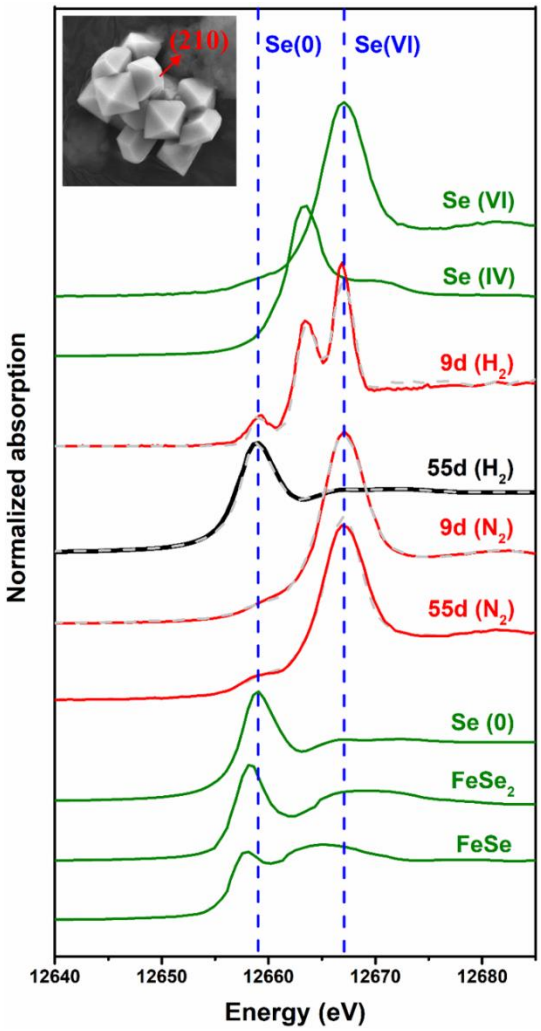

Figure 5.1. Se K-edge HERFD XANES of the samples and reference compounds.

5.4. Implications for the fate of Se in the environment

Pyrite is one of the main Se-bearing mineral in recent and old sediments and H_2 rich atmosphere in real geological waste disposal sites has a key impact for the reduction retention of Se by pyrite. Our study revealed that although Se(VI) was not significantly

sorption on natural pyrite under N_2 and H_2 conditions, Se-sorbed was totally reduced to Se(0) by natural pyrite under H_2 condition while only 12.2 % Se(VI)-sorbed was reduced to Se(0) under N_2 condition after 55 days. This finding is particularly relevant in the context of Se fate in real geological waste disposal sites.

Supporting Information

Associated content

The chemical composition of the COx pore water. The XRD result of the solid. The SEM images of natural pyrite. The calibration curves of S(VI) and Se(VI) and the relative retention time of the two ions. The description of Se-XANES spectroscopy. The parameters of the suspensions. Quantification of Se species by LCF of XANES. Thermodynamic Simulation by Phreeqc using the Andra THERMOCHIMIE database.

Table S5.1. Chemical composition of the pore water (25 °C) in the Callove-Oxfordian argillite and our synthesized solution (concentration are given in mM)

	Na	K	Ca	Mg	S	Sr
Natural solution composition	45.6	1	7.4	6.7	15.6	0.2
Experimental solution composition	43.2	1	7.2	7.0	15.8	0.2

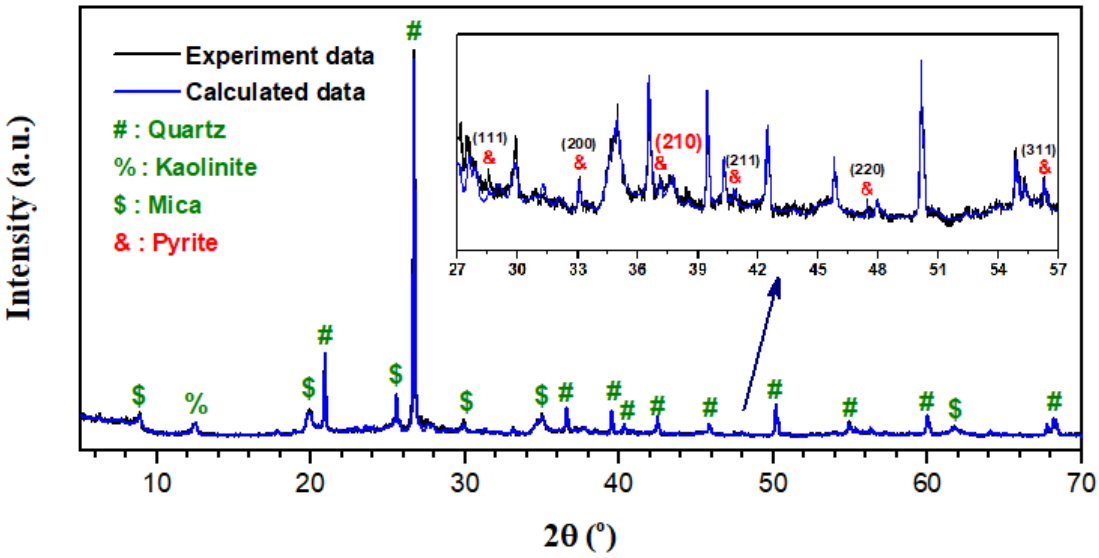

Figure S1. The XRD result of the solid.

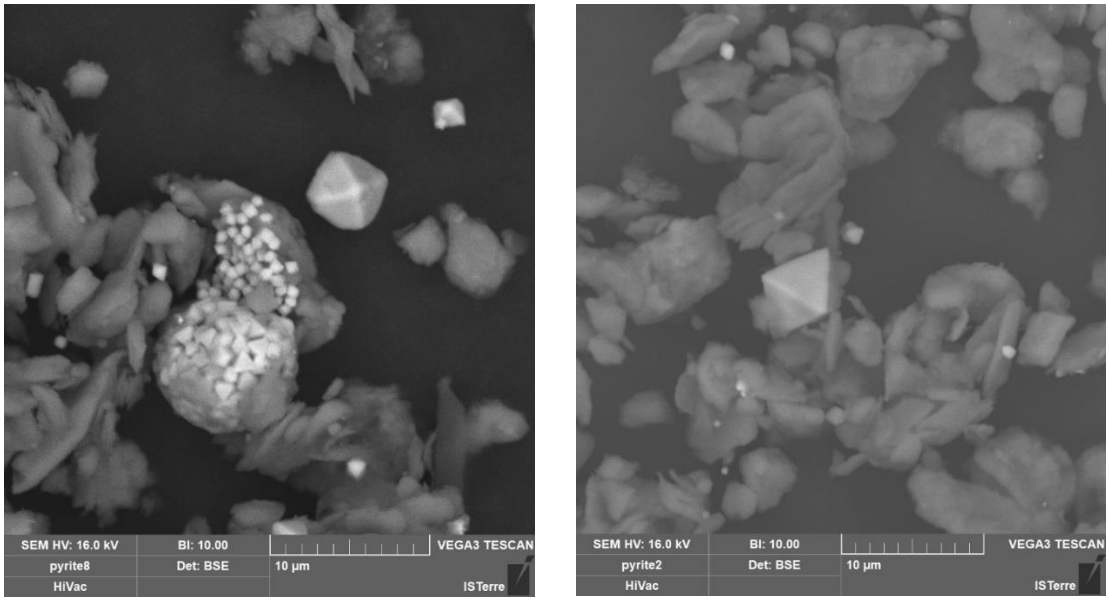

Figure S2. The SEM images of natural pyrite.

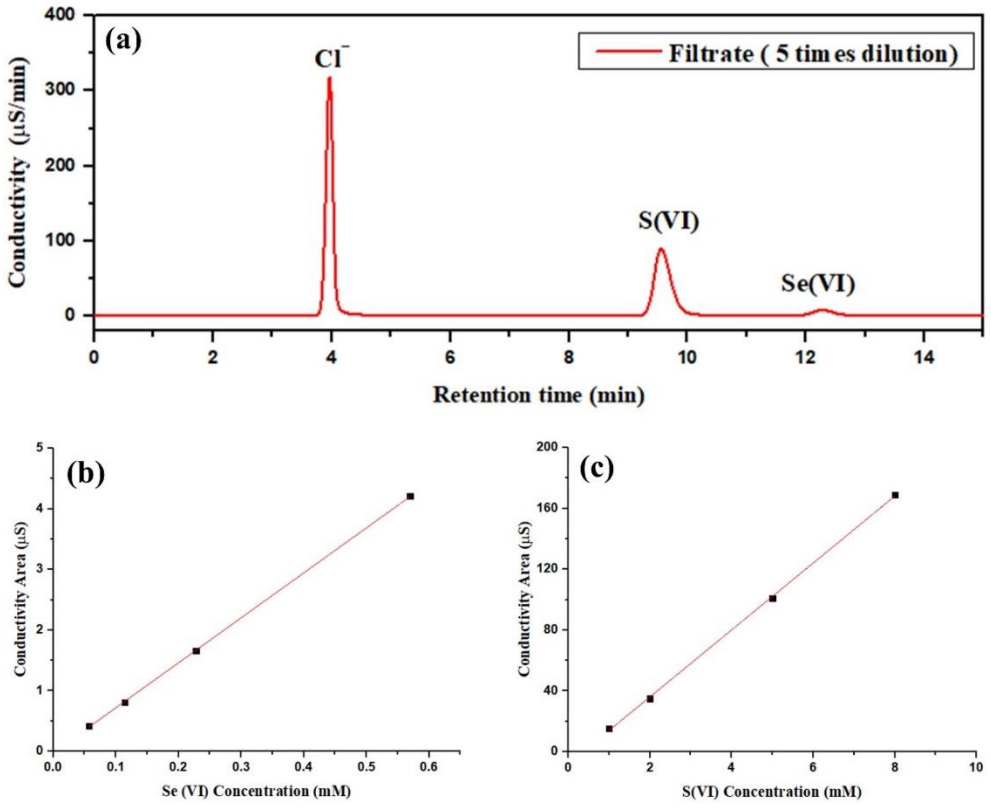

Figure S5.3. The aqueous results measured by ion chromatography. (a) The relative retention time of Se(VI) and S(VI) species in the filter with 5 times dilution of sample of Se(VI) reaction with natural pyrite for 9 days under N_2 condition, (b) and (c) The calibration curves of Se(VI) and S(VI) in 0.1 M NaCl solutions, respectively. Here it should be note that the peaks of Se(IV) and other S species (e.g,. S(-II) and S(IV)) was

not checked in all the filters.

Text S5.1. To determine the oxidation states of Se of Se-sord samples under N_2 and H_2 conditions, the Se K-edge (12.658 keV) XAS analysis was conducted at the Rossendorf Beamline (ROBL) at the European Synchrotron Radiation Facility (ESRF), Grenoble, France. The beamline used a Si(111) crystal monochromator was to select particular energy from the incident whitebeam and elemental Au foil (energy 11.919 keV) was used for energy calibrations. Se references were prepared as pellets with a cellulose matrix and measured in transmission mode. Se-sorbed samples were double-face sealed using polyimide tape and measured in fluorescence mode. Samples and the references were measured at about 15 K using a He cryostat to avoid beam damage and to minimize thermal disorder in the structure.

Table S5.2. The parameters of the suspensions after reaction 9 and 55 days under N_2 and H_2 conditions.

Conditions	RT	pH	Eh (V)	$[Se]_{tot}$ (mM)	Se[VI] (mM)	$[S]_{tot}$ (mM)	$[Fe]_{tot}$ (μM)	K_d (mL/g)
N_2	9 d	8.74	0.247	2.26	2.12	16.2	0.8	1.8
	55 d	8.27	0.143	2.20	2.16	16.1	0.9	4.5
H_2	9 d	7.98	-0.176	2.27	2.14	16.5	15.0	1.3
	55 d	7.55	-0.058	2.21	2.24	16.6	1.1	4.1

RT: Reaction Time

Table S5.3. Quantification of Se species (molar fraction) by LCF of XANES

Conditions	Sample	Se^0 (%)	Na_2SeO_3 (%)	Na_2SeO_4 (%)	∑(%)	χ^2 (10^{-3})
N_2	9 d	3.2 (0.4)	-	96.8 (0.6)	100.0	0.6
	55 d	8.0 (0.6)		88.3 (0.5)	96.3	1.0
H_2	9 d	12.2 (0.8)	45.7 (0.8)	47.0 (0.8)	104.9	0.7
	55 d	100.0(0.4)	-	-	100.0	0.8

RT: Reaction Time

Table S5.4. Thermodynamic Simulation by Phreeqc using the Andra THERMOCHIMIE database (concentration are given in mM).

	Distribution of species						**Fe-solid**	**Se-solid**
	Se(-II)	Se(IV)	Fe(II)	Fe(III)	S(VI)	S(-II)		
N_2	1.42	0.88	0.27	0.48	17.3	0	e.g., $Fe(OH)_2$, $Fe(OH)_3$, Fe_2O_3	Se(s), $FeSe_2$, $FeSeO_3$
H_2	2.11	-	-	-	-	14.5	FeS_2	Se(0)

General conclusions

For the safety assessment of nuclear waste repositories, a reliable prediction of RNs migration behavior under the relevant geochemical conditions is needed. Reinforced cementitious structures were selected as the potential engineered barriers of near-field nuclear waste repository in Callovo-Oxfordian clay system in France.[99] ^{79}Se and ^{99}Tc, as their long half-life and potentially high environmental mobility, are the key redox-sensitive radionuclides, which are needed to be investigated. Besides, enriched Se contamination associated with human activities has attracted significant attention as it could cause great harm to ecosystems. Redox-active minerals, e.g., pyrite, magnetite and mackinawite, not only are naturally present in water-logged soils, ore deposits, anoxic aquifers and sedimentary.[2, 28-30] but also occur as the steel corrosion product in cement-rich radioactive waste repositories under anaerobic geochemical conditions.[119-120] Therefore, studies on the adsorption/reduction of Se(IV), Se(VI) and Re(VII), as a chemical surrogate of Tc(VII), by mackinawite, magnetite and pyrite are quite important. In my thesis, the adsorption experiments of Se(IV), Se(VI) and Re(VII) by mackinawite, magnetite and pyrite in cement pore water (CPW), 0.1 M NaCl solutions and Callovo-Oxfordian pore water were conducted. A combination of XAS, XPS, S/TEM, XRD and PHREEQC chemical equilibrium modelling was used to reveal the interaction mechanisms between redox-sensitive RNs and the three Fe phases, to evaluate the impact of dissolved H_2 and O_2 for RNs retention and to determine the Eh values under hyperalkaline and chemically reducing conditions.

The general conclusions were as follows:

Reduction of Se(IV) by mackinawite in CPW

Considering that the geochemistry of selenite has close relationship with the chemical cycles of iron and sulfur in cement-rich repositories. A deeper knowledge about the interplay between selenite and mackinawite under the chemical environment of underground concrete structures (i.e., hyperalkaline and reducing conditions) is strongly required. Using a comprehensive characterization on both aqueous and solid speciation, I successfully monitored the whole interaction process between selenite and

mackinawite in hyperalkaline conditions. Results show similar chemical environments for Se(IV) and S^{2-}/S_n^{2-} at the mackinawite-water interface, verifying an immediate reduction. After 192 h reaction, Se(IV) was reduced to Se^0 and SeS_2, accompanied by the oxidation of S^{2-}/S_n^{2-} to $S_2O_3^{2-}$ and Fe(II) to Fe(III) in mackinawite. Aqueous results showed that ~99 % of aqueous selenium was present as Se_4S nano-particles due to the dissolution of Se from the solid. In parallel, ~62% of S^{2-}/S_n^{2-} was released into the solution, with mackinawite transforming to magnetite, $Fe(OH)_3$ and $FeS_2O_3^+$ complexed to Cl^- or OH^- species, and magnetite subsequently dispersed in the solution. The schematic diagram of reaction processes is shown in Figure G1.

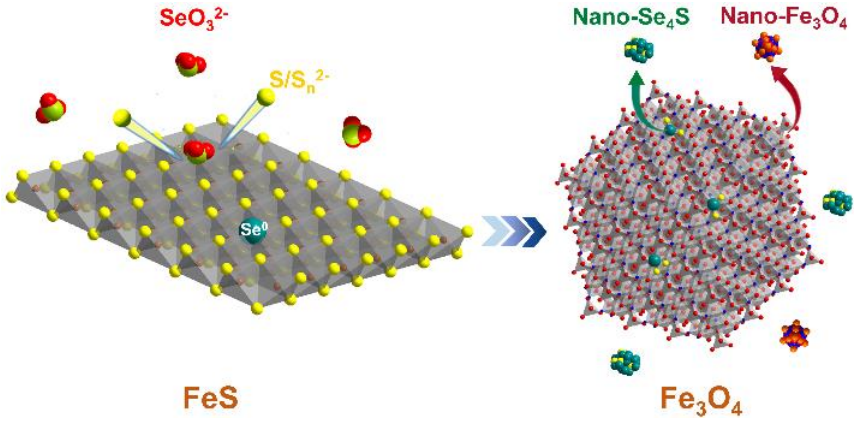

Figure G1. The schematic diagram of Se(VI) reaction with mackinawite

Cement pore water redox reaction: Eh measurement and Eh modeling

Redox potential (Eh) is of great essence for the migration behavior of redox-sensitive RNs and will be largely controlled by the corrosion of embedded steel in cement-rich radioactive waste repositories. Here, the sorption experiments of Se(VI) and Se(IV) on mackinawite, pyrite and magnetite in cement pore water (CPW) were conducted and the Eh values of the systems were obtained by using the Nernst equation based on chemical/spectroscopic measurements. LCF results of Se-XANES spectra suggested that Se(VI) was mainly reduced into FeSe and Se(IV) with the oxidation of mackinawite to goethite, which was identified by XRD and XPS. This Eh value with -0.388 V appears to be controlled by by FeO(OH)/FeS couple. Furthermore, Magnetite could catalyze the reduction of Se(VI) to produce Se(IV) and Se(0), accompanied by the oxidation of Fe(II) to Fe(III), but no redox transformation occurred for Se(IV). The

measured Eh was probably determined by Fe_3O_4/Fe^{2+} couple. Besides, Se(VI) immobilization mechanisms included nonredox and reductive complexations on pyrite, but Se(IV) could be reduced to FeSe in CPW. the Eh (-0.350 V) in Se(VI) system was mainly controlled by $Fe(OH)_3/Fe(OH)_3^-$ couple and the Fe concentration could have a critical role for the Eh determining.

H_2 and O_2 impact on the reduction of RNs by Fe phases

Fe(II)-bearing minerals have the potential for the retention of selenium (Se) enriched compounds in natural confinement and radionuclides (e.g., ^{79}Se and ^{99}Tc) in case of eventual leakage in nuclear waste repositories. Here, we investigated the reduction of Se(VI) and Re(VII), as the chemical surrogate for Tc(VII), by pyrite, magnetite and mackinawite under air, N_2 and H_2 atmospheres. Results indicate that Se(VI) was mainly reduced to trigonal γ-Se structure as nanoneedles by magnetite. Aqueous H_2 favored the reduction of Se(IV) and Se(VI) to Se(0). Furthermore, Se(VI) was reduced to monoclinic β-Se and FeSe by mackinawite under N_2 atmosphere, accompanied by the oxidation of mackinawtie to goethite, magnetite and sulfur. Only β-Se was formed under air atmosphere and aqueous H_2 favored the production of FeSe. The formation of amorphous Se(0) and FeSe via Se(VI) reduction by pyrite under N_2 atmosphere, of Se(IV) species under air atmosphere and of $FeSe_2$ under H_2 atmosphere. Aqueous H_2, not FeS_2, probably play a key role for the reduction of Se(VI) by pyrite. The retention mechanism of Re(VII) by magnetite, mackinawite and pyrite followed nonredox complexation and reduction to ReO_3 under air atmosphere, but reductive precipitation, i.e., Re(IV), under N_2 and H_2 atmospheres.

H_2 impact on the reduction of Se(VI) by claystone pyrite

Se(VI) reduction by natural pyrite extracted from Callovo-Oxfordian formation claystone was investigated under N_2 and H_2/CO_2 conditions. Wet chemistry methods reveals that Se(VI) uptake was not significant with quite the same uptake (K_d = 4~5 mL/g) on Callovo-Oxfordian in both N_2 and H_2 conditions. Among Se(VI)-sorbed under N_2, 12.2 % was reduced to Se(0) after reaction for 55 days, according to Se K-edge X-ray absorption spectroscopy (XAS) and linear combination fit (LCF) analysis. However,

under H_2 /CO_2 condition, 12.2% Se(0) and 45.7% Se(IV) were checked after 9 days reaction and all adsorption Se(VI) was reduced to Se(0) by natural pyrite after 55 days, which indicated stepwise reduction of Se(VI) to Se(IV) and then to Se(0). H_2 could dissociate into H· on pyrite (210) surface and H· probably favored the reduction of Se(VI).

Perspectives

The Nucleation of Fe phases

In my thesis, the synthetic experiments of Fe phases including magnetite, pyrite and mackinawite were performed in a 99.99 % N_2-filled glovebox (O_2 < 2 ppm, using NaOH as the CO_2 trap) and the three Fe phases were used for the retention of Se(IV), Se(VI) and Re(VII) in different matrixs. Magnetite and mackinawite suspensions were prepared following the method reported by previously[16] and the pyrite was synthesized according to the protocol published by D. Wei et al., Liu X et al. and Ma et al.[106-108] In our cases, the specific surface area of Fe phases was determined to be 102.3 m^2/g (mackinawite), 63.6 m^2/g (magnetite) and 2.5 m^2/g (pyrite) by the Brunauer−Emmett−Teller (BET) N_2 absorption method. The size and shape of the iron phases were characterized by TEM/SEM as illustrated in Figure P1. Despite the existence of many synthesis methods leading to the different size and special surface area, the formation mechanisms of the minerals are actively investigated and frequently debated. The coprecipitation reaction method for magnetite synthesis, also used in my thesis, is most widespread in laboratory and at an industrial scale. Recently, Montes-Hernandez et al. conducted two series of experiments to study the nucleation of magnetite, showing that the direct nucleation process by injection of an mixed-valent iron solution into an alkaline solution and the indirect nucleation process though the formation of iron dehydration and green rust as the transient phase.[136] Matamoros-Veloza documented that the existence, identity and structure of a highly reactive nanocrystalline solid Fe-S precursor phase that is structurally different to mackinawite and that is a required precursor to the formation of mackinawite.[88] FeS_2 structures have been synthesized with different methods and phases. Liang et al. used hydrothermal method with different precursors to obtain various morphologies and size of pyrite.[137] FeS_2 nanowires, nanoribbons and nanotubes were also synthesized by solvothermal method at low temperature.[138] As the presence of defects on Fe minerals surface could plays an important role in enhancing reactive properties, further research work should be conducted on the study of defects. Also, the high quality and purity of Fe minerals,

especially for pyrite, is also the future direction.

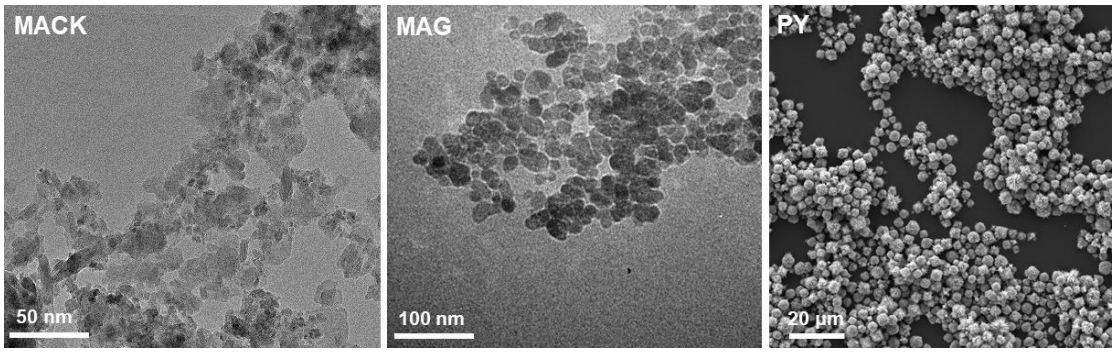

Figure P1. Characterization synthetic magnetite (MAG), mackinawite (MACK) and pyrite (PY) by TEM for mackinawite and magnetite as well as SEM for pyrite.

Retention behavior of Selenium oxyanions on iron phases in CPW

The safe disposal ^{79}Se is a requisite to the sustainable development of nuclear industry. The CEM-V/A cement, highly resistant to sulfate corrosion, is being evaluated as an engineered barrier for deep underground radioactive waste disposal in France. The Fe phases can be formed at steel corrosion interfaces, which are critical to the retardation behavior of Se oxyanions. In Chapter 2 and 3, redox/adsorption interactions between Se oxyanions and Fe phases in hyperalkaline conditions were investigated. Results show similar chemical environments for Se(IV) and S^{2-}/S_n^{2-} at the mackinawite-water interface, verifying an immediate reduction. After 192 h reaction, Se(IV) was reduced to solid Se(0) and SeS_2 species, accompanied by the oxidation of S^{2-}/S_n^{2-} to $S_2O_3^{2-}$ and Fe(II) to Fe(III) in mackinawite. Aqueous results showed that ~99 % of aqueous selenium was present as Se_4S nano-particles due to the dissolution of Se from the solid. Furthermore, Se(VI) was mainly reduced into FeSe and Se(IV) with the oxidation of mackinawite to goethite. Magnetite could catalyze the reduction of Se(VI) to produce Se(IV) and Se(0), accompanied by the oxidation of Fe(II) to Fe(III), but no redox transformation occurred for Se(IV). Besides, Se(VI) immobilization mechanisms included nonredox and reductive complexations on pyrite, but Se(IV) could be reduced to FeSe in CPW. In our case, we mainly focused on Se oxyanions behavior in CPW, but the retardation mechanisms of other redox-sensitive radionuclides (RNs), such as ^{238}U and ^{99}Tc, by iron phases have not been conducted in CPW for a correct safety

assessment. Furthermore, most of the research focuses on the interaction of iron sulfide with Se oxyanions, while other inorganic sulfides, such as manganese sulfide, copper sulfide and zinc sulfide, have not been proposed systematically, which still needs further research to determine if their reduction processes and fate are similar to sulfur reduction by iron sulfide.

Eh determination in hyperalkaline conditions

The redox potential (Eh) in reinforced cementitious structures is of great importance to assess the mobility of RNs. Redox reactions are kinetically slow and the systems are the lack of thermodynamic equilibrium. This implies that large discrepancies exist between the experimental Eh values commonly measured by a Pt-electrode and the computed Nernstian Eh values, which was proved by most natural water systems.[103-105] Furthermore, the measured Eh values may pose large uncertainties under hyperalkaline conditions. In Chapter 3, the measured Eh values using Pt-electrode were compared with all the calculated Eh values of Se(VI) half-reactions and redox coupled species using the Nernst equation based on chemical/spectroscopic measurements. The measured Eh represents a mixed potential resulting from many different simultaneous ongoing electro-chemical reactions. Among the different redox couples studied in our systems, the FeO(OH)/FeS couple can be considered as a master redox couple in the Se(VI) reaction with mackinawite in CPW system. The Eh value of Se(VI) reaction with magnetite in CPW system is probably imposed by the Fe_3O_4/Fe^{2+} couple. As for the system of Se(VI) reaction with pyrite in CPW, the Eh was mainly controlled by the $Fe(OH)_3/Fe(OH)_3^-$ couple. The total Fe concentration could have a critical role for correcting Eh calibration. In addition, Se couples including Se(VI)/Se(IV), Se(VI)/Se(0) and Se(VI)/FeSe in our study are not useful as "indicator" couples due to the redox reactions of Se(VI) by Fe phases in CPW lack of equilibrium among themselves within 8 days. However, far fewer studies have addressed the determination of redox potential in cementitious environment via abiotic redox transformations, even it's important for the retention and diffusion behavior of RNs. Therefore, more efforts should be devoted to the development of new methods for the determination of the Eh in under extreme

experimental conditions and on the Fe phases formed as a result of steel corrosion. The determination of experimental Eh values seems to be a current important research subject for the community.

Retention of Selenium oxyanions on iron phases in natural water

Selenium contaminated waters are produced by various industrial activities such as mining (coal, hard rock, uranium and phosphate), refineries (metal and oil), power generation (coal-fired power plants), and agriculture (irrigation waters and selenium fortification).[139] In Chapter 4, the interaction between Se(VI) and Fe(II)-bearing minerals (magnetite, mackinawite and pyrite) under air, N_2 and H_2 atmospheres were investigated. Results indicate that the reduction species, Se nanoparticles, had three different morphologies and structures as well as aqueous O_2 and H_2, deeply affecting the Eh of solutions, had an impact for the reduction species of Se after 105 d reaction. Se(VI) was mainly reduced to trigonal γ-Se structure as nano-needles by magnetite. Aqueous H_2 favored the reduction of Se(IV) to Se(0). In addition, Se(VI) was reduced to a mixture of monoclinic β-Se and $FeSe_2$ under N_2 atmosphere, accompanied by the oxidation of mackinawite to goethite, magnetite and sulfur. However, only Se^0 formed under air atmosphere and aqueous H_2 promoted to produce FeSe. In pyrite system, Se(VI) could be reduced to amorphous Se(0) and FeSe under N_2 atmosphere, to Se(IV) species under air atmosphere and to $FeSe_2$ under H_2 atmosphere. Aqueous H_2, not FeS_2, probably play a key role for the reduction of Se(VI) by pyrite. Although extensive studies have been conducted in the retention of RNs by Fe phases under aerobic and anaerobic conditions in both natural and laboratory settings, rare data reported the effect of H_2 on other RNs and heavy metals reduction on Fe phases in literatures. This requires more investigation in order to make an applicable and cost-effective technology that can tackle real applications.

H_2/NOM impact for the reduction of RN oxyanions by natural pyrite

Hydrogen (H_2) is naturally produced by biotic as well as abiotic pathways in the Earth's crust, e.g. (1) the activity of certain fermentative anaerobic bacteria and cyanobacteria, (2) the radiolysis of water due to U, Th, and K radioactive decay, and (3)

the oxidation of Fe(II)-bearing minerals (e.g. olivine, pyroxene) into magnetite leading to the concomitant reduction of water into H_2. Pyrite not only is ubiquitous in clay-rich formations,[2, 28, 130] but also occurs as the steel corrosion product in nuclear waste disposal under anaerobic geochemical conditions. Recent research reported that H_2 dissociative adsorption unsaturated-coordination sulfur atom on (210) surface of pyrite is favorable both in thermodynamics and kinetics. Thus, H_2 potentially affect the reduction mechanism of RNs on natural pyrite. In Chapter 5, it was evidenced that Se(VI) could be easily be reduced to Se(0) in the presence of dissolved H_2 compared with anaerobic conditions. Here we only investigated the mobile Se(VI), much more efforts should be paid on other mobile redox-sensitive RNs, such as $^{235, 238}U$, ^{99}Mo and ^{99}Tc and on the detailed reduction mechanism. Furthermore, natural organic matters (NOM) are widespread in claystone[140-142] and have the potential to interact with natural pyrite on the surface to form co-existing constituents, which could interfere with the retention mechanism for RNs.[9, 53, 141] Therefore, the impact of NOM for the reduction of RNs by natural pyrite in claystone and the reaction mechanism among the materials need to be further investigated.

Formation and evolution of secondary phases and surface altered layers during borosilicate glass corrosion in pore water

Abstract

The emergent secondary phases and surface altered layers (SALs) have great impact on chemical durability of glasses. However, the formation and evolution of these structures are still unclear. Here, by studying the borosilicate glass powders and coupon altered in DIW pore water at 90 ℃, we found that secondary phases were formed during glass powders alternation in two paths: 1. the consumption of saturation ions from the solution could form analcime, zeolite, calcium silicate and barite; 2. the reorganization of silica aggregates could form smectite. SAXS and cross-sectional SEM results showed that releasing souble elements and forming smectite and gaps could significnatly increase the porosity of SALs. The reorganization of SALs would result in the decrease of porosity. In addition, external layer with smectite coupling in time and space reorganized inwardly from the surface of altered glass powders, while the growing gaps at the interface of SALs/pristine glass spread outwardly. The dissolution of glass including powders and couple was followed an interface-coupled dissolution-reprecipitation process. Our finding provide fundamental understanding of potential long-term structural variation of the high–level nuclear waste glasses. Methodology, especially WAXS and SAXS, of this study could be further extended for natural glass and mineral weathering.

Key Words: borosilicate glass, alteration, secondary phases, surface altered layers, smectite, gap, interface-coupled dissolution-reprecipitation process.

Introduction

The chemical durability of silicate/borosilicate glasses in contact with aqueous fluids over geological scale raises challenging scientific issues, especially for predicting the long-term radionuclide retention potential in geologic repositories.[143-144] Furthermore, the weathering of basaltic glass, as the main composition of oceanic crust, by seawater is vital for carbonate precipitation and sedimentation in the oceans.[145] Archaeological glasses corrosion is also important for sample dating and preservation.[146]

Two models of surface altered layers (SALs) formation were prevailed in the past: (i) the congruent dissolution of glass followed by the formation of passivation layer by interface-coupled dissolution-precipitation mechanism (ICDP),[147-148] and (ii) the incongruent dissolution, mainly B, Na and Ca, followed by in situ reorganization of the relict silicate network processes.[149-153] Hydrolysis of glass results in the existence of a rapid initial dissolution rate (r_0) and then it dramatically decrease, named residual or steady-state corrosion rate (r_r), as the formation of passivation layer.[154] The silica passivation layer could passivate the glass dissolution via the limit of water diffusion.[155] The pore closure of gel, which was caused by the densification, could sharply decreased the corrosion rate.[156] Furthermore, the dissolution kinetics of glass could be described as a function of glass composition and experimental conditions such as pH, temperature, glass-surface-area-to-solution-volume (S/V) ratio and the solution chemistry.[157-159] Ojovan reported that the formation of new gaps in SALs, resulting in freshly formed glass surfaces, lead to an effective increase of leaching rate.[160] As aqueous silica becomes saturated in solution, secondary phases such as phyllosilicates and zeolites may precipitate.[161-163] The precipitation of secondary phases could also impact the properties of passivation layer and drive the corrosion rate by depleting the dissolved ion concentrations in solution.[164]

Concerning the understanding of glass alteration mechanisms and its effect for glass dissolution, it is crucial to study the formation and evolution of the SALs and the

secondary phases.[151, 158, 162] Although the research on glass alteration in aqueous fluids has been conducted for decades, there is still lack of understanding on the evolution of secondary phases during glass corrosion. Moreover, the understanding for the formation and evolution of SALs and how it impacts the glass corrosion have not been fully unraveled. Therefore, we use scanning electron microscopy (SEM), (scanning) transmission electron microscopy ((S)TEM) with a high-angle annular dark-field (HAADF) detector, laboratory and synchrotron X–ray diffraction, including both small–angle X–ray scattering (SAXS) and wide–angle X–ray scattering (WAXS), and Geochemist's Workbench code to study the formation and evolution of secondary phases and SALs of borosilicate glass altered in DIW pore water at 90 ℃. This work provides a fundamental mechanism for long-term glass dissolution, especially in the framework of the high level nuclear waste glasses.

Materials and methods

Glass leaching experiment

The borosilicate glass was produced by melting a mixing of SiO_2 (51.66 %), H_3BO_3 (14.87 %), Na_2CO_3 (11.44 %), Al_2O_3 (3.54 %), MgO (1.85 %), CaO (5.38 %), $Ba(NO_3)_2$ (0.02 %), Fe_2O_3 (3.23 %), Na_2SO_4 (0.66 %), ZrO_2 (0.15 %) and other compositions at 1150 ℃ for 3 h and then cast into graphite crucibles with 6 cm × 30 cm. The samples were annealed for 1 h at 500 ℃ and cooled to room temperature. The glass was ground with a grinder and fractionated by sieving with the size of 75-149 μm and the specific surface area of the glass powders, determined by the Brunauer−Emmett−Teller (BET) N_2 absorption method, was 0.07 ± 0.001 m^2/g. The glass coupon of 10 × 10 × 2 mm^3 was cut from the glass blocks by diamond saw and polished to obtain a surface roughness of less than 1 μm. The AFM result of glass coupon surface after polishing was shown in Figure S1. The glass (powders and coupon) weathering experiments were performed in deionized water (DIW) pore water at 90 ℃. The schematic diagram of experimental reactor was shown in Figure S2. The measurement method of pore water,

the water retained in the space among glass, in glass was described in text S1 and the volume of pore water was 3.11 mL in 10 g glass powders and one coupon. After reaction for 3, 7, 20, 90, 180, 380, 540 and 760 d, 3.11 mL DIW was added into the samples and let them equilibrate for 1 d at room temperature to get enough liquid for aqueous analysis, and then the suspension was filtered by 0.22 μm nitrocellulose membrane. Considering the low equilibrium constant of secondary phases, such as zeolite[165] and analcime,[166] it was reasonable to neglect the effect of post-addition of DIW on the dissolution of the secondary phases in 1 d at room temperature. The total concentrations of B and Si in the filtrate were analyzed by inductively coupled plasma optical emission spectrometry (ICP-OES) with a Varian 720-ES apparatus. The dried altered glass powders were characterized using SEM, TEM, WAXS, SAXS and X-ray diffraction (XRD) (Bruker axs, D8 advance) with Vortex-EX detector (Hitachi) under Cu Kα radiation. The Geochemist's Workbench® code was used to model the formation of secondary phases during glass weathering. A couple of glass altered for 760 d was measured by (S)TEM-HAADF.

Scanning X-ray microdiffracion

Scanning X-ray microdiffractions were carried out at the ID13 beamline at the European Synchrotron Radiation Facility (ESRF), Grenoble, France. X-ray was focused to a size of 2 μm × 2 μm with energy of 13 keV and flux of ~2.0 × 10^{12} photons/s. 2D area detector Eiger 4M was used to collect diffraction pattern covering reciprocal space q ranging from 0.05 to 4 $Å^{-1}$, which contains both SAXS/WAXS signal. The glass powder samples were spread on Kapton tape. A region of ~ 200 μm × 200 μm was scanned by micro X-ray with step size 2 μm. Scanning X-ray microdiffraction patterns were azimuthal averaged to 1D intensity profile by custom developed python package.

Scanning and transmission electron microscopy (SEM and TEM)

For the thickness measurement of SALs, the glass powders altered for certain times were embedded into epoxy resin and then the cross section of the samples were polished to 9, 6, 3, 1 and 0.25 μm step-by-step. After polishing, the cross-section part was washed by DIW and ethanol for six time to remove diamond particles and other possible pollutants during polishing. The dried cross-sectional part was covered with a thin carbon layer (~20 nm) for conductivity during SEM analysis. For the surface morphology and secondary phases analysis, the altered glass powders were directly dispersed on the carbon tape and covered with ~ 1 nm gold layer and then analyzed by SEM. The SEM (ZEISS Ultra 55) was equipped with energy selected X-Ray microanalysis system (EDS) and SDD Detector (BRUKER AXS-30mm²). The average thickness of SALs of altered glass powders was obtained the statistics of 120 positions of backscattered electron (BSE) images measured by SEM (Vega3 Tescan) with EDS and SDD Detector. For the study of the glass coupon, an ultrathin electron transparent cross-sectional sample prepared by focused ion beam (FIB) was analyzed by TEM (JEM-2100F) with energy dispersive X-ray spectroscopy (EDS). TEM images were collected at 200 keV. Gatan Digital Micrograph software was used to analyze the images.

Results and discussion

Leaching kinetics

Aqueous analysis was mainly used to evaluate the dissolution rate of glass. The calculated pH, aqueous concentrations of Si and B, the equivalent thickness (Eth) calculated from B concentration and the dissolution rate (r) of glass powders during alteration were shown in Figure 1. The methods for Eth(B) and r calculation were described in text S2. Due to the fact that glass was altered in DIW pore water, the pH of pore suspension could not be measured directly. The Geochemist's Workbench® code [167] was adopted to calculate the pH of the suspension during glass alteration and the calculated result was shown in Figure 1(a). The initial rise of pH can be explained by

the release of cations during glass dissolution coupling with a decrease of H^+ in solution to maintain charge balance. The decrease of pH at the rest reaction process was probably correlated with the formation of smectite to produce H^+.[168-169] Figure 1(b) showed that the concentrations of B and Si increased rapidly within 90 d, then slightly increased for the rest of the test, which may be related to form passivating layers on the surface of glass.[158, 170] A slightly oversaturated Si at 90 d (156 mg/L) in solution enabled passivating layers and secondary phases formation.[171] The Si concentration was oversaturated from 90 to 760 d probably caused by the leaching rate of Si higher than its precipitation rate. The equivalent thickness of altered glass (Eth) (Figure 1c) of aqueous B reached to 2.81 μm at 90 d and 8.35 μm at 760 d, respectively. The glass dissolution rate, given by the release time of B showed that the rate decrease is ~ 11 times from 3 d (~ 58.5 nm/d) to 760 d (~ 5.5 nm/d) (Figure 1 d) and the average corrosion rate was about 11.0 nm/d, which is comparable with but higher than that (6.3 nm/d) of SON68 glass under Si-rich solutions at 90 ℃.[172] The discrepancy could probably due to the static conditions with a sufficiently high surface area-to-solution volume (S/V) ratio and different glass compositions in our study.[156, 158, 173]

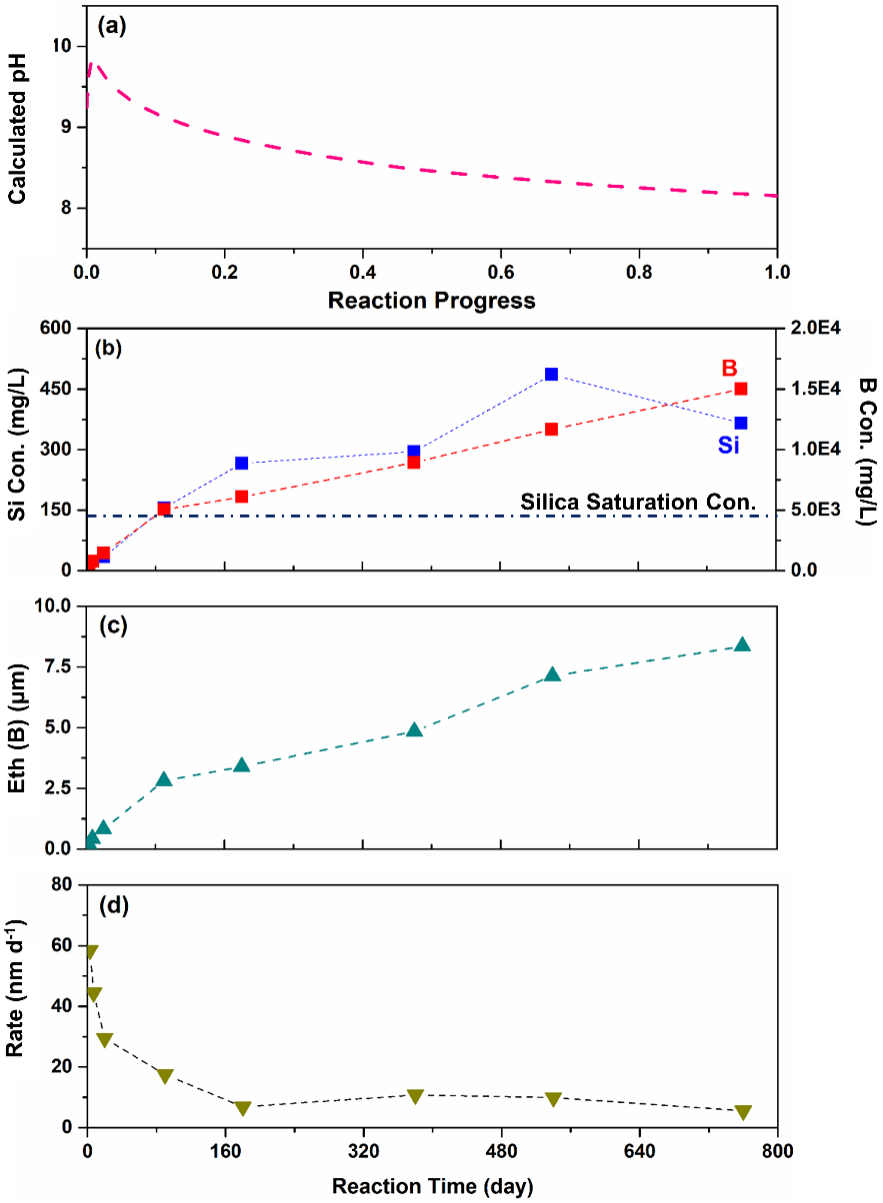

Figure 1. (a) The calculated pH with reaction process, (b) time evolution of the concentration of Si and B, (c) the equivalent thickness of altered glass (ETh), calculated from B released into solution and (d) the glass dissolution rate determined by aqueous B concentration.

Formation and evolution of the secondary phases

The secondary phases formed during glass alteration were identified by XRD and the results were showed in Figure 2. No obvious crystalline phases were present at 20 d. Here we should note that the detection limit of XRD is 1 %. However, with alternation

time increase to 90 d, that the appearance reflections were emerged at 2θ around 12.5, 21.7, 28.1 and 33.4 indicated the formation of zeolite (Na_6Al_6 $Si_{10}O_{32}\cdot 12H_2O$) (PDF 39-0219), and the reflections around 15.9, 26.1 and 30.6 suggested that analcime ($NaSi_2AlO_6\cdot H_2O$) (PDF 41-1478) was formed. Previous studies reported that different types of glass altered in alkaline solution, the pH higher than our calculated pH (Figure 1 a), could induce variations of zeolite phases.[161, 174-175] The formation of secondary phases was as a consequence of silica saturation at 90 d. In addition, the emergence of reflection at 2θ around 19.9 indicated the primary formation of smectite at 180 d and the gradual precipitation of analcime was observed. Smectite, as the main secondary phase, was also present in experiments of glass corroded by DIW and 0.03 - 0.1 M NaOH solutions at 150 °C.[176] A lesser extent of calcium silicate ($CaSiO_3$) (PDF 45-0156) was identified with reflections at 2θ around 17.6, 28.1 and 29.5 after 380 d. However, the absence of main lattice planes of at 2θ around 12.5, 17.6 and 21.7 suggested that zeolite probably dissolved or transformed to other phases such as analcime at 760 d. $CaSi_2O_5$ phases (CSH) precipitated during CJ8 glass alteration in DIW after 12.8 y and the glass has the same content of Ca with our glass.[177] Although previous study reported that the precipitation of CSH and zeolite by consuming Si, Al and/or Ca dramatically drove the dissolution of glass,[164] the formation of the secondary phases did not trigger the sharp dissolution of glass (Figure 1b) in our system. This could due to the persistent oversaturation with respect to silica in accelerated alteration experiment with static mode.

SEM images of glass powders at different alternation times are shown in Figure 3. No obvious particles were observed on the surface of glass powder after 20 d in Figure 3(a) but imprinting, especially at the edge of glass powder, due to corrosion can be observed. With alternation time increased to 90 d, the glass powders were covered by different morphologies (Figure 3b) of precipitates and EDX results showed analcime (point 1) with chemical composition $NaAlSiO_4$ was checked and the particle pointed as 2 with an enrichment of Ca was probably $CaSiO_3$. Furthermore, we can clearly see

plenty of precipitated phases with μm size (point 3) were comprised of Si, Na, Al as well as Mg and the main elements of bright nanoparticle (point 4) were Ba, S, Si, Mg and Na. The two particles were probably zeolite and barite ($BaSO_4$). It should be noted that content of Mg in point 3 and 4 was probably originated from SALs (Mg-smectite) of glass, which will be discussed in the following text. Barite was not identified by XRD as its low content (< 1 %, XRD detection limit) and the overlap of main diffraction peak at 2θ around 25.9 between analcime and barite. Interestingly, the presence of pores due to corrosion was observed under the secondary phases at 90 d (Figure 3c). More and more $BaSO_4$ precipitated at 180 d in Figure 3d and the size of $BaSO_4$ increased with alteration time. In addition, the gaps in the SALs were observed at 380 d (Figure 3e) and the size of the gaps increased from nm to μm during alteration. The formation and evolution of gaps will be further discussed in Section 3.3. With the increase of alteration time to 540 d and 760 d, layered minerals preferred face-to-face stacking were observed and the main elements were Na, Mg, Al, Si and Ca, which was smectite identified by XRD in Figure 1. An idealized formula of smectite is $M_{0.33}^{+}Al_2Si_{3.67}Al_{0.33}O_{10}OH_2$, where M^+ typically refers to Ca^{2+} and Mg^{2+}.[178] An order of magnitude higher content of Si (20.8 atomic %) than Al (2.1 atomic %) in the layered minerals based on EDS analysis suggests that it still inherited part of the relict silicon glass network. Generally, smectite is the main mineral formed during Na and Ba borosilicate glass corrosion.[179] Furthermore, the thickness of smectite was several hundred nanometers though the observation from gaps in Figure 3f. Combining with the morphological evolution and EDS analysis, it seems that smectite was formed in SALs, not by the precipitation from saturated ions in solution, which is different from the formation of other secondary phases in our cases. EDS analysis of point 6 indicated that the particle contains Ca and Si, with a tiny amount content of Na, confirmed as $CaSiO_3$ by XRD. Moreover, we also found that smaller particles were came off from the glass powders after alteration for 540 d and 760 d and it was probably smectite (Figure S3). Previous studies reported that smectite and phyllosilicate precipitation induced the decrease of pH as the presence of hydroxyl groups in their composition,[168, 180-181] and the formation of secondary

phases lead to the increase of alteration rate by ions consumption from solution and diminishing gel lay protective properties.[182-183] The Geochemist's Workbench® code [167] was used to model the formation of secondary phases during glass weathering at 90 °C and 1.01 bar, which was consistent with the experimental conditions. The main calculated secondary phases shown in Figure S3 were quartz (SiO_2), wollastonite ($CaSiO_3$), nontronite ($Na_{0.3}Fe_2(Si,Al)_4O_{10}(OH)_2 \cdot nH_2O$), analcime ($NaSi_2AlO_6 \cdot H_2O$), sanbornite ($BaSi_2O_5$), and mesolite ($Na_2Ca_2(Al_2Si_3O_{10})_3 \cdot 8H_2O$). Quartz was thermodynamically favored but not identified by XRD and SEM, probably caused by the slow formation kinetics. The simulated precipitation of wollastonite, nontronite (as a member of smectite group), analcime and mesolite (zeolite group) were in agreement with experiment observations, while sanbornite was not present in our experiment data. Here, barite, with trace little amount, was also be predicted in our calculation. In conclusion, there are two paths for the formation of the secondary phases: one was though the consumption of Si, Al, Mg, Ca, Ba and S elements from solution to form analcime, zeolite, calcium silicate and barite; another was though the reorganization of leached layer after depletion of soluble elements such as B and Na to form smectite.

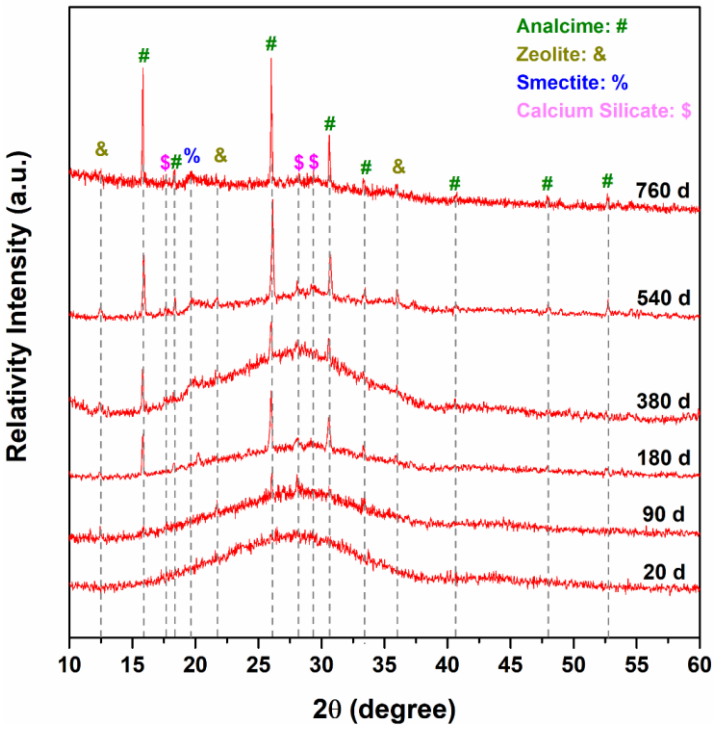

Figure 2. XRD patterns of secondary phases with alteration time.

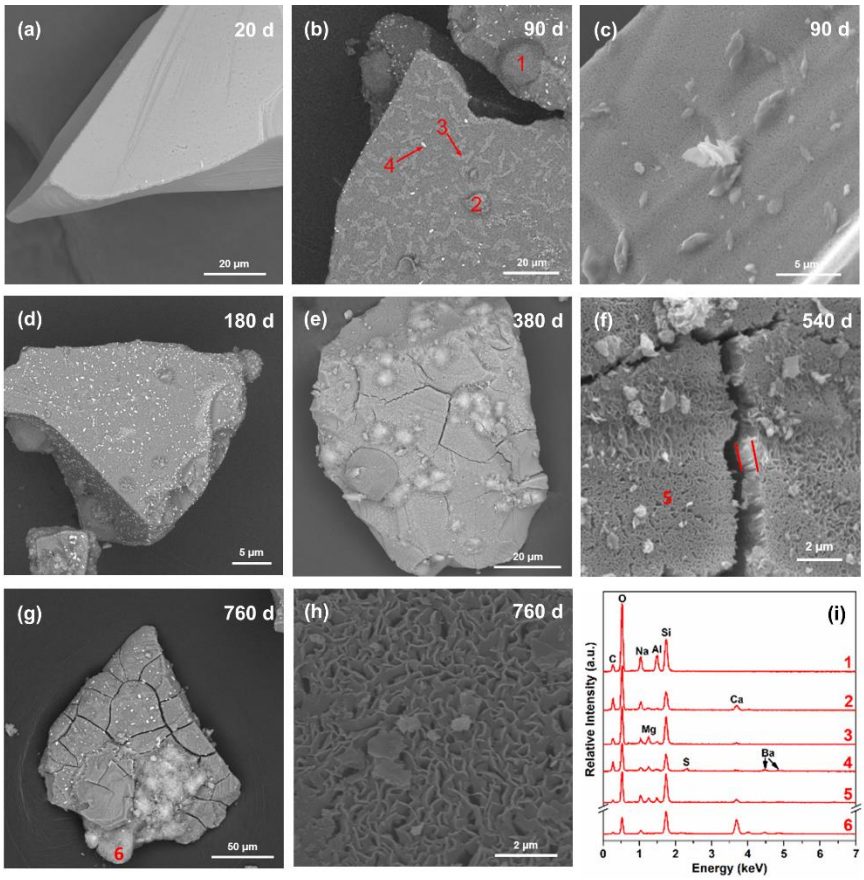

Figure 3. SEM images of secondary phases formed on the surface of glass powders with alteration time. (a) the morphology of glass surface at 20d, (b) and (c) the formation of different morphological precipitates and pores at 90 d, (d) the formation of plenty of barite nanoparticles at 180 d , (e) the morphology of gaps formed at 380 d, (f) smectite with several hundred nanometers observed though the gaps at 540 d, (g) and (h)the morphology of calcium silicate and magnification of smectite at 760 d, and (i) the relative EDS analysis of particles from point 1 to 7.

Formation and evolution of surface altered layers (SALs)

A fundamental understanding of the SALs and the stability is essential for the prediction of the long-term performance of glass. Scanning X-ray microdiffraction was performed to identify the secondary phases and monitor the evolution of the SALs on

the dried altered glass powders. Scanning microdiffraction patterns contained both SAXS and WAXS signal for a raster grid with 2 μm spatial resolution. The overall morphologies of glass powders with alteration times were shown in Figure 4a. Analcime, zeolite, calcium silicate and barite were identified (Figure 4b), which is in consistent with the SEM and XRD results. In order to check the reorganization of smectite in SALs, WAXS patterns in the range of q from 1.32 Å to 1.50 Å was also used. The test zones, without invisible secondary phases interfere, were marked as red circles in Figure 4a. The WAXS results in Figure 4c suggested that no phase was identified at 20 d, smectite was initially presented after 90 d and the crystallinity of smectite was gradually increased during alteration. Previous studies suggested that the formation of smectite could lead to two antagonistic effects: 1. the decrease of alteration rate caused by the clogging of the gel layer; 2. the increase of alteration rate due to the depletion of gel layer.[156, 182-183] The SAXS information was also collected from the red circle zones and Porod's law was used to determine the porosity and roughness of these areas. The SAXS curves correlated to evolution samples were shown in Figure 4e. The variation of intensity profiles at Porod region indicated a structural reorganization of the SALs during alternation. The size and distribution of pores within glass would give rise to scattering pattern at Porod region, for q ranging from 0.02 to 0.1 $Å^{-1}$. Increasing of size of pores could lead the fitting of power of q increasing from -2 to -4. Detail of fitting of Porod law had been discussed in SI text3. Figure 4e showed the distinct SAXS curves of sample altered for 20 d from samples altered for longer duration. There is significant increase for porosity of SALs altered for 90 d. This is probably caused by the release of soluble species for SALs to form a porous structure and then the reorganization of the relict silica in SALs by hydrolysis and recondensation. The power of q showing an overall upward trend with alteration time from 90 d to 760 d indicates that the restructuring of the SALs leads to the closure of the pores on the surface of the glass during alteration.

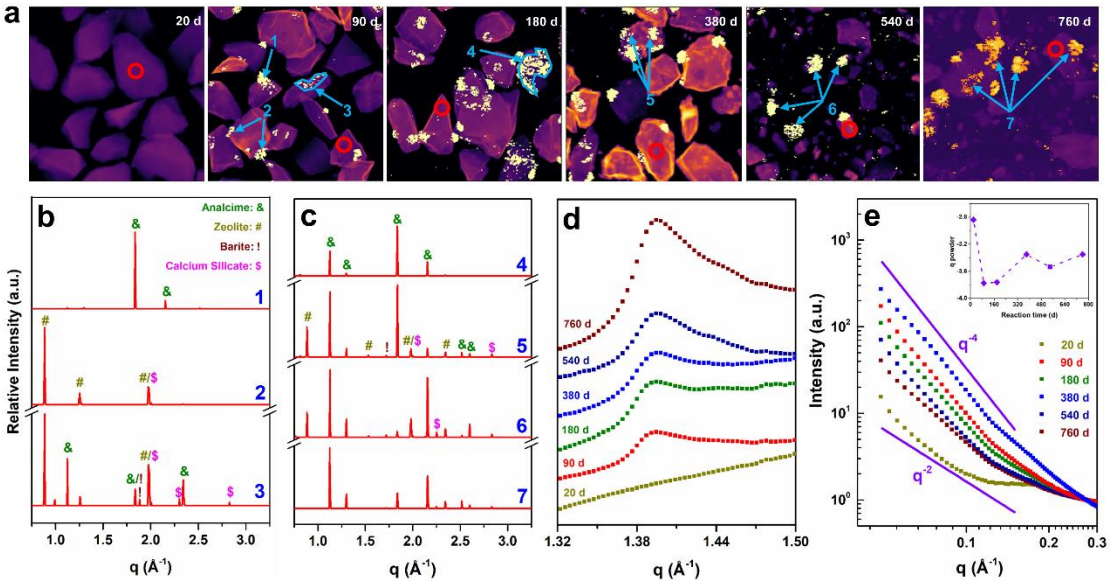

Figure 4. WAXS and SAXS results. (a) the morphologies of glass powders in 200 × 200 μm zone at different alteration times, (b and c) WAXS patterns of secondary phases numbered as 1 to 7 in (a), (d) WAXS patterns with q ranging from 1.32 Å to 1.50 Å of red circle zones in (a) without invisible secondary phases interference to check the reorganization of smectite with alteration time, (e) SAXS intensity versus scattering-vector modulus (q) of red circle zones in (a) to evaluate the porosity of passivation layer during alteration. The power of q with reaction time was shown in the upper right part.

The cross-sectional SEM images of glass powders to study the formation and evolution of SALs and the results were shown in Figure 5. Figure 5a and Figure S5a shown that the thickness of SALs formed at 20 d was about 126 nm. This leached layer was composited of packed silica aggregates with the size of several tens nanometers, which was also observed in previous studies.[184-185] Since interfacial water has different physical and chemical properties with bulk water,[186-187] amorphous silica could nucleate and precipitate in the alteration zone even in unsaturated pore water (34.3 mg/L). Besides, the aggregation of silica grow in alkaline solutions (the calculated pH > 8 in our system) by direct precipitation of silica onto silica particles by Ostwald ripening, which forms a silica gel.[184] Both paths for silica aggregates are followed by interface-coupled dissolution–reprecipitation (ICDP) mechanism. Therefore, we speculated that

the formation of silica aggregates in altered glass powders at 20 d can be explained by the ICDP process. However, the thickness of SALs increased to 2.36 μm at 90d and two different morphologies named as external layer and central layer was present in SALs (Figure 5b). The external layer was ~ 423 nm with regular shape, which was identified as smectite by WAXS in Figure 4d. The central layer was with the larger size and the dissolution front was with irregular shape. The significantly different morphologies between 20 and 90 d strongly evidenced the structural reorganization of the SALs during corrosion. An EDS mapping performed on cross-sectional SEM image of glass powder altered 90 d alteration in Figure S6 showed that Na was completely leached out, Ca and Al exhibited a limit retention and Si still inherited, in contrast, Fe and Mg were enriched in the alteration layer. Fe could precipitate with silicate in the altered layer to from Fe-silicate as their large affinity.[188] Mg and Ca could be incorporated as charge compensators for AlO_4^- in SALs.[182, 189] Previous studies reported the gel layer enriched Al and Ca in SON68 nuclear glass and Ca was enriched in the gel layer of Complex Glass.[144, 161] Combining with the SEM image in Figure 3c that the pore structure of smectite was originated from the alternation of glass powders, we can then propose that the external layer with regular shape was formed by the reorganization of packed silica aggregates in SALs, not by the precipitation of silica saturated in solution. The morphologies of the smectite layer, silica aggregates and the interface of glass powders altered for 540 d can be clearly seen in Figure 5g. The visible porous structure between silica aggregates was a consequence of the condensation reactions between reactive monomeric silica/surface silanol groups.[184] The EDS results in Figure S7 (point 4 and 5) and Tables S1 showed that the external layer was Mg-smectite and the content of Si in this layer was lower than that of silica aggregates, indicating that Si could release into bulk solution as the result of aqueous Si concentration increase in Figure 1b during silica aggregates-smectite reorganization. More importantly, the ratio (14.25) of Si/Al in external layer, much higher than the ideal data (1.84) of smecite,[178] supported that smectite was not the only phase existing in this layer. The depth of SALs at different alteration times was collected by the statistics of 120 positions of backscattered electron

(BSE) images and the representative images are shown in Figure S8. The depth of SALs increased with alteration time (Figure 5l), which is in good agreement with the Eth(B) result within the error. Similar trend has been observed for the external layer in Figure 5h, suggesting the reorganization of smectite coupling in time and space reorganized inwardly from the surface of altered glass. It is also noted that gaps began to form in the interface of SALs/pristine glass at 90 d and the size-growing gap spread outwardly with alteration time. Our observation was well agreed with the results from Geisler et al. , who reported a water-rich zone in situ glass samples and a gap in dried sample at alteration layer/glass interface.[148] The explanation for the formation of gaps was that the silica molecules in the reaction interface was energetically favored to attach pre-existing silica particles compared with the deposition onto the dissolving glass surface, followed by ICDR mechanism.[148, 184] It can be concluded that the dissolution front in our study can result from the congruent dissolution of the glass powders and underwent ICDR process. The increase of gap size from nm to μm was probably caused by the interface dissolution rate is higher than the reprecipitation rate of silica. We speculated that molecular silica or aqueous silica colloids was partially filled with the gaps but it needs the further in-suit investigation. Furthermore, we found an increase of the porosity from central layer towards the external layer in Figure S5b and Figure S7, indicating a more important pore and silica aggregates ripening nearby the external layer. Previous study reported that the formation of gaps and new surface of pristine glass probably resulted the jump of leaching process,[160] while a relatively modest increase based on Eth (B) and cross-sectional depth (Figure 5i) was observed even the gaps were formed in our cases after 380 d. The difference of alteration rate was probably due to the continuous oversaturation with respect to silica in static mode to inhibit alteration rate renewals. Thus, our data support the formation of SALs includes the interfacial congruent dissolution followed by the ICDP process and the reorganization of external layer with smectite from packed silica aggregates.

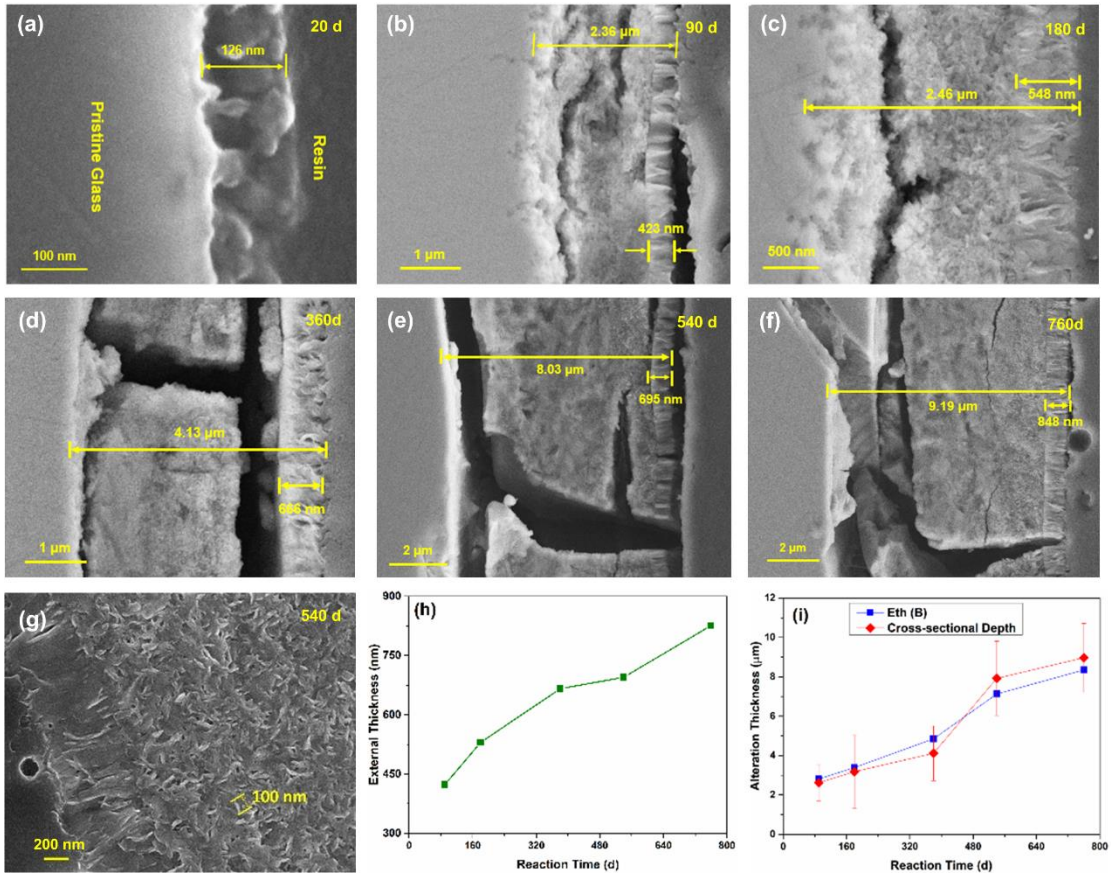

Figure 5. (a) - (f) Cross-sectional SEM images of glass powders with different alteration times, (g) magnification of the smectite, aggregates and porosity, (h) the evolution of exteral layer with semctite as a function of alteration time, and (i) comparison of the alteration depth by Eth(B) and cross-sectional SEM results.

Insight into glass coupon by (S)TEM

In order to discriminate SALs from the pristine glass and decipher the nanometre-scale evidence of the interface, the glass coupon altered for 760 d was characterized by (scanning) transmission electron microscopy ((S)TEM) with a high-angle annular dark-field (HAADF) detector. The SALs width of glass coupon was 3.2 µm in Figure 6(a). which was lower than that (9.0 µm) of glass powders with a faster leaching rate at the same time. Furthermore, the porosity in the central layer was observed and the size of pore closer to external layer was larger than that in the inner area, which is agreement with the cross-sectional SEM results of altered glass powders. However, no gaps were

present in glass coupon. The SALs displayed four sublayers based on the chemicals profiles in Figure 6(e): external layer, central layer and two gradient layers. Si, Al, Fe and Mg were enriched in external layer as its composition with Mg-smectite and the large affinity between Fe and Si.[188] The interface between external layer and central layer analyzed by energy filtered TEM (EFTEM) in Figure 6(b) was distinct and very sharp. The width of this interface was ~ 12 nm. As the 6.0 nm step size, the width (~ 60 nm) of the chemical gradients in external/central layer (Figure 6e) is notably larger than the width derived from EFTEM image. The structural interface between the pristine glass and SALs showed in Figure 6c was not a distinct linear band but the chemical gradients based on Si and Na in this interface was sharp (Figure 6f). The sharp structural interface was generally attributed to ICDP mechanism.[147] Moreover, nanoparticles smaller than 5 nm were observed on the top of external layer in Figure 6d. Here, we did not analyze their composition due to the fine size. Gin et al, also found that the rounded crystallized grains but with larger size (30-50 nm) were present in gel layer these grains were rich Ag, Te and S in the borosilicate glass altered for 26 y at 90 ℃.[190]

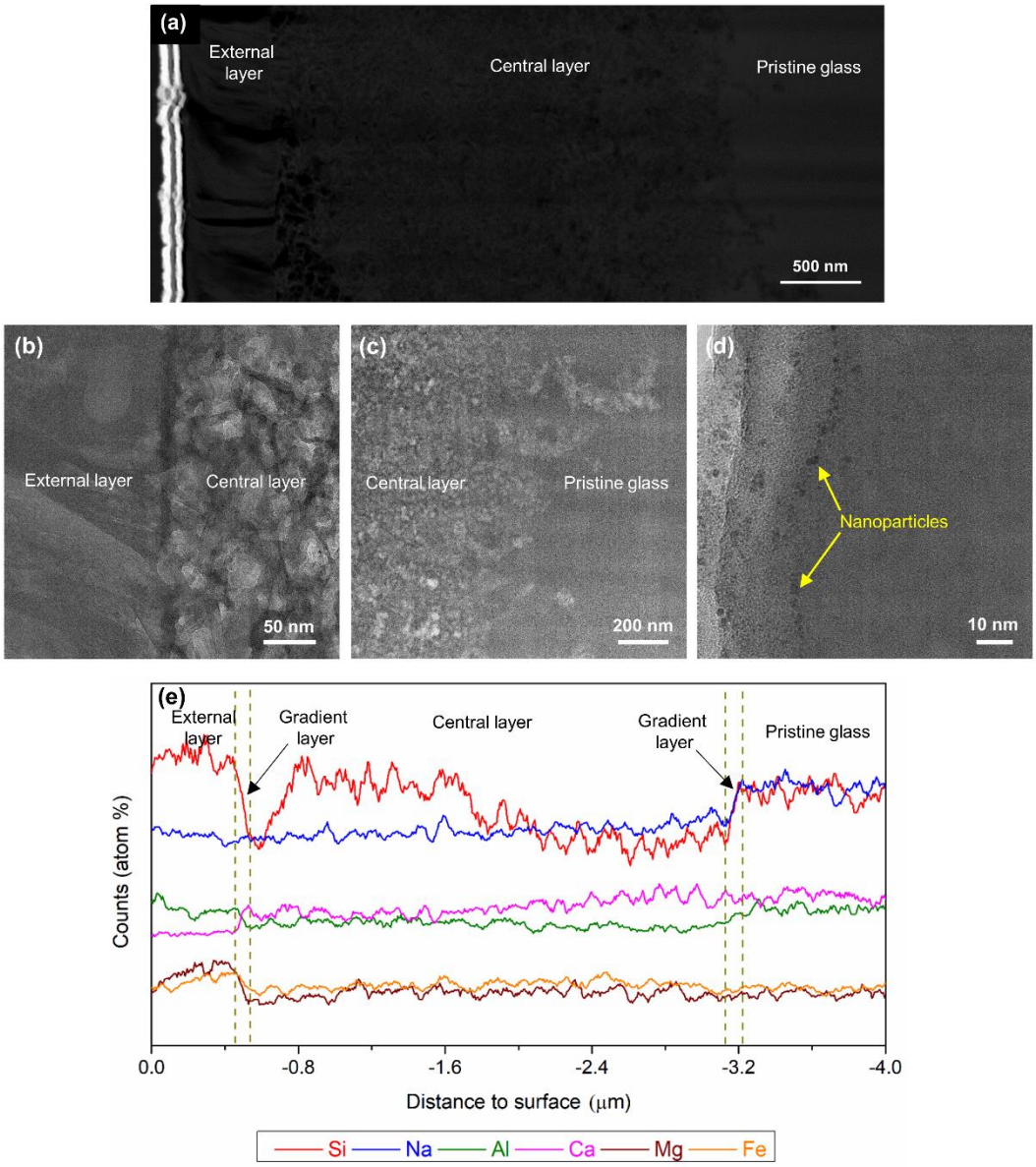

Figure 6. (S)TEM images and EFTEM elemental profiles of a FIB foil extracted from the glass coupon altered for 760 d in DIW pore water at 90 °C. (a) HAADF image showing SALs and porosity, (b) and (c) TEM images of interfaces in external/central layers and central layer/pristine glass respectively, and (d) elemental profiles.

Conclusion.

Understanding the formation and evolution of the SALs and the secondary phases is crucial for the determining of glass alteration mechanisms and the alteration rate

evolution.[151, 158, 162] Here, we studied borosilicate glass altered in DIW pore water at 90 ℃. We had found that, firstly, the secondary phases such as analcime ($NaSi_2AlO_6 \cdot H_2O$), zeolite ($Na_6Al_6\ Si_{10}O_{32} \cdot 12H_2O$), calcium silicate ($CaSiO_3$) and barite ($BaSO_4$) were formed by the precipitation of the (over)saturation ions in solution. However, the formation of smectite was followed by reorganization of silica aggregates and the crystallinity was gradually increased with alteration time. Analcime, zeolite and smectite, as the common secondary phases, were also formed during other glasses corroded.[161, 180, 182, 191] Meanwhile, we also identified unprecedently reported calcium silicate and barite during glass alternation. Secondly, there was a significant increase of porosity at 90d as a consequence of release of souble elements, while the overall decreasing trend of porosity from 90 to 760 d was probably caused by the reorganization of the SALs. The pore closure of the SALs were also observed in previous studies.[156, 171, 192] Thirdly, external layer with smectite coupling in time and space reorganized inwardly from glass surface, while the growth of gaps at the interface of SALs/pristine glass spread outwardly. Moreover, the alteration of glass powders and coupon was followed by ICDP process. In sum, we comprehensively studied the formation and evolution of secondary phases and SALs. This study was focused on borosilicate glasses, but it could be extended to silicate and natural glasses as well as minerals, such as on basaltic glasses or feldspars as their similarities on secondary phases, SALs, gaps and alteration mechanism.[156, 182, 184, 193] Furthemore, we studied the glass alternation under actual diposal conditions ($T \geqslant 90$ ℃, unsaturated/saturated with respect to water) with the extrally low kinetics of movement of underground wate.[194-196] Hence, this study could provide fundamental assessment on the potential uncertainty for long-term of the high level nuclear waste glasses.

Supporting Information

Associated content. Additional materials referenced in the text are available free of charge. The AFM image of coupon surface. The schematic diagram of experimental set up. The measurement method for DIW pore water. The calculation methods of the equivalent thickness (Eth) and the dissolution rate (r). The SEM images. The predicted secondary phases calculated by Geochemist's Workbench® code. The Cross-sectional SEM images of glass powders. The BSE image and the EDS mappings. The cross-section SEM image and the EDS analysis. The main elemental contents. The representative BSE images.

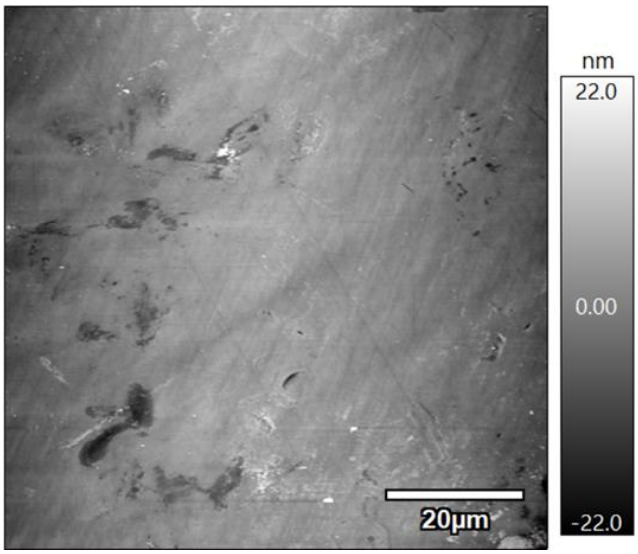

Figure S1. The AFM image of coupon surface after polishing showing the roughness less than 1 μm.

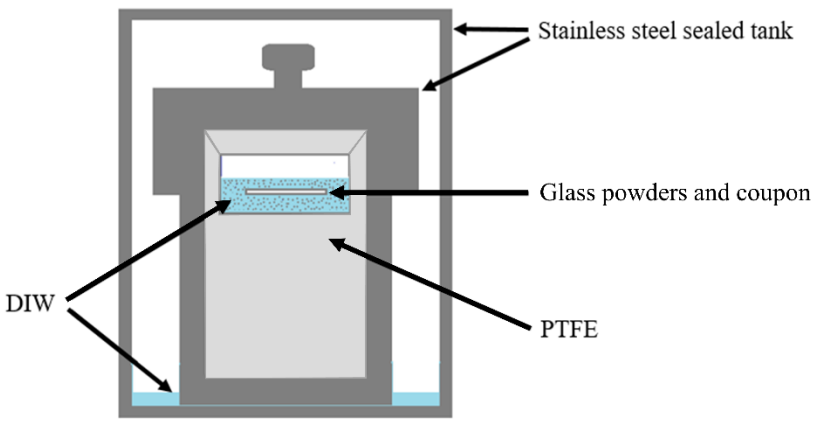

Figure S2. The schematic diagram of experimental set up. In order to reduce evaporation effect, the reactor was tightly closed after filling with 10.00 g glass powders, one glass coupon and 3.11 mL DIW (the volume of pore water) in polytetrafluoroethylene (PTFE), and then was placed in the stainless steel sealed tank containing a small amount of DIW. The tank was sealed with welding and put it in the oven at 90 ℃ for reaction. The blank experiments, adding 3.11 DIW but without glass in PTFE, to check the water loss were conducted in the same set up and the result suggested that the loss of water was within 7% in 380 d.

Text S1. 10.00 g of glass powders and 1 coupon were added in a sand core filter funnel with 5-15 μm pore size and then the total mass was A. Next, we added a certain amount of DIW, just covering the surface of glass powders and coupon, in the sand core filter funnel. The free water was filtered out by its gravity but the pore water between glass powders was retained. The total mass was B and the difference (B – A) was the mass of pore water. The average data of pore water in 10.00 glass powders and 1 coupon was 3.11g (3.11 mL) by six groups of experiments.

Text S2. The calculation of the equivalent thickness (Eth) and the dissolution rate (r) followed Gin et al. paper.[171] Eth(B)of altered glass powders was calculated from the measured concentration of B at t alteration as follows:

$$Eth(B)_t = Eth(B)_{t-1} + \frac{(C(B)_t - C(B)_{t-1})V_t}{\rho * S * x_B} \quad (1)$$

Where C(B) is the B concentration, V_t is the volume of the solution at t and it is 3.11 mL in our system, ρ is the density of glass (2.5 g/cm^3), S is the special surface area of glass powders (0.07 ± 0.001 m^2/g) and we neglected that of monolith, x_B is the mass fraction of B in glass (3.19 %). The dissolution rate (r) is calculated by:

$$r = \frac{d(Eth(B))}{dt} \quad (2)$$

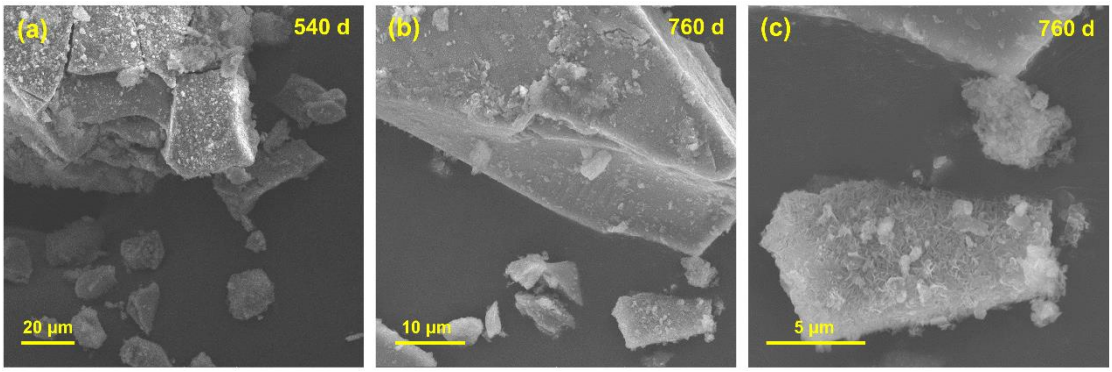

Figure S3. The SEM images of glass powders after alteration for 540 (a) and 760 (b and c). The smaller particles came off from the glass powders was likely smectite.

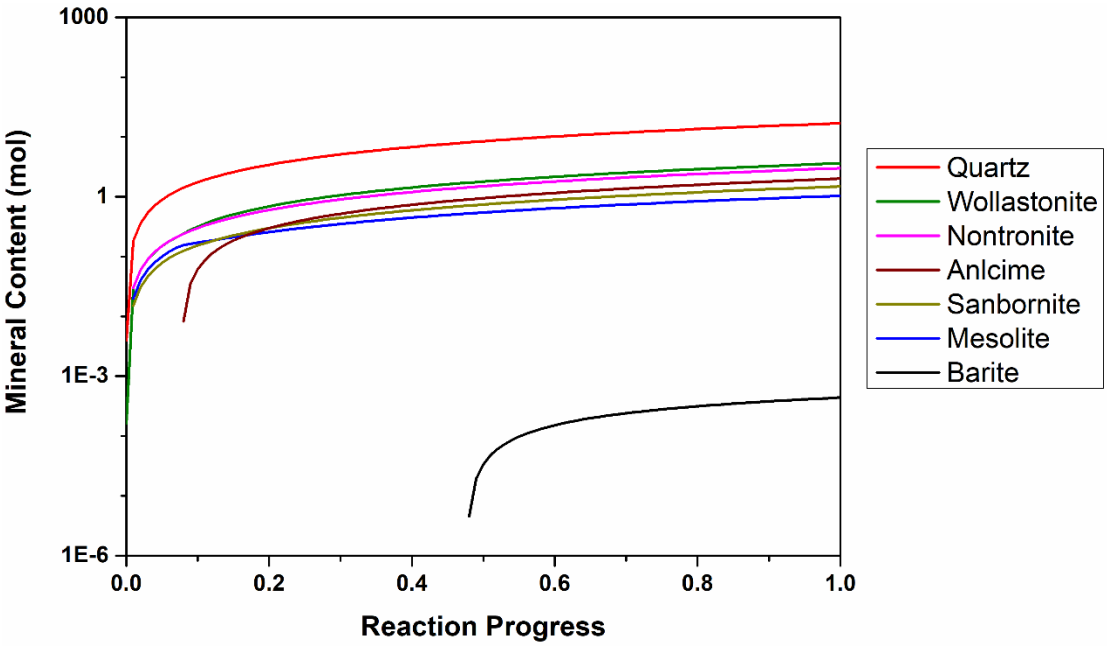

Figure S4. The predicted secondary phases calculated by Geochemist's Workbench® code during glass weathering at 90 °C and 1.01 bar.

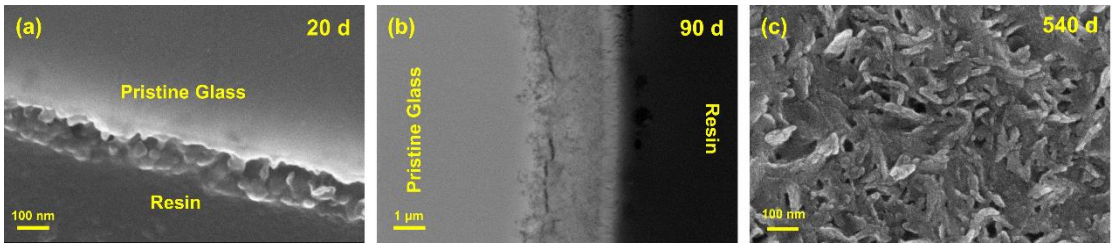

Figure S5. The Cross-sectional SEM images of glass powders with different alteration times. (a) magnification of silica aggregates at 20 d, (a) the distribution of porosity showing an increase of the porosity from the gaps towards the smectite layer, and (c) magnification of the silica aggregates and porosity in central layer at 540 d.

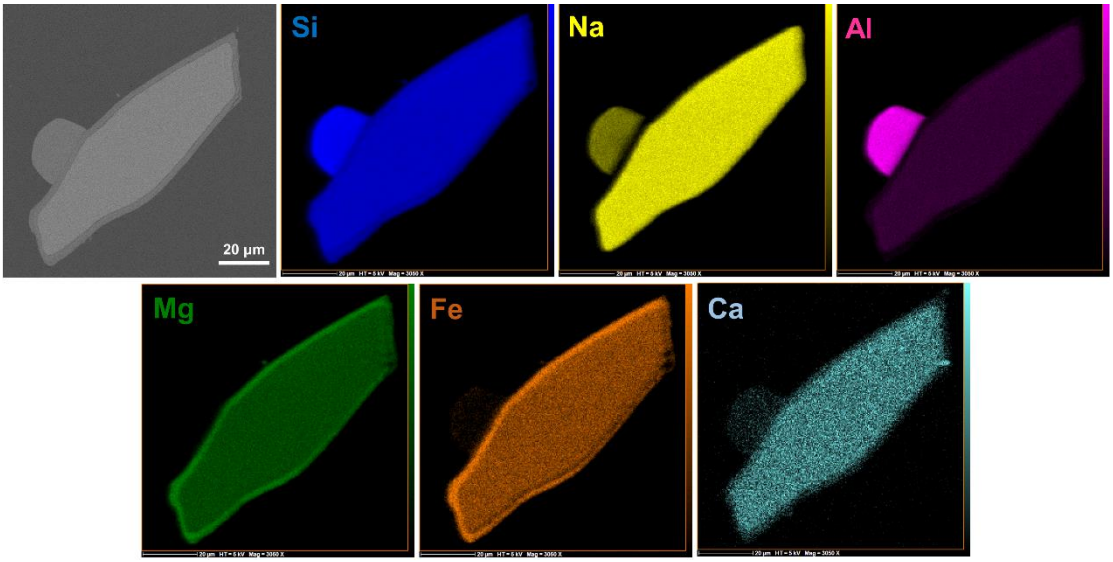

Figure S6. The cross-sectional backscattered electron (BSE) image of glass powder at 90 d and the EDS mappings. The particle with semicircle shape is analcime ($NaSi_2AlO_6 \cdot H_2O$).

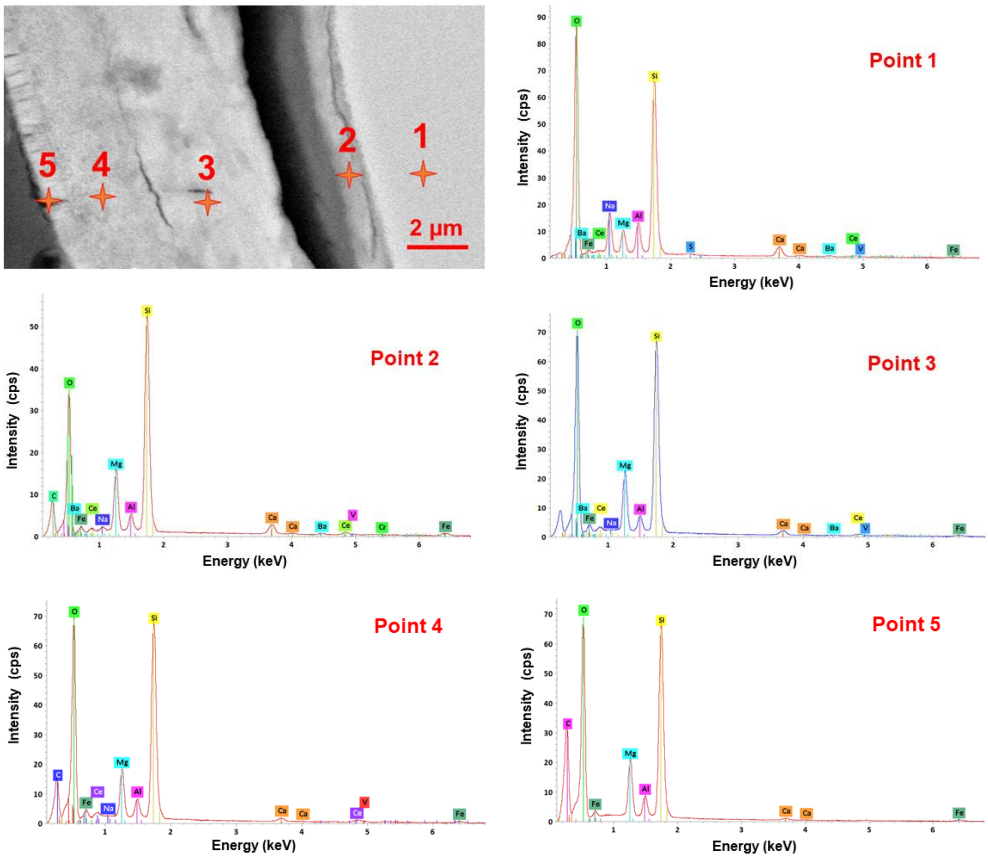

Figure S7. The cross-section SEM image of glass powder after reaction for 540 d and the EDS analysis at 10 kV at different positions.

Table S1. The main elemental contents (atomic %) of point 1 to 5 in Figure S4. (except

for oxygen)

Points	Si	Mg	Al	Na	Ca	Fe
1	24.48	2.47	3.12	5.05	3.13	1.18
2	36.40	7.76	1.93	0.39	3.14	3.83
3	29.85	7.19	1.69	0.07	1.87	2.37
4	29.75	5.63	2.00	-	1.16	2.17
5	23.37	4.83	1.64	-	0.55	1.84

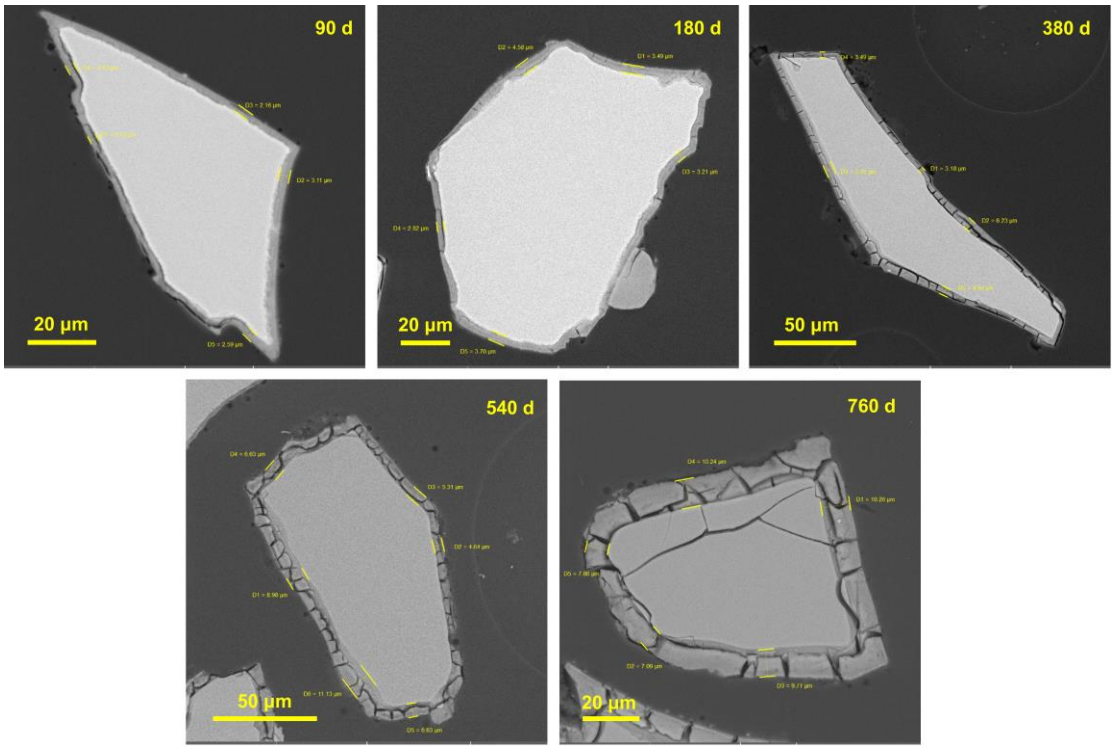

Figure S8. The representative cross-sectional backscattered electron (BSE) images of glass powders at different alteration times.

References:

1. SKB, Horizontal deposition of canisters for spent nuclear fuel. *Technical Report* **2008,** *TR08-03*.

2. Gaucher, E.; Robelin, C.; Matray, J. M.; Negral, G.; Gros, Y.; Heitz, J. F.; Vinsot, A.; Rebours, H.; Cassagnabere, A.; Bouchet, A., ANDRA underground research laboratory: interpretation of the mineralogical and geochemical data acquired in the Callovian-Oxfordian formation by investigative drilling. *Physics and Chemistry of the Earth* **2004,** *29* (1), 55-77.

3. ANDRA, Safetyevaluation of a geological repository, Dossier 2005 argile. **2005**.

4. Vinsot, A.; Mettler, S.; Wechner, S., In situ characterization of the Callovo-Oxfordian pore water composition. *Physics and Chemistry of the Earth* **2008,** *33*, S75-S86.

5. Mosser-Ruck, R.; Sterpenich, J.; Michau, N.; Jodin-Caumon, M. C.; Randi, A.; Abdelmoula, M.; Barres, O.; Cathelineau, M., Serpentinization and H-2 production during an iron-clay interaction experiment at 90C under low CO2 pressure. *Applied Clay Science* **2020,** *191*.

6. Trotignon, L.; Peycelon, H.; Bourbon, X. In *Performance assessment of CEM-I and CEM-V concrete engineered barriers in a clayey geological medium*, MIGRATION 2005, 10 international conference on chemistry and migration behaviour of actinides and fission products in the geosphere, France, France, 2005.

7. Fernández-Martínez, A.; Charlet, L., Selenium environmental cycling and bioavailability: a structural chemist point of view. *Reviews in Environmental Science and Bio/Technology* **2009,** *8* (1), 81-110.

8. Breynaert, E.; Bruggeman, C.; Maes, A., XANES-EXAFS analysis of se solid-phase reaction products formed upon contacting Se(IV) with FeS2 and FeS. *Environmental Science & Technology* **2008,** *42* (10), 3595-3601.

9. Bruggeman, C.; Maes, A.; Vancluysen, J.; Vandenmussele, P., Selenite reduction in Boom clay: Effect of FeS2, clay minerals and dissolved organic matter. *Environmental Pollution* **2005,** *137* (2), 209-221.

10. Charlet, L.; Scheinost, A. C.; Tournassat, C.; Greneche, J. M.; Gehin, A.; Fernandez-Martinez, A.; Coudert, S.; Tisserand, D.; Brendle, J., Electron transfer at the mineral/water interface: Selenium reduction by ferrous iron sorbed on clay. *Geochimica Et Cosmochimica Acta* **2007,** *71* (23), 5731-5749.

11. Sun, W. L.; Renew, J. E.; Zhang, W. L.; Tang, Y. Z.; Huang, C. H., Sorption of Se(IV) and Se(VI) to coal fly ash/cement composite: Effect of Cat(2+) and high ionic strength. *Chemical Geology* **2017,** *464*, 76-83.

12. Ma, B.; Fernandez-Martinez, A.; Wang, K. F.; Made, B.; Henocq, P.; Tisserand, D.; Bureau, S.; Charlet, L., Selenite Sorption on Hydrated CEM-V/A Cement in the Presence of Steel Corrosion Products: Redox vs Nonredox Sorption. *Environmental Science & Technology* **2020,** *54* (4), 2344-2352.

13. Bonhoure, I.; Baur, I.; Wieland, E.; Johnson, C. A.; Scheidegger, A. M., Uptake of Se(IV/VI) oxyanions by hardened cement paste and cement minerals: An X-ray absorption spectroscopy study. *Cement and Concrete Research* **2006,** *36* (1), 91-98.

14. Onoguchi, A.; Granata, G.; Haraguchi, D.; Hayashi, H.; Tokoro, C., Kinetics and mechanism of selenate and selenite removal in solution by green rust-sulfate. *Royal Society Open Science* **2019,** *6* (4).

15. Xu, L.; Huang, Y. H., Kinetics and mechanism of selenite reduction by zero valent iron under anaerobic condition activated and enhanced by dissolved Fe(II). *Science of the Total Environment* **2019,** *664*, 698-706.

16. Scheinost, A. C.; Charlet, L., Selenite reduction by mackinawite, magnetite and siderite: XAS characterization of nanosized redox products. *Environmental Science & Technology* **2008,** *42* (6), 1984-1989.

17. Wu, J.; Zeng, R. J., In Situ Preparation of Stabilized Iron Sulfide Nanoparticle-Impregnated Alginate Composite for Selenite Remediation. *Environmental Science & Technology* **2018,** *52* (11), 6487-6496.

18. Wu, J.; Zhao, J.; Li, H.; Miao, L. Z.; Hou, J.; Xing, B. S., Simultaneous Removal of Selenite and Selenate by Nanosized Zerovalent Iron in Anoxic Systems: The Overlooked Role of Selenite. *Environmental Science & Technology* **2021,** *55* (9), 6299-

6308.

19. Yalcintas, E.; Scheinost, A. C.; Gaona, X.; Altmaier, M., Systematic XAS study on the reduction and uptake of Tc by magnetite and mackinawite. *Dalton Transactions* **2016,** *45* (44), 17874-17885.

20. Giffaut, E.; Grive, M.; Blanc, P.; Vieillard, P.; Colas, E.; Gailhanou, H.; Gaboreau, S.; Marty, N.; Made, B.; Duro, L., Andra thermodynamic database for performance assessment: ThermoChimie. *Applied Geochemistry* **2014,** *49*, 225-236.

21. Poineau, F.; Fattahi, M.; Den Auwer, C.; Hennig, C.; Grambow, B., Speciation of technetium and rhenium complexes by in situ XAS-electrochemistry. *Radiochimica Acta* **2006,** *94* (5), 283-289.

22. Zachara, J. M.; Heald, S. M.; Jeon, B. H.; Kukkadapu, R. K.; Liu, C. X.; McKinley, J. P.; Dohnalkova, A. C.; Moore, D. A., Reduction of pertechnetate Tc(VII) by aqueous Fe(II) and the nature of solid phase redox products. *Geochimica Et Cosmochimica Acta* **2007,** *71* (9), 2137-2157.

23. Peretyazhko, T. S.; Zachara, J. M.; Kukkadapu, R. K.; Heald, S. M.; Kutnyakov, I. V.; Resch, C. T.; Arey, B. W.; Wang, C. M.; Kovarik, L.; Phillips, J. L.; Moore, D. A., Pertechnetate (TcO4-) reduction by reactive ferrous iron forms in naturally anoxic, redox transition zone sediments from the Hanford Site, USA. *Geochimica Et Cosmochimica Acta* **2012,** *92*, 48-66.

24. Ma, B.; Charlet, L.; Fernandez-Martinez, A.; Kang, M.; Made, B., A review of the retention mechanisms of redox-sensitive radionuclides in multi-barrier systems. *Applied Geochemistry* **2019,** *100*, 414-431.

25. NIAIST, Atlas of Eh-pH diagrams, Intercomparison of thermodynamic databases. **2005,** *No.419*.

26. Altmann, S., 'Geo'chemical research: A key building block for nuclear waste disposal safety cases. *Journal of Contaminant Hydrology* **2008,** *102* (3-4), 174-179.

27. Grambow, B., Mobile fission and activation products in nuclear waste disposal. *Journal of Contaminant Hydrology* **2008,** *102* (3-4), 180-186.

28. Breynaert, E.; Scheinost, A. C.; Dom, D.; Rossberg, A.; Vancluysen, J.; Gobechiya,

E.; Kirschhock, C. E. A.; Maes, A., Reduction of Se(IV) in Boom Clay: XAS Solid Phase Speciation. *Environmental Science & Technology* **2010,** *44* (17), 6649-6655.

29. Borsig, N.; Scheinost, A. C.; Shaw, S.; Schild, D.; Neumann, T., Retention and multiphase transformation of selenium oxyanions during the formation of magnetite via iron(II) hydroxide and green rust. *Dalton Transactions* **2018,** *47* (32), 11002-11015.

30. Gallegos, T. J.; Fuller, C. C.; Webb, S. M.; Betterton, W., Uranium(VI) Interactions with Mackinawite in the Presence and Absence of Bicarbonate and Oxygen. *Environmental Science & Technology* **2013,** *47* (13), 7357-7364.

31. Duro, L.; Domenech, C.; Grive, M.; Roman-Ross, G.; Bruno, J.; Kallstrom, K., Assessment of the evolution of the redox conditions in a low and intermediate level nuclear waste repository (SFR1, Sweden). *Applied Geochemistry* **2014,** *49*, 192-205.

32. Charlet, L.; Kang, M. L.; Bardelli, F.; Kirsch, R.; Gehin, A.; Greneche, J. M.; Chen, F. R., Nanocomposite Pyrite-Greigite Reactivity toward Se(IV)/Se(VI). *Environmental Science & Technology* **2012,** *46* (9), 4869-4876.

33. Han, D. S.; Batchelor, B.; Abdel-Wahab, A., Sorption of selenium(IV) and selenium(VI) onto synthetic pyrite (FeS2): Spectroscopic and microscopic analyses. *Journal of Colloid and Interface Science* **2012,** *368*, 496-504.

34. Kang, M. L.; Bardelli, F.; Charlet, L.; Gehin, A.; Shchukarev, A.; Chen, F. R.; Morel, M. C.; Ma, B.; Liu, C. L., Redox reaction of aqueous selenite with As-rich pyrite from Jiguanshan ore mine (China): Reaction products and pathway. *Applied Geochemistry* **2014,** *47*, 130-140.

35. Curti, E.; Aimoz, L.; Kitamura, A., Selenium uptake onto natural pyrite. *Journal of Radioanalytical and Nuclear Chemistry* **2013,** *295* (3), 1655-1665.

36. Ma, B.; Fernandez-Martinez, A.; Kang, M. L.; Wang, K. F.; Lewis, A. R.; Maffeis, T. G. G.; Findling, N.; Salas-Colera, E.; Tisserand, D.; Bureau, S.; Charlet, L., Influence of Surface Compositions on the Reactivity of Pyrite toward Aqueous U(VI). *Environmental Science & Technology* **2020,** *54* (13), 8104-8114.

37. Bruggeman, C.; Maes, N., Uptake of Uranium(VI) by Pyrite under Boom Clay Conditions: Influence of Dissolved Organic Carbon. *Environmental Science &*

Technology **2010,** *44* (11), 4210-4216.

38. Veeramani, H.; Scheinost, A. C.; Monsegue, N.; Qafoku, N. P.; Kukkadapu, R.; Newville, M.; Lanzirotti, A.; Pruden, A.; Murayama, M.; Hochella, M. F., Abiotic Reductive Immobilization of U(VI) by Biogenic Mackinawite. *Environmental Science & Technology* **2013,** *47* (5), 2361-2369.

39. Wharton, M. J.; Atkins, B.; Charnock, J. M.; Livens, F. R.; Pattrick, R. A. D.; Collison, D., An X-ray absorption spectroscopy study of the coprecipitation of Tc and Re with mackinawite (FeS). *Applied Geochemistry* **2000,** *15* (3), 347-354.

40. Rodriguez, D. M.; Mayordomo, N.; Schild, D.; Azzam, S. S. A.; Brendler, V.; Muller, K.; Stumpf, T., Reductive immobilization of Tc-99(VII) by FeS2: The effect of marcasite. *Chemosphere* **2021,** *281*.

41. Descostes, M.; Schlegel, M. L.; Eglizaud, N.; Descamps, F.; Miserque, F.; Simoni, E., Uptake of uranium and trace elements in pyrite (FeS2) suspensions. *Geochimica Et Cosmochimica Acta* **2010,** *74* (5), 1551-1562.

42. Wang, T.; Qian, T. W.; Huo, L. J.; Li, Y. F.; Zhao, D. Y., Immobilization of hexavalent chromium in soil and groundwater using synthetic pyrite particles. *Environmental Pollution* **2019,** *255*.

43. Huo, L. J.; Xie, W. B.; Qian, T. W.; Guan, X. H.; Zhao, D. Y., Reductive immobilization of pertechnetate in soil and groundwater using synthetic pyrite nanoparticles. *Chemosphere* **2017,** *174*, 456-465.

44. Liang, X. L.; Wei, G. L.; Xiong, J.; Tan, F. D.; He, H. P.; Qu, C. C.; Yin, H.; Zhu, J. X.; Zhu, R. L.; Qin, Z. H.; Zhang, J., Adsorption isotherm, mechanism, and geometry of Pb(II) on magnetites substituted with transition metals. *Chemical Geology* **2017,** *470*, 132-140.

45. Zhou, J. M.; Chen, S.; Liu, J.; Frost, R. L., Adsorption kinetic and species variation of arsenic for As(V) removal by biologically mackinawite (FeS). *Chemical Engineering Journal* **2018,** *354*, 237-244.

46. Kirsch, R.; Fellhauer, D.; Altmaier, M.; Neck, V.; Rossberg, A.; Fanghanel, T.; Charlet, L.; Scheinost, A. C., Oxidation State and Local Structure of Plutonium Reacted

with Magnetite, Mackinawite, and Chukanovite. *Environmental Science & Technology* **2011,** *45* (17), 7267-7274.

47. Jeong, H. Y.; Klaue, B.; Blum, J. D.; Hayes, K. F., Sorption of mercuric ion by synthetic manocrystalline mackinawite (FeS). *Environmental Science & Technology* **2007,** *41* (22), 7699-7705.

48. Scheinost, A. C.; Kirsch, R.; Banerjee, D.; Fernandez-Martinez, A.; Zaenker, H.; Funke, H.; Charlet, L., X-ray absorption and photoelectron spectroscopy investigation of selenite reduction by Fe-II-bearing minerals. *Journal of Contaminant Hydrology* **2008,** *102* (3-4), 228-245.

49. Marshall, T. A.; Morris, K.; Law, G. T. W.; Mosselmans, J. F. W.; Bots, P.; Parry, S. A.; Shaw, S., Incorporation and Retention of 99-Tc(IV) in Magnetite under High pH Conditions. *Environmental Science & Technology* **2014,** *48* (20), 11853-11862.

50. Saslow, S. K.; Um, W.; Pearce, C. I.; Engelhard, M. H.; Bowden, M. E.; Lukens, W.; Leavy, II; Riley, B. J.; Kirn, D. S.; Schweiger, M. J.; Kruger, A. A., Reduction and Simultaneous Removal of Tc-99 and Cr by Fe(OH)(2)(s) Mineral Transformation. *Environmental Science & Technology* **2017,** *51* (15), 8635-8642.

51. Hoving, A. L.; Munch, M. A.; Bruggeman, C.; Banerjee, D.; Behrends, T., Kinetics of selenite interactions with Boom Clay: adsorption-reduction interplay. In *Multiple Roles of Clays in Radioactive Waste Confinement*, Norris, S.; Neeft, E. A. C.; VanGeet, M., Eds. 2019; Vol. 482, pp 225-239.

52. Savoye, S.; Schlegel, M. L.; Frasca, B., Mobility of selenium oxyanions in clay-rich media: A combined batch and diffusion experiments and synchrotron-based spectroscopic investigation. *Applied Geochemistry* **2021,** *128*.

53. Bleyen, N.; Small, J. S.; Mijnendonckx, K.; Hendrix, K.; Albrecht, A.; De Canniere, P.; Surkova, M.; Wittebroodt, C.; Valcke, E., Ex and In Situ Reactivity and Sorption of Selenium in Opalinus Clay in the Presence of a Selenium Reducing Microbial Community. *Minerals* **2021,** *11* (7).

54. He, H. Y.; Liu, J.; Dong, Y.; Li, H. H.; Zhao, S. W.; Wang, J.; Jia, M. L.; Zhang, H.; Liao, J. L.; Yang, J. J.; Yang, Y. Y.; Liu, N., Sorption of selenite on Tamusu clay in

simulated groundwater with high salinity under aerobic/anaerobic conditions. *Journal of Environmental Radioactivity* **2019,** *203*, 210-219.

55. Bock, W.-D.; Brühl, H.; Trapp, C.; Winkler, A., Sorption properties of natural sulfides with respect to technetium. *MRS Online Proceedings Library (OPL)* **1988,** *127*.

56. Lieser, K.; Bauscher, C., Technetium in the hydrosphere and in the geosphere. Pt. 2. *Radiochimica Acta* **1988,** *44* (pt. 1), 125-128.

57. Liu, Y.; Terry, J.; Jurisson, S. S., Pertechnetate immobilization in aqueous media with hydrogen sulfide under anaerobic and aerobic environments. *Radiochimica Acta* **2007,** *95* (12), 717-725.

58. Lukens, W. W.; Bucher, J. J.; Shuh, D. K.; Edelstein, N. M., Evolution of technetium speciation in reducing grout. *Environmental science & technology* **2005,** *39* (20), 8064-8070.

59. Bruggeman, C.; Maes, A.; Vancluysen, J., The identification of FeS2 as a sorption sink for Tc(IV). *Physics and Chemistry of the Earth* **2007,** *32* (8-14), 573-580.

60. Wang, T.; Qian, T. W.; Zhao, D. Y.; Liu, X. N.; Ding, Q. W., Immobilization of perrhenate using synthetic pyrite particles: Effectiveness and remobilization potential. *Science of the Total Environment* **2020,** *725*.

61. Baur, I.; Johnson, C. A., Sorption of selenite and selenate to cement minerals. *Environmental Science & Technology* **2003,** *37* (15), 3442-3447.

62. Zhang, M.; Reardon, E. J., Removal of B, Cr, Mo, and Se from wastewater by incorporation into hydrocalumite and ettringite. *Environmental Science & Technology* **2003,** *37* (13), 2947-2952.

63. Rojo, H.; Scheinost, A. C.; Lothenbach, B.; Laube, A.; Wieland, E.; Tits, J., Retention of selenium by calcium aluminate hydrate (AFm) phases under strongly-reducing radioactive waste repository conditions. *Dalton Transactions* **2018,** *47* (12), 4209-4218.

64. Grambow, B.; Lopez-Garcia, M.; Olmeda, J.; Grive, M.; Marty, N. C. M.; Grangeon, S.; Claret, F.; Lange, S.; Deissmann, G.; Klinkenberg, M.; Bosbach, D.; Bucur, C.; Florea, I.; Dobrin, R.; Isaacs, M.; Read, D.; Kittnerova, J.; Drtinova, B.;

Vopalka, D.; Cevirim-Papaioannou, N.; Ait-Mouheb, N.; Gaona, X.; Altmaier, M.; Nedyalkova, L.; Lothenbach, B.; Tits, J.; Landesman, C.; Rasamimanana, S.; Ribet, S., Retention and diffusion of radioactive and toxic species on cementitious systems: Main outcome of the CEBAMA project. *Applied Geochemistry* **2020,** *112*.

65. Isaacs, M.; Lange, S.; Deissmann, G.; Bosbach, D.; Milodowski, A. E.; Read, D., Retention of technetium-99 by grout and backfill cements: Implications for the safe disposal of radioactive waste. *Applied Geochemistry* **2020,** *116*.

66. Ma, B.; Fernandez-Martinez, A.; Made, B.; Findling, N.; Markelova, E.; Salas-Colera, E.; Maffeis, T. G. G.; Lewis, A. R.; Tisserand, D.; Bureau, S.; Charlet, L., XANES-Based Determination of Redox Potentials Imposed by Steel Corrosion Products in Cement-Based Media. *Environmental Science & Technology* **2018,** *52* (20), 11931-11940.

67. Truche, L.; Bazarkina, E., Natural hydrogen the fuel of the 21 st century. *E3S Web of Conferences* **2019,** *98*.

68. Kausch, M. F.; Pallud, C. E., Modeling the impact of soil aggregate size on selenium immobilization. *Biogeosciences* **2013,** *10* (3), 1323-1336.

69. Finck, N.; Dardenne, K., Interaction of selenite with reduced Fe and/or S species: An XRD and XAS study. *Journal of Contaminant Hydrology* **2016,** *188*, 44-51.

70. Jung, B.; Safan, A.; Batchelor, B.; Abdel-Wahab, A., Spectroscopic study of Se(IV) removal from water by reductive precipitation using sulfide. *Chemosphere* **2016,** *163*, 351-358.

71. Nathalie MACE, P. N., Nathalie COREAU, Emilie THORY, Patrick LE BESCOP, Gaëtan TOUZE, Spécifications techniques: Préparation et caractérisations des PCH CEM V/A ROMBAS dans le cadre du GL CTEC DPC/SECR/ST/2015/057 indice A. **2015**.

72. Markelova, E.; Parsons, C. T.; Couture, R. M.; Smeaton, C. M.; Made, B.; Charlet, L.; Van Cappellen, P., Deconstructing the redox cascade: what role do microbial exudates (flavins) play? *Environmental Chemistry* **2017,** *14* (8), 515-524.

73. Ravel, B.; Newville, M., ATHENA, ARTEMIS, HEPHAESTUS: data analysis for

X-ray absorption spectroscopy using IFEFFIT. *Journal of Synchrotron Radiation* **2005,** *12*, 537-541.

74. Ankudinov, A. L.; Ravel, B.; Rehr, J. J.; Conradson, S. D., Real-space multiple-scattering calculation and interpretation of x-ray-absorption near-edge structure. *Physical Review B* **1998,** *58* (12), 7565-7576.

75. Han, D. S.; Batchelor, B.; Abdel-Wahab, A., Sorption of selenium(IV) and selenium(VI) to mackinawite (FeS): Effect of contact time, extent of removal, sorption envelopes. *J. Hazard. Mater.* **2011,** *186* (1), 451-457.

76. Mitchell, K.; Couture, R. M.; Johnson, T. M.; Mason, P. R. D.; Van Cappellen, P., Selenium sorption and isotope fractionation: Iron(III) oxides versus iron(II) sulfides. *Chemical Geology* **2013,** *342*, 21-28.

77. Kang, M. L.; Ma, B.; Bardelli, F.; Chen, F. R.; Liu, C. L.; Zheng, Z.; Wu, S. J.; Charlet, L., Interaction of aqueous Se(IV)/Se(VI) with FeSe/FeSe2: Implication to Se redox process. *J. Hazard. Mater.* **2013,** *248*, 20-28.

78. Diener, A.; Neumann, T.; Kramar, U.; Schild, D., Structure of selenium incorporated in pyrite and mackinawite as determined by XAFS analyses. *Journal of Contaminant Hydrology* **2012,** *133*, 30-39.

79. Geoffroy, N.; Demopoulos, G. P., The elimination of selenium(IV) from aqueous solution by precipitation with sodium sulfide. *J. Hazard. Mater.* **2011,** *185* (1), 148-154.

80. Sasaki, K.; Blowes, D. W.; Ptacek, C. J., Spectroscopic study of precipitates formed during removal of selenium from mine drainage spiked with selenate using permeable reactive materials. *Geochemical Journal* **2008,** *42* (3), 283-294.

81. Prasad, K. S.; Vaghasiya, J. V.; Soni, S. S.; Patel, J.; Patel, R.; Kumari, M.; Jasmani, F.; Selvaraj, K., Microbial Selenium Nanoparticles (SeNPs) and Their Application as a Sensitive Hydrogen Peroxide Biosensor. *Appl. Biochem. Biotechnol.* **2015,** *177* (6), 1386-1393.

82. Rapid growth of t-Se nanowires in acetone at room temperature and their photoelectrical properties. *Frontiers of Optoelectronics in China* **2011,** *4* (2), 188-194.

83. Turgeman, R.; Gedanken, A., Crystallization of ZnO on crystalline magnetite

nanoparticles in the presence of ultrasound radiation. *Crystal Growth & Design* **2006,** *6* (10), 2260-2265.

84. Wolthers, M.; Charlet, L.; Van der Linde, P. R.; Rickard, D.; Van der Weijden, C. H., Surface chemistry of disordered mackinawite (FeS). *Geochimica Et Cosmochimica Acta* **2005,** *69* (14), 3469-3481.

85. Lothenbach, B.; Rentsch, D.; Wieland, E., Hydration of a silica fume blended low-alkali shotcrete cement. *Physics and Chemistry of the Earth* **2014,** *70-71*, 3-16.

86. Mullet, M.; Boursiquot, S.; Abdelmoula, M.; Genin, J. M.; Ehrhardt, J. J., Surface chemistry and structural properties of mackinawite prepared by reaction of sulfide ions with metallic iron. *Geochimica Et Cosmochimica Acta* **2002,** *66* (5), 829-836.

87. Herbert, R. B.; Benner, S. G.; Pratt, A. R.; Blowes, D. W., Surface chemistry and morphology of poorly crystalline iron sulfides precipitated in media containing sulfate-reducing bacteria. *Chemical Geology* **1998,** *144* (1-2), 87-97.

88. Matamoros-Veloza, A.; Cespedes, O.; Johnson, B. R. G.; Stawski, T. M.; Terranova, U.; de Leeuw, N. H.; Benning, L. G., A highly reactive precursor in the iron sulfide system. *Nature Communications* **2018,** *9*.

89. Beauvais, M. L.; Chupas, P. J.; O'Nolan, D.; Parise, J. B.; Chapman, K. W., Resolving Single-layer Nanosheets as Short-lived Intermediates in the Solution Synthesis of FeS. *Acs Materials Letters* **2021,** *3* (6), 698-703.

90. Kang, M. L.; Bardelli, F.; Ma, B.; Charlet, L.; Chen, F. R.; Yang, Y. Q., The influence of pH and reaction time on the formation of FeSe2 upon selenite reduction by nano-sized pyrite-greigite. *Radiochimica Acta* **2016,** *104* (9), 649-656.

91. Benning, L. G.; Wilkin, R. T.; Barnes, H. L., Reaction pathways in the Fe-S system below 100 degrees C. *Chemical Geology* **2000,** *167* (1-2), 25-51.

92. Hunger, S.; Benning, L. G., Greigite: a true intermediate on the polysulfide pathway to pyrite. *Geochemical Transactions* **2007,** *8*.

93. Bourdoiseau, J. A.; Jeannin, M.; Remazeilles, C.; Sabota, R.; Refait, P., The transformation of mackinawite into greigite studied by Raman spectroscopy. *Journal of Raman Spectroscopy* **2011,** *42* (3), 496-504.

94. Ma, B.; Kang, M. L.; Zheng, Z.; Chen, F. R.; Xie, J. L.; Charlet, L.; Liu, C. L., The reductive immobilization of aqueous Se(IV) by natural pyrrhotite. *J. Hazard. Mater.* **2014,** *276*, 422-432.

95. Hua, B.; Deng, B. L., Reductive Immobilization of Uranium(VI) by Amorphous Iron Sulfide. *Environmental Science & Technology* **2008,** *42* (23), 8703-8708.

96. Lothenbach, B.; Le Saout, G.; Ben Haha, M.; Figi, R.; Wieland, E., Hydration of a low-alkali CEM III/B-SiO2 cement (LAC). *Cement and Concrete Research* **2012,** *42* (2), 410-423.

97. Han, D. S.; Batchelor, B.; Abdel-Wahab, A., XPS analysis of sorption of selenium(IV) and selenium(VI) to mackinawite (FeS). *Environmental Progress & Sustainable Energy* **2013,** *32* (1), 84-93.

98. Lan, Y.; Butler, E. C., Iron-Sulfide-Associated Products Formed during Reductive Dechlorination of Carbon Tetrachloride. *Environmental Science & Technology* **2016,** *50* (11), 5489-5497.

99. Landais, P., Advances in geochemical research for the underground disposal of high-level, long-lived radioactive waste in a clay formation. *Journal of Geochemical Exploration* **2006,** *88* (1-3), 32-36.

100. Saheb, M.; Descostes, M.; Neff, D.; Matthiesen, H.; Michelin, A.; Dillmann, P., Iron corrosion in an anoxic soil: Comparison between thermodynamic modelling and ferrous archaeological artefacts characterised along with the local in situ geochemical conditions. *Applied Geochemistry* **2010,** *25* (12), 1937-1948.

101. Kim, Y.; Yuan, K.; Ellis, B. R.; Becker, U., Redox reactions of selenium as catalyzed by magnetite: Lessons learned from using electrochemistry and spectroscopic methods. *Geochimica Et Cosmochimica Acta* **2017,** *199*, 304-323.

102. Goberna-Ferron, S.; Asta, M. P.; Zareeipolgardani, B.; Bureau, S.; Findling, N.; Simonelli, L.; Greneche, J. M.; Charlet, L.; Fernandez-Martinez, A., Influence of Silica Coatings on Magnetite-Catalyzed Selenium Reduction. *Environmental Science & Technology* **2021,** *55* (5), 3021-3031.

103. Lindberg, R. D.; Runnells, D. D., Ground Water Redox Reactions: An Analysis

of Equilibrium State Applied to Eh Measurements and Geochemical Modeling. *Science* **1984,** *225* (4665), 925-927.

104. Stefansson, A.; Amorsson, S.; Sveinbjornsdottir, A. E., Redox reactions and potentials in natural waters at disequilibrium. *Chemical Geology* **2005,** *221* (3-4), 289-311.

105. Kumar, A. R.; Riyazuddin, P., Seasonal variation of redox species and redox potentials in shallow groundwater: A comparison of measured and calculated redox potentials. *Journal of Hydrology* **2012,** *444*, 187-198.

106. Wei, D. W.; OsseoAsare, K., Particulate pyrite formation by the Fe3+/HS- reaction in aqueous solutions: Effects of solution composition. *Colloids and Surfaces a-Physicochemical and Engineering Aspects* **1996,** *118* (1-2), 51-61.

107. Liu, X.; Fattahi, M.; Montavon, G.; Grambow, B., Selenide retention onto pyrite under reducing conditions. *Radiochimica Acta* **2008,** *96* (8), 473-479.

108. Ma, B.; Nie, Z.; Liu, C. L.; Kang, M. L.; Bardelli, F.; Chen, F. R.; Charlet, L., Kinetics of FeSe2 oxidation by ferric iron and its reactivity compared with FeS2. *Science China-Chemistry* **2014,** *57* (9), 1300-1309.

109. Bebie, J.; Schoonen, M. A. A.; Fuhrmann, M.; Strongin, D. R., Surface charge development on transition metal sulfides: An electrokinetic study. *Geochimica Et Cosmochimica Acta* **1998,** *62* (4), 633-642.

110. Schaufuss, A. G.; Nesbitt, H. W.; Kartio, I.; Laajalehto, K.; Bancroft, G. M.; Szargan, R., Incipient oxidation of fractured pyrite surfaces in air. *Journal of Electron Spectroscopy and Related Phenomena* **1998,** *96* (1-3), 69-82.

111. Demoisson, F.; Mullet, M.; Humbert, B., Investigation of pyrite oxidation by hexavalent chromium: Solution species and surface chemistry. *Journal of Colloid and Interface Science* **2007,** *316* (2), 531-540.

112. Zhang, F.; Jiao, Y. Q.; Wu, L. Q.; Rong, H., Relations between pyrite morphologies and uranium mineralization in the Shuanglong region, northern China. *Ore Geology Reviews* **2022,** *141*.

113. Rodriguez, D. M.; Mayordomo, N.; Scheinost, A. C.; Schild, D.; Brendler, V.;

Muller, K.; Stumpf, T., New Insights into Tc-99(VII) Removal by Pyrite: A Spectroscopic Approach. *Environmental Science & Technology* **2020,** *54* (5), 2678-2687.

114.Gotic, M.; Koscec, G.; Music, S., Study of the reduction and reoxidation of substoichiometric magnetite. *Journal of Molecular Structure* **2009,** *924*, 347-354.

115.Lemly, A. D., Aquatic selenium pollution is a global environmental safety issue. *Ecotoxicology and Environmental Safety* **2004,** *59* (1), 44-56.

116.Nriagu, J. O.; Wong, H. K., SELENIUM POLLUTION OF LAKES NEAR THE SMELTERS AT SUDBURY, ONTARIO. *Nature* **1983,** *301* (5895), 55-57.

117.Gerson, A. R.; Fan, R.; Qian, G. J.; Schumann, R. C.; Olin, P.; Howard, D. L.; Smart, R. S. C., Examination of multiple sources of selenium release from coal wastes and strategies for remediation. *J. Hazard. Mater.* **2022,** *422*.

118.Bourchy, A.; Saslow, S. A.; Williams, B. D.; Avalos, N. M.; Um, W.; Canfield, N. L.; Sweet, L.; Smith, G. L.; Asmussen, R. M., The evolution of hydrated lime-based cementitious waste forms during leach testing leading to enhanced technetium retention. *J. Hazard. Mater.* **2022,** *430*.

119.Bouakkaz, R.; Abdelouas, A.; El Mendili, Y.; David, K.; Grambow, B., Alteration of Si-29-doped SON68 borosilicate nuclear waste glass in the presence of near field materials. *Applied Geochemistry* **2019,** *111*.

120. Smart, N. R.; Rance, A. P.; Werme, L. O., The effect of radiation on the anaerobic corrosion of steel. *Journal of Nuclear Materials* **2008,** *379* (1-3), 97-104.

121. Tang, C. L.; Huang, Y. P.; Zhang, Z. Q.; Chen, J. J.; Zeng, H.; Huang, Y. H., Rapid removal of selenate in a zero-valent iron/Fe3O4/Fe2+ synergetic system. *Applied Catalysis B-Environmental* **2016,** *184*, 320-327.

122. Chaudhary, S.; Umar, A.; Mehta, S. K., Selenium nanomaterials: An overview of recent developments in synthesis, properties and potential applications. *Progress in Materials Science* **2016,** *83*, 270-329.

123. Guleria, A.; Neogy, S.; Adhikari, S., Room temperature ionic liquid assisted synthesis of highly stable amorphous Se nanoparticles: A rapid and facile methodology.

Materials Letters **2018,** *217*, 198-201.

124. Tougerti, A.; Cristol, S.; Berrier, E.; Briois, V.; La Fontaine, C.; Villain, F.; Joly, Y., XANES study of rhenium oxide compounds at the L-1 and L-3 absorption edges. *Physical Review B* **2012,** *85* (12).

125. Kim, E.; Boulegue, J., Chemistry of rhenium as an analogue of technetium: Experimental studies of the dissolution of rhenium oxides in aqueous solutions. *Radiochimica Acta* **2003,** *91* (4), 211-216.

126. Kobayashi, T.; Scheinost, A. C.; Fellhauer, D.; Gaona, X.; Altmaier, M., Redox behavior of Tc(VII)/Tc(IV) under various reducing conditions in 0.1 M NaCl solutions. *Radiochimica Acta* **2013,** *101* (5), 323-332.

127. Murray, H.; Kelty, S.; Chianelli, R.; Day, C., Structure of rhenium disulfide. *Inorganic Chemistry* **1994,** *33* (19), 4418-4420.

128. Liu, J. J.; Yang, T.; Peng, Q.; Yang, Y.; Li, Y. W.; Wen, X. D., Theoretical exploration of the interaction between hydrogen and pyrite-type FeS2 surfaces. *Applied Surface Science* **2021,** *537*.

129. Fu, Y. H.; Nie, X.; Qin, Z. H.; Li, S. S.; Wan, Q., Effect of Particle Size and Pyrite Oxidation on the Sorption of Gold Nanoparticles on the Surface of Pyrite. *Journal of Nanoscience and Nanotechnology* **2017,** *17* (9), 6367-6376.

130. Frohlich, D. R.; Amayri, S.; Drebert, J.; Grolimund, D.; Huth, J.; Kaplan, U.; Krause, J.; Reich, T., Speciation of Np(V) uptake by Opalinus Clay using synchrotron microbeam techniques. *Analytical and Bioanalytical Chemistry* **2012,** *404* (8), 2151-2162.

131. Frasca, B.; Savoye, S.; Wittebroodt, C.; Leupin, O. X.; Michelot, J. L., Comparative study of Se oxyanions retention on three argillaceous rocks: Upper Toarcian (Tournemire, France), Black Shales (Tournemire, France) and Opalinus Clay (Mont Terri, Switzerland). *Journal of Environmental Radioactivity* **2014,** *127*, 133-140.

132. Beauwens, T.; De Canniere, P.; Moors, H.; Wang, L.; Maes, N., Studying the migration behaviour of selenate in Boom Clay by electromigration. *Engineering Geology* **2005,** *77* (3-4), 285-293.

133. Xu, W. P.; Qin, H. B.; Zhu, J. M.; Johnson, T. M.; Tan, D. C.; Liu, C. S.; Takahashi, Y., Selenium isotope fractionation during adsorption onto montmorillonite and kaolinite. *Applied Clay Science* **2021,** *211*.

134. Goldberg, S., Modeling Selenate Adsorption Behavior on Oxides, Clay Minerals, and Soils Using the Triple Layer Model. *Soil Science* **2014,** *179* (12), 568-576.

135. Suzuki, T.; Sue, K.; Morotomi, H.; Niinae, M.; Yokoshima, M.; Nakata, H., Immobilization of selenium(VI) in artificially contaminated kaolinite using ferrous ion salt and magnesium oxide. *Journal of Environmental Chemical Engineering* **2019,** *7* (1).

136. Montes-Hernandez, G.; Findling, N.; Renard, F., Direct and Indirect Nucleation of Magnetite Nanoparticles from Solution Revealed by Time-Resolved Raman Spectroscopy. *Crystal Growth & Design* **2021,** *21* (6), 3500-3510.

137. Liang, Y. X.; Bai, P. P.; Zhou, J.; Wang, T. Q.; Luo, B. W.; Zheng, S. Q., An efficient precursor to synthesize various FeS2 nanostructures via a simple hydrothermal synthesis method. *Crystengcomm* **2016,** *18* (33), 6262-6271.

138. Kar, S.; Chaudhuri, S., Solvothermal synthesis of nanocrystalline FeS2 with different morphologies. *Chemical Physics Letters* **2004,** *398* (1-3), 22-26.

139. Chapman, P.; Adams, W.; Brooks, M.; Delos, C.; Luoma, S.; Maher, W.; Ohlendorf, H.; Presser, T.; Shaw, D., Ecological assessment of selenium in the aquatic environment: Summary of a SETAC Pellston Workshop. *Society of Environmental Toxicology and Chemistry, Pensacola* **2009**.

140. Schafer, T.; Claret, F.; Bauer, A.; Griffault, L.; Ferrage, E.; Lanson, B., Natural organic matter (NOM)-clay association and impact on Callovo-Oxfordian clay stability in high alkaline Solution: Spectromicroscopic evidence. *Journal De Physique Iv* **2003,** *104*, 413-416.

141. Claret, F.; Schafer, T.; Rabung, T.; Wolf, M.; Bauer, A.; Buckau, G., Differences in properties and Cm(III) complexation behavior of isolated humic and fulvic acid derived from Opalinus clay and Callovo-Oxfordian argillite. *Applied*

Geochemistry **2005,** *20* (6), 1158-1168.

142. Wang, K. F.; Zhao, Y. F.; Yang, Z. W.; Lin, Z. M.; Tan, Z. Y.; Du, L.; Liu, C. L., Concentration and characterization of groundwater colloids from the northwest edge of Sichuan basin, China. *Colloids and Surfaces a-Physicochemical and Engineering Aspects* **2018,** *537*, 85-91.

143. Grambow, B., Nuclear waste glasses - How durable? *Elements* **2006,** *2* (6), 357-364.

144. Guittonneau, C.; Gin, S.; Godon, N.; Mestre, J. P.; Dugne, O.; Allegri, P., A 25-year laboratory experiment on French SON68 nuclear glass leached in a granitic environment - First investigations. *Journal of Nuclear Materials* **2011,** *408* (1), 73-89.

145. Dessert, C.; Dupre, B.; Gaillardet, J.; Francois, L. M.; Allegre, C. J., Basalt weathering laws and the impact of basalt weathering on the global carbon cycle. *Chemical Geology* **2003,** *202* (3-4), 257-273.

146. Silvestri, A.; Molin, G.; Salviulo, G., Roman and medieval glass from the Italian area: Bulk characterization and relationships with production technologies. *Archaeometry* **2005,** *47*, 797-816.

147. Hellmann, R.; Cotte, S.; Cadel, E.; Malladi, S.; Karlsson, L. S.; Lozano-Perez, S.; Cabie, M.; Seyeux, A., Nanometre-scale evidence for interfacial dissolution-reprecipitation control of silicate glass corrosion. *Nature Materials* **2015,** *14* (3), 307-311.

148. Geisler, T.; Dohmen, L.; Lenting, C.; Fritzsche, M. B. K., Real-time in situ observations of reaction and transport phenomena during silicate glass corrosion by fluid-cell Raman spectroscopy. *Nature Materials* **2019,** *18* (4), 342-+.

149. Geisler, T.; Janssen, A.; Scheiter, D.; Stephan, T.; Berndt, J.; Putnis, A., Aqueous corrosion of borosilicate glass under acidic conditions: A new corrosion mechanism. *Journal of Non-Crystalline Solids* **2010,** *356* (28-30), 1458-1465.

150. Hellmann, R., *Mechanisms of Glass Corrosion by Aqueous Solutions*. Encyclopedia of Glass Science, Technology, History, and Culture, 2021; Vol. Chapter 5.12.

151. Gin, S.; Guo, X. L.; Delaye, J. M.; Angeli, F.; Damodaran, K.; Testud, V.; Du, J. C.; Kerisit, S.; Kim, S. H., Insights into the mechanisms controlling the residual corrosion rate of borosilicate glasses. *Npj Materials Degradation* **2020,** *4* (1).

152. Gin, S.; Neill, L.; Fournier, M.; Frugier, P.; Ducasse, T.; Tribet, M.; Abdelouas, A.; Parruzot, B.; Neeway, J.; Wall, N., The controversial role of inter-diffusion in glass alteration. *Chemical Geology* **2016,** *440*, 115-123.

153. Gin, S.; Collin, M.; Jollivet, P.; Fournier, M.; Minet, Y.; Dupuy, L.; Mahadevan, T.; Kerisit, S.; Du, J. C., Dynamics of self-reorganization explains passivation of silicate glasses. *Nature Communications* **2018,** *9*.

154. Frankel, G. S.; Vienna, J. D.; Lian, J.; Guo, X. L.; Gin, S.; Kim, S. H.; Du, J. C.; Ryan, J. V.; Wang, J. W.; Windl, W.; Taylor, C. D.; Scully, J. R., Recent Advances in Corrosion Science Applicable To Disposal of High-Level Nuclear Waste. *Chemical Reviews* **2021,** *121* (20), 12327-12383.

155. Thorpe, C. L.; Neeway, J. J.; Pearce, C. I.; Hand, R. J.; Fisher, A. J.; Walling, S. A.; Hyatt, N. C.; Kruger, A. A.; Schweiger, M.; Kosson, D. S.; Arendt, C. L.; Marcial, J.; Corkhill, C. L., Forty years of durability assessment of nuclear waste glass by standard methods. *Npj Materials Degradation* **2021,** *5* (1).

156. Cailleteau, C.; Angeli, F.; Devreux, F.; Gin, S.; Jestin, J.; Jollivet, P.; Spalla, O., Insight into silicate-glass corrosion mechanisms. *Nature Materials* **2008,** *7* (12), 978-983.

157. Vienna, J. D.; Ryan, J. V.; Gin, S.; Inagaki, Y., Current Understanding and Remaining Challenges in Modeling Long-Term Degradation of Borosilicate Nuclear Waste Glasses. *International Journal of Applied Glass Science* **2013,** *4* (4), 283-294.

158. Gin, S.; Frugier, P.; Jollivet, P.; Bruguier, F.; Curti, E., New Insight into the Residual Rate of Borosilicate Glasses: Effect of S/V and Glass Composition. *International Journal of Applied Glass Science* **2013,** *4* (4), 371-382.

159. McGrail, B. P.; Ebert, W. L.; Bakel, A. J.; Peeler, D. K., Measurement of kinetic rate law parameters on a Na-Ca-Al borosilicate glass for low-activity waste. *Journal of Nuclear Materials* **1997,** *249* (2-3), 175-189.

160. Ojovan, M. I., On Alteration Rate Renewal Stage of Nuclear Waste Glass Corrosion. *Mrs Advances* **2020,** *5* (3-4), 111-120.

161. Mercado-Depierre, S.; Fournier, M.; Gin, S.; Angeli, F., Influence of zeolite precipitation on borosilicate glass alteration under hyperalkaline conditions. *Journal of Nuclear Materials* **2017,** *491*, 67-82.

162. Frugier, P.; Gin, S.; Minet, Y.; Chave, T.; Bonin, B.; Godon, N.; Lartigue, J. E.; Jollivet, P.; Ayral, A.; De Windt, L.; Santarini, G., SON68 nuclear glass dissolution kinetics: Current state of knowledge and basis of the new GRAAL model. *Journal of Nuclear Materials* **2008,** *380* (1-3), 8-21.

163. Valle, N.; Verney-Carron, A.; Sterpenich, J.; Libourel, G.; Deloule, E.; Jollivet, P., Elemental and isotopic (Si-29 and O-18) tracing of glass alteration mechanisms. *Geochimica Et Cosmochimica Acta* **2010,** *74* (12), 3412-3431.

164. Gin, S.; Jollivet, P.; Fournier, M.; Berthon, C.; Wang, Z. Y.; Mitroshkov, A.; Zhu, Z. H.; Ryan, J. V., The fate of silicon during glass corrosion under alkaline conditions: A mechanistic and kinetic study with the International Simple Glass. *Geochimica Et Cosmochimica Acta* **2015,** *151*, 68-85.

165. Ma, B.; Lothenbach, B., Synthesis, characterization, and thermodynamic study of selected K-based zeolites. *Cement and Concrete Research* **2021,** *148*.

166. Wilkin, R. T.; Barnes, H. L., Solubility and stability of zeolites in aqueous solution: I. Analcime, Na-, and K-clinoptilolite. *American Mineralogist* **1998,** *83* (7-8), 746-761.

167. Bethke, C. M., The geochemist's workbench. Release 10.0. GWB essentials guide. *Aqueous Solutions LLC* **2014**.

168. Verney-Carron, A.; Gin, S.; Frugier, P.; Libourel, G., Long-term modeling of alteration-transport coupling: Application to a fractured Roman glass. *Geochimica Et Cosmochimica Acta* **2010,** *74* (8), 2291-2315.

169. Wang, Y. F.; Jove-Colon, C. F.; Kuhlman, K. L., Nonlinear dynamics and instability of aqueous dissolution of silicate glasses and minerals. *Scientific Reports* **2016,** *6*.

170. Gin, S.; Ryan, J. V.; Schreiber, D. K.; Neeway, J.; Cabie, M., Contribution of atom-probe tomography to a better understanding of glass alteration mechanisms: Application to a nuclear glass specimen altered 25 years in a granitic environment. *Chemical Geology* **2013,** *349*, 99-109.

171. Gin, S.; Jollivet, P.; Fournier, M.; Angeli, F.; Frugier, P.; Charpentier, T., Origin and consequences of silicate glass passivation by surface layers. *Nat Commun* **2015,** *6*, 6360.

172. Bouakkaz, R.; Abdelouas, A.; El Mendili, Y.; Grambow, B.; Gin, S., SON68 glass alteration under Si-rich solutions at low temperature (35-90 degrees C): kinetics, secondary phases and isotopic exchange studies. *Rsc Advances* **2016,** *6* (76), 72616-72633.

173. Reiser, J. T.; Parruzot, B.; Gin, S.; Bonnett, J. F.; Smoljan, C. S.; Seymour, L. M.; Ryan, J. V.; Vienna, J. D., Effects of Al:Si and (Al plus Na):Si ratios on the static corrosion of sodium-boroaluminosilicate glasses. *International Journal of Applied Glass Science* **2022,** *13* (1), 94-111.

174. Ribet, S.; Gin, S., Role of neoformed phases on the mechanisms controlling the resumption of SON68 glass alteration in alkaline media. *Journal of Nuclear Materials* **2004,** *324* (2-3), 152-164.

175. Trivelpiece, C. L.; Rice, J. A.; Clark, N. L.; Kabius, B.; Jantzen, C. M.; Pantano, C. G., Corrosion of ISG fibers in alkaline solutions. *Journal of the American Ceramic Society* **2017,** *100* (10), 4533-4547.

176. Inagaki, Y.; Shinkai, A.; Idemistu, K.; Arima, T.; Yoshikawa, H.; Yui, M., Aqueous alteration of Japanese simulated waste glass P0798: Effects of alteration-phase formation on alteration rate and cesium retention. *Journal of Nuclear Materials* **2006,** *354* (1-3), 171-184.

177. Gin, S.; Beaudoux, X.; Angeli, F.; Jegou, C.; Godon, N., Effect of composition on the short-term and long-term dissolution rates of ten borosilicate glasses of increasing complexity from 3 to 30 oxides. *Journal of Non-Crystalline Solids* **2012,** *358* (18-19), 2559-2570.

178. Schulze, D. G., CLAY MINERALS. In *Encyclopedia of Soils in the Environment*, Hillel, D., Ed. Elsevier: Oxford, 2005; pp 246-254.

179. Kumar, A.; Shrivastava, J. P.; Meenakshi; Chopra, S.; Chakraborty, S., Impact glass applied as a standard for long-term performance assessment of Na-Ba borosilicate glass forms in geological environment. *Applied Geochemistry* **2020,** *114*.

180. Arena, H.; Godon, N.; Rebiscoul, D.; Frugier, R.; Podor, R.; Garces, E.; Cabie, M.; Mestre, J. P., Impact of iron and magnesium on glass alteration: Characterization of the secondary phases and determination of their solubility constants. *Applied Geochemistry* **2017,** *82*, 119-133.

181. Narayanasamy, S.; Jollivet, P.; Godon, N.; Angeli, F.; Gin, S.; Cabie, M.; Cambedouzou, J.; Le Guillou, C.; Abdelouas, A., Influence of composition of nuclear waste glasses on vapor phase hydration. *Journal of Nuclear Materials* **2019,** *525*, 53-71.

182. Arena, H.; Godon, N.; Rebiscoul, D.; Podor, R.; Garces, E.; Cabie, M.; Mestre, J. P., Impact of Zn, Mg, Ni and Co elements on glass alteration: Additive effects. *Journal of Nuclear Materials* **2016,** *470*, 55-67.

183. Fleury, B.; Godon, N.; Ayral, A.; Gin, S., SON68 glass dissolution driven by magnesium silicate precipitation. *Journal of Nuclear Materials* **2013,** *442* (1-3), 17-28.

184. Geisler, T.; Nagel, T.; Kilburn, M. R.; Janssen, A.; Icenhower, J. P.; Fonseca, R. O. C.; Grange, M.; Nemchin, A. A., The mechanism of borosilicate glass corrosion revisited. *Geochimica et Cosmochimica Acta* **2015,** *158*, 112-129.

185. Dohmen, L.; Lenting, C.; Fonseca, R. O. C.; Nagel, T.; Heuser, A.; Geisler, T.; Denkler, R., Pattern Formation in Silicate Glass Corrosion Zones. *International Journal of Applied Glass Science* **2013,** *4* (4), 357-370.

186. Fenter, P.; Sturchio, N. C., Mineral-water interfacial structures revealed by synchrotron X-ray scattering. *Progress in Surface Science* **2004,** *77* (5-8), 171-258.

187. Marry, V.; Rotenberg, B.; Turq, P., Structure and dynamics of water at a clay surface from molecular dynamics simulation. *Physical Chemistry Chemical Physics* **2008,** *10* (32), 4802-4813.

188. Michelin, A.; Burger, E.; Rebiscoul, D.; Neff, D.; Bruguier, F.; Drouet, E.; Dillmann, P.; Gin, S., Silicate Glass Alteration Enhanced by Iron: Origin and Long-Term Implications. *Environmental Science & Technology* **2013,** *47* (2), 750-756.

189. Thien, B. M. J.; Godon, N.; Ballestero, A.; Gin, S.; Ayral, A., The dual effect of Mg on the long-term alteration rate of AVM nuclear waste glasses. *Journal of Nuclear Materials* **2012,** *427* (1-3), 297-310.

190. Gin, S.; Guittonneau, C.; Godon, N.; Neff, D.; Rebiscoul, D.; Cabié, M.; Mostefaoui, S., Nuclear Glass Durability: New Insight into Alteration Layer Properties. *The Journal of Physical Chemistry C* **2011,** *115* (38), 18696-18706.

191. Strachan, D. M.; Neeway, J. J., Effects of alteration product precipitation on glass dissolution. *Applied Geochemistry* **2014,** *45*, 144-157.

192. Jollivet, P.; Angeli, F.; Cailleteau, C.; Devreux, F.; Frugier, P.; Gin, S., Investigation of gel porosity clogging during glass leaching. *Journal of Non-Crystalline Solids* **2008,** *354* (45-46), 4952-4958.

193. Hellmann, R.; Penisson, J. M.; Hervig, R. L.; Thomassin, J. H.; Abrioux, M. F., An EFTEM/HRTEM high-resolution study of the near surface of labradorite feldspar altered at acid pH: evidence for interfacial dissolution-reprecipitation. *Physics and Chemistry of Minerals* **2003,** *30* (4), 192-197.

194. Plas, F.; Wendling, J. In *The geological research in France - The Dossier 2005 Argile*, 30th Symposium on Scientific Basis for Nuclear Waste Management, Boston, MA, Nov 27-Dec 01; Boston, MA, 2006; pp 493-+.

195. Stuckless, J. S.; Dudley, W. W., The geohydrologic setting of Yucca Mountain, Nevada. *Applied Geochemistry* **2002,** *17* (6), 659-682.

196. Wang, J.; Chen, L.; Su, R.; Zhao, X. G., The Beishan underground research laboratory for geological disposal of high-level radioactive waste in China: Planning, site selection, site characterization and in situ tests. *Journal of Rock Mechanics and Geotechnical Engineering* **2018,** *10* (3), 411-435.